Applications of Physical Chemistry in Solar Energy, Membrane Biophysics, and Cultural Heritage

Glennis Elizabeth Rayermann

A dissertation

submitted in partial fulfillment of the

requirements for the degree of

Doctor of Philosophy

University of Washington

2018

Reading Committee:

Sarah L. Keller, Chair

Anne B. McCoy

Ashleigh B. Theberge

Program Authorized to Offer Degree:

Chemistry

University of Washington

Abstract

Applications of Physical Chemistry in Solar Energy, Membrane Biophysics, and Cultural Heritage

Glennis Elizabeth Rayermann

Chair of the Supervisory Committee:
Professor Sarah L. Keller
Departments of Chemistry and Physics

This dissertation records detailed applications of concepts and techniques in physical chemistry to a wide range of systems. Topics include: 1) A review of electrical scanning probe microscopy (SPM) methods for analyzing properties of solar energy materials, particularly organic photovoltaics (OPVs), on the nanoscale. 2) Detection of charge traps induced by photooxidative damage in bulk heterojunction (BHJ) OPVs via time-resolved electrostatic force microscopy (tr-EFM). 3) Development of a novel SPM technique with sub-microsecond time resolution. 4) Investigation of the morphology dependence of charge trap formation in BHJ OPVs using tr-EFM. 5) Direct observation of hallmarks of micron-scale liquid-liquid phase separation in the membranes of unperturbed, living cells via fluorescence microscopy. 6) A scientific investigation of the Indianapolis Museum of Art's (IMA) *Madonna and Child* (IMA#51.98), a modern fake of a Trecento panel painting attributed to the artist, restorer, and forger Icilio Federico Joni. This body of work underscores the applicability and value of methods

in physical chemistry to quantitative problems important in a wide range of fields. Here, those fields include solar energy, membrane biophysics, and cultural heritage.

TABLE OF CONTENTS

LIST OF FIGURES

LIST OF TABLES

ACKNOWLEDGEMENTS

For the solar energy research, thanks to: Prof. David S. Ginger, Rajiv Giridharagopal, Prof. Cody W. Schlenker, Dr. Obadiah G. Reid, Dr. Guozheng Shao, Dr. David T. Moore, Dr. Kristina Knesting, and Dr. Elisabeth Starr.

For the membrane biophysics research, thanks to: Prof. Sarah L. Keller, Prof. Alexey J. Merz, Dr. Scott Rayermann, Caitlin Cornell, Rachael Plemel, Mengtong (Tom) Duan, Dr. Aaron Halpern, Tyler Chozinski, Marco Howard, Lauren Gagnon, Prof. Joshua Vaughan, and members of the amphiphiliphiles past and present – with special thanks to Dr. Joan Bleecker, Dr. Jonathan Litz, Brenda Kessenich, Chantelle Leveille, and Catherine Chang.

For the cultural heritage conservation science research, thanks to: Dr. Gregory D. Smith, Anna Stein, Fiona Beckett, Erica Schuler, Kurt Hostettler, Dr. Victor Chen, Dr. Sara Hubbard, Leslie Freitas, Rebecca Norris, Sue Dupuis, David Miller, Erin Hornbach, and the security and staff at the Indianapolis Museum of Art at Newfields.

DEDICATION

To my parents, who always prioritized and supported my education.

And to George, without whom this would have been so much harder. Thanks for keeping me fed and caffeinated (with all the *good* coffee).

Chapter 1. ELECTRICAL SCANNING PROBE MICROSCOPY ON SOLAR CELL MATERIALS

My contributions to this work: I collaborated in crafting the outline of the chapter content. I was the primary author of sections 1.4, "AC-Mode AFM;" 1.5, "Electrostatic Force Microscopy;" and 1.7, "Time-resolved Electrostatic Force Microscopy." I performed the literature search and provided summaries of references for cAFM, pcAFM, and SKPM on inorganic photovoltaics. I co-edited all drafts of the chapter. I generated Figure 1.6 with design input from my co-authors.

1.1 INTRODUCTION

Solar power is a compelling research topic because sunlight is the most abundant renewable energy source available. However, deploying solar power on the terawatt scale necessary to achieve a global impact on our energy supply is a major undertaking. Such an effort will benefit from new materials that can lower systems costs while requiring less energy to manufacture. To this end, a host of nanostructured materials are being explored for next generation solar cells. These materials range from nanocrystal quantum dots for carrier multiplication[1,2] to colloidal inks for printed CIGS and CZTS cells[3–7] and from nanostructures for enhanced light trapping[8,9] to nanostructured bulk heterojunctions to achieve large internal surface area in organic photovoltaics (OPVs).[10–16] Beyond the active semiconductor layers, the transparent conductive oxides that are widely used as contacts in thin film solar cells are also known to exhibit nanoscale heterogeneities that could affect device performance.[17,18]

Characterizing how local structural and electronic heterogeneity affect solar cell performance is thus an important challenge facing many thin film solar cell technologies — including both organic bulk heterojunctions as well as solution processed inorganic thin films.[11-14] From a fundamental standpoint, it is important to understand the microscopic origins of photocurrent, recombination centers, defect propagation, and so on. From an engineering perspective, there is a great demand to accelerate the rate at which laboratory scale "champion cell" efficiencies are translated to manufacturing scales. In many cases, changes in film morphology due to changes in processing conditions are culprits in the ensuing efficiency losses, and the ability to examine how local performance is degrading in parallel with local structure is needed to speed up this translational work.

Scanning probe microscopy (SPM) techniques are ideally suited to these challenges because they can probe functioning solar cell materials and devices under operating conditions. While most modern analytical and microscopy methods have important roles to play in understanding materials for next generation solar cells, SPM methods are unique in their ability to directly correlate local film structure with local properties such as photocurrent, carrier mobility, recombination rate, and photovoltage. Although SPM is often thought of as a surface technique,[19] and this may be true of topography-only images, functional SPM methods can convey information about processes occurring throughout the depth of a film — even probing buried interfaces.[20–22]

In this chapter, we discuss some of the basic applications of these electrical and optoelectronic scanning probe microscopy methods for probing thin film photovoltaic systems. Rather than providing a comprehensive review, we emphasize practical aspects of implementing and interpreting SPM on thin film solar cells and review some of the key concepts related to the theory of these SPM methods under common experimental conditions. Because many examples are drawn from our own research, there is a natural bias towards the discussion of organic thin film materials. Nevertheless, many of these techniques can find analogous applications in inorganic thin films.[23,24]

While the physics of organic solar cells has been reviewed elsewhere[10,16,25,26] we provide a brief summary of the relevant device structure and operational principles here, because they are important to many of the example systems discussed below.

In organic semiconductors, light absorption produces neutral singlet excitons with a Coulombic binding energy of ~0.5 eV. To generate a photocurrent, these excitons must be dissociated at an interface, typically one between two semiconductors with different electron

affinities. The role of nanoscale film texture (morphology) is critical because there is an inherent length mismatch between the ~10 nm exciton diffusion length in organic semiconductors and the 150–200 nm thickness required to absorb a significant proportion of incoming light. To account for both of these issues, the active layer in organic devices is often a *bulk heterojunction*, wherein the electron donor and electron acceptor materials are co-deposited onto the substrate to form an active layer of thickness ~100–200 nm, with interpenetrating nanoscale domains of donor and acceptor.[11,13] Bulk heterojunction structures are usually achieved by mixing a conjugated polymer and fullerene derivative together in a common solvent, though other work has focused on vacuum co-deposition of semiconducting oligomers and fullerenes,[27] or conjugated polymers and inorganic nanocrystals[28–32] to achieve the same effect. In the ideal case, the resulting layers possess both a large interfacial surface area between the donor and acceptor domains as well as interconnected pathways for all carriers to reach the extracting electrodes.

We summarize some typical scanning probe methods in Table 1.1. The different methods each have unique applications to energy systems. cAFM and pcAFM are contact-mode techniques, while EFM, SKPM, and trEFM are noncontact mode techniques. There are some limitations to these methods, which are discussed further below. Though STM use is widespread in the semiconductor literature,[33] we do not discuss it here because the conductivity variations in typical organic bulk heterojunctions impede many STM experiments.

Table 1.1. Some types of scanning probe methods commonly used on solar cells.

Method	Resolution (nm)	Selected Uses in Energy Systems
Electrostatic Force Microscopy (EFM)	<50	Charge trapping/injection via measuring potential/field profiles
Scanning Kelvin Probe Microscopy (SKPM)	<50	Photovoltage, work function
Time-Resolved Electrostatic Force Microscopy (trEFM)	<80	Quantum efficiency mapping, transient charging, photodegradation/trap formation
Conductive Atomic Force Microscopy (cAFM)	5-10	Hole and electron transport, local mobility, materials contrast by injection barrier
Photoconductive Atomic Force Microscopy (pcAFM)	5-10	Photocurrent, local light I-V curves and mapping
Scanning Tunneling Microscopy (STM)	<1, atomic	Molecular charge transfer, density of states mapping

1.2 Conducting Atomic Force Microscopy (cAFM)

Conducting atomic force microscopy (cAFM) is usually implemented as a contact-mode technique that simultaneously records topography and electrical current information. Unlike STM, which uses tunneling current as a feedback mechanism, cAFM uses force feedback. The tip is brought close to the surface until it is deflected by a preset value, effectively contacting the film at constant force. In cAFM, a voltage is applied between a metal AFM tip and a substrate and the current is recorded at each pixel in the image, yielding a current map with spatial resolution close to that of the tip radius. If the tip position is held constant and the voltage swept,

a local *I-V* curve is acquired. It is possible, though time-consuming, to record such curves at each pixel to yield a rich set of electrical information about the substrate.

In solar cell materials, particularly nanostructured bulk heterojunction systems, cAFM data are useful for probing the lateral variation in photocurrent, as well as the extraction or injection of either electrons or holes, depending on the bias polarity.[34,35] The injection barrier heights as a function of bias can be used to map materials composition at the surface, which in heterogeneous solar cells is not always obvious from the topography.[36,37]

cAFM is commonly used in inorganic systems as well. Conductive AFM has been employed to image the local current variations of amorphous and crystalline silicon, silicon nanowires, and mixed-phase silicon,[38–42] grain boundaries in CIGS[24,43] and CdTe,[44] antiphase domains of GaAs on Ge,[45] and ZnO nanorods used for dye-sensitized solar cells.[46] Furthermore, cAFM can be used to collect *I-V* curves at specific locations, such as on individual ZnO nanorods,[46] random vs. (112)-preferential CIGS films in order to distinguish between recombination- and diffusion-dominated current,[43] or on individual silicon nanowires to determine their conductivity and resistivity.[38]

Solar cells are photodiodes, so cAFM *I-V* data often yield diode-like curves. In effect, the tip forms the top contact of a transient nanoscopic device pixel. However, when performing cAFM on either organic or inorganic materials, one should always keep in mind that the tip/sample contact is both physically and chemically different from the top contact that is used in a completed device structure. For example, it is possible to measure relative local charge mobilities by making space charge limited current (SCLC) measurements with cAFM.[47–49] However, extracting quantitative local mobility values requires accounting for the local tip geometry, dielectric factors, and sample thickness.[48]

We note that the physical contact of the tip with the sample in cAFM is both a strength and a weakness. As a strength, it provides robust topographic feedback on samples that would be difficult or impossible to image with STM due to regions of low conductivity. As a weakness, it means both the tip and sample are subject to potential wear. In practice this means the user must often optimize both the tip material and set point force and approach the imaging of any new system with care. A quick way to assess physical sample damage is to image a small area, then to widen the scan area to image a larger region containing the previous image. On the other hand, damage to the tip can be harder to spot, aside from decreases in current or resolution over the course of an image set. Fortunately, there is a wide range of commercially available conducting tips, from Au and Pt coated cantilevers to doped diamond and metal carbide tips that one can experiment with.

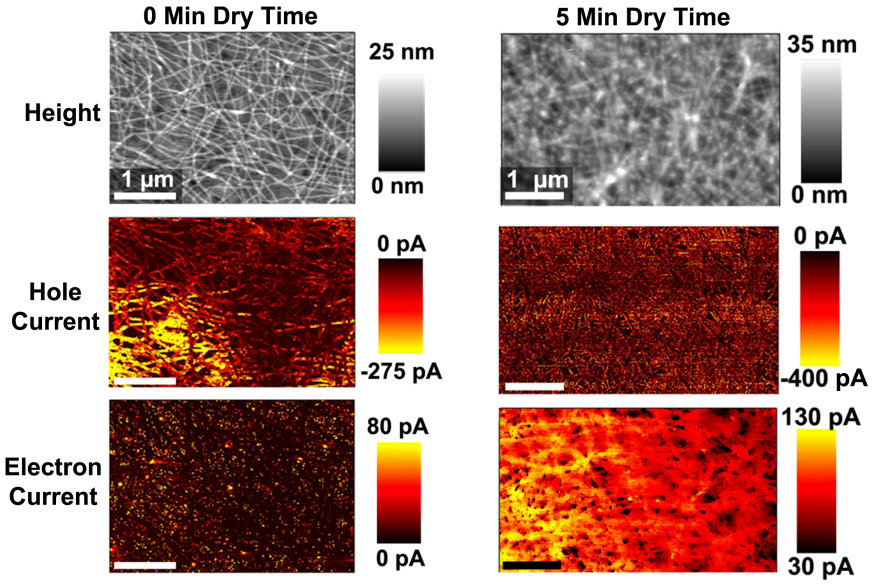

Figure 1.1. Correlated topography, dark hole current (+3 V applied to the tip), and dark electron current (−3 V applied to the tip) on a P3HT nanowire: PCBM film with 0 and 5 minutes pre-spin drying time.[35]

We have generally found that working in adhesive contact mode works well for soft samples, even permitting the imaging of polymer nanowires solar cell blends formed using

different processing steps (Figure 1.1).[35] The voltage polarity allows us to map the electron and hole current over the same area, and the relative current magnitudes can be used to determine the composition of the top layer. However, while adhesive mode is attractive from both a tip and sample wear perspective, it can be challenging to implement even for an experienced user.

1.3 PHOTOCONDUCTIVE ATOMIC FORCE MICROSCOPY (PCAFM)

Conventional cAFM requires a bias in order to generate a current. However, in a solar cell under illumination there is a current even at 0 V bias (called the short-circuit current, J_{SC}). The J_{SC} and the open-circuit voltage V_{OC} are two of the critical metrics in evaluating a solar cell's efficiency. In AFM, it is possible to generate a photocurrent image similar to the current images in conventional cAFM by illuminating the tip-sample junction. The laser generates photocurrent, which at 0 V bias corresponds to a local J_{SC}. This technique, photoconductive AFM (pcAFM), measures lateral variations in photoinduced charge generation and collection over the surface. Sweeping the voltage yields *I-V* curves spanning J_{SC} to the open circuit voltage V_{OC}. pcAFM is one of the more popular AFM methods to combine both optical and electrical information on organic materials.[34,35,37,50-54] pcAFM is applied to inorganic semiconductors as well, and has aided investigations into the underlying causes of difference in performance on ZnO nanorods[55, 56] and grain boundaries in CIGS.[24]

Because of the small contact area from the tip, generating an easily measured current in pcAFM can require a fairly high optical power density. A decent solar cell might have a short circuit current density on the order of ~10–30 mA/cm^2. Operating at 1 sun illumination, an AFM tip with a 40-nm-diameter contact would thus be expected to generate a DC photocurrent on the order of only ~100–300 fA, which can be experimentally challenging to measure while imaging. If one does measure pA photocurrents with only 1000 W/m^2 intensity, it is easy to conclude that

the photocurrent is being collected from an area much larger than the tip size — even if the experiment is able to resolve very fine features (often due to surface/contact variations).

To circumvent this intensity/current bottleneck, we have favored implementing pcAFM using a diffraction limited laser spot co-aligned with the AFM tip.[14] A diffraction limited laser spot from a small laser can easily achieve an intensity that is tens or thousands[57] of times that of natural sunlight, bringing the measured currents up to the level of pA or tens of pA.

The advantage of using a very small laser spot at these high intensities is that the total power delivered is still very low and is delivered into a small volume with a large surface area, which helps to minimize any appreciable sample heating[57] and limits accelerated photodegradation from areas of the device that are not being imaged. Nevertheless, if the goal is to map short circuit current, care must be taken so as not to drive the device into a current density range where higher-order recombination processes dominate. It is good practice to measure the current density as a function of light intensity, and to work in the linear range (assuming the device being studied gives a photocurrent linear with light intensity near AM1.5) whenever possible.[50,58]

As noted in the cAFM section, using a soft setpoint (at least for organic PV measurements) is often required because of the soft nature of these materials. Even with low setpoints, mechanical damage can still occur, thereby making it impossible to reliably image the same area of the film twice (to correlate pcAFM and dark cAFM over the same features, for example). Some particularly soft or sticky polymer surfaces require that the setpoint be set to *negative* deflection after engaging the surface, which results in an “attractive mode” cAFM or pcAFM image.[35] Measured currents tend to be lower because the tip is in softer contact with the surface, and the drift must be minimal or the feedback loop may disengage the tip from the

surface. However, this technique allows for repeatable imaging over most OPV systems with limited damage assuming that current preamplifier signal:noise and lateral drift are kept sufficiently low.

The pcAFM method can be a powerful probe of the active layer of a solar cell. Our group has shown with pcAFM that most bulk heterojunction solar cells can be viewed as a parallel array of solar cells wired together, each with different performance. The result is that there is often a wide distribution of J_{SC} values across a device, with some areas of the film working more efficiently than others.

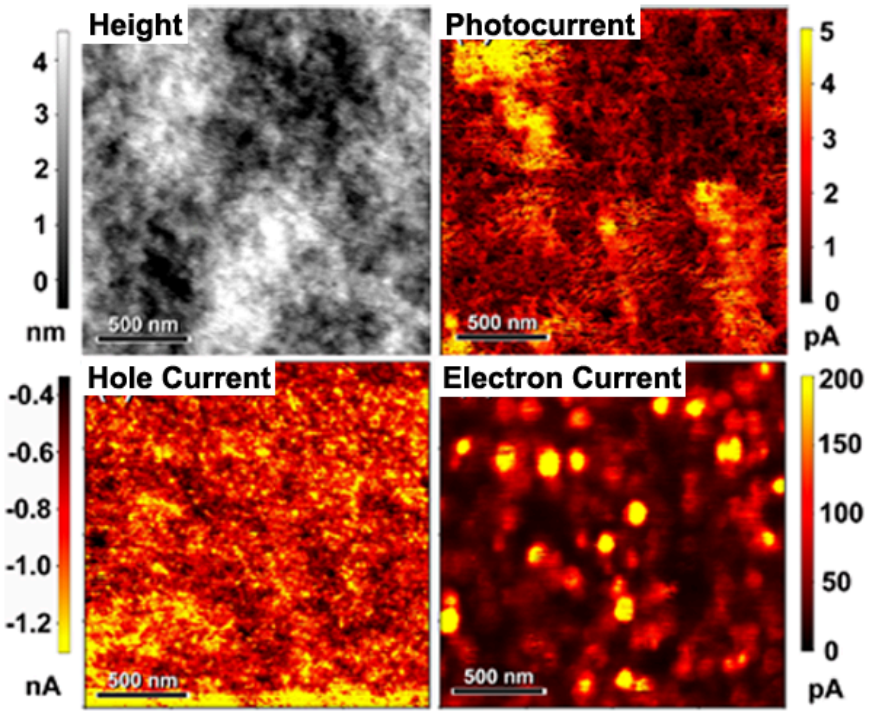

Figure 1.2. Topography, pcAFM short-circuit photocurrent (0 V applied), cAFM dark hole current (+5 V applied to the tip), cAFM dark electron current (−5 V applied to the tip) for an annealed P3HT:PCBM blend.[34]

pcAFM can also be used to look for particular bottlenecks in device performance. For instance, in Figure 1.2 it is clear that the short-circuit photocurrent, and electron and hole dark currents, are not strongly correlated. This is because dark currents require a connected pathway

between the top surface and bottom electrode for injection and extraction of the same carrier type, while the photocurrent requires a donor-acceptor interface and paths for electrons and holes traveling in opposite directions.

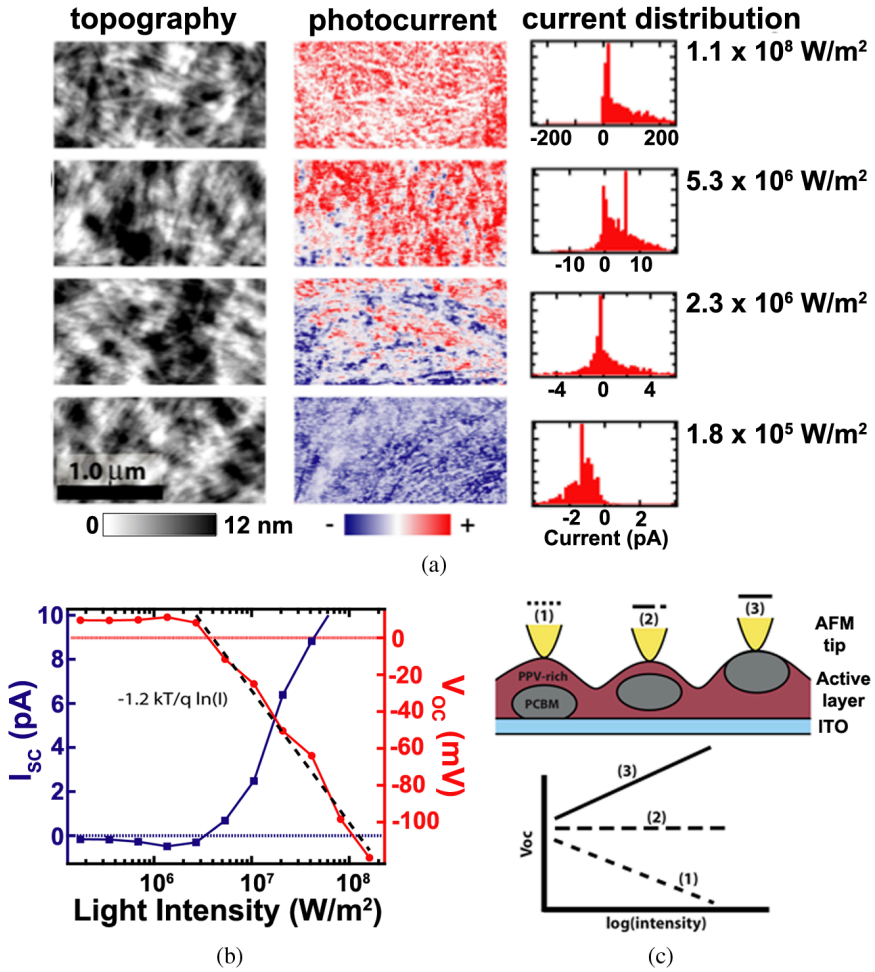

Figure 1.3. (a) Topography, pcAFM short-circuit photocurrent, and spatial distribution in the short-circuit photocurrent with changes in light intensity. (b) V_{OC} (circles, right axis) and I_{SC} (squares, left axis) as a function of light intensity measured from *I-V* curves on the surface. The black dashed line fits the V_{OC} data using the intensity-dependent V_{OC} expression found in Reid et al. *Journal of Applied Physics* **108**, 084320 (2010). (c) Simplified schematic for a polymer:fullerene system showing how the V_{OC} vs. light intensity slope changes with vertical anisotropy. All data were taken with a 532 nm laser.[57]

Going beyond 2D imaging, it is possible to use pcAFM to infer information about local vertical film structure by examining the intensity dependence of pcAFM data.[57] In Figure 1.3, the surface shows the surprising result that not only the magnitude, but also the *sign* of the short-

circuit photocurrent varies with position, an effect which is amplified as the laser intensity changes.

This varying contrast can occur when the drift current (due to the work function difference of the tip and substrate) and the intensity-dependent diffusion current from photogenerated charge gradients (which depend on local junction orientation) have different signs. At a high enough intensity, the diffusion current dominates; depending on the vertical structure, this effect could cause the photocurrent to switch directions.[57] The slope of the V_{OC} vs. intensity plot in Figure 1.3(b) can be viewed as an ideality factor. If one were to raster scan a laser while, at each point, controlling the intensity, it would in principle be possible to construct an ideality factor map. *This effect also underlies an important experimental detail in pcAFM — the intensity should be calibrated and kept constant across samples if they are to be compared with confidence.*

Indeed, interpretation of pcAFM data can be complicated in part because most conductive tip coatings are high work function materials (Au or Pt/Ir). In "normal" OPV cell architectures (as opposed to "inverted" architectures[59,60]), electrons are extracted through the top of the device. However, the high work function tip favors hole extraction. Hamadani, *et al*. showed that using low work function tips (e.g. doped diamond) on normal devices and high work function tips on inverted devices yield the correct *I-V* curve behavior, though there is a significant reverse bias photocurrent in pcAFM whose origin is under debate.[52] Additionally, the quantum efficiencies for photocurrent extraction using pcAFM can sometimes be orders of magnitude lower than that in a typical device, in which case it can be hard to quantitatively correlate the data with device external quantum efficiencies. This issue is compounded by the difficulty in acquiring multiple images on a surface before the tip is irreparably damaged.

pcAFM is a powerful optoelectronic tool. However, it must be applied with care, calibrated, and compared against device measurements for each new materials system. It is possible that noncontact techniques may offer more routine alternatives, at the cost of developing more complicated instrumentation.

1.4 AC-MODE AFM

AFM is often performed in non-contact/intermittent-contact mode[61] rather than in the contact mode used in cAFM. This method is called by a number of different names in the literature: AC mode, intermittent-contact, or tapping mode. Here, we use AC mode. An AFM tip can be regarded as a damped driven harmonic oscillator (DDHO). The cantilever has a resonance frequency determined by its mass and spring constant. In AC mode, the cantilever is driven at (or near) its resonance frequency to induce oscillation, and its subsequent motion can be described by the familiar DDHO equation:[62]

$$\frac{d^2z}{dt^2} + 2\beta\frac{dz}{dt} + \omega_0^2 z = (F_0/m)\cos(\omega t) \tag{1.1}$$

where z is the tip displacement, ω is the driving voltage frequency applied to the tip, ω_0 is the cantilever resonance frequency and is determined by the cantilever spring constant k and mass m, $\beta = \omega_0/2Q$ is the damping factor where Q represents the cantilever quality factor, and F_0 is the driving force applied to the cantilever. As the tip approaches the surface, Van der Waals attraction provides a damping force that reduces the oscillation amplitude. The feedback loop in AC mode most commonly adjusts the z-position of the tip to maintain a constant oscillation amplitude, and the z-position is then mapped as the topography of the substrate. If an additional loop is used to respond to changes in the resonance frequency of the cantilever due to interaction with the substrate, then so-called frequency modulation AFM (FM-AFM) can be performed.[63]

While FM-AFM topographic imaging is comparatively rare in ambient environments due to the additional complexity, the idea of measuring frequency shifts underpins many advanced electrical scanning probe techniques. For example, say the tip is oscillated at or near its resonance frequency above the sample surface outside of the range of Van der Waals forces but close enough to be affected by longer range interactions such as electrostatic forces. In this regime, changes in tip-sample interactions such as capacitance or surface potential can then be mapped as a function of position. In this case, we should rewrite Eq. (1) as:

$$\frac{d^2z}{dt^2} + 2\beta\frac{dz}{dt} + \omega_0(t)^2 z = (F_0/m)\cos(\omega t) + F_e(t)/m \tag{1.2}$$

where F_e is some time-dependent external force, such as electrostatic or magnetic forces acting on the cantilever, and $\omega_0(t)$ now is time-dependent. Any variations in F_e will result in changes in the force gradient, $(\partial F/\partial z)$, which is proportional to changes in the resonance frequency, $\Delta\omega_0$. The change in cantilever resonance frequency is proportional to the differential capacitive gradient in the tip-sample direction and exhibits a quadratic dependence on the voltage difference between the tip and the sample:[64]

$$\Delta\omega_0 \propto \frac{\partial^2 C}{\partial z^2}(V_{tip} - V_{surface})^2 \tag{1.3}$$

The interaction between tip-sample forces can be detected either in terms of changes in cantilever amplitude or frequency. If the cantilever is driven at a constant frequency while experiencing an electrostatic force gradient, the amplitude and phase will decrease and increase, respectively. In amplitude detection, changes in the *force* are detected by changes in the cantilever oscillation amplitude magnitude, while in force detection changes in the *force gradient* are detected as shifts in the cantilever phase relative to the drive signal and a shift in the cantilever resonance frequency. This effect is illustrated in Figure 1.4(a). As the voltage is

applied, the tip resonance frequency decreases as per Eq. $\Delta\omega_0 \propto \frac{\partial^2 C}{\partial z^2}(V_{tip} - V_{surface})^2$ (1.3).

In this case, the photovoltaic sample also exhibits a further shift in resonance frequency when illuminated due to the accumulation of photoinduced charge. Similarly, if the tip voltage is swept across a wide range, it is easy to observe the parabolic shape of the resonance frequency vs. voltage curve predicted by Eq. $\Delta\omega_0 \propto \frac{\partial^2 C}{\partial z^2}(V_{tip} - V_{surface})^2$ (1.3) [Figure 1.4 (b)].

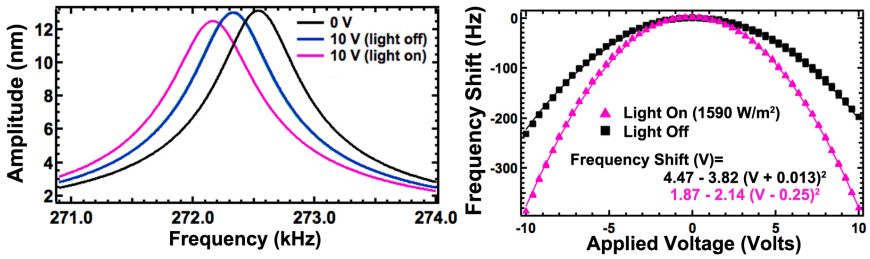

(a) (b)

Figure 1.4. (a) Cantilever oscillation amplitude curves on an organic photodiode (PFB:F8BT) taken at 0 V (black), 10 V (blue), and 10 V under 405 nm illumination (pink), across a range of drive frequencies. (b) Example of the frequency shift response showing the expected quadratic dependence on applied voltage as well as the change in differential capacitance gradient due to illumination. Data were taken at 10 nm above the same sample with approximately 1590 W/m^2 intensity.[99]

The frequency shift occurs faster than the natural cantilever time constant,[63,64] while at the same time being less sensitive to tip and cantilever beam effects, therefore the FM method often yields better results, particularly in electrical methods. Since the longer-range forces detected in non-contact mode are dependent upon tip-sample distance, it is imperative that this distance be held constant as data is collected. In a two-pass frequency shift method, the AFM initially takes a normal topography scan across a single line. On the retrace over the same line, the tip is raised ~10–50 nm and the recorded height data is used to keep the tip-sample distance constant. In the frequency shift-detection method, an additional feedback loop is used on the

retrace to record the phase and frequency of the cantilever's oscillation. The feedback loop on the retrace can be implemented in different ways: we base ours on the change in resonance frequency and the AFM controller changes the driving frequency to keep the relative phase constant but an alternative implementation is to keep the resonance frequency constant by changing some parameter like tip voltage. In SKPM, an additional feedback loop is required, as we discuss below.

1.5 Electrostatic Force Microscopy (EFM)

We cover electrostatic force microscopy (EFM) briefly because it is of relevance to the topics below, though we note that EFM methods have been reviewed in detail elsewhere.[14,64,79] Depending on the feedback mechanism, EFM measures variations in the electrostatic force and/or force gradient that arise from local differences in chemical potential and/ or dipole moment.[64] In a popular implementation of EFM, a constant voltage is applied between the sample and a conductive cantilever and the total shift in resonance frequency at each point above the sample is recorded. Typically, the shift is recorded while the cantilever is retracted from the topography during the retrace in a two-pass scan as described above. The resolution of EFM is in the tens of nanometers. Interpretation of EFM data can be made problematic due to issues of the cantilever and beam effects,[65,66] tip shape,[65] and scan height.[67] Beam effects are reduced in gradient detection,[68] as mentioned above, but must be considered nonetheless.

Keeping these factors in mind, EFM can be extremely powerful. For instance, the data extracted from EFM can be used to quantitatively map charge trapping within a semiconductor layer.[69–71] By measuring the electrostatic potential as a function of position, then taking the derivative to find the electric field, the Marohn group has been able to make direct tests of different models of carrier injection at the metal/semiconductor interfaces[72,73] in organic field-

effect transistors. EFM has also been used on solar cells like CdTe/CdS, GaInP and GaInP/GaAs/Ge devices to indentify the *n-p*[74] and triple junctions present[75] and to study carrier transport in systems of relevance to solar energy harvesting like PbSe quantum dot arrays.[76] If illumination is used, comparing the EFM data can shed additional light on the system of interest. EFM under illumination was used to study photocharging of pentacene islands[77] and alignment at pentacene-metal interfaces.[78] In $GaInP_2$, it was reported that the EFM profile changes significantly at the front window and back surface field regions as the light intensity increases, with the ultimate effect being evidence of enhanced V_{OC}.[74]

EFM is particularly valuable because it can yield information about trap character and defect density in devices. Wavelength-dependent spectra of potential drops measured via EFM were used to investigate the trap-clearing mechanisms in pentacene thin film transistors.[70] Degradation mechanisms are important to understand for many photovoltaic technologies, and we anticipate similar approaches will be utilized on solar cells.

1.6 SCANNING KELVIN PROBE MICROSCOPY (SKPM)

SKPM is one of the most common electrical scanning probe methods.[79] It is available on many common commercial AFM systems, but the exact details of implementation (amplitude feedback, frequency shift feedback, ambient, ultrahigh vacuum) vary widely from one machine to another. As noted above, frequency shift methods are generally viewed as more robust. Regardless of implementation, SKPM provides a measure of the contact potential difference (CPD) between a reference probe and the substrate, measured by nulling out the force or force gradient signal with a feedback loop that adjusts a tip-sample bias to null out the CPD.[14] Thus, SKPM is a relative measurement. If one has a reference sample with a known work function, then it is possible to use SKPM to measure relative local work function variations in an unknown

sample. However, exact comparisons between values from SKPM and values from methods like ultraviolet photoemission (UPS) are not generally expected to exhibit quantitative agreement unless SKPM itself is done in UHV on meticulously clean materials, as most surfaces exhibit work function shifts of several hundred meV upon exposures to any kind of atmosphere.[80]

SKPM provides a powerful way to study the lateral variations in energetic properties on organic devices, ranging from charge injection in polymer transistors[79,81,82] to spatial variations in potential distributions and bottom contact transport rates in organic solar cells.[83–86] Several studies have been performed with SKPM on the nature of band bending at grain boundaries in CIGS,[87,88] including the influence of crystal orientation,[23,89] the vertical structure of the grains,[88] and what model best describes the band bending.[23,90] SKPM is also useful in evaluating potential profiles in cross-sectional samples.[87,91]

In fact, not only does SKPM offer high spatial resolution for local work function measurements, but it too can be combined with photoexcitation. If two SKPM images are taken, one in the dark and one under constant illumination, the difference provides a surface photovoltage image.[82,83,85,92,93] Surface photovoltage is a well-established technique for measuring properties such as diffusion lengths and band bending in bulk solar cell materials. SKPM combined with optical excitation thus offers the potential to map these properties with nanoscale resolution. For instance, surface photovoltage data have used to study cross sections of III-V $CuGaSe_2$ devices, where they used the photovoltage to describe a possible band diagram.[91]

In nanostructured organic solar cells, SKPM and surface photovoltage studies have provided much valuable information[82–85,92] but sometimes have been a challenge to interpret. For instance, SKPM often shows the expected contrast change between the donor and acceptor materials under illumination: the donor often becomes more positively charged relative to the

acceptor. However, *both* the donor and the acceptor domains often show net negative overall absolute shifts relative to the dark.[83,85,94] Kemerink and coworkers have explained this shift in terms of the relative rates of charge transfer, generation, and recombination/extraction at the bottom contact.[85] An example of this is shown in Figure 1.5 with a photovoltaic blend of poly[2-methyloxy-5-(3′7′-dimethyloctyloxy)-*p*-phenylene vinylene]:1-(3-methoxycarbonyl)-propyl-1-phenyl[6,6]C_{61} (MDMO- PPV:PCBM). This material is known to form PCBM-rich regions surrounded by a matrix of approximately 1:1 MDMO-PPV:PCBM.[50,57,95] After illumination, the entire surface exhibits a negative shift in potential, as opposed to only the acceptor-rich domains (as many had expected). This effect is attributed to the excess electrons generated in the MDMO-PPV:PCBM matrix due to efficient hole transport to the bottom electrode. The electrons can laterally diffuse into the PCBM-crystallite regions, and thus the entire surface contains excess negative charge and the contrast shifts accordingly.

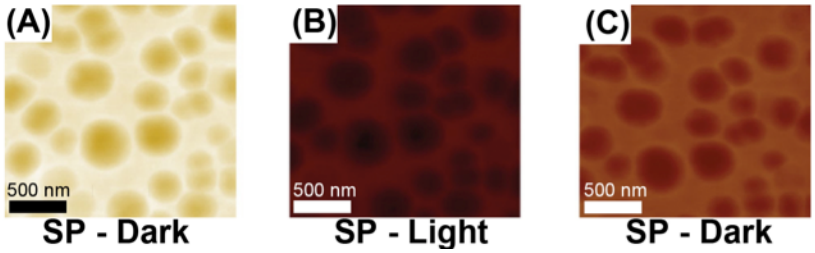

Figure 1.5. SKPM data taken in the (a) dark, (b) under white light illumination, and (c) after illumination of a MDMO-PPV:PCBM film. The scale in each of the images is from 0–20 meV. The contrast between the dark and light can be interpreted in terms of lateral electron diffusion from the MDMO-PPV:PCBM matrix to the PCBM crystallites.[85]

Variations in domain connectivity in both the lateral and vertical film morphology can also play a role in image contrast, and SKPM and surface photovoltage data have also been used to infer vertical film structure.[84,92] While these different pictures are not necessarily mutually exclusive, they are not always perfectly self-consistent either, and we note that the interpretation of surface photovoltage contrast in different specific organic photovoltaic system remains a

subject of active research. As is true of almost any technique, it is often helpful to seek independent confirmation of structural models inferred from SKPM data on organic systems.

SKPM and surface photovoltage have also been used to measure aging and stability in organic solar cell materials.[21,96] However, at least for some materials, the trap density required to generate contrast in a surface photovoltage image can be quite severe in terms of overall device performance, motivating the search for more sensitive local probes such as trEFM.[21]

1.7 Time-Resolved Electrostatic Force Microscopy (trEFM)

Traditional EFM and SKPM are powerful tools, but they only measure steady-state, or near steady-state, behaviors occurring on time scales on the order of seconds or longer. As a result almost all transient information of relevance to solar cell operation is lost. As noted above, the equilibrium properties accessible via EFM or SKPM can provide information about certain specific processes (the use of surface photovoltage to measure carrier diffusion lengths for instance),[97] or can be used to measure the evolution of properties over long times (trapping over minutes to hours).[98] However, many transient properties can be difficult to access with EFM or SKPM, a problem we address with time-resolved electrostatic force microscopy (trEFM).

As the name implies, trEFM involves measuring the cantilever dynamics following a change in the electrical properties of a sample (such as induced by a voltage or light step or pulse) and using that dynamic information to study the material underneath the scanning probe tip. Since we are interested primarily in photovoltaic systems in this chapter, we will mainly consider the response of the cantilever following a change in the illumination (such as a step change from dark to light). Experimentally, such transient perturbation can be conveniently provided at intensities both above and below AM 1.5 by an LED focused on the sample plane

and coaligned with the tip. In trEFM, a voltage is applied followed by an LED pulse for photoinduced charge generation.

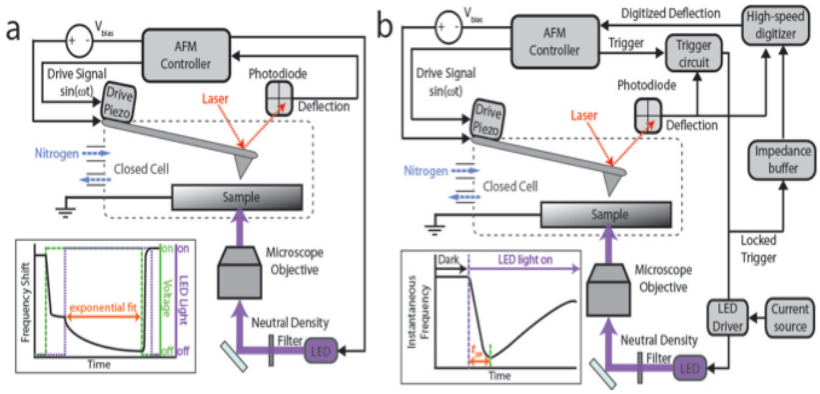

Figure 1.6. (a) Schematic of the trEFM instrumentation. Shown in the inset is a diagram of the triggered voltage pulse (green), LED light pulse (purple), and tr-EFM frequency shift (black) with the exponential fit region highlighted. (b) Schematic of the FF-trEFM instrumentation. The inset diagrams show the demodulated instantaneous frequency response in the dark and the light, as well as the time to first frequency peak.

The initial voltage causes a frequency shift due to the electrostatic force as in steady-state EFM [Figure 1.6(a) inset]. After illumination, the photoinduced charge carriers generated by the LED in the active material move to the top of the sample due to the tip-sample bias. The accumulated charge beneath the tip changes the electrostatic force and force gradient. Another way to view this is that the tip-sample capacitor plate distance is changing with time as the charges fill the top surface of the film. The resonance frequency is recorded with time and exhibits near single-exponential behavior during the photoinduced charging process. This process is shown schematically in Figure 1.6(a) where the resonance frequency shift decays exponentially to a new equilibrium value. Fitting a single exponential function to this decay yields the local charging time constant and thus the charging rate, and the process is repeated at each pixel along the retrace to generate a charging rate image.

Frequency-shift detection provides the basis for trEFM operation. Figure 1.6 illustrates two methods for detecting transient force gradient information, with and without a feedback loop. We have successfully utilized a frequency-shift feedback loop to measure the cantilever frequency with a time-resolution of ~100 microseconds [Figure 1.6(a)].[21,58] Recently, we have shown it is possible to discriminate transient rise times as short as ~100 ns, if one bypasses the feedback loop [Figure 1.6(b)] and extracts the rise time of the transient through an analysis of the raw displacement vs. time data.[99]

In the trEFM method in Figure 1.6(a), the feedback loop uses a lock-in amplifier implemented in the AFM controller to measure the change in phase between the cantilever oscillation and the driving signal as the resonance frequency changes due to the electrostatic force gradient. The feed- back loop then adjusts the drive frequency to maintain a constant phase and keep the tip on resonance. By recording these changes in drive frequency as a function of time, the Δf curves at each pixel can be constructed. The gains for this phase feedback loop are optimized to minimize ringing in the Δf response after the bias is applied but before the light is turned on. Inherent in the trEFM method are two practical consequences: the feedback loop bandwidth (currently ~10 kHz) and the signal:noise of the phase or frequency response. In the former case, the ultimate time- resolution is intrinsically determined by the speed of the feedback electronics while in the latter case, the S/N detection limit is dependent upon the feedback loop's sensitivity to the gain settings. While trEFM lends itself to mapping local efficiency on photovoltaic samples, these feedback limitations mean that either <1 Sun intensities and/or low-efficiency materials below the current state-of-the art must be used in these studies.

The motivation for using trEFM rather than SKPM or EFM is evident when looking at photocurrent in an organic solar cell. Photocurrent (charge collected per unit time under

illumination) cannot be effectively probed by traditional EFM or SKPM methods. As an example Figure 1.7 compares the external quantum efficiency (EQE) and the surface photovoltage measured for a model organic solar cell over a range of active layer formulations. As the blend composition is changed, the EQE first increases by nearly a factor of ~100×, peaks, then decreases by ~100× due to changes in the semiconducting active layer. In contrast, the accompanying surface photovoltage measured by SKPM changes only monotonically, and by only about 100 mV. Although photocurrent (and thus EQE) can be mapped by pcAFM, it is difficult to make pcAFM completely quantitative due to tip contact effects as noted above.[37] Here, we consider how time-resolved electrostatic force microscopy methods (trEFM) can be used to map dynamic variables like photocurrent, trapping, and charge recombination.

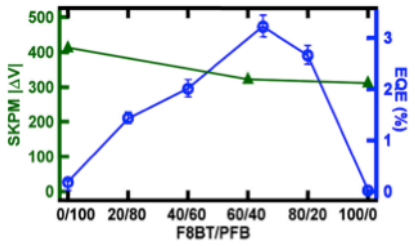

Figure 1.7. Spatially-averaged surface potential (left) and external quantum efficiency (right) as a function of composition ratio in a PFB:F8BT bulk heterojunction blend.

trEFM essentially measures the time it takes to charge the tip-sample capacitor with a photocurrent at each pixel, which can thus be used to map local photoactivity of a thin semiconductor film (Figure 1.8(a)). If the top contact is not a bottleneck in the completed device structure, trEFM can provide *quantitative* information about local quantum efficiency. We have shown that the spatially-averaged charging rate values measured by trEFM correlate to EQE values measured on a finished solar cell for multiple materials, under different conditions [Figure 1.8(b)].[21,58,99] In other words, once calibrated, Figure 1.8(b) shows that trEFM can predict the

external quantum efficiency of a given solar cell simply by taking an image of the active layer material prior to deposition of the top contact.

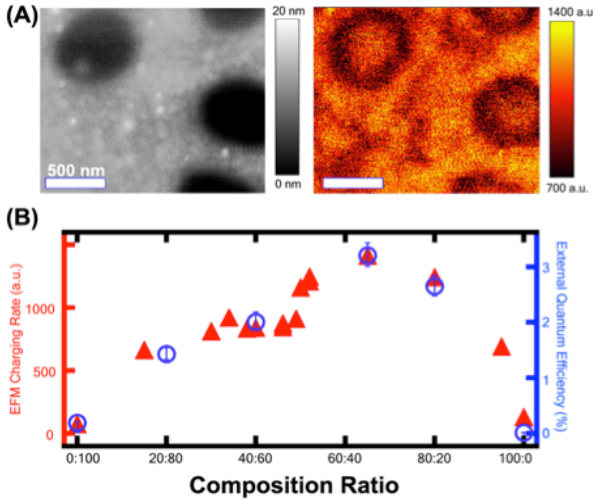

Figure 1.8. (a) trEFM topography and charging rate images for a poly[(9,9′-dioctylfluorene-alt-(bis(N,N′-(4-butylphenyl))-bis(N,N′-phenyl-1,4-phenylenediamine)] (PFB) and poly[9,9′-dioctylfluorene-alt-1,4-benzothiadiazole] (F8BT) film; (b) a graph of trEFM charging rate correlated with device EQE.[58]

Aside from being predictive of performance, trEFM data are also highly sensitive to local trapping. For example, as shown in Figure 1.9, trEFM can be used to map trap formation in a solar cells at levels below those accessible by SKPM techniques.[21] To produce Figure 1.9, a semiconducting polymer blend of PFB:F8BT was photooxidized at nine different locations for varying lengths of time, thereby creating a grid where each spot exhibits a different level of photochemical degradation. The SKPM data only show a significant change in photovoltage at the highest intensity levels — at which point the device performance has been almost completely degraded [Figure 1.9(e)], while the trEFM data can detect trap formation at much lower levels. Figure 1.9(e) shows that the surface photovoltage data show no simple correlation with external quantum efficiency. The higher sensitivity of trEFM to trap density is expected given that a single trap can serve as a recombination center for many carriers, dramatically decreasing the

photocurrent. On the other hand, a photovoltage depends indirectly on the carrier generation rate through the *log* of the generated photocurrent,[57,101,102] and will also be affected by shifts associated with chemical changes in the semiconductor bulk (or at the surface) associated with trap formation.

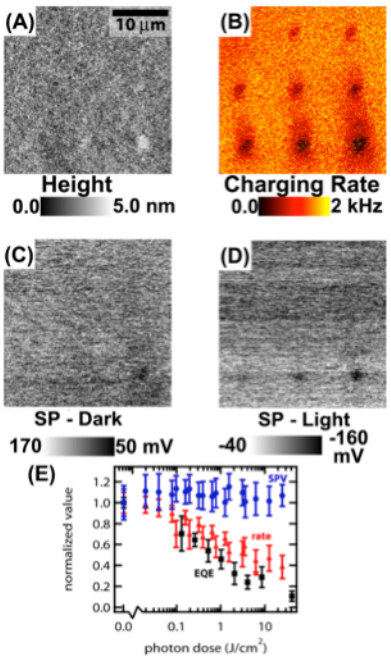

Figure 1.9. (a) Topography and (b) charging rate of a PFB:F8BT blend. The film was exposed to a 405 nm laser in air at different photon doses at nine spots on the film. (c) Surface potential measured via SKPM in the dark and (d) under 460 nm illumination. (e) A graph of surface photovoltage (SPV), device EQE, and the trEFM charging rate.[21]

The data in Figure 1.9(b) and (d) illustrate another advantage of trEFM methods. The banding observed in Figure 1.9(d) is typical of SKPM images where small changes in tip surface contamination lead to jumps in the tip potential. On the other hand, since trEFM is measuring the rate of change from an initial to final point (rather than the absolute value of those points), it is much less sensitive to small levels of contamination that are commonly encountered on soft, chemically prepared samples outside of UHV environments.

Current implementations of trEFM as in Figure 1.6(a) have a spatial resolution of ~100 nm and a time resolution of ≥100 μs. The time resolution is a side effect of the feedback loop and can be circumvented using a new method developed by our group [Figure 1.6 (b)], fast free trEFM (FF-trEFM).[99] As with trEFM, voltage and light pulses are triggered during the retrace, but instead of a feedback loop, the raw cantilever displacement is recorded directly from the AFM during these pulses at a high sampling rate (~5–50 MHz) using an external digitizer. A trigger-circuit is employed to ensure that the light pulse is turned on at the same phase of the cantilever's oscillation to allow a high S/N for averaged data. This free cantilever oscillation data is recorded multiple times at each pixel. Because no feedback loop is employed to keep the drive frequency on resonance in response to the transient electrostatic force gradient that arises from photoinduced charge generation, the amplitude, phase, and instantaneous frequency of the oscillating cantilever all change over the duration of the light pulse.[63]

In order to extract these changes, the raw displacement data is post- processed. Each pixel's data is averaged, then filtered by a finite impulse response bandpass filter with a Blackman windowing function. Finally, the numerical Hilbert transform is taken in order to extract the amplitude $A(t)$, phase $\theta(t)$, and instantaneous frequency $f(t)$ as is common in signal processing literature.[102,103] Briefly, the Hilbert transform inputs the original signal $u(t)$, calculates $\hat{u}(t)$, which is the original signal phase shifted by $\pi/2$,[103] and outputs:

$$A(t) = \sqrt{u(t)^2 + \hat{u}(t)^2} \tag{1.1}$$

$$\theta(t) = tan^{-1}[-\hat{u}(t)/u(t)] \tag{1.2}$$

$$f(t) = \frac{1}{2\pi}\frac{d}{dt}\theta(t) = \frac{1}{2\pi}\frac{d}{dt}[\tan^{-1}[-\hat{u}(t)/u(t)]] \tag{1.3}$$

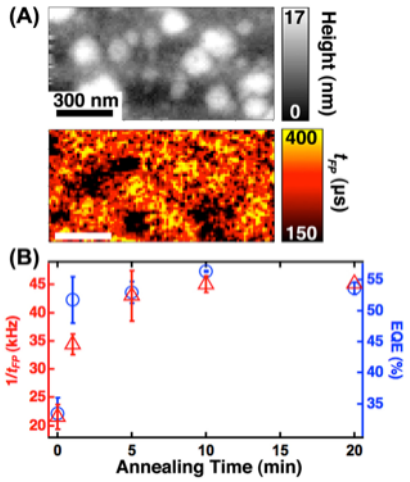

Figure 1.10. (a) FF-trEFM topography and $1/t_{FP}$ images for MDMO-PPV:PCBM; (b) a graph showing the correlation between FF-trEFM $1/t_{FP}$ and EQE as a function of annealing time for a series of P3HT:PCBM devices.[99]

Similar to trEFM, we are interested in the time-dependent $f(t)$ behavior, an example of which is graphed in Figure 1.10 using FF-trEFM on polymer:fullerene devices. Here, the parameter of interest, called the time to frequency shift peak or t_{FP}, is the difference between the time at which the light pulse turns on and the time at which the $f(t)$ response is greatest relative to the equilibrium value before the light turns on, when $f_{drive} = f_{resonance}$. Thus, for FF-trEFM, t_{FP} is analogous to the charging rate of trEFM in that it captures information about local performance. In Figure 1.10(a), an MDMO-PPV:PCBM film exhibits charging over the surface in a manner not obviously predicted by the topography. In Figure 1.10(b), the spatially-averaged t_{FP} values for a series of polymer solar cells are correlated with the device EQE in a manner similar to that previously done with classic trEFM data. While the spatial resolution remains the same, FF-trEFM improves the time resolution limit to ~100 ns, enabling the study of higher-efficiency materials at typical light intensities. FF-trEFM has allowed us to demonstrate similar relationships to those in feedback-based trEFM for materials with quantum efficiencies as high at ~60%.[100] For both trEFM and FF-trEFM the ability to correlate morphology to bulk photovoltaic

performance with ~80–100 nm lateral resolution, all with a noncontact method, represents a significant contribution to nanoscale metrology.

1.8 Conclusions and Future Outlook

It is an exciting time in both the fields of scanning probe microscopy and in solar energy. New scanning probe instruments with advanced capabilities are becoming increasingly accessible to a wide audience — for instance, most high-end commercial AFMs have the hardware capabilities necessary to perform fast trEFM. At the same time, the use of nanostructured thin films from organics,[15] to sintered chacogenides,[104] to quantum dot solids,[105] is exploding in solar energy applications. Only a few of these systems have been studied in detail by scanning probe methods. Those that have been examined have often taught us that microscopic examination can overturn the "obvious" hypothesis for how the device works.[58]

It seems likely that techniques like cAFM, pcAFM, EFM, SKPM, and trEFM will continue to be honed and applied to answer emerging questions in new semiconductors being developed for low cost solar energy applications. At the same time there are major opportunities for techniques such as scanning impedance microscopy,[106] scanning capacitance,[107] band excitation methods,[108] and perhaps even near-field methods,[109] to characterize local electronic and chemical properties of semiconductors under optical excitation.

1.9 Acknowledgements

This comprehensive review is based on a body of work spanning many years. The fast trEFM work described above was funded as part of the Center for Interface Science: Solar Electric Materials, an Energy Frontier Research Center funded by the US Department of Energy, Office of Science, Office of Basic Energy Sciences, under Award Number DE-SC0001084

(supporting new instrumentation and hardware development to probe interfacial phenomena with high resolution). Additional portions of this work, writing, and literature review, have been supported by the Air Force Office of Scientific Research, FA9550-10-1-0474, and the NSF (DMR 1005504). GER received additional support from an ARCS fellowship from the University of Washington.

1.10 REFERENCES

1. Nozik A J, 2008. Multiple exciton generation in semiconductor quantum dots, *Chem Phys Lett* 457:3–11.

2. Semonin O E, *et al.,* 2011. Peak external photocurrent quantum efficiency exceeding 100% via MEG in a quantum dot solar cell, *Science* 334: 1530–1533.

3. Ford G M, Guo Q, Agrawal R and Hillhouse H W, 2011. Earth abundant element $Cu_2Zn(Sn_{1-x}Ge_x)S_4$ nanocrystals for tunable band gap solar cells: 6.8% efficient device fabrication, *Chem Mater* 23:2626–2629.

4. Guo Q, Ford G M, Hillhouse H W and Agrawal R, 2009. Sulfide nanocrystal inks for dense $Cu(In_{1-x}\ Ga_x)(S_{1-y}Se_y)_2$ absorber films and their photovoltaic performance, *Nano Lett*, 9:3060–3065.

5. Guo Q, Hillhouse H W and Agrawal R, 2009. Synthesis of Cu_2ZnSnS_4 nanocrystal ink and its use for solar cells, *J Am Chem Soc* 131:11672–11673.

6. Todorov T K, Reuter K B and Mitzi D B, 2010. High-efficiency solar cell with earth-abundant liquid-processed absorber, *Adv Mater* 22:E156–E159.

7. Wang K, *et al.,* 2010. Thermally evaporated Cu_2ZnSnS_4 solar cells, *Appl Phys Lett* 97:143508.

8. Atwater H A and Polmar A, 2010. Plasmonics for improved photovoltaic devices, *Nat Mater* 9:205–213.

9. Kulkarni A P, Noone K M, Munechika K, Guyer S R and Ginger D S, 2010. Plasmon-enhanced charge carrier generation in organic photovoltaic films using silver nanoprisms, *Nano Lett* 10:1501–1505.

10. Deibel C and Dyakonov V, 2010. Polymer–fullerene bulk heterojunction solar cells, *Rep Prog Phys* 73:096401.

11. Giridharagopal R and Ginger D S, 2010. Characterizing morphology in bulk heterojunction organic photovoltaic systems, *J Phys Chem Lett* 1: 1160–1169.

12. Giridharagopal R, Shao G, Groves C and Ginger D S, 2010. New SPM techniques for analyzing OPV materials, *Mater Today* 13:50–56.

13. Groves C, Reid O G and Ginger D S, 2010. Heterogeneity in polymer solar cells: Local morphology and performance in organic photovoltaics studied with scanning probe microscopy, *Acc Chem Res* 43:612–620.

14. Pingree L S C, Reid O G and Ginger D S, 2009. Electrical scanning probe microscopy on active organic electronic devices, *Adv Mater* 21:19–28.

15. Dennler G, Scharber M C and Brabec C J, 2009. Polymer-fullerene bulk-heterojunction solar cells, *Adv Mater* 21:1323–1338.

16. Servaites J D, Ratner M A and Marks T J, 2011. Organic solar cells: A new look at traditional models, *Energy Environ Sci* 4:4410–4422.

17. Armstrong N A, Veneman P A, Ratcliff E L, Placencia D and Brumbach M, 2009. Oxide contacts in organic photovoltaics: Characterization and control of near-surface composition in indium-tin oxide (ITO) electrodes, *Acc Chem Res* 42:1748–1757.

18. Brumbach M, *et al.,* 2007. Surface composition and electrical and electrochemical properties of freshly deposited and acid-etched indium tin oxide electrodes, *Langmuir* 23:11089–11099.

19. Delongchamp D M, Kline R J and Herzing A, 2012. Nanoscale structure measurements for polymer-fullerene photovoltaics, *Energy Environ Sci* 5:5980–5993.

20. Coffey D C and Ginger D S, 2005. Patterning phase separation in polymer films with dip-pen nanolithography, *J Am Chem Soc* 127:4564–4565.

21. Reid O G, Rayermann G E, Coffey D C and Ginger D S, 2010. Imaging local trap formation in conjugated polymer solar cells: A comparison of time-resolved electrostatic force microscopy and scanning Kelvin probe imaging, *J Phys Chem C* 114:20672–20677.

22. Takano H, Wong S, Harnisch J A and Porter M D, 2000. Mapping the subsurface composition of organic films by electric force microscopy, *Langmuir* 16:5231–5233.

23. Fuertes Marrón D, Sadewasser S, Meeder A, Glatzel T and Lux-Steiner M C, 2005. Electrical activity at grain boundaries of Cu(In,Ga)Se_2 thin films, *Phys Rev B* 71:033306.

24. Sadewasser S, *et al.,* 2011. Nanometer-scale electronic and microstructural properties of grain boundaries in Cu(In,Ga)Se_2, *Thin Solid Films* 519:7341–7346.

25. Pivrikas A, Sariciftci N S, Juska G and Osterbacka R, 2007. A review of charge transport and recombination in polymer/fullerene organic solar cells, *Progress in Photovoltaics* 15:677–696.

26. Blom P W W, Mihailetchi V D, Koster L D A and Markov D E, 2007. Device physics of polymer:fullerene bulk heterojunction solar cells, *Adv Mater* 19:1551–1566.

27. Levichkova M, *et al.,* 2011. Dicyanovinyl sexithiophene as donor material in organic planar heterojunction solar cells: Morphological, optical, and electrical properties, *Org Elec* 12:2243–2252.

28. Huynh W U, Dittmer J J and Alivisatos A P, 2002. Hybrid nanorod-polymer solar cells, *Science* 295:2425–2427.

29. Greenham N C, Peng X and Alivisatos A P, 1996. Charge separation and transport in conjugated-polymer/semiconductor-nanocrystal composites studied by photo-luminescence quenching and photoconductivity, *Phys Rev B* 54:17628–17637.

30. Noone K M, *et al.,* 2009. Absence of photoinduced charge transfer in blends of PbSe quantum dots and conjugated polymers, *ACS Nano* 3:1345–1352.

31. Noone K M, *et al.,* 2010. Broadband absorbing bulk heterojunction photovoltaics using low-bandgap solution-processed quantum dots, *Nano Lett* 10:2635–2639.

32. Jones M, Nedeljkovic J, Ellingson R J, Nozik A J and Rumbles G, 2003. Photoenhancement of luminescence in colloidal CdSe quantum dot solutions, *J Phys Chem B* 107:11346–11352.

33. Romero M J, Jiang C-S, Noufi R and Al-Jassim M, 2005. Lateral electron transport in Cu(In,Ga)Se_2 investigated by electro-assisted scanning tunneling microscopy, *Appl Phys Lett* 87:172106.

34. Pingree L S C, Reid O G and Ginger D S, 2009. Imaging the evolution of nanoscale photocurrent collection and transport networks during annealing of polythiophene/ fullerene solar cells, *Nano Lett* 9:2946–2952.

35. Rice A H, *et al.,* 2011. Controlling vertical morphology within the active layer of organic photovoltaics using poly(3-hexylthiophene) nanowires and phenyl-C61-butyric acid methyl ester, *ACS Nano* 5:3132–3140.

36. Dang X-D, *et al.,* 2010. Nanostructure and optoelectronic characterization of small molecule bulk heterojunction solar cells by photoconductive atomic force microscopy, *Adv Func Mater* 20:3314–3321.

37. Dang X-D, Mikhailovsky A and Nguyen T-Q, 2010. Measurement of nanoscale external quantum efficiency of conjugated polymer:fullerene solar cells by photoconductive atomic force microscopy, *Appl Phys Lett* 97:113303.

38. Alvarez J, *et al.,* 2011. Conductive-probe atomic force microscopy characterization of silicon nanowire, *Nanoscale Res Lett* 6:110.

39. Kleider J P, *et al.,* 2011. Characterization of silicon heterojunctions for solar cells, *Nanoscale Res Lett* 6:152.

40. Rezek B, Stuchlik J, Fejfar A and Kocka J, 1999. Local characterization of electronic transport in microcrystalline silicon thin films with submicron resolution, *Appl Phys Lett* 74:1475–1477.

41. Mates T, *et al.,* 2006. Detailed structural study of low temperature mixed-phase Si films by X-TEM and ambient conductive AFM, *J Non-Crystalline Solids* 352:1011–1015.

42. Yan B J, *et al.,* 2007. Local current flow in amorphous and nanocrystalline mixed-phase silicon solar cells, *J Appl Phys* 101:033712.

43. Shin R H, Jo W, Kim D-W, Yun J H and Ahn S, 2011. Local current-voltage behaviors of preferentially and randomly textured Cu(In,Ga)Se_2 thin films investigated by conductive atomic force microscopy, *Appl Phys A-Mater Science and Processing* 104:1189–1194.

44. Visoly-Fisher I, Cohen S R, Gartsman K, Ruzin A and Cahen D, 2006. Understanding the beneficial role of grain boundaries in polycrystalline solar cells from single-grain-boundary scanning probe microscopy, *Adv Funct Mater* 16:649–660.

45. Galiana B, *et al.,* 2011. Characterization of antiphase domains on GaAs grown on Ge substrates by conductive atomic force microscopy for photovoltaic applications, *Solar Energy Mater and Solar Cells* 95: 1949–1954.

46. Beinik I, *et al.,* 2011. Electrical properties of ZnO nanorods studied by conductive atomic force microscopy, *J Appl Phys* 110:052005.

47. Dante M, Garcia A and Nguyen T-Q, 2009. Three-dimensional nanoscale organization of highly efficient low band-gap conjugated polymer bulk heterojunction solar cells, *J Phys Chem C* 113:1596–1600.

48. Reid O G, Munechika K and Ginger D S, 2008. Space charge limited current measurements on conjugated polymer films using conductive atomic force microscopy, *Nano Lett* 8:1602–1609.

49. Douhéret O, *et al.,* 2006. Nanoscale electrical characterization of organic photovoltaic blends by conductive atomic force microscopy, *Appl Phys Lett* 89:032107.

50. Coffey D C, Reid O G, Rodovsky D B, Bartholomew G P and Ginger D S, 2007. Mapping local photocurrents in polymer/fullerene solar cells with photoconductive atomic force microscopy, *Nano Lett* 7:738–744.

51. Hamadani B H, Jung S, Haney P M, Richter L J and Zhitenev N B, 2010. Origin of nanoscale variations in photoresponse of an organic solar cell, *Nano Lett* 10: 1611–1617.

52. Hamadani B H, Gergel-Hackett N, Haney P M and Zhitenev N B, 2011. Imaging of nanoscale charge transport in bulk heterojunction solar cells. *J Appl Phys* 109:124501.

53. Xin H, *et al.,* 2010. Polymer nanowire/fullerene bulk heterojunction solar cells: How nanostructure determines photovoltaic properties, *ACS Nano* 4:1861–1872.

54. Tsoi W C, *et al.,* 2011. Surface and subsurface morphology of operating nanowire:fullerene solar cells revealed by photoconductive-AFM, *Energy Environ Sci* 4:3646–3651.

55. Fan Z Y, *et al.,* 2006. Electrical and photoconductive properties of vertical ZnO nanowires in high density arrays, *Appl Phys Lett* 89:213110.

56. Heng L P, *et al.,* 2010. Local photoelectric conversion properties of titanylphthalocyanine (TiOPc) coated aligned ZnO nanorods, *Chem Comm* 46: 1162–1164.

57. Reid O G, Xin H, Jenekhe S A and Ginger D S, 2010. Nanostructure determines the intensity-dependence of open-circuit voltage in plastic solar cells, *J Appl Phys* 108:084320.

58. Coffey D C and Ginger D S, 2006. Time-resolved electrostatic force microscopy of polymer solar cells, *Nat Mater* 5:735–740.

59. Hau S K, *et al.,* 2008. Air-stable inverted flexible polymer solar cells using zinc oxide nanoparticles as an electron selective layer, *Appl Phys Lett* 92:253301.

60. Kim C S, Lee S S, Gomez E D, Kim J B and Loo Y-L, 2009. Transient photovoltaic behavior of air-stable, inverted organic solar cells with solution-processed electron transport layer, *Appl Phys Lett* 94:113302.

61. Martin Y, Williams C C and Wickramasinghe H K, 1987. Atomic force microscope-force mapping and profiling on a sub 100 Å scale, *J Appl Phys* 61:4723–4729.

62. Thornton S T and Marion J B, 2003. *Classical Dynamics of Particles and Systems.* Brooks Cole: Belmont, CA.

63. Albrecht T R, Grutter P, Horne D and Rugar D, 1991. Frequency-modulation detection using high-Q cantilevers for enhanced force microscopy sensitivity, *J Appl Phys* 69:668–673.

64. Silveira W R, Muller E M, Ng T N, Dunlap D H and Marohn J A, 2007. S V Kalinin and A Gruverman (eds.). In *Scanning Probe Microscopy: Electrical and Electromechanical Phenomena at the Nanoscale*, Springer, New York: Ch. 10, pp. 788–832.

65. Sacha G M, Sahagun E and Saenz J J, 2007. A method for calculating capacitances and electrostatic forces in atomic force microscopy, *J Appl Phys* 101:024310.

66. Belaidi S, Girard P and Leveque G, 1997. Electrostatic forces acting on the tip in atomic force microscopy: Modelization and comparison with analytic expressions, *J Appl Phys* 81:1023–1030.

67. Leveque G, Cadet P and Arinero R, 2005. Sensitivity and resolution in non-contact electrostatic force microscopy in the case of a constant potential, *Phys Rev B* 71:205419.

68. Glatzel T, Sadewasser S and Lux-Steiner M C, 2003. Amplitude or frequency modulation-detection in Kelvin probe force microscopy, *Appl Surf Sci* 210:84–89.

69. Muller E M and Marohn J A, 2005. Microscopic evidence for spatially inhomogeneous charge trapping in pentacene, *Adv Mater* 17:1410–1414.

70. Luria J L, Schwarz K A, Jaquith M J, Hennig R G and Marohn J A, 2011. Spectroscopic characterization of charged defects in polycrystalline pentacene by time- and wavelength-resolved electric force microscopy, *Adv Mater* 23:624–628.

71. Jaquith M J, Anthony J E and Marohn J A, 2009. Long-lived charge traps in functionalized pentacene and anthradithiophene studied by time-resolved electric force microscopy, *J Mater Chem* 19:6116–6123.

72. Silveira W R and Marohn J A, 2004. Microscopic view of charge injection in an organic semiconductor, *Phys Rev Lett* 93:116104.

73. Ng T N, Silveira W R and Marohn J A, 2007. Dependence of charge injection on temperature, electric field, and energetic disorder in an organic semiconductor, *Phys Rev Lett* 98:066101.

74. Jiang C-S, Moutinho H R, Geisz J F, Friedman D J and Al-Jassim M M, 2002. Direct measurement of electrical potentials in $GaInP_2$ solar cells, *Appl Phys Lett* 81:2569–2571.

75. Ballif C, Moutinho H R and Al-Jassim M M, 2001. Cross-sectional electrostatic force microscopy of thin-film solar cells, *J Appl Phys* 89:1418–1424.

76. Hu Z, Fischbein M D and Drndic M, 2005. Local charge transport in two-dimensional PbSe nanocrystal arrays studied by electrostatic force microscopy, *Nano Lett* 5:1463–1468.

77. Chen L, Cherniavskaya O, Shalek A and Brus L E, 2005. Photoinduced interfacial charging and "explosion" of monolayer pentacene islands, *Nano Lett* 5:2241–2245.

78. Kim C, and Jeon D, 2009. Electric force microscopy imaging of charge accumulation and barrier lowering at Al/pentacene junction, *Appl Phys Lett* 95:153302.

79. Palermo V, Palma M and Samori P, 2006. Electronic characterization of organic thin films by Kelvin probe force microscopy, *Adv Mater* 18: 145–164.

80. Hwang J, Wan A and Kahn A, 2009. Energetics of metal–organic interfaces: New experiments and assessment of the field, *Mat Sci Eng R* 64:1–31.

81. Bürgi L, Richards T J, Friend R H and Sirringhaus H, 2003. Close look at charge carrier injection in polymer field-effect transistors, *J Appl Phys* 94:6129.

82. Palermo V, *et al.,* 2007. A Kelvin probe force microscopy study of the photogeneration of surface charges in all-thiophene photovoltaic blends, *Adv Funct Mater* 17:472–478.

83. Spadafora E J, Demadrille R, Ratier B and Grévin B, 2010. Imaging the carrier photo-generation in nanoscale phase segregated organic heterojunctions by Kelvin probe force microscopy, *Nano Lett* 10:3337–3342.

84. Hoppe H, *et al.,* 2005. Kelvin Probe Force Microscopy study on conjugated polymer/fullerene bulk heterojunction organic solar cells, *Nano Lett* 5: 269–274.

85. Maturová K, Kemerink M, Wienk M M, Charrier D S H and Janssen R A J, 2009. Scanning Kelvin probe microscopy on bulk heterojunction polymer blends, *Adv Funct Mater* 19:1379–1386.

86. Glatzel T, Hoppe H, Sariciftci N S, Lux-Steiner M C and Komiyama M, 2005. Kelvin probe force microscopy study of conjugated polymer/fullerene organic solar cells, *Japanese J Appl Phys* 44:5370–5373.

87. Sadewasser S, *et al.,* 2003. Kelvin probe force microscopy for the nano scale characterization of chalcopyrite solar cell materials and devices, *Thin Solid Films* 431–432: 257–261.

88. Jiang C-S, *et al.,* 2004. Local built-in potential on grain boundary of $Cu(In,Ga)Se_2$ thin films, *Appl Phys Lett* 84:3477–3479.

89. Hanna G, *et al.,* 2006. Texture and electronic activity of grain boundaries in $Cu(In,Ga)Se_2$ thin films, *Appl Phys A-Mater Science and Processing* 82:1–7.

90. Leendertz C, Streicher F, Lux-Steiner M C and Sadewasser S, 2006. Evaluation of Kelvin probe force microscopy for imaging grain boundaries in chalcopyrite thin films, *Appl Phys Lett* 89:113120

91. Glatzel T, Fuertes Marrón D, Schedel-Niedrig T, Sadewasser S and Lux- Steiner M C, 2002. $CuGaSe_2$ solar cell cross section studied by Kelvin probe force microscopy in ultrahigh vacuum, *Appl Phys Lett* 81:2017–2019.

92. Chiesa M, *et al.,* 2005. Correlation between surface photovoltage and blend morphology in polyfluorene-based photodiodes, *Nano Lett* 5:559–563.

93. Hoppe H, *et al.,* 2005. Efficiency limiting morphological factors of MDMO-PPV:PCBM plastic solar cells, *Thin Solid Films* 511–512:587–592.

94. Lin Y-Y, *et al.,* 2009. Interfacial nanostructuring on the performance of polymer/TiO_2 nanorod bulk heterojunction solar cells, *J Am Chem Soc* 131:3644–3649.

95. Hoppe H, *et al.,* 2004. Nanoscale morphology of conjugated polymer/fullerene-based bulk-heterojunction solar cells, *Adv Funct Mater* 14:1005–1011.

96. Sengupta E, *et al.,* 2011. Photoinduced degradation studies of organic solar cell materials using Kelvin probe force and conductive scanning force microscopy, *J Phys Chem C* 115:19994–20001.

97. Schroder D K, 2001. Surface voltage and surface photovoltage: History, theory and applications, *Meas Sci Technol* 12, R16–R31.

98. Jaquith M J, Muller E M and Marohn J A, 2007. Time-resolved electric force microscopy of charge trapping in polycrystalline pentacene, *J Phys Chem B* 111:7711–7714.

99. Giridharagopal R, *et al.,* 2012. Sub-microsecond time resolution atomic force microscopy for probing nanoscale dynamics, *Nano Lett* 12:893–898.

100. Ramsdale C S, *et al.,* 2002. The origin of the open-circuit voltage in polyfluorene-based photovoltaic devices, *J Appl Phys* 92:4266–4270.

101. Koster L J A, Mihailetchi V D, Ramaker R and Blom P M W, 2005. Light intensity dependence of open-circuit voltage of polymer:fullerene solar cells, *Appl Phys Lett* 86:123509.

102. Yazdanian S M, Marohn J A and Loring R F, 2008. Dielectric fluctuations in force microscopy: Noncontact friction and frequency jitter, *J Chem Phys* 128:224706.

103. Boashash B, 1992. Estimating and interpreting the instantaneous frequency of a signal, I. Fundamentals, *Proceedings of the IEEE* 80:520–538.

104. Niki S, *et al.,* 2010. CIGS absorbers and processes, *Progress in Photovoltaics: Research and Applications* 18:453–466.

105. Noone K M and Ginger D S, 2009. Doping for speed: Colloidal nanoparticles for thin-film optoelectronics, *ACS Nano* 3:261–265.

106. Leever B J, Bailey C A, Marks T J, Hersam M C and Durstock M F, 2012. *In Situ* characterization of lifetime and morphology in operating bulk heterojunction organic photovoltaic devices by impedance spectroscopy, *Adv Energy Mater* 2:120–128.

107. Visoly-Fisher I, Cohen S R, Cahen D and Ferekides C S, 2003. Electronically active layers and interfaces in polycrystalline devices: Cross-section mapping of CdS/CdTe solar cells, *Appl Phys Lett* 83:4924–4926.

108. Jesse S, Kalinin S V, Proksch R, Baddorf A P and Rodriguez B J, 2007. The band excitation method in scanning probe microscopy for rapid mapping of energy dissipation on the nanoscale, *Nanotechnology* 18:435503.

109. Wang X *et al.,* 2010. High-resolution spectroscopic mapping of the chemical contrast from nanometer domains in P3HT:PCBM organic blend films for solar-cell applications, *Adv Funct Mater* 20:492–499.

Chapter 2. IMAGING LOCAL TRAP FORMATION IN CONJUGATED POLYMER SOLAR CELLS: A COMPARISON OF TIME-RESOLVED ELECTROSTATIC FORCE MICROSCOPY AND SCANNING KELVIN PROBE IMAGING

http://pubs.acs.org/articlesonrequest/AOR-MQ6e5ZJAY8tjF3E6PypM

My contributions to this work: I collected data included in Figure 1(b) and (c); Figure 3, and Figure 4. I collected all data for and generated Figure 2. I aided in editing the manuscript and submitted the initial manuscript for review. I was primarily responsible for responding to reviewer comments and updating the manuscript for final submission.

20672 *J. Phys. Chem. C* **2010,** *114,* 20672–20677

Imaging Local Trap Formation in Conjugated Polymer Solar Cells: A Comparison of Time-Resolved Electrostatic Force Microscopy and Scanning Kelvin Probe Imaging†

Obadiah G. Reid,‡ Glennis E. Rayermann, David C. Coffey,‡ and David S. Ginger*

Department of Chemistry, University of Washington, Seattle, Washington 98195, United States

Received: June 19, 2010; Revised Manuscript Received: September 27, 2010

We study local photooxidation and trap formation in all-polymer bulk-heterojunction organic photovoltaics (OPVs) using both time-resolved electrostatic force microscopy (trEFM) and conventional scanning Kelvin probe microscopy (SKPM). We create electron-trapping defects at known locations by locally photooxidizing blends of poly[(9,9′-dioctylfluorene-*alt*-(bis(*N,N*′-(4-butylphenyl))-bis(*N,N*′-phenyl-1,4-phenylenediamine)] and poly[9,9′-dioctylfluorene-*alt*-1,4-benzothiadiazole]. We then compare the local surface photovoltage shifts measured via SKPM and the changes in local photoinduced charging rates measured via trEFM with changes in the performance of macroscopic photodiodes that have been exposed to similar photooxidation. We find that the trEFM charging rate images can identify local photooxidation and trap formation with much better sensitivity than conventional SKPM images. In addition, the changes in the trEFM charging rates correlate well with the external quantum efficiencies of the macroscopic photodiodes. In contrast, the SKPM images not only are less sensitive to trap formation but also show a more complicated response. We conclude that trEFM is well suited to studying local trap formation in organic solar cells and caution that SKPM data by itself can be difficult to interpret on OPV films, especially when materials have been exposed to photooxidation.

Introduction

Organic solar cells are the subject of intense academic and industrial research because they may one day enable cheap, ubiquitous, solar energy conversion.[1−5] The most efficient organic solar cells to date are bulk heterojunction photodiodes, consisting of a blend of electron-donating and electron-accepting materials.[6−8] Bulk heterojunction solar cells are intrinsically nanostructured devices, and it is well accepted that materials and processing can dramatically alter the nanoscale morphology, and thus performance, of bulk heterojunction organic photovoltaics.[9−11] Charge trapping in these complicated blends can reduce carrier mobility and increase recombination losses, leading to decreased performance.[12−16] To date, however, the nature of charge traps in organic semiconductors remains one of the most poorly understood aspects of these complex blended materials. There are reasons to suspect that trap formation may be associated with specific morphological features in blends; indeed, recent studies on pentacene and anthradithiophene have produced evidence that trapping can be as sensitive as mobility is to film morphology in transistors.[17] If true, this would provide a route by which the lifetime of materials could be altered or improved via better processing. However, studies correlating local trap formation with device performance on organic solar cells are practically nonexistent, in part, because there are few methods that can image local trap formation.

To address this experimental challenge, we explored the suitability of two scanning-probe techniques, time-resolved electrostatic force microscopy (trEFM) and scanning Kelvin probe microscopy (SKPM), to study the trap formation in model blends of the conjugated polymers poly[(9,9′-dioctylfluorene-*alt*-(bis(*N,N*′-(4-butylphenyl))-bis(*N,N*′-phenyl-1,4-phenylenediamine)] (PFB) and poly[9,9′-dioctylfluorene-*alt*-1,4-benzothiadiazole] (F8BT) (see Figure 1a for chemical structures). These blends were chosen not because they offer any particular performance advantages but because they represent a well-studied model system, both morphologically[18−26] and photochemically.[27−30] In particular, it has been demonstrated that photooxidation of polyfluorenes leads to the formation of electron-trapping fluorenone defects.[28,29,31−33] Methods for imaging charge trap formation in organic photovoltaic blends using scanning probe microscopy are not well-established. Thus, as a first step, we take the approach of intentionally creating local trap sites via photooxidation of the polyfluorene blends and comparing the resulting trEFM and SKPM images. We find that, although average values from local trEFM measurements on photooxidized samples correlate well with macroscopic device efficiency, the surface photovoltage measured via SKPM does not. The SKPM data only indirectly track local performance changes due to photooxidation, most likely reflecting the density of charge traps via the steady-state surface charge density. These results have important implications not only for future studies of nanoscale charge trapping in OPVs but also, more generally, for the growing field of scanning probe microscopy on organic electronic devices.[34]

Experimental Methods

The devices used in this study were bulk heterojunction blends of PFB and F8BT. The polymers were obtained from American Dye Source and used as received, with molecular weights and PDI values of 23 kg mol^{-1} and 2.7 for the PFB and either 28 kg mol^{-1} and 2.2 or 30 kg mol^{-1} and 3.7 for the F8BT. Solutions of each polymer were prepared in a glovebox using anhydrous chlorobenzene at a concentration of 20 mg/mL. The solutions were heated for ∼4 h at 50 °C before being mixed together and filtered sequentially though 1, 0.45, and 0.2 μm PTFE filter

† Part of the "Mark A. Ratner Festschrift".

* To whom correspondence should be addressed. Phone: 206-685-2331. Fax: 206-685-8665. E-mail: ginger@chem.washington.edu.

‡ Current address: National Renewable Energy Laboratory, 1617 Cole Blvd., Golden, CO 80401-3305.

10.1021/jp1056607
Published on Web 10/14/2010

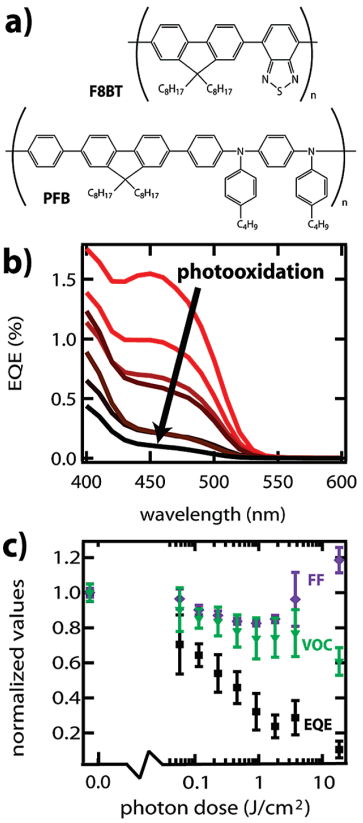

Figure 1. (a) Chemical structures of the electron donor PFB and acceptor F8BT. (b) External quantum efficiency (EQE) spectra of photochemically degraded PFB/F8BT blend bulk heterojunction solar cells spin-coated from chlorobenzene. As expected, with increasing photooxidation (red to black curves), the quantum efficiency decreases. (c) Normalized average device characteristics plotted as a function of a 405 nm photon energy dose in air, including the fill factor (FF, purple diamonds), open-circuit voltage (V_{OC}, inverted green triangles), and EQE (black squares). Error bars represent the standard deviation of the mean.

membranes using all-polypropylene syringes. The blend solution was mixed and allowed to stand at 50 °C for ~1 h before spin-coating at 2000 rpm for 2 min. The substrates comprised 15 × 15 mm squares of ITO-coated glass (TFD Inc.) coated in ~40 nm of cured poly(ethylene dioxythiophene):poly(styrene-sulfonate) (PEDOT:PSS; Baytron P). After spin-coating, the samples were allowed to dry in a nitrogen glovebox for at least 1 h before being subjected to controlled photooxidation. The devices were completed by depositing 75 nm thick aluminum top-contacts at 0.2 nm/s via thermal evaporation. The completed devices had an active area of ~1.5 mm^2, defined by the overlap of the ITO and Al electrodes. All device fabrication steps except for spin-coating and annealing of the PEDOT:PSS and controlled photooxidation were carried out in a dry nitrogen glovebox (<1 ppm O_2 and <0.1 ppm H_2O, typical).

Controlled photooxidation was performed in ambient air by exposing the samples to a measured dose of 405 nm radiation from either an LED (LEDtronics L200CUV405-8D) with an absorbed power of 4.8 W/m^2 or a 405 nm laser (CrystalLaser, intensity adjusted with neutral density filters). The LED source was used to uniformly dose the entire surface area of the low photon-dose films and before contact evaporation for the devices. To obtain the high photon doses for the PL and IR measurements, samples were exposed to 405 nm radiation from an LED (LedEngin LZ1-00UA05) with an absorbed power of 17.1 W/m^2. For the SKPM and trEFM measurements, an unexposed film was loaded into the AFM and exposed in situ using the laser source. The laser was set at a fixed intensity (attenuated with neutral density filters) and focused on the sample. The sample stage was then moved at intervals so that different areas of the sample could be exposed in a controlled fashion. The total dose was controlled by the dwell time of the laser spot on any given location. This latter strategy allows comparison of different degrees of photooxidation in the same image and substantially reduces experimental variation in the AFM experiments by reducing the influence of tip changes or other artifacts in evaluating the relative signal.

Macroscopic devices were tested in a home-built vacuum chamber at a pressure of <10 mbar. A monochromated (Acton Research Corp., 2150i) xenon lamp source with a total power of 75 W (Newport Oriel Photo Max lamp housing) was used for external quantum efficiency (EQE) spectrum measurements. The currents in the EQE and the $I-V$ experiments were measured using a Keithley 2400 source-measure unit. All illuminated $I-V$ curves were performed at a wavelength of 460 nm, to match that used in our SKPM and trEFM experiments. Using 460 nm illumination will cause most of the light to be absorbed by the F8BT. However, the very fine phase separation in the active layer is on a significantly smaller scale (<100 nm) than the photooxidized spots. The focus of the present study is thus on the identification of the photooxidized regions using scanning probe methods and not on resolving any differences between the PFB and F8BT domains.

Photoluminescence (PL) spectra on the bulk photooxidized films were measured on an optical microscope (Nikon TE2000, 50× magnification) using a fiber-coupled spectrometer (Ocean Optics USB2000). A metal halide lamp (Nikon LHS-H100C-1) with a 405 nm band-pass filter was used for excitation, and a 430 nm long-pass filter was used to block the excitation light from the spectrometer. The samples were sealed in a custom-built nitrogen-purged chamber for all PL measurements.

IR spectra were taken using a ThermoFischer Scientific Nicolet-8700-FTIR equipped with a HgCdTe detector, Harrick GATR grazing angle ATR accessory with a 65° fixed incident angle, and a 56 in-oz slip-clutch. The spectrometer and accessory were purged with N_2 gas. All spectra were signal-averaged over 256 scans with a resolution of 1 cm^{-1} and were baseline-corrected.

AFM experiments were conducted using an Asylum Research MFP-3D. All samples were imaged under dry nitrogen using the Asylum flow cell accessory. Ambient air, with a relative humidity between 20 and 50%, was deliberately introduced into the cell for in situ photooxidation experiments and subsequently purged with N_2 for >30 min before imaging. We stress that no sample damage was observed even at relatively high photon doses (>100 J/cm^2) when the samples were maintained under N_2; only the combination of light exposure with the deliberate introduction of air resulted in photooxidation. Both our trEFM and SKPM experiments were implemented in custom software written in-house for Igor Pro and the Asylum Research XOP. In both cases, we implement a two-pass imaging procedure, with frequency shift or phase feedback for electrostatic measurements. Both the trEFM and the SKPM implementations are described in detail elsewhere.[25,34] Sample illumination for trEFM and SKPM measurements was provided by a 455 nm LED (Luxeon LXHLNRR8, 20 nm fwhm), whose intensity was varied using a set of neutral-density filters.

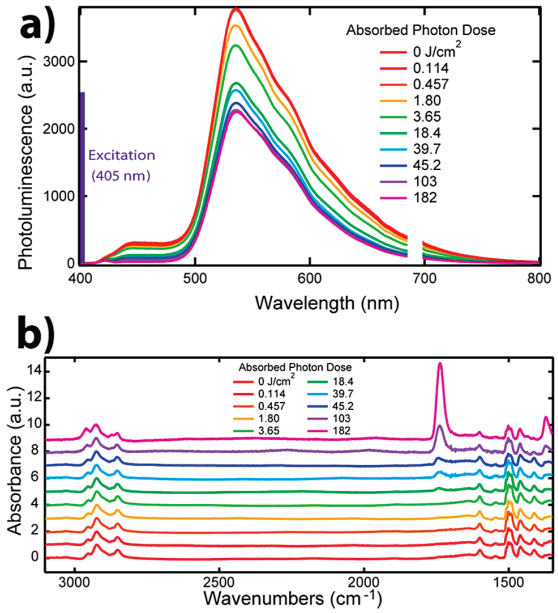

Figure 2. (a) Photoluminescence (PL) spectra of PFB/F8BT films that have received 405 nm photon doses in air ranging from 0 to 182 J/cm^2, as indicated in the legend. The shoulder at 460 nm is attributed to the luminescence of the PFB, whereas the peak at 540 nm is attributed to luminescence from F8BT. A decrease in photoluminescence intensity with increasing photooxidation is evident (light in the range of 680−699 nm has been removed from the spectrum). (b) Fourier-transform infrared attenuated total reflectance (FTIR-ATR) spectra of PFB/F8BT films exposed in air to photon doses from 0 to 182 J/cm^2 (as indicated in the legend; traces offset for clarity.) The spectral feature of interest is the absorbance peak at ∼1737 cm^{-1}, consistent with the keto stretch of fluorenone. This absorbance peak is only detectable for films with the higher photon doses.

Results and Discussion

First, we discuss the effects of intentional photooxidation on the performance of the polymer photodiodes. Figure 1b shows the EQE spectra from a series of PFB/F8BT devices that have received varying 405 nm absorbed photon doses from 0.04 to 11 J/cm^2 in ambient air. As expected, the overall device efficiency decreases rapidly with increasing exposure, and the photocurrent peak attributed to the absorption of the F8BT is preferentially suppressed. Figure 1c shows the trends for EQE, open-circuit voltage (V_{OC}), and fill-factor (FF) on a logarithmic scale of energy dose, each averaged over at least four different batches of devices and measured at 460 nm. The EQE shows a rapid exponential decay, declining to ∼50% of its initial value at an absorbed photon dose of only ∼0.4 J/cm^2, whereas the FF and V_{OC} show much more gradual declines (with the FF actually increasing at larger exposures). This decreasing performance is consistent with that expected from photooxidation of the active layer[35] and formation of keto defects that lead to increased trapping[12,14,31] and decreased carrier mobility[32,33] in polyfluorenes.

We used photoluminescence and infrared spectroscopies in an attempt to detect the fluorenone defects we expected as the primary photooxidation product in these polymers. Figure 2a shows the fluorescence spectra of PFB/F8BT films that have absorbed photon doses of 0−182 J/cm^2. Of these films, those with doses of 0, 0.114, 0.457, 1.83, 3.65, and 18.4 correspond to device efficiencies of 100, 64, 45, 24, 29, and 11%, relative to unexposed devices. The spectra are dominated by a green peak at 540 nm with a long red tail and a small blue shoulder at 460 nm. The effect of photochemical degradation can be seen from the decrease in photoluminescence intensity. This decrease in PL intensity is consistent with the formation of keto defects in the polyfluorenes, which are electron-trap sites and which quench the polyfluorene photolumniscence.[27,28,36,37] At the lowest doses, consistent with the lower range of device doses tested, the change in PL intensity is difficult to detect, even though we observe a decrease in device efficiency and trEFM charging rate.

Figure 2b is a comparison of the infrared spectra of PFB/F8BT films that were exposed to photon doses of 0−182 J/cm^2. The absorbance at ∼1737 cm^{-1}, consistent with the carbonyl stretch of fluorenone,[29,30,38,39] is only observed in the IR spectra of the films with higher photon doses (18.4−182 J/cm^2). Over the range of doses for devices tested, only that with the highest dose (18.4 J/cm^2) has an IR spectrum with a detectable keto peak. In combination with the PL spectra, the IR spectra confirm the formation of fluorenone defects by photooxidation, at least at high photon doses. It is interesting to note, however, that we can only detect chemical changes with FTIR-ATR in the film at higher photon doses, though device performance is affected by significantly lower photon doses. Although we believe that the absence of fluorenone signatures in IR and PL data are simply due to the detection limits, it is possible that, at low photon doses, some other chemical species may be responsible for the decrease in charging rate. For instance, because these films were photooxidized under ambient conditions, electron transfer from the excited polymer to reduce O_2 in the presence of H_2O may occur, as has been reported as a trap species in transistor measurements.[40] Regardless, the key result of this data is that the electrical device performance is much more sensitive to the presence of photooxidative exposure than PL or FTIR spectroscopy and that a new method is needed if we are to study photooxidative damage at the local (nanoscale) level.

We next examine the corresponding scanning probe microscopy data. Figure 3a shows a schematic of our in situ photooxidation experiment. The 405 nm laser diode is focused sequentially on discrete spots that are selectively photooxidized using the laser in a 3 × 3 matrix (10 μm spacing, left-to-right, top-to-bottom) over a 900 μm^2 area. Each spot received twice the dose of the previous spot (dose range, ∼0.04−11 J/cm^2). Figure 3b−e shows a set of topography (b), trEFM (c), and SKPM (dark (d) and light (e)) images of a sample area that has been photochemically patterned as described above. The trEFM image is a map of the charging rate, which describes the charging of the tip−sample capacitor as free charge carriers are generated under illumination.[25] Immediately, we notice that, whereas the charging rate in the trEFM image (Figure 3c) declines rapidly with increasing photon dose over this range, we see very little change in the surface potential (SP) measured via SKPM in either dark (Figure 3d) or illuminated (Figure 3e) conditions except at the highest photon doses. At the highest photon doses, there is a detectable negative surface photovoltage shift. However, the regions of increased negative photovoltage are associated with the regions of the highest photooxidation, demonstrating that increased local photovoltage magnitudes do not necessarily indicate better local performance.

Figure 4 summarizes the results of both the macroscopic photodiode measurements and the local scanning probe experiments. With increasing photooxidation, Figure 4 shows that the device EQE and local charging rate measured via trEFM both decrease with increasing photooxidation. In contrast, the surface photovoltage (the difference between SP in the light and dark)

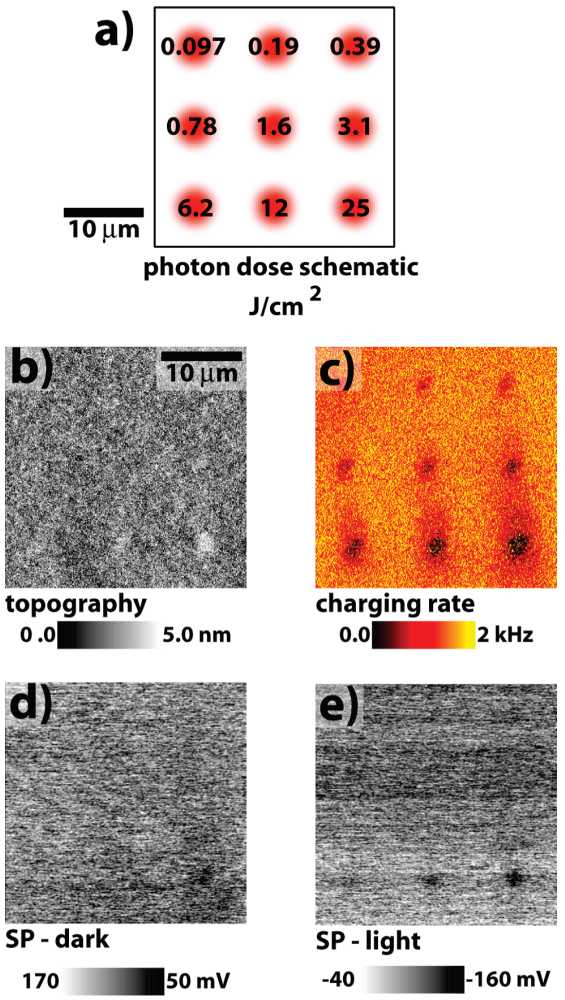

Figure 3. (a) Schematic of the local photooxidation experiment showing areas that were exposed to the 405 nm laser in air at different photon doses. The total absorbed energy dose in J/cm^2 in each area for the AFM images in panels b−e is noted on the spots. (b) Topography of a PFB/F8BT blend spin-coated from chlorobenzene. (c) Charging rate image of the same area measured with trEFM. The trEFM image is a map of the charging rate. The charging rate describes how fast the tip−sample capacitor fills as free charge carriers are generated under illumination. (d) Surface potential measured in the dark (at least 30 min since the last illumination). (e) Surface potential measured in the light (460 nm, general illumination).

shows very little change with photooxidation. These experiments were repeated over multiple sample sets, averaged, and normalized to the initial values before photooxidation. The AFM data are the averages of five samples in the lower dosage range and two in the upper dosage range. The device data are an average of five different samples. In each case, the measurements were made at ∼460 nm illumination. The qualitative trend observed previously in Figure 3b−e is quantified over many images in Figure 4: the relative changes in charging rate and external quantum efficiency correlate very well with one another across multiple samples, whereas the surface photovoltage is relatively insensitive to increasing photooxidation and actually increases slightly in magnitude over the unexposed case. Indeed, comparison of Figure 3 with Figure 1c shows that the surface photovoltage does not correlate well with any of the observed device performance characteristics.

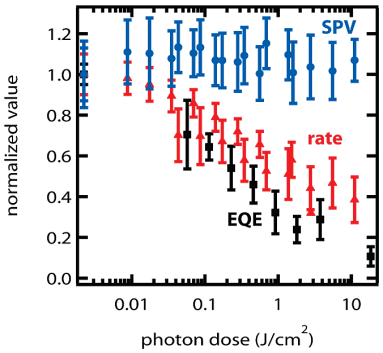

Figure 4. Normalized average values from AFM images and device measurements plotted as a function of a 405 nm photon dose in air, including surface photovoltage (SPV, blue circles), trEFM charging rate (rate, red triangles), and external quantum efficiency (EQE, black squares). Error bars represent the standard deviation of the mean. The lowest photon doses of zero are displayed on the semilog plot at ∼0.002 J/cm^2.

As suggested above, these results appear to contradict previous reports of a correlation between surface photovoltage and open-circuit voltage[41] and/or local charge separation efficiency,[42−49] as our data are not consistent with either of these hypotheses, at least as a function of photooxidation in PFB/F8BT blends. On the other hand, the trEFM charging rate measurements, which are well correlated with the macroscopic quantum efficiency, do demonstrate a clear decline in local charging rate with increasing photochemical degradation.

These contradictions can be explained, in part, by the differences in the material systems and experimental configurations but nevertheless highlight the difficulty in using basic SKPM data to draw conclusions about device performance. For instance, Palermo and co-workers have shown that, at least on insulating substrates, the surface photovoltages of neighboring donors and acceptors shift as one would expect: the acceptor becomes more negative, whereas the donor becomes more positive, consistent with electron and hole accumulation in each material.[44−46] However, studies on active device structures incorporating a conductive substrate (as is the case for the measurements presented herein) typically show a concerted shift in the potential of the entire surface, sometimes irrespective of the local structure.[47−51] On the basis of this observation in conjunction with detailed numerical simulations, Kemerink and co-workers[51] have argued convincingly that the surface photovoltage in device-like organic photodiode structures is dominated by the difference in transport rates for electrons and holes and the injection barrier at the bottom contact, where an imbalance leads to an excess of a single carrier throughout the film. The steady-state concentration of each carrier under illumination is determined by a competition between charge generation, recombination, transport, and trapping. However, since only changes in *net* charge density lead to shifts in surface potential, the relative rates of generation and recombination are not likely to be important (being equal for both carriers) unless there is a large-scale separation of pure donor and acceptor phases that are electrically isolated. Thus, on device structures with conducting substrates, the generally asymmetric rates of charge transport, injection, and trapping dominate.

Consistent with this latter hypothesis, we interpret our SKPM data as being the result of an increased electron-trap density as the polymers are photochemically degraded. We attribute the initial increase in (negative) surface photovoltage magnitude,

and the more negative surface potential we observe on highly exposed areas of the film (Figure 3d,e), to an increase in electron-trap density that increases the steady-state electron density under illumination. However, these photovoltage shifts are difficult to detect via SKPM until the photooxidation is relatively severe. At low photon doses, where the device performance is already clearly degraded, we measure almost no shift in surface potential. On the other hand, at these same photon doses, we are able to clearly resolve differences in the trEFM charging rates.

We draw several conclusions from these results. First, trEFM measurements appear to provide a straightforward measurement of the changes in local quantum efficiency due to photooxidation, but SKPM measurements of the surface photovoltage, in general, do not. Furthermore, the changes we observe in surface photovoltage measured via SKPM are not clearly correlated with changes in the device fill factor or open-circuit voltage. Second, the trEFM charging rate measurement appears to be much more sensitive to low levels of photochemical exposures than that of surface potential, IR spectroscopy, or PL spectroscopy and is thus well suited to future experiments correlating local morphology with charge trap formation. Given the large difference in the sensitivities of the techniques used, it is difficult to identify the exact chemical species responsible for device degradation at the lowest photon doses; however, the IR and PL data confirm the formation of fluorenone defects at higher doses, consistent with previous literature.[28,38,52−54] Third, following the model proposed by Kemerink and co-workers,[51] the change in surface photovoltage with increasing photochemical exposure we observe could be explained by an increase in trap density for electrons relative to that for holes. This result suggests the possibility of using SKPM in conjunction with another measure of local device efficiency (as we have done here) to discern not merely what areas of an organic solar cell composite perform poorly or well but also perhaps to answer whether observed changes in local efficiency are caused by trapping of either carrier. Further experiments might also be combined with thermally stimulated current (TSC) spectroscopy on bulk samples in order to determine the activation energy and concentration of charge traps.[55−57] In the future, if a sufficiently sensitive current detector becomes available, then it may be possible to perform TSC measurements locally using cAFM. Finally, it is interesting to note the very small energy doses required in ambient air to effect substantial changes in device performance, local charging rate, and measurable increases in electron-trap density in these polymers. At the very least, this result severely complicates interpretation of optoelectronic SPM data acquired in air on organic semiconductors and highlights the need for inert-atmosphere conditions in this class of experiments.[58]

Conclusions

In summary, we have performed trEFM and SKPM measurements on PFB/F8BT bulk heterojunction blend films that have been locally photooxidized and compared our microscopy results with the performance of similarly degraded macroscopic photodiodes. We find that, whereas the local charging rate measured via trEFM correlates very well with the quantum efficiency for photochemically degraded regions of the film, the surface photovoltage measured via SKPM is not easily connected to any of the photochemically induced changes in macroscopic device properties in this system. With the polymers we used, only small photon doses were required in ambient air to photochemically degrade the devices to 50% of their original quantum efficiency (1 J/cm^2 incident, ∼0.4 J/cm^2 absorbed), corresponding to a level of photochemical damage that is difficult to discern through PL or FTIR measurements. Our results caution against the use of surface-potential measurements by themselves as a primary characterization tool of these materials unless one performs detailed modeling.[51] We further caution against the use of any optoelectronic scanning probe method on organic semiconductors in air. Most importantly, these results demonstrate that it should be possible to use SKPM combined with trEFM to correlate the local steady-state charge distributions in organic semiconductors with the local device performance and thus should enable future studies of trapping and trap formation kinetics as a function of local morphology.

Acknowledgment. This work was supported by the National Science Foundation (DMR 0449422) and the STC Program of the National Science Foundation (DMR 0120967). This research utilized equipment purchased with support of the AFOSR and the Murdock Foundation. D.S.G also thanks the Camille Dreyfus Teacher-Scholar Awards Program for support. O.G.R. was an NSF IGERT fellowship recipient (NSF no. DGE-0504573) during part of this work. G.E.R. is an ARCS fellowship recipient.

References and Notes

(1) Dennler, G.; Scharber, M. C.; Brabec, C. J. *Adv. Mater.* **2009**, *21*, 1323–1338.
(2) Kippelen, B.; Bredas, J. L. *Energy Environ. Sci.* **2009**, *2*, 251–261.
(3) Brabec, C. J.; Durrant, J. R. *MRS Bull.* **2008**, *33*, 670–675.
(4) Brabec, C. J.; Sariciftci, N. S.; Hummelen, J. C. *Adv. Funct. Mater.* **2001**, *11*, 15–26.
(5) Gunes, S.; Neugebauer, H.; Sariciftci, N. S. *Chem. Rev.* **2007**, *107*, 1324–1338.
(6) Liang, Y.; Xu, Z.; Xia, J.; Tsai, S.-T.; Wu, Y.; Li, G.; Ray, C.; Yu, L. *Adv. Mater.* **2010**, *22*, 1–4.
(7) Park, H. J.; Kang, M. G.; Ahn, S. H.; Guo, L. J. *Adv. Mater.* **2010**, *22*, E247–E253.
(8) Yu, G.; Gao, J.; Hummelen, J. C.; Wudl, F.; Heeger, A. J. *Science* **1995**, *270*, 1789–1791.
(9) Groves, C.; Reid, O. G.; Ginger, D. S. *Acc. Chem. Res.* **2010**, *43*, 612–620.
(10) Giridharagopal, R.; Ginger, D. S. *J. Phys. Chem. Lett.* **2010**, *1*, 1160–1169.
(11) Peet, J.; Heeger, A. J.; Bazan, G. C. *Acc. Chem. Res.* **2009**, *42*, 1700–1708.
(12) Kawano, K.; Adachi, C. *Adv. Funct. Mater.* **2009**, *19*, 3934–3940.
(13) Kazukauskas, V.; Pranaitis, M.; Kajzar, F.; Glatthaar, M.; Hinsch, A. *Mol. Cryst. Liq. Cryst.* **2008**, *484*, 739–747.
(14) Liu, R.; Lei, Y. L.; Chen, P.; Song, Q. L.; Xiong, Z. H. *J. Phys. D: Appl. Phys.* **2009**, *42*, 145112.
(15) Matsushima, T.; Yahiro, M.; Adachi, C. *Appl. Phys. Lett.* **2007**, *91*, 103505.
(16) Burgi, L.; Richards, T.; Chiesa, M.; Friend, R. H.; Sirringhaus, H. *Synth. Met.* **2004**, *146*, 297–309.
(17) Jaquith, M. J.; Anthony, J. E.; Marohn, J. A. *J. Mater. Chem.* **2009**, *19*, 6116–6123.
(18) McNeill, C. R.; Watts, B.; Thomsen, L.; Belcher, W. J.; Greenham, N. C.; Dastoor, P. C.; Ade, H. *Macromolecules* **2009**, *42*, 3347–3352.
(19) McNeill, C. R.; Watts, B.; Swaraj, S.; Ade, H.; Thomsen, L.; Belcher, W.; Dastoor, P. C. *Nanotechnology* **2008**, *19*, 424015.
(20) McNeill, C. R.; Watts, B.; Thomsen, L.; Ade, H.; Greenham, N. C.; Dastoor, P. C. *Macromolecules* **2007**, *40*, 3263–3270.
(21) McNeill, C. R.; Watts, B.; Thomsen, L.; Belcher, W. J.; Greenham, N. C.; Dastoor, P. C. *Nano Lett.* **2006**, *6*, 1202–1206.
(22) McNeill, C. R.; Frohne, H.; Holdsworth, J. L.; Dastoor, P. C. *Nano Lett.* **2004**, *4*, 2503–2507.
(23) Snaith, H. J.; Arias, A. C.; Morteani, A. C.; Silva, C.; Friend, R. H. *Nano Lett.* **2002**, *2*, 1353–1357.
(24) Arias, A. C.; MacKenzie, J. D.; Stevenson, R.; Halls, J. J. M.; Inbasekaran, M.; Woo, E. P.; Richards, D.; Friend, R. H. *Macromolecules* **2001**, *34*, 6005–6013.
(25) Coffey, D. C.; Ginger, D. S. *Nat. Mater.* **2006**, *5*, 735–740.
(26) Halls, J. J. M.; Arias, A. C.; MacKenzie, J. D.; Wu, W. S.; Inbasekaran, M.; Woo, E. P.; Friend, R. H. *Adv. Mater.* **2000**, *12*, 498–502.

(27) Becker, K.; Lupton, J. M.; Feldmann, J.; Nehls, B. S.; Galbrecht, F.; Gao, D. Q.; Scherf, U. *Adv. Funct. Mater.* **2006**, *16*, 364–370.

(28) Jaiser, F.; Yang, X.; Neher, D.; Guentner, R.; de Freitas, P. S.; Forster, M.; Scherf, U. In *Organic Light-Emitting Materials and Devices VII*; 1 ed.; SPIE: San Diego, CA, USA, 2004; Vol. 5214, p 207−215.

(29) List, E. J. W.; Guentner, R.; de Freitas, P. S.; Scherf, U. *Adv. Mater.* **2002**, *14*, 374–378.

(30) Bliznyuk, V. N.; Carter, S. A.; Scott, J. C.; Klarner, G.; Miller, R. D.; Miller, D. C. *Macromolecules* **1998**, *32*, 361–369.

(31) Kadashchuk, A.; Schmechel, R.; von Seggern, H.; Scherf, U.; Vakhnin, A. *J. Appl. Phys.* **2005**, *98*, 024101.

(32) Noh, Y. Y.; Kim, D. Y.; Yoshida, Y.; Yase, K.; Jung, B. J.; Lim, E.; Shim, H. K.; Azumi, R. *J. Appl. Phys.* **2005**, *97*, 104504.

(33) Noh, Y. Y.; Kim, D. Y.; Yoshida, Y.; Yase, K.; Jung, B. J.; Lim, E.; Shim, H. K.; Azumi, R. *Appl. Phys. Lett.* **2004**, *85*, 2953–2955.

(34) Pingree, L. S. C.; Reid, O. G.; Ginger, D. S. *Adv. Mater.* **2009**, *21*, 19–28.

(35) Jo, J.; Vak, D.; Noh, Y. Y.; Kim, S. S.; Lim, B.; Kim, D. Y. *J. Mater. Chem.* **2008**, *18*, 654–659.

(36) Bliznyuk, V. N.; Carter, S. A.; Scott, J. C.; Klarner, G.; Miller, R. D.; Miller, D. C. *Macromolecules* **1999**, *32*, 361–369.

(37) Sims, M.; Bradley, D. D. C.; Ariu, M.; Koeberg, M.; Asimakis, A.; Grell, M.; Lidzey, D. G. *Adv. Funct. Mater.* **2004**, *14*, 765–781.

(38) Asada, K.; Takahashi, H.; Naito, H. *Thin Solid Films* **2006**, *509*, 202–206.

(39) Kulkarni, A. P.; Kong, X.; Jenekhe, S. A. *J. Phys. Chem. B* **2004**, *108*, 8689–8701.

(40) Aguirre, C. M.; Levesque, P. L.; Paillet, M.; Lapointe, F.; St-Antoine, B. C.; Desjardins, P.; Martel, R. *Adv. Mater.* **2009**, *21*, 3087.

(41) Chiesa, M.; Burgi, L.; Kim, J. S.; Shikler, R.; Friend, R. H.; Sirringhaus, H. *Nano Lett.* **2005**, *5*, 559–563.

(42) Zeng, T. W.; Hsu, F. C.; Tu, Y. C.; Lin, T. H.; Su, W. F. *Chem. Phys. Lett.* **2009**, *479*, 105–108.

(43) Dabirian, R.; Feng, X.; Ortolani, L.; Liscio, A.; Morandi, V.; Mullen, K.; Samori, P.; Palermo, V. *Phys. Chem. Chem. Phys.* **2010**, *12*, 4473–4480.

(44) Liscio, A.; Palermo, V.; Samori, P. *Acc. Chem. Res.* **2010**, *43*, 541–550.

(45) Palermo, V.; Otten, M. B. J.; Liscio, A.; Schwartz, E.; de Witte, P. A. J.; Castriciano, M. A.; Wienk, M. M.; Nolde, F.; De Luca, G.; Cornelissen, J.; Janssen, R. A. J.; Mullen, K.; Rowan, A. E.; Nolte, R. J. M.; Samori, P. *J. Am. Chem. Soc.* **2008**, *130*, 14605–14614.

(46) Liscio, A.; De Luca, G.; Nolde, F.; Palermo, V.; Muellen, K.; Samori, P. *J. Am. Chem. Soc.* **2008**, *130*, 780–781.

(47) Palermo, V.; Ridolfi, G.; Talarico, A. M.; Favaretto, L.; Barbarella, G.; Camaioni, N.; Samori, P. *Adv. Funct. Mater.* **2007**, *17*, 472–478.

(48) Cao, J.; Sun, J. Z.; Hong, J.; Yang, X. G.; Chen, H. Z.; Wang, M. *Appl. Phys. Lett.* **2003**, *83*, 1896–1898.

(49) Lin, Y. Y.; Chu, T. H.; Li, S. S.; Chuang, C. H.; Chang, C. H.; Su, W. F.; Chang, C. P.; Chu, M. W.; Chen, C. W. *J. Am. Chem. Soc.* **2009**, *131*, 3644–3649.

(50) Hoppe, H.; Glatzel, T.; Niggemann, M.; Hinsch, A.; Lux-Steiner, M. C.; Sariciftci, N. S. *Nano Lett.* **2005**, *5*, 269–274.

(51) Maturova, K.; Kemerink, M.; Wienk, M. M.; Charrier, D. S. H.; Janssen, R. A. J. *Adv. Funct. Mater.* **2009**, *19*, 1379–1386.

(52) Becker, K.; Lupton, J. M.; Feldmann, J.; Nehls, B. S.; Galbrecht, F.; Gao, D. Q.; Scherf, U. *Adv. Funct. Mater.* **2006**, *16*, 364–370.

(53) Dias, F. B.; Knaapila, M.; Monkman, A. P.; Burrows, H. D. *Macromolecules* **2006**, *39*, 1598–1606.

(54) Grisorio, R.; Suranna, G. P.; Mastrorilli, P.; Nobile, C. F. *Adv. Funct. Mater.* **2007**, *17*, 538–548.

(55) Arif, M.; Yun, M.; Gangopadhyay, S.; Ghosh, K.; Fadiga, L.; Galbrecht, F.; Scherf, U.; Guha, S. *Phys. Rev. B* **2007**, *75*, 5.

(56) Nguyen, T. P.; Renaud, C.; Huang, C. H.; Lo, C. N.; Lee, C. W.; Hsu, C. S. *J. Mater. Sci.: Mater. Electron.* **2008**, *19*, S92–S95.

(57) Renaud, C.; Huang, C. H.; Lee, C. W.; Le Rendu, P.; Nguyen, T. P. *Thin Solid Films* **2008**, *516*, 7209–7213.

(58) Alexeev, A.; Loos, J. *Org. Electron.* **2008**, *9*, 149–154.

JP1056607

Chapter 3. SUBMICROSECOND TIME RESOLUTION ATOMIC FORCE MICROSCOPY FOR PROBING NANOSCALE DYNAMICS

My contributions to this work: I co-created the numerical damped, driven harmonic oscillator simulation to model the cantilever motion. This model provided a computationally tractable means for me to investigate the cantilever dynamics and provide insight for optimizing demodulation as well as data collection and processing methods. I generated the data for and created Figure 1(B). I generated data used in Figure 2(C) and Figure 2(D). I aided in editing the manuscript.

Note: See appendix for the United States patent granted for submicrosecond time resolution atomic force microscopy.

NANO LETTERS

Letter

pubs.acs.org/NanoLett

Submicrosecond Time Resolution Atomic Force Microscopy for Probing Nanoscale Dynamics

Rajiv Giridharagopal, Glennis E. Rayermann, Guozheng Shao, David T. Moore,[‡] Obadiah G. Reid,[§] Andreas F. Tillack, David. J. Masiello, and David S. Ginger*

Department of Chemistry, University of Washington, Seattle, Washington 98195, United States

Supporting Information

ABSTRACT: We propose, simulate, and experimentally validate a new mechanical detection method to analyze atomic force microscopy (AFM) cantilever motion that enables noncontact discrimination of transient events with ~100 ns temporal resolution without the need for custom AFM probes, specialized instrumentation, or expensive add-on hardware. As an example application, we use the method to screen thermally annealed poly(3-hexylthiophene):phenyl-C_{61}-butyric acid methyl ester photovoltaic devices under realistic testing conditions over a technologically relevant performance window. We show that variations in device efficiency and nanoscale transient charging behavior are correlated, thereby linking local dynamics with device behavior. We anticipate that this method will find application in scanning probe experiments of dynamic local mechanical, electronic, magnetic, and biophysical phenomena.

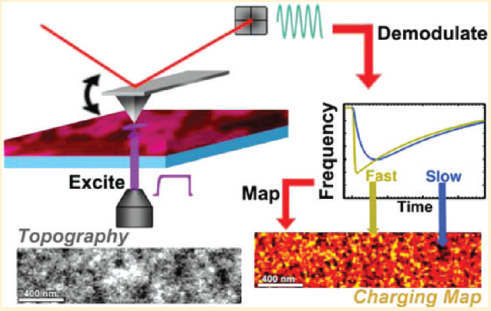

KEYWORDS: *Scanning probe microscopy, electrostatic force microscopy, organic solar cells, bulk heterojunction, P3HT:PCBM*

Atomic force microscopy (AFM) is widely used across many scientific disciplines to study systems with nanoscale spatial resolution, from semiconductor physics to surface chemistry to biological phenomena. Through the use of mechanical and electrical feedback modes, AFM methods are used to study such diverse problems as mechanical properties and glass transitions in polymer blends,[1] surface polarization in ferroelectrics,[2] photogeneration of charge in solar cells,[3] and energy storage in batteries.[4] However, despite the widespread availability of commercial AFM equipment, the ability to study dynamic processes below the diffraction limit with scanning probes has generally been limited to relatively slow processes on the order of milliseconds[5,6] or to specialized methods restricted to limited physical processes[7] that often involve custom-fabricated probes.[1,8] The fastest AFM methods typically acquire image scan lines at rates of ~3 kHz,[9] while studies reporting time-resolved AFM measurements with commercial instruments often measure local processes on time scales of, at best, several cantilever cycles in specific experimental designs[10] or much longer in more general designs.[5]

Attempts to study faster dynamic phenomena with scanning probe instruments have largely employed sophisticated combinations of pulsed laser optics with either near-field scanning optical microscopy[11,12] nonlinear mixing using heterodyning[13] or scanning tunneling microscopy (STM).[14,15] More recently, nonoptical time-resolved STM methods limited to the current preamplifier bandwidth,[16] using radio frequency STM,[17] and electronic pump−probe STM[18] have been reported. These techniques can provide powerful probes in systems with specific optical or electronic properties but generally require complex, expensive specialty hardware and are restricted in their ability to study materials with low optical contrast or high conductivity. As a result, these probes have been limited primarily to niche applications.

To address these shortcomings, our group has previously used fast frequency shift feedback methods to measure fast processes, such as the accumulation of photogenerated charges in low-efficiency polymer solar cells on time scales approaching ~100 μs using time-resolved electrostatic force microscopy (trEFM).[3,19,20] While fast compared to most AFM methods, even 100 μs is insufficient to study many processes of relevance in physical systems of interest (including more efficient organic and inorganic solar cells).[21] One could achieve better time resolution by using more sophisticated feedback controls. However, any feedback system will ultimately face a signal/noise stability limit. Here, we describe a feedback-free approach to obtaining information about fast local force transients in an AFM and show that the method is capable of discerning useful information about fast local dynamics with transient rise times as short as ~100−200 ns. We anticipate that this method, hereafter fast free time-resolved electrostatic force microscopy (FF-trEFM), may find application in scanning probe experiments of fast local changes, including carrier dynamics,[14]

Received: November 10, 2011
Revised: December 26, 2011

   dx.doi.org/10.1021/nl203956q | *Nano Lett.* XXXX, XXX, XXX−XXX

biological processes,[7,22] and transient magnetic resonance measurements.[23,24]

The method, summarized in Figure 1A, relies upon analyzing the free oscillation dynamics of an atomic force microscope

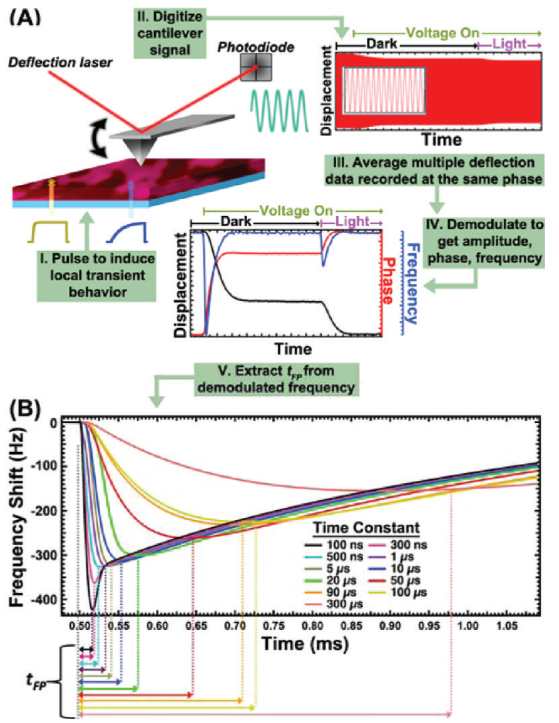

Figure 1. Schematic and operation of FF-trEFM. (A) Block diagram illustrating FF-trEFM operation. After feedback is turned off, the cantilever signal is digitized and recorded with high sampling rate (typically 50 MHz for point scans, 5−50 MHz for images). Multiple runs, with the excitation applied at the same phase, are averaged and demodulated to acquire the instantaneous frequency (typically 1500 for point scans and 6−10 per pixel for images). The metric of interest is the time between excitation and maximum frequency shift from steady-state (time to frequency shift peak, t_{FP}). (B) Instantaneous frequency of simulated cantilever behavior, using realistic cantilever parameters (ω_0 = 247.329 kHz, Q = 363, k = 27.7 N/m) with transient perturbations of root exponential form with characteristic time constants from 100 ns to 300 μs, showing the monotonic behavior of t_{FP} with perturbation rise time. Arrows at the bottom illustrate the t_{FP} time.

cantilever operating in conventional ac-mode on a commercial AFM with custom software and low-cost external hardware. The cantilever oscillation is digitized, while a transient perturbation, such as a voltage pulse or light pulse, is triggered to initiate the local dynamics of interest. Importantly, a triggering circuit is employed to phase lock the trigger event to the cantilever motion (Figure S2A, Supporting Information) so that the trigger always occurs at the same point in the cantilever oscillation (Figure S2B, Supporting Information), thereby improving the efficacy of signal averaging and thus the time resolution.

The challenge then becomes extracting the interesting dynamic behavior of the system from the cantilever motion. In ac-mode AFM, the cantilever motion is usually described as a damped driven harmonic oscillator.[25] Following a transient perturbation, the force $F(t)$ and force gradient dF/dz experienced by the AFM tip may both change in time. These changes in turn alter the harmonic motion of the cantilever. The objective is thus to recover the time profiles of the $F(t)$ and/or dF/dz signals of interest from the resulting fast cantilever motion. In principle, with sufficient computational resources and some basic information about the system under investigation, one could attempt to reconstruct the temporal evolution of $F(t)$ and $\partial F/\partial z$ by numerically integrating the equations of motion and fitting the resulting motion to the real tip data. Practically, we have found it faster and more convenient to employ a simplified data analysis procedure as described below.

As a proof of principle, we first consider detecting transients in a model damped driven harmonic oscillator (DDHO) governed by the classic equation of motion:[25]

$$\frac{d^2z}{dt^2} + 2\beta\frac{dz}{dt} + \omega_0(t)^2 z = (F_0/m)\cos(\omega t) + F_e(t)/m \quad (1)$$

where z is the tip displacement, F_0 is the driving force applied to the cantilever, m is the effective cantilever mass, ω_0 is the resonance frequency of the cantilever that depends on factors, such as the spring constant k and m, and ω is the frequency of the driving force signal applied to the cantilever. F_e is an external force of interest acting on the cantilever that varies with time, and $\beta = \omega_0/2Q$ is the damping factor where Q is defined as the quality factor. Transient changes in the cantilever motion will arise from changes in the both force F_e, and its derivative with respect to tip height, $\partial F_e/\partial z$. The latter effectively modifies the spring constant and thus shifts the instantaneous resonance frequency, with the shift $\Delta\omega_0$ being proportional to $(\partial F/\partial z)$.[26]

As exponential decays are among the most ubiquitous signals resulting from small perturbations to a system, we consider a time-dependent force $F_e(t)$ and resonant frequency $\omega_0(t)$ of the form:

$$F_e(t \geq 0) \approx F_e(\infty)[1 - \exp(-t/\tau)] \quad (2)$$

$$\omega_0(t \geq 0) = \omega_0(0) + \Delta\omega_0[1 - \exp(-t/\tau)] \quad (3)$$

where τ is the characteristic decay time. Following a time-dependent change in $F_e(t)$ and $\partial F/\partial z$ (which causes a transient change in ω_0), the system will return to a steady-state sinusoidal oscillation with a new equilibrium amplitude on a characteristic time scale $2Q/\omega_0$, or ~3 ms for typical AFM cantilevers. However, the details of the fast transient motion, in particular the instantaneous phase and frequency, prior to reaching the new steady state do encode information about τ on much shorter times and thus form the basis for subcycle time resolution. Extraction of this information is a matter of signal processing.

To demonstrate the feasibility of distinguishing different transient rise times or decays on fast time scales, we first consider a theoretical damped driven harmonic oscillator governed by eq 1. This form represents the transient expected in many systems of interest, such as the charge accumulation[3] and decay[27] in nanostructured solar cells, and of systems exhibiting first-order or pseudofirst-order kinetics in general. To analyze the cantilever motion at early times, we use numerical demodulation of the digitized cantilever signal[8] and

dx.doi.org/10.1021/nl203956q | Nano Lett. XXXX, XXX, XXX−XXX

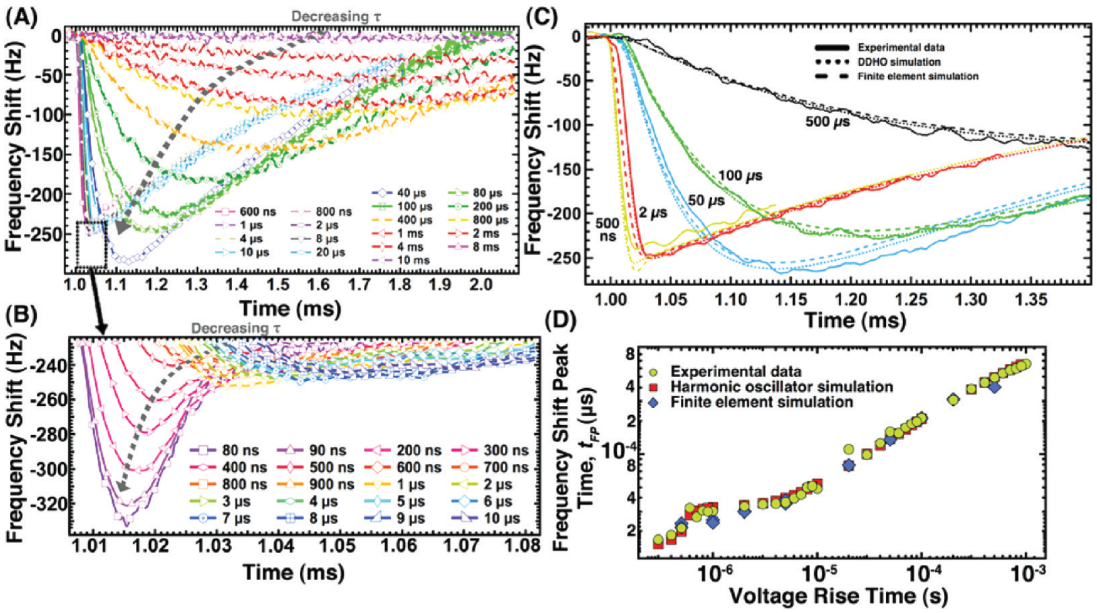

Figure 2. Resolution limits and modeling of FF-trEFM (A) Instantaneous frequency data following exponentially shaped voltage pulses with rise times ranging from 600 ns to 10 ms. From 50 μs to 10 ms, as the rise time increases, the net frequency shift generally decreases due to an overlap between transient and steady-state harmonic oscillator behavior, while the t_{FP} consistently increases monotonically. (B) Data from 80 ns to ~10 μs showing the t_{FP} values decrease monotonically even as the cantilever behavior becomes increasingly complicated at subcycle times. (C) Comparing DDHO simulation (dotted), finite element simulation (dashed), and experimental (solid) instantaneous frequency at different rise times. (D) t_{FP} data for voltage pulses across four decades of rise times. Experimental data (yellow circles) are compared with the data generated using the modified DDHO equations (red squares) and data generated using a finite element model simulation (blue diamonds) from 500 ns to 800 μs. Markers are spaced every 225 samples in (a) and every 40 samples in (b). Number of averaged pulses N = 1250, with the same cantilever parameters as Figure 1.

extract the envelope amplitude, instantaneous phase, and instantaneous frequency of the oscillating cantilever. Details are provided in the Supporting Information. Briefly, "instantaneous frequency" is defined as the time derivative of the instantaneous phase, as is common in the signal processing literature[28] and selected scanning probe papers.[8,29] We extract the instantaneous phase from the analytic signal computed in software via a Hilbert transform of the cantilever position vs time data.[29] Though it may seem counterintuitive, this definition of frequency allows for rapid measurements of frequency changes with subcycle resolution.

Figure 1B shows the instantaneous frequency recovered from a simulated cantilever following a transient change in F_e and $\partial F/\partial z$ according to eqs 2−3 over 3 orders of magnitude, from 100 ns to 300 μs, while the cantilever parameters, such as β, ω_0, F_e, and k were chosen to agree with typical AFM experiments. Importantly, Figure 1B shows that the cantilever oscillation behavior is distinguishable for different $\tau \ll 2Q/\omega_0$ and even for $\tau \ll 1$ cantilever oscillation period. While the instantaneous frequency does not directly measure either F_e or $\partial F/\partial z$, the data suggest a straightforward way to recover τ from an experimental data set. Notably, the time it takes for the instantaneous cantilever frequency to shift farthest from ω before relaxing, hereafter the time to first frequency shift peak (t_{FP}), is a monotonic function of τ. Thus, given adequate signal/noise, one can in principle measure rise times or decays as short as 100−200 ns with widely available AFM cantilevers by generating a calibration curve of t_{FP} versus τ. At present, we believe the factors limiting time resolution are primarily the photodiode detector bandwidth and the 100 ns smoothing window (see Supporting Information).

To demonstrate this method in practice, we use electrostatic force microscopy (EFM) as a test bed. In EFM, the tip and sample form a capacitor structure, and changes in the potential difference between the tip and sample change both the force and force gradient experienced by the oscillating cantilever.[26] We can thus use programmed voltages applied to the tip by an arbitrary waveform generator to provide a model system with which to explore the performance of different data acquisition and analysis methods. Furthermore, since EFM can be used to detect photogenerated charge, time-resolved EFM has practical application in the local detection of charge carrier behavior below the diffraction limit in nanostructured semiconductors.[3,5,19]

Figure 2A shows the instantaneous frequency obtained from the filtered, demodulated experimental data. A voltage with an exponential rise time was applied at t = 1 ms to a Pt-coated cantilever oscillating 10 nm above the Au substrate. As with the simulated data, the real cantilever exhibits a transient response followed by a return to a steady-state oscillation at the drive frequency ω. The cantilever relaxes to a new amplitude on a time scale governed by $2Q/\omega_0$. The phase exhibits a transient response faster than this time constant, and the equilibrium phase takes longer to reach than the measurements of interest here. More importantly, Figure 2A further shows that, as for the simulated data, the t_{FP} is clearly different for each value of τ. We have verified that the t_{FP} parameter is insensitive to cantilever lift height (Figures S5−6, Supporting Information) and can be robustly extracted even at signal/noise levels well below those

dx.doi.org/10.1021/nl203956q | Nano Lett. XXXX, XXX, XXX−XXX

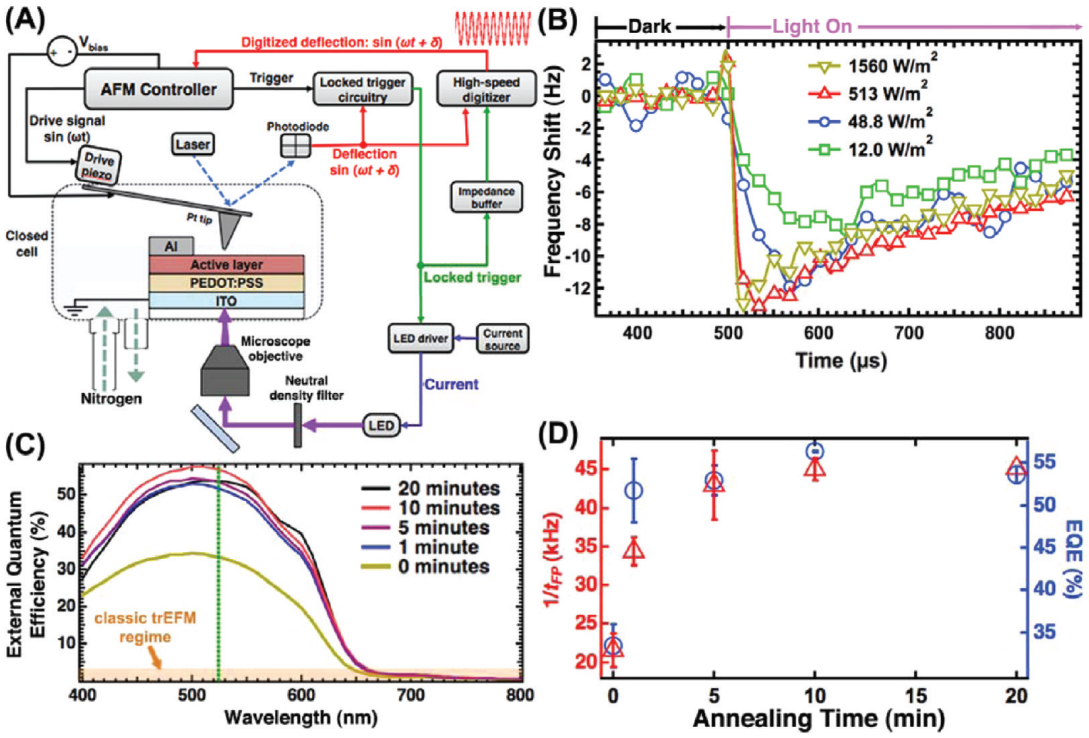

Figure 3. FF-trEFM as a screening tool on an efficient OPV blend. (A) Instrumentation schematic for OPV characterization, showing the sample purged under constant nitrogen flow and transient perturbation caused by photoinduced charging via a pulsed LED. (B) Instantaneous frequency data for a range of light intensities on a ∼51% EQE P3HT:PCBM film showing that photoinduced charging represents a transient force and force gradient effect similar to a root-exponential voltage of characteristic τ as in Figure 2. (C) External quantum efficiency (EQE) measurements on five P3HT:PCBM devices annealed at 110 °C for 0 (unannealed), 1, 5, 10, and 20 min. The green line is at the LED wavelength (∼523 nm). The shaded region indicates previously accessible device efficiencies using traditional feedback-based methods. (D) Plot of spatially averaged $1/t_{FP}$ values (red triangles) versus EQE (blue circles) for the four devices measured. The error bars represent standard deviation of the mean for several areas (t_{FP}) and several pixels (EQE).

shown here (Figure S7, Supporting Information) with high lateral resolution of better than ∼80 nm (Figure S8, Supporting Information).

Along with the experimental data, Figure 2B plots instantaneous frequency vs time for a full finite element simulation of a conical-shaped tip with the tip−sample force F_z calculated by integrating the Maxwell stress tensor $E_z^2\varepsilon_0\varepsilon_r$ over the tip surface (Figure S3, Supporting Information), where E_z is the electric field in the z direction and r is the radius of the tip at given height, as well as instantaneous frequency vs time for a simple damped driven harmonic oscillator using experimentally derived tip parameters. Notably, both the full finite element method and the simple harmonic oscillator model are able to reproduce the data across many orders of magnitude using these parameters and accounting for z-drift in the simulations (Figure 2C). Indeed, there is near quantitative agreement between the simulations and the experimental behavior at rise times from submicrosecond to 900 μs. At very short times, there are small deviations in the frequency shift between the three values that may be attributable in part to nonideal tip shape, higher-order force corrections, cantilever beam contributions,[30] or numerical issues. Though the quantitative frequency shift magnitude begins to differ, the t_{FP} value still scales with the rise time, with excellent agreement between the experiment and the different simulation methods (Figure 2D).

The data in Figure 2A−C are striking. They demonstrate that experimentally, one can use the demodulated frequency to quantify rise or decay times for signals as fast as τ = 100−200 ns, shorter than even a single cantilever oscillation period. To our knowledge, this is the fastest mechanically detected signal rise time that has been measured with AFM without heterodyning[13] by orders of magnitude. We emphasize that, while performed with custom hardware and software, the core instrumentation was a commercial AFM, and the method does not rely on expensive add-on instrumentation or rare custom probes and should therefore be readily accessible to a wide range of AFM users. Indeed, we envision that with appropriate software modification, the present generation of commercial AFMs has the hardware specifications necessary to implement time-resolved AFM with submicrosecond accuracy.

Next, we demonstrate one potential use of our method for achieving faster resolution applied to the field of organic photovoltaics. Previously we have used a feedback-based time-resolved EFM (trEFM) method to study photoinduced charge generation in donor/acceptor polyfluorene copolymer blends used in organic photovoltaics.[3] We have shown that charge accumulation following illumination is well approximated by single exponential kinetics with the photocharging rate being directly proportional to the local quantum efficiency and incident light intensity.[3,19] However, operating under physically

dx.doi.org/10.1021/nl203956q | Nano Lett. XXXX, XXX, XXX−XXX

relevant (~1 sun) illumination conditions, characteristic charging times (determined by the rate at which photogenerated charges fill the tip−sample capacitor) are on the order of ~30−50 μs for blends with quantum efficiencies in the range of ~50−70%. In other words, the most interesting nanostructured organic systems, such as polymer:fullerene blends, remained inaccessible.

As a proof-of-concept, we apply FF-trEFM to the well-known polymer:fullerene OPV blend poly(3-hexylthiophene):phenyl-C_{61}-butyric acid methyl ester (P3HT:PCBM) by photoexciting the sample with a light step pulse and detecting the changes in resulting cantilever motion (Figure 3A). Figure 3B shows the light intensity dependence of t_{FP}. At lower intensities, it takes longer for the film to become filled with enough photogenerated charge to screen the tip potential (i.e., τ increases), therefore t_{FP} shifts to longer times. The similar behavior from both photoinduced charging and exponential voltage signals lends confidence to our treatment of light-induced charging using eqs 1−3. Taken together, the two experiments imply that, at the same light intensity, the difference in t_{FP} reflects a difference in force gradient rise time τ, which in this case corresponds to local charging efficiency.

P3HT:PCBM samples prepared with different thermal annealing times (Figure 3C) are well-known to produce dramatically different external quantum efficiencies (EQE), an effect attributed to changes in nanoscale film structure.[31−33] However, even for the least efficient, unannealed blend classic feedback-based trEFM data are limited by instrument response (Figure S4, Supporting Information); the shaded region in Figure 3C shows the approximate EQE range accessible to classic feedback-based trEFM with our hardware.

Figure 3D shows a plot of $1/t_{FP}$, demonstrating that feedback-free trEFM can readily distinguish the differences between the samples with different EQEs as result from the different annealing times. For these experiments, we performed FF-trEFM and EQE measurements on the exact same organic semiconductor films that we made into photovoltaic devices. The data in Figure 3D show that the measured $1/t_{FP}$ value averaged over the image is proportional to EQE. In fact, the data indicate that FF-trEFM can be used directly to predict the EQE that would be obtained from a photovoltaic device fabricated from a given P3HT/PCBM film morphology.

Figure 4A shows a topography and $1/t_{FP}$ image for a film with an average EQE of 54%. When comparing the distribution of $1/t_{FP}$ times across images of different films, the average and standard deviations of $1/t_{FP}$ both increase with device efficiency as shown in Figure 4B. This result is consistent with observations of nanoscale short-circuit photocurrent distributions on P3HT:PCBM devices,[32] yet without the complications from tip work function and sample damage that can arise from such measurements,[34] further confirming the utility of the FF-trEFM method. Each such FF-trEFM image requires approximately 1 h to acquire. The images are reconstructed via postprocessing of the data using script-level code, and the computation time is resource dependent but currently takes up to 90 min. Faster computers, dedicated hardware, optimized coding, or fewer averages per point could reduce the time considerably. The Supporting Information includes additional imaging data and the images associated with Figure 3D.

We expect that FF-trEFM will not only enable studies of charge accumulation in more efficient nanostructured solar cells but will also enable the study of local recombination rates, which often have time constants in the range of 1−100 μs in

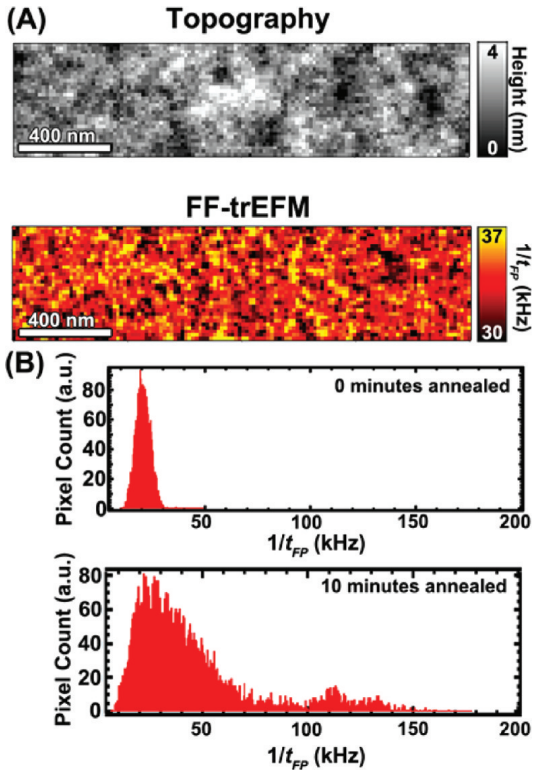

Figure 4. Spatial charging time variations in an OPV blend. (A) Topography (top) and FF-trEFM image (bottom) of a ~51% EQE P3HT:PCBM film showing spatial variation in the $1/t_{FP}$ values with values as low as sub-30 μs when exposed to 523 nm LED illumination at an intensity of ~513 W/m^2. (B) Histograms of FF-trEFM $1/t_{FP}$ values for an unannealed (top) and 1 min annealed film (bottom) showing that the average and standard deviation both increase with annealing time, consistent with reported short-circuit photocurrent image data. Images acquired using 6 averages per pixel at 5 MHz sampling rate.

OPV blends.[21,27] Since any experiment with a time-dependent force gradient can use FF-trEFM, it might be possible to utilize these methods in applications ranging from time-dependent magnetic force experiments to studies of fast local structural changes in biological samples. Because the method can in principle be implemented on many current generation AFM hardware, we hope it will ultimately become widely accessible.

■ ASSOCIATED CONTENT

Supporting Information

Experimental materials and methods (cantilever calibration, FF-trEFM measurement and triggering, data processing to extract instantaneous frequency and t_{FP}, finite element simulation methods), supporting data (feedback-based time resolution limits, FF-trEFM control experiments for lift height, low signal:noise sensitivity of FF-trEFM, FF-trEFM lateral resolution, and additional image data on MDMO-PPV:PCBM and P3HT:PCBM films), and additional references. This material is available free of charge via the Internet at http://pubs.acs.org.

dx.doi.org/10.1021/nl203956q | *Nano Lett.* XXXX, XXX, XXX−XXX

AUTHOR INFORMATION

Corresponding Author

*E-mail: ginger@chem.washington.edu.

Present Addresses

‡Department of Materials Science and Engineering, Cornell University, Ithaca, New York 14853.

§National Renewable Energy Lab, Golden, Colorado 80401−3305.

ACKNOWLEDGMENTS

The authors thank K. M. Knesting (University of Washington) for providing the Au substrates. This manuscript is based on work funded as part of the Center for Interface Science: Solar Electric Materials, an Energy Frontier Research Center funded by the U.S. Department of Energy, Office of Science, Office of Basic Energy Sciences, under award no. DE-SC0001084 (supporting new instrumentation and hardware development to probe interfacial phenomena with high resolution). Additional previous funding was from Air Force Office of Sponsored Research (supporting the purchase of the AFM hardware) and the NSF (DMR 0449422) (supporting the numerical modeling by G.E.R. and G.S.). O.G.R. was supported by a NSF IGERT fellowship during portions of this work. G.E.R. received additional support from an ARCS fellowship from the University of Washington.

REFERENCES

(1) Sahin, O.; Magonov, S.; Su, C.; Quate, C. F.; Solgaard, O. *Nat. Nanotechnol.* **2007**, *2*, 507−514.
(2) Kalinin, S.; Bonnell, D. *Phys. Rev. B* **2002**, *65*, 125408.
(3) Coffey, D. C.; Ginger, D. S. *Nat. Mater.* **2006**, *5*, 735−740.
(4) Balke, N.; Jesse, S.; Kim, Y.; Adamczyk, L.; Tselev, A.; Ivanov, I. N.; Dudney, N. J.; Kalinin, S. V. *Nano Lett.* **2010**, *10*, 3420−3425.
(5) Jaquith, M. J.; Muller, E. M.; Marohn, J. A. *J. Phys. Chem. B* **2007**, *111*, 7711−7714.
(6) Maturová, K.; Kemerink, M.; Wienk, M. M.; Charrier, D. S. H.; Janssen, R. A. J. *Adv. Funct. Mater.* **2009**, *19*, 1379−1386.
(7) Hosokawa, Y.; Hagiyama, M.; Iino, T.; Murakami, Y.; Ito, A. *Proc. Natl. Acad. Sci. U.S.A.* **2011**, *108*, 1777−1782.
(8) Yazdanian, S. M.; Hoepker, N.; Kuehn, S.; Loring, R. F.; Marohn, J. A. *Nano Lett.* **2009**, *9*, 3668−3668.
(9) Ando, T.; Uchihashi, T.; Fukuma, T. *Prog. Surf. Sci.* **2008**, *83*, 337−437.
(10) Stark, M.; Stark, R.; Heckl, W.; Guckenberger, R. *Proc. Natl. Acad. Sci. U.S.A.* **2002**, *99*, 8473−8478.
(11) Nechay, B.; Siegner, U.; Achermann, M.; Bielefeldt, H.; Keller, U. *Rev. Sci. Instrum.* **1999**, *70*, 2758−2764.
(12) Schade, W.; Preusser, J.; Osborn, D.; Lee, Y.; deGouw, J.; Leone, S. *Opt. Commun.* **1999**, *162*, 200−204.
(13) Ho, F.; Hou, A. S.; Nechay, B. A.; Bloom, D. M. *Nanotechnology* **1996**, *7*, 385−389.
(14) Terada, Y.; Yoshida, S.; Takeuchi, O.; Shigekawa, H. *Nat. Photonics* **2010**, *4*, 869−874.
(15) Weiss, S.; Ogletree, D.; Botkin, D.; Salmeron, M.; Chemla, D. *Appl. Phys. Lett.* **1993**, *63*, 2567−2569.
(16) Moore, A. M.; Mantooth, B. A.; Donhauser, Z. J.; Yao, Y.; Tour, J. M.; Weiss, P. S. *J. Am. Chem. Soc.* **2007**, *129*, 10352−10353.
(17) Kemiktarak, U.; Ndukum, T.; Schwab, K. C.; Ekinci, K. L. *Nature* **2007**, *450*, 85−89.
(18) Loth, S.; Etzkorn, M.; Lutz, C. P.; Eigler, D. M.; Heinrich, A. J. *Science* **2010**, *329*, 1628−1630.
(19) Reid, O. G.; Rayermann, G. E.; Coffey, D. C.; Ginger, D. S. *J. Phys. Chem. C* **2010**, *114*, 20672−20677.
(20) Giridharagopal, R.; Shao, G.; Groves, C.; Ginger, D. S. *Mater. Today* **2010**, *13*, 50−56.
(21) Clarke, T. M.; Durrant, J. R. *Chem. Rev.* **2010**, *110*, 6736−6767.
(22) Rousso, I.; Khachatryan, E.; Gat, Y.; Brodsky, I.; Ottolenghi, M.; Sheves, M.; Lewis, A. *Proc. Natl. Acad. Sci. U.S.A.* **1997**, *94*, 7937−7941.
(23) Moore, E. W.; Lee, S.; Hickman, S. A.; Wright, S. J.; Harrell, L. E.; Borbat, P. P.; Freed, J. H.; Marohn, J. A. *Proc. Natl. Acad. Sci. U.S.A.* **2009**, *106*, 22251−22256.
(24) Rugar, D.; Budakian, R.; Mamin, H.; Chui, B. *Nature* **2004**, *430*, 329−332.
(25) Albrecht, T.; Grutter, P.; Horne, D.; Rugar, D. *J. Appl. Phys.* **1991**, *69*, 668−673.
(26) Silveira, W. R.; Muller, E. M.; Ng, T. N.; Dunlap, D. H.; Marohn, J. A. High-Sensitivity Electric Force Microscopy of Organic Electronic Materials and Devices. In *Scanning Probe Microscopy: Electrical and Electromechanical Phenomena at the Nanoscale*; Kalinin, S. V., Gruverman, A., Eds.; Springer: New York, 2007; pp 788−832.
(27) Shuttle, C. G.; O'Regan, B.; Ballantyne, A. M.; Nelson, J.; Bradley, D. D. C.; de Mello, J.; Durrant, J. R. *Appl. Phys. Lett.* **2008**, *92*, 093311.
(28) Boashash, B. *Proc. IEEE* **1992**, *80*, 520−538.
(29) Yazdanian, S. M.; Marohn, J. A.; Loring, R. F. *J. Chem. Phys.* **2008**, *128*, 224706.
(30) Colchero, J.; Gil, A.; Baró, A. *Phys. Rev. B.* **2001**, *64*, 245403.
(31) Giridharagopal, R.; Ginger, D. S. *J. Phys. Chem. Lett.* **2010**, *1*, 1160−1169.
(32) Pingree, L. S. C.; Reid, O. G.; Ginger, D. S. *Nano Lett.* **2009**, *9*, 2946−2952.
(33) Yang, X.; Loos, J.; Veenstra, S.; Verhees, W.; Wienk, M.; Kroon, J.; Michels, M.; Janssen, R. A. *Nano Lett.* **2005**, *5*, 579−584.
(34) Hamadani, B.; Gergel-Hackett, N.; Haney, P. M.; Zhitenev, N. B. *J. Appl. Phys.* **2011**, *109*, 124501.

Supporting Online Material for
Sub-Microsecond Time Resolution Atomic Force Microscopy for Probing Nanoscale Dynamics

Rajiv Giridharagopal, Glennis E. Rayermann, Guozheng Shao, David T. Moore, Obadiah G. Reid, Andreas F. Tillack, David. J. Masiello, David. S. Ginger*

*To whom correspondence should be addressed: ginger@chem.washington.edu

This PDF file includes:

MATERIALS AND METHODS

Sample Preparation

Au samples were prepared on n-type Si(100) substrates (Silicon Quest International) with a 1 μm SiO_2 layer. The Si substrates were cleaved and sonicated in acetone and isopropyl alcohol prior to evaporation. Au films were formed by evaporating a 2.5 nm Cr adhesion layer followed by 55 nm Au. Au samples were sonicated in acetone and plasma cleaned prior to imaging.

Substrates for the OPV films were 1.5 x 1.5 cm^2 indium tin oxide (ITO)-coated glass substrates (TFD Inc.). Poly(ethylene dioxythiophene):poly(styrene-sulfonate) (PEDOT:PSS, Baytron P) was filtered and heated to 50 °C and deposited on the ITO and annealed at 100 °C for ~1 hour. Poly(3-hexylthiophene):phenyl-C_{61}-butyric acid methyl ester (P3HT:PCBM) films were formed from a 1:1 blend of P3HT (Rieke Metals, 90-93% RR) and PCBM (Nano-C, 99.5% pure) in chlorobenzene at ~42 mg/mL. The solution was stirred at 500 RPM at 55 °C overnight and was spin-coated warm onto the substrates at approximately 1500 RPM for 2 min. Aluminum top electrodes (85 nm) were then evaporated, creating devices of approximately 1.8 mm^2 based on overlap of ITO and Al electrodes. Films were annealed for various times at 110°C on a preheated aluminum block mounted on a hot plate. All active layer preparation was in an inert environment, and all films were stored covered in aluminum foil in the glove box until imaged.

In the supplemental data below, we also use poly(9,9′-dioctylfluorene-*co*-bis-*N,N′*-(4-butylphenyl)-bis-*N,N′*-phenyl-1,4-phenylenediamine:poly-(9,9′-dioctylfluorene-*co*-benzothiadiazole) (PFB:F8BT) films prepared on ITO/PEDOT:PSS substrates. Films were prepared using 1:1 blend of PFB:F8BT (American Dye Source) at ~20 mg/mL solutions in chlorobenzene or xylenes using a procedure recently reported by our group.[1]

Instrumentation

All FF-trEFM data were acquired using an MFP3D-BIO AFM (Asylum Research). Experiments on Au films were performed in ambient conditions, whereas those on P3HT:PCBM were performed under nitrogen using a closed fluid cell. For the Au data, we applied root exponential voltage pulses using an arbitrary waveform generator programmed via GPIB. For the P3HT:PCBM blends, we illuminated the samples using a 5W, 523 nm LED (LedEngin LZ1-10G105) focused on the top surface of the film and co-aligned with the tip. Feedback-based trEFM data were acquired similar to that reported in previous work.[1, 2] In each case, the cantilever deflection signal was routed into a triggering box (see below) to ensure that each light pulse was applied at the same phase. For voltage pulse tests on Au the same circuit was used as well. The sample was grounded relative to the tip in each case. Device measurements (external quantum efficiency) were performed under vacuum using a monochromated, 75 W Xenon lamp, with eight device pixels per film. External quantum efficiency measurements and FF-trEFM data were collected from at least 3 batches of devices.

Measuring Initial Cantilever Parameters

The cantilever in AFM behaves as a typical damped driven harmonic oscillator (DDHO), whose behavior is described by the well-known equations:[3]

$$z(t<0) = A\cos(\omega t - \delta) \tag{1}$$

$$A = \frac{(F_0/m)}{\sqrt{(\omega_0{}^2 - \omega^2)^2 + 4\omega^2\beta^2}} \tag{2}$$

$$\delta = \tan^{-1}\left[2\omega\beta/(\omega_0{}^2 - \omega^2)\right] \tag{3}$$

where A is the amplitude, δ is the phase of the cantilever relative to the driving signal, F_0 is the driving force applied to the cantilever, m is the cantilever mass, ω_0 is the resonance frequency, ω is the frequency of the driving force signal applied to the cantilever, F_e is the electrostatic force due to the charging of the surface, and $\beta = \omega_0/2Q$ is the damping factor. When the drive frequency $\omega = \omega_0$, the amplitude and phase are at a peak and at $\pi/2$ respectively. As the resonance frequency shifts and $\omega \neq \omega_0$, the amplitude and phase change accordingly.

Prior to the initial experimental run, we measure the cantilever parameters such as the spring constant k, m, Q, β, the change in ω_0 both with voltage and with applied light, and electrostatic force F_e in order to properly model the motion (Figure S1 and Table S1). We record the cantilever amplitude, phase, and deflection as the frequency is swept over a ~5 kHz range centered at the initial 0 V resonance frequency. We do this both far from the surface (10 μm) and close to the surface (10 to 100 nm). We then changed the drive frequency applied to the cantilever and monitored the amplitude, phase, and deflection both before and after applying a voltage to the tip to acquire the approximate electrostatic force. On OPV films such as P3HT:PCBM (but not on Au), we additionally measure the cantilever characteristics before and after applying light with the tip at 10 V to acquire the approximate frequency shift and force due to photoinduced charging.

Figure S1A shows how the amplitude of the AFM cantilever behaves with no voltage, an applied voltage, and an applied voltage and constant illumination on a PFB:F8BT film at a height of 20 nm above the sample. The amplitude decreases and the resonance frequency peak shifts to a lower frequency as $\partial^2 C/\partial z^2$ changes increasingly by first applying a voltage and then by adding the photogenerated charges. Under illumination, $\partial^2 C/\partial z^2$ increases and therefore the curvature in the parabola increases as shown in Figure S1B.[2] From the cantilever amplitude, phase, and deflection signals recorded across a range of drive frequencies before and after excitation, we can extract the relevant system parameters such as Q, β, k, amplitude, force, and resonance frequency as tabulated in Table S1.

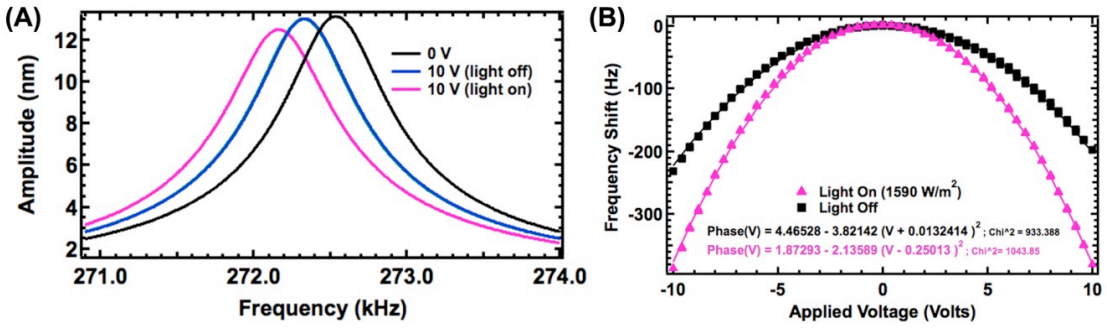

Figure S1.

Resonance frequency response to changes in the electrostatic force gradient. (A) Cantilever oscillation amplitude curves on an organic photodiode (PFB:F8BT) taken at 0 V (black), 10 V (blue), and 10 V under 405 nm illumination (pink), across a range of drive frequencies. (B) Example frequency shift response showing the expected quadratic dependence on applied voltage as well as the change in differential capacitance gradient due to illumination. Data taken at 10 nm above the same sample with approximately 1590 W/m2 intensity.

Calibration Parameters	10 µm, 0 V		
Thermal Resonance Frequency (Hz)	272614		
Thermal Spring Constant (N/m)	22.807		
DEFINVOLS (m/V)	4.5273E-08		
AMPINVOLS (m/V)	4.9348E-08		
Mass (kg)	7.7758E-12		
Q Factor	475.107		
Beta (/s)	1802.35		
Electrostatic Force Gradient dF/dZ (N/m)	-3.38189		
	10 nm, 0 V (Dark)	**10 nm, 10 V (Dark)**	**10 nm, 10 V (LED on)**
Resonance Frequency (Hz)	272544	272325	272164
Amplitude (m)	1.3143E-08	1.3022E-08	1.2508E-08
Q Factor	427.578	421.701	406.168
Beta/Damping (/s)	2002.49	2028.77	2105.11
Driving Force (N)	7.0103E-10	7.0314E-10	7.0152E-10
Spring Constant (N/m)	22.807	22.7704	22.7804
		10 V versus 0 V	**10 V, LED Off versus On**
Net Electrostatic Force (N)		9.8038E-09	2.1314E-09
Net Frequency Shift (Hz)		-219	-159
Change in Spring Constant (N/m)		-0.0366372	-0.0266255
Change in Peak Amplitude (nm)		-1.2077E-10	-5.0787E-10

Table S1.

Cantilever parameters for the system in Figure S1. The data taken at 10 nm in Figure S1 show how the *Q*, resonance frequency, and spring constant all decrease. The net electrostatic force is much larger from turning on the voltage than from turning on the light. LED power is ~1590 W/m^2. AMPINVOLS and DEFINVOLS are the inverted optical lever sensitivity settings for converting the amplitude and deflection signals, respectively, from V to nm.

FF-trEFM Measurement

FF-trEFM experiments were performed using in-house Igor Pro code and C-language XOP code to operate an external digitizer (Gage Compuscope USB 14400) for recording the cantilever. The tip is actuated using the drive signal with frequency ω to shake the tip with an oscillation of 10 – 12 nm. At the same time, the MFP3D hardware is used to bias the tip (usually at 10 V). The deflection signal is fed into a trigger circuit. The circuit consists of two integrated circuits, a comparator that converts the DC filtered deflection signal from a sine wave into a square wave, and a D-flip flop that uses the square wave as a triggering clock signal. The trigger signal is only passed at, approximately, the positive zero-crossing of the deflection signal; the phase can conceivably be changed depending on the reference signal sent to the comparator. The subsequent locked trigger is then used to simultaneously power the LED (for OPV tests) or the function generator (for voltage pulse tests) and to trigger the digitizer. The LED, with a peak wavelength at 405 nm or 523 nm, is optionally attenuated via neutral density filters and focused through an objective onto the top surface of the sample.

The deflection signal is averaged by recording numerous runs, typically 1000 to 1250 for point scans and 6-10 per pixel for imaging, at sample rates of 50 MHz and 5-50 MHz, respectively. Without the circuitry (shown schematically in Figure S2A), there is substantial noise in the resulting averaged wave of +/- a cycle, as in Figure SB. The triggering circuit ensures that each wave is acquired at the same point and eliminates this time-resolution bottleneck.

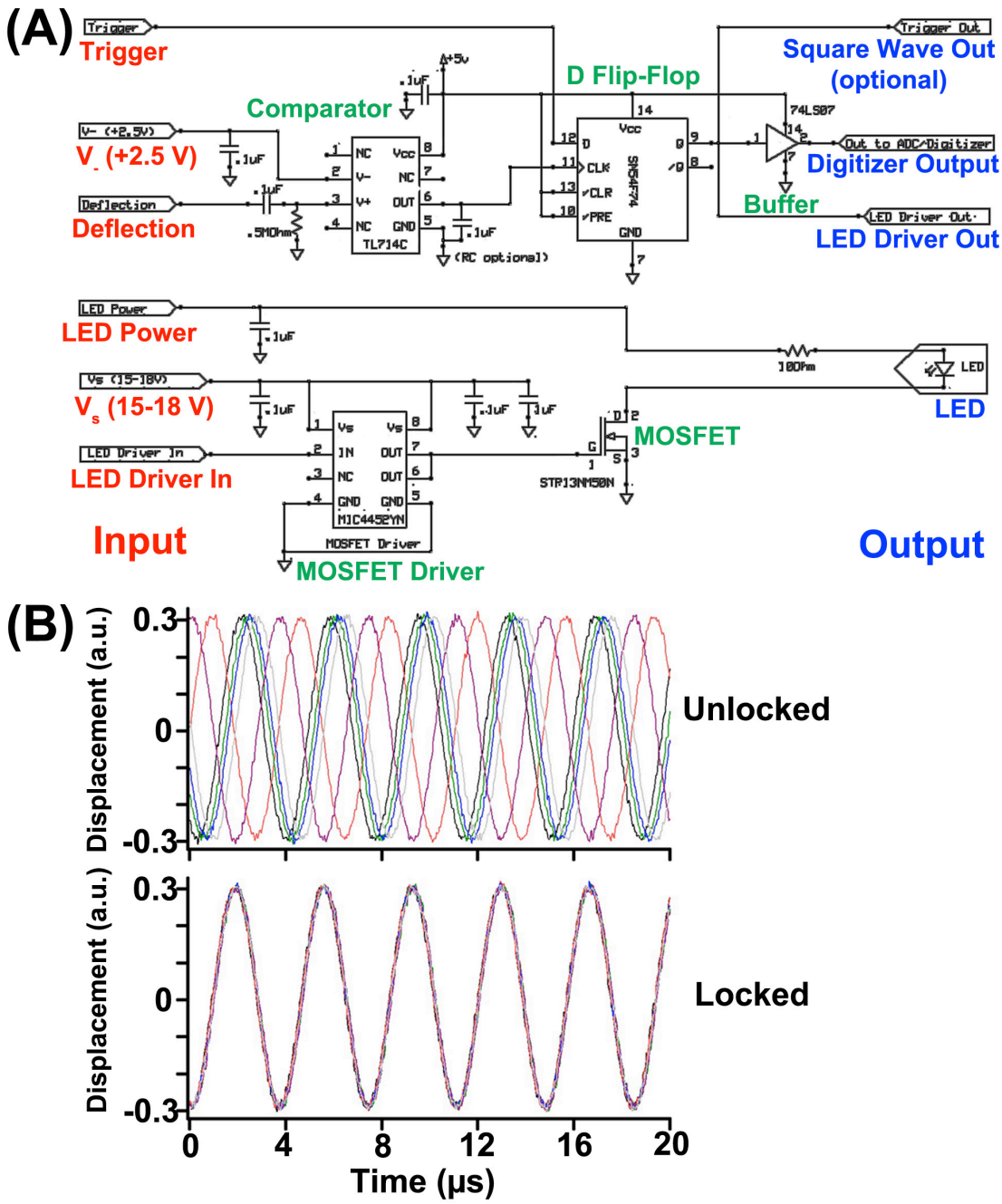

Figure S2

Using a phase-detecting circuit improves the time resolution. (A) Circuit schematic showing how to convert a trigger input to occur only at the rising zero-crossing edge of an input sine wave such as the deflection signal. (B) Consecutive digitized deflection waves showing high amount of jitter without (top) and with (bottom) a triggering circuit. The circuit ensures that the voltage and light are applied at the same point in the cycle, thus improving averaging by eliminating the averaging errors that can occur in the unlocked trigger case.

Data Processing

The averaged deflection signal $z(t)$ is filtered using a software finite impulse response bandpass filter and a standard Blackman windowing function in Igor Pro. The filtering does not adversely affect the t_{FP} as long as the bandpass window contains a sufficient number of coefficients (usually 999). The bandpass filter is centered at the frequency with a bandwidth of 20 kHz. Furthermore, to preserve the integrity of the step response, particularly for fast perturbations, we use a causal form of the filter with limited time shift by zeroing the negative coefficients (the large number of coefficients necessary and limited acquisition time make this the only viable option to create an edge-preserving causal filter). For the frequency curves plotted in, for example, Figure 1B in the main text, the data are only shifted in time by ~10 μs. Using a typical noncausal filter results in no such shift at the expense of blurring the start time of the resulting pulse. For most of the data, the frequency curves are smoothed using a 100 ns window, hence the lower limit for our claims of resolution. This process is not necessary when signal:noise is high (such as voltage pulses) and is primarily to make curve fitting easier (see below). For the OPV data, we optimize the fitting for a 1 ms window, since that balances the typical t_{FP} values observed with measurement time. Igor Pro code is available upon request.

The envelope amplitude $A(t)$ and the instantaneous phase $\theta(t)$ are digitally extracted through a standard software Hilbert Transform demodulation.[4, 5] Functionally, the Hilbert Transform phase shifts a signal by $\pi/2$; by combining the original signal $u(t)$ with the phase-shifted signal $\hat{u}(t)$ it is possible to acquire $A(t)$ and $\theta(t)$, and subsequently the instantaneous frequency $f(t)$ through these equations:

$$A(t) = \sqrt{u(t)^2 + \hat{u}(t)^2} \tag{4}$$

$$\theta(t) = \tan^{-1}[-\hat{u}(t)/u(t)] \tag{5}$$

$$f(t) = \frac{1}{2\pi}\frac{d}{dt}\theta(t) = \frac{1}{2\pi}\frac{d}{dt}\left[\tan^{-1}[-\hat{u}(t)/u(t)]\right] \tag{6}$$

For an arbitrary sinusoidal signal of the form $A(t)\exp[j(\omega t + \delta)]$, $\theta(t) = \omega t + \delta$. However, in our case the signal δ is really $\delta(t)$, and it is the signal of interest as it is the phase offset from the drive signal. The behavior of $\delta(t)$ reflects how the resonance frequency $\omega_0(t)$ changes, so to isolate this we simply subtract ωt from the $\theta(t)$ signal. The resulting instantaneous frequency shift $f(t)$ is therefore $f(t) = d\theta(t)/dt = d\delta(t)/dt$. The $z(t)$ data are smoothed over a 100 ns range prior to taking the derivative. We use the built-in Hilbert Transform function in Igor Pro (`HilbertTransform`) to numerically demodulate the signal. Functionally, this process is equivalent to taking the Fourier Transform, removing the negative frequency components and then doing the inverse Fourier Transform, as mentioned in the supporting information by Yazdanian, et al.[4]

The value of t_{FP} involves finding the lowest value of the frequency wave, $f(t)$. We fit a polynomial curve to the lowest frequency peak in the demodulated $f(t)$ to find this value; the purpose of the curve is not physical in origin, it is to extract a value from the $f(t)$. For the imaging data in Figure 3 from the main text we take multiple images over the same location and average the waves at each location to reduce signal:noise. The resulting image is gaussian-filtered to reduce the noise effects; this does not change the average value reported in Figure 3D and primarily eliminates erroneous low-t_{FP} value spikes that can be detected due to the limited number of averages per point. While there are certainly other ways to probe the system (the time it takes for the phase of the signal to initially change, for example, or the time for the system to

shift some set frequency from the drive), the choice of using t_{FP} is deliberate after numerous tests found this metric to be the most robust to sample drift, tip condition, and lift height.

Signal:noise is, we believe, possibly limited by photodiode detector response based on private communication with the corresponding author of Ref. 4. Using a faster response or lower-noise detector, we might be able to acquire data where the limit may approach thermal or shot-noise limits. We are beginning investigations into these matters.

Simulation Methods

DDHO simulations were performed using Igor Pro with the equations described in the main text. The parameters were chosen to represent those of a typical experiment run using the calibration measurement described above and shown in Table S1.

The tip response was also numerically calculated via finite element simulations in COMSOL. The tip is modeled with 2D axis geometry, as shown in Figure S3. The left side is the symmetry axis, the upper boundary is the bottom of the cantilever and tip, the lower boundary is the top of the sample surface, and the area in between represents air. The tilted line revolves around the axis to form the tip geometry, where the radius of the tip is 25 nm. The tip length and width are set to 6 μm and 1 μm, respectively. These are smaller than actual values (cantilevers used are typically 15 μm tall) and we do not include the full beam. The rationale behind this is that a predominately large portion of electric force is from the tip and we therefore balance computation time with simulation accuracy.

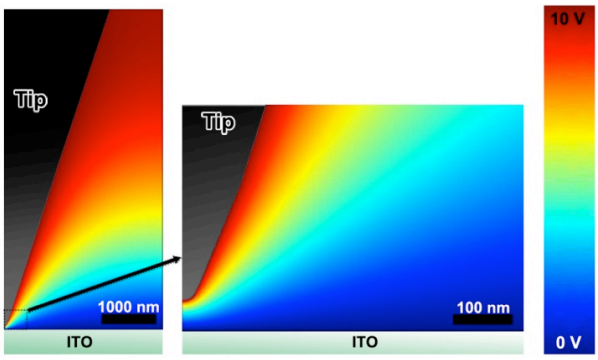

Figure S3
Numerical simulations of the tip-sample system. Electrostatic potential maps (z-component) of the tip-sample junction, where the sample and tip are metals (such as Pt and indium tin oxide, respectively)

Movement of the tip is governed by the DDHO equations, and the time-dependent electric force between the tip and sample is calculated with the Maxwell stress tensor as discussed in the main text. In each time step of the simulation, the tip position is recalculated using the harmonic oscillation as well as the effect of force via the Maxwell stress tensor.

SUPPORTING DATA

Time-Resolution Limitations of Feedback-Based trEFM

Classic time-resolved electrostatic force microscopy (trEFM) uses a feedback-based method to track the change in resonance frequency. We discuss in the main text how this method is limited to a time-resolution of ~100 μs.[2] In a typical organic photovoltaic film such as

PFB:F8BT, prepared using a method similar to that reported previously by our group,[1] the charging rate of the film scales with the light intensity.[2] This effect is shown in Figure S4A, as the incident light intensity increases the change in $\partial F/\partial z$, the change in $\Delta\omega$ increases until becoming a step function when the limit of the feedback electronics is reached, as evidenced by the trEFM data taken at light intensities beyond ~430 W/m^2. For an efficient blend like P3HT:PCBM, the behavior is different (possibly due to higher charge carrier mobility than in PFB:F8BT) but $\Delta\omega$ changes as a step function even at low light intensities of <1 W/m^2 (Figure S4B). The time resolution limit can be determined by using consecutive voltage pulses and observing the point at which they can be distinguished, as we reported in previous work.[6]

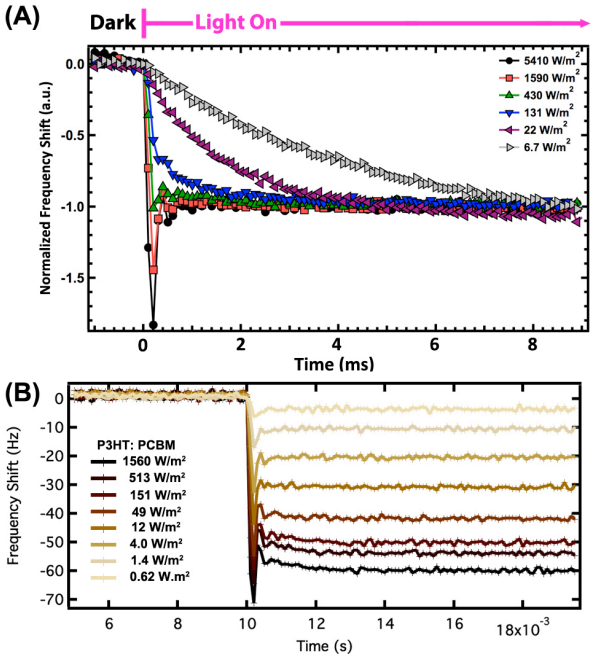

Figure S4
Limits of time-resolution due to feedback. (A) Typical normalized classic trEFM data curves of the same PFB:F8BT organic photovoltaic sample, showing the time-resolved behavior in the frequency shift. As the intensity increases the frequency shift response resembles a step function due to the time resolution limit, with ringing due to the feedback circuit, in this case occurring at an incident 405 nm LED intensity of ~430 W/m^2. (B) For an efficient OPV blend, P3HT:PCBM, saturation occurs even at intensities as low as <1 W/m^2 using a 523 nm LED in this case.

FF-trEFM Data with Variations in Lift Height

The frequency shift is proportional to the force gradient and therefore decreases as the tip moves farther from the surface. However, Figure S5 indicates that the t_{FP} does not vary considerably when the lift height is changed. The dashed lines (50 nm) show approximately the same t_{FP} value as the solid lines (10 nm) when looking at the intersection of the t_{FP} lines with the respective curves.

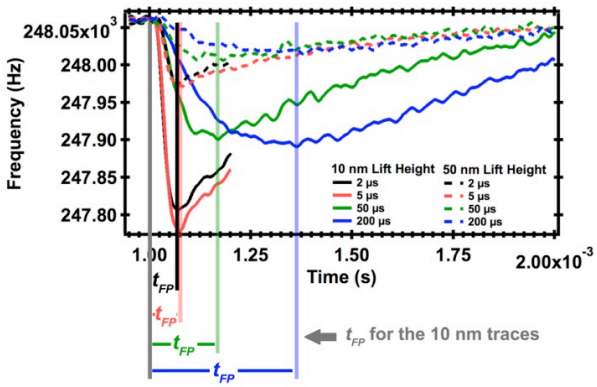

Figure S5
Lift height dependence of t_{FP} values. At four different voltage pulse rise times taken at 10 nm (solid) and 50 nm (dashed) lift heights, the t_{FP} values are approximately the same. These data indicate that the t_{FP} metric is robust against vertical drift effects unlike metrics used in steady-state EFM such as frequency shift magnitude.

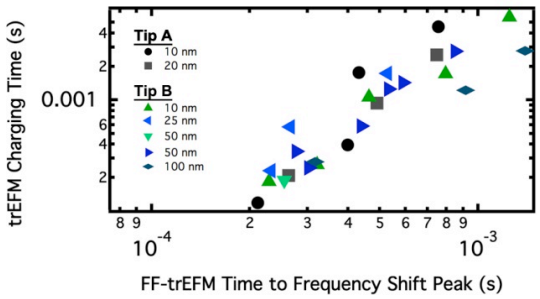

Figure S6
Lift height data comparing FF-trEFM and feedback-based trEFM on a PFB:F8BT film. Data were acquired at several lift heights and light intensities (405 nm LED, intensities range from 1560 W/m^2 to 1.4 W/m^2) with two different tips. As expected, there is a correlation between the classic charging time (y-axis) and t_{FP} value (x-axis) and both techniques are fairly robust to lift height variations given that the data points fall on the same general trendline.

Figure S6 shows the monotonic link between t_{FP} and charging rate time for a PFB:F8BT film with two different tips. Below 100 nm lift heights, most of the data fall along the same trend line. At 100 nm, it is possible that as the distance increases the electrostatic force is no longer dominated by the intense field at the apex but rather is a sum of the tip apex, the conical tip structure, and the cantilever beam.[7] Additionally, the signal-to-noise is much lower as the lift height increases due to the smaller net frequency shift. We find that using 10 to 50 nm for the lift height is optimal.

Voltage Dependence and Low Signal:Noise Sensitivity of t_{FP}

We can use averaging to measure signals at low signal:noise. In Figure S7 we change the voltage while keeping other parameters the same and monitor the instantaneous frequency. Because the frequency shift scales with V^2, decreasing the applied voltage from 10 V to 1 V causes the net frequency shift to go from ~280 Hz (black) to ~2.8 Hz (blue) with a signal:noise level reduced by ~99%. However, the t_{FP} values are approximately constant as can be observed

by the overlapping behavior of the frequency curves at various voltage levels, meaning that we can use FF-trEFM processing for signals operating near, for example, the typical V_{OC} level in a photovoltaic cell.

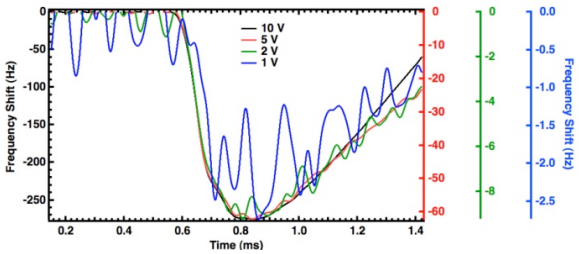

Figure S7
Instantaneous frequency with changes in applied voltage. The instantaneous frequency is shown for a 150 µs rise time voltage pulse with four different voltages: 10 V (black), 5 V (red), 2 V (green), and 1 V (blue). The t_{FP} value is approximately the same in that the instantaneous frequency trend is consistent the same across all voltages. The signal:noise varies with ΔV^2, therefore at 1 V the frequency data exhibit 1% the signal:noise level yet the trend is still observable for a frequency shift of only ~2.8 Hz versus a drive frequency of 248.603 kHz.

FF-trEFM Image Resolution

In Figure S8 we show an image taken at a Au-silicon interface. On silicon, the slightly longer t_{FP} value relative to Au results in a clear step in the FF-trEFM image. The graph in Figure S8 shows the height and $1/t_{FP}$. The substantially lower frequency shift magnitude on silicon increases the fitting error and thus the noise. We determine the lateral resolution to be at worst ~80 nm by finding the point beyond the metal edge where the error decreases to 50% of its average value. The resolution is similar to that observed in other EFM work as well as that reported previously by our group.[2]

Finally, we show additional polymer:fullerene images. In Figure S9 we show an example image on an OPV blend of poly(2-methoxy-5-(3′,7′-dimethyl-octyloxy)-*p*-phenylenevinylene (MDMO-PPV) with PCBM. The films were cast from 1:4 MDMO-PPV:PCBM blends in xylenes to intentionally create larger domains. The vertical structure of these blends has been characterized in previous work,[8, 9] and it is known that the topographically high domains consist of PCBM crystallites floating within a polymer-rich region. As a result, Figure S9B and S9D show different charging times that are not always correlated to the features– that is, some of the features are more efficient OPV materials than others even if topographically similar. The relatively low efficiency of these blends yields slightly longer t_{FP} values (200-300 µs range) than are usually observed for P3HT:PCBM.

The data were acquired using sampling rates of 10 MHz and 10 samples-per-pixel (Figure S9B) as well as 50 MHz with 5 samples-per-pixel (Figure S9D). Increasing the number of averages per point and the sampling rate dramatically improve the signal:noise during imaging, though it does increase data processing time. Data acquisition time is not significantly affected by increasing the sampling rate. The 50 MHz images take significant time to reconstruct, but improvements in coding should reduce this bottleneck.

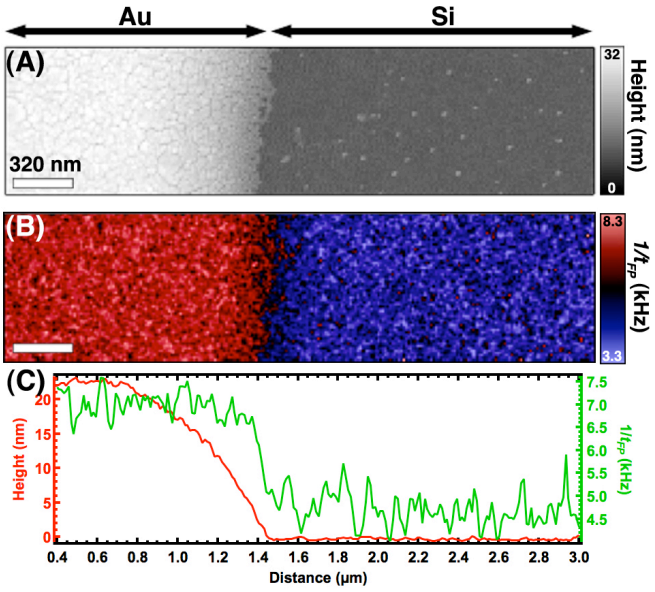

Figure S8

FF-trEFM resolution at an Au-Si edge. (a) Topography and (b) FF-trEFM $1/t_{FP}$ data show the resolution at the Au edge. The FF-trEFM data show slower charging over the silicon than over the Au. (c) Representative trace from this data showing the height and $1/t_{FP}$. Over silicon, the much smaller frequency shift causes an increase in the error, but overall the $1/t_{FP}$ value decreases with a steep drop at the Au-Si edge. These data indicate a resolution limit of better than ~80 nm. Data were taken using voltage pulses as in Figure 2, in this case with a 10 V, 20 μs characteristic rise time signal applied to the tip.

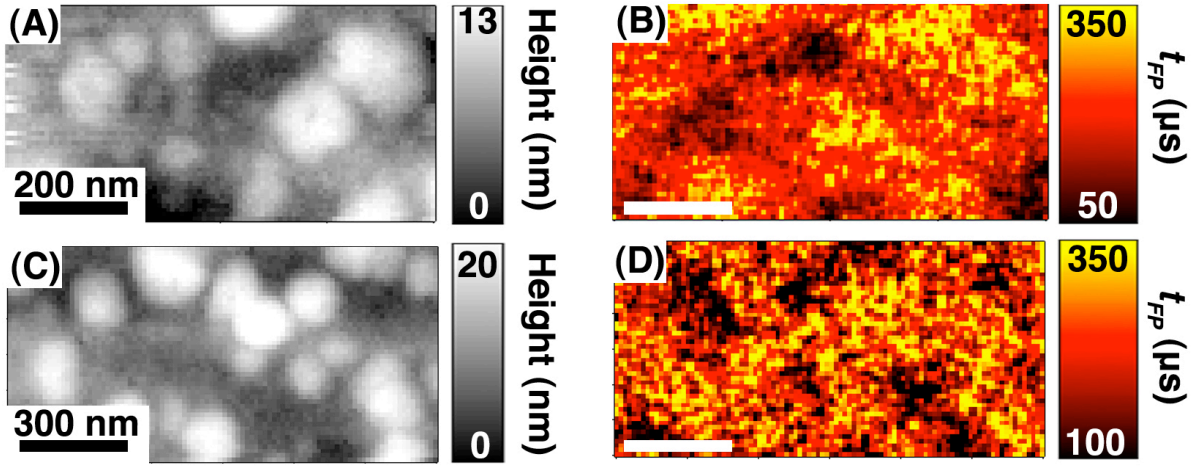

Figure S9.

Additional OPV image data on MDMO-PPV:PCBM blends. (A) Topography and (b) FF-trEFM t_{FP} image of a MDMO-PPV:PCBM film cast from xylenes using a 523 nm LED. The topographic features appear similar yet exhibit varying internal structure, therefore some areas of the film exhibit faster charging than others.

In Figure S10 we show the images corresponding to the data from Figure 3D in the main text, here shown with the same relative color scale. At shorter annealing times, the change in performance is dramatic as indicated by the increased high $1/t_{FP}$ regions.

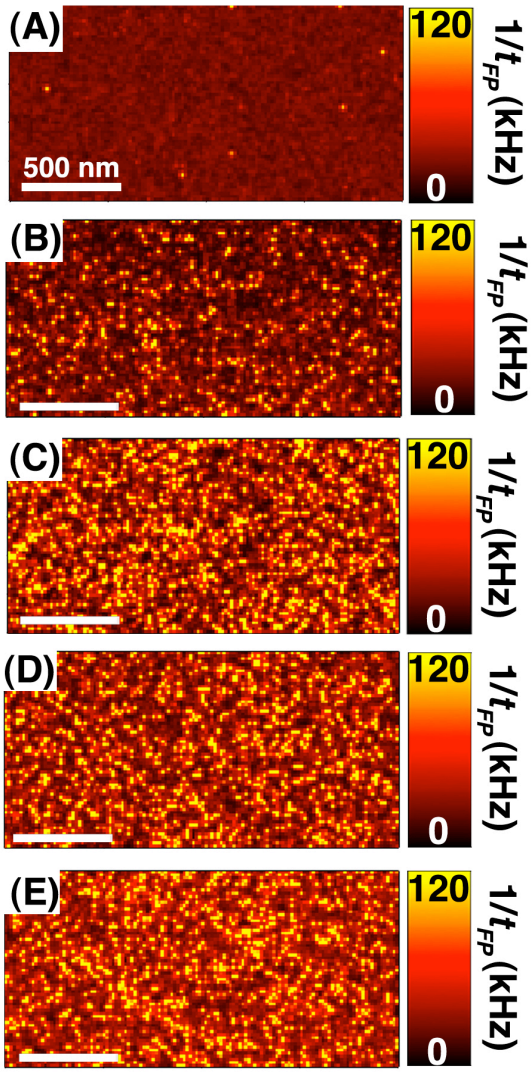

Figure S10
Additional P3HT:PCBM image data. FF-trEFM images corresponding to the plot in Figure 3D with annealing times of (A) 0 min, (B) 1 min, (C) 5 min, (D) 10 min and (E) 20 min, all with the same relative color scale.

REFERENCES

1. Reid, O. G.; Rayermann, G. E.; Coffey, D. C.; Ginger, D. S. *J. Phys. Chem. C* **2010,** 114, 20672-20677.
2. Coffey, D. C.; Ginger, D. S. *Nat. Mater.* **2006,** 5, 735-740.
3. Thornton, S. T.; Marion, J. B., *Classical Dynamics of Particles and Systems*. Brooks Cole: Belmont, CA, 2003.
4. Yazdanian, S. M.; Marohn, J. A.; Loring, R. F. *J. Chem. Phys.* **2008,** 128, 224706.
5. Jensen, S. E.; Dougherty, W. M.; Garbini, J. L.; Sidles, J. A. *J. Appl. Phys.* **2007,** 102, 054503.
6. Giridharagopal, R.; Shao, G.; Groves, C.; Ginger, D. S. *Mat. Today* **2010,** 13, 50-56.
7. Belaidi, S.; Girard, P.; Leveque, G. *J. Appl. Phys.* **1997,** 81, 1023-1030.
8. Coffey, D. C.; Reid, O. G.; Rodovsky, D. B.; Bartholomew, G. P.; Ginger, D. S. *Nano Lett.* **2007,** 7, 738-744.
9. Reid, O. G.; Xin, H.; Jenekhe, S. A.; ginger, D. S. *J. Appl. Phys.* **2010,** 108, 084320.

Chapter 4. MORPHOLOGY-DEPENDENT TRAP FORMATION IN BULK HETEROJUNCTION PHOTODIODES

My contribution to this work: I performed preliminary experiments using trEFM and GATR-FTIR. I developed protocols for GATR-FTIR data collection, including photooxidation of thin films with calibrated photon doses and data processing. I trained and supervised EMS, who applied the GATR-FTIR protocols to collect data in Figure 7.

THE JOURNAL OF PHYSICAL CHEMISTRY B

Article

pubs.acs.org/JPCB

Morphology-Dependent Trap Formation in Bulk Heterojunction Photodiodes

Guozheng Shao, Glennis E. Rayermann, Eric M. Smith, and David S. Ginger*

Department of Chemistry, University of Washington, Seattle Washington 98195, United States

Supporting Information

ABSTRACT: We show that local structural variation affects the rate of aging in nanostructured polymer solar cells by comparing time-resolved electrostatic force microscopy (trEFM) and conventional device measurements on model polymer blends. Specifically, we study photovoltaic devices made from 1:1 blends of the polyfluorene copolymers poly(9,9′-dioctylfluorene-*co*-bis-*N*,*N*′-(4-butylphenyl)-bis-*N*,*N*′-phenyl-1,4-phenylene-diamine) (PFB) and poly(9,9′-dioctylfluorene-*co*-benzothiadiazole) (F8BT). We photooxidize these films in situ using 365, 405, and 455 nm illumination under ambient conditions, with the wavelengths chosen to preferentially excite the different components. During photooxidation, we observe a faster loss of photocurrent generation from F8BT-rich domains, leaving the PFB-rich phases to show higher photoresponse even at wavelengths absorbed predominantly by F8BT. We propose that this effect is due to the more rapid degradation of PFB hole-transport pathways in the F8BT-rich regions, resulting in a loss of percolation pathways for hole transport in the F8BT-rich phase.

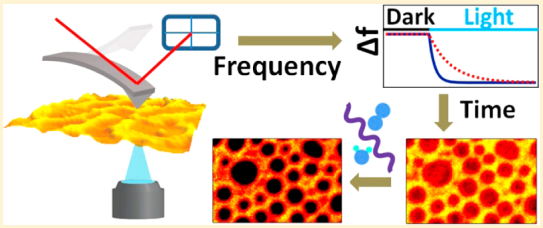

1. INTRODUCTION

Since the first reports of blended polymer heterojunctions,[1,2] the efficiency of organic photovoltaics (OPVs) has improved dramatically, with reports of single-layer devices now approaching 10%[3] and tandem organic solar cells exceeding 10%.[4,5] Over the same time period, scientific interest in these materials has also increased—in part because of the potential to achieve large-area, low-cost solar cells via solution processing of flexible organic semiconductors.[6−9] Nevertheless, a major concern that could limit the widespread use of OPVs is their long-term stability.[10]

Studies have shown that OPV device performance tends to degrade over time because of several causes,[10,11] including chemical interactions at the metal/organic interface,[12] morphological instabilities in the blended active layers,[13] and both reversible and irreversible chemical changes of the semiconductor materials.[14] To some extent, inverted device architectures have mitigated the need for reactive metal cathodes,[15,16] and a variety of cross-linking and other strategies can be used to stabilize polymer film morphologies.[17−19] Suppressing chemical changes in the organic semiconductors is still largely achieved via encapsulation.[10]

Even if OPVs ultimately use some form of encapsulation, a better fundamental understanding of the mechanisms that lead to chemical degradation of active organic semiconductor layers in bulk heterojunction OPVs could still enable better design, synthesis, and processing strategies to achieve more stable OPV devices. Whereas there has been a limited amount of work in this area,[10,11,20] the correlations between local film structure and photooxidation/trap formation in OPVs are essentially unknown. This is unfortunate because heterogeneity is ubiquitous in organic semiconductors,[9,21,22] and one might expect local compositional or structural variations to lead to variations in degradation rates.

Photooxidation of OPVs is often studied by optical methods,[10,23,24] which yield chemical specificity but lack electrical information. Furthermore, optical probes are typically diffraction-limited with resolutions of hundreds of nanometers.[23,24] Electrical scanning probe microscopy methods have the potential to probe local variations in OPV properties such as charge transport, photocurrent collection, and trapping/recombination.[25−30] Indeed, we have previously shown that time-resolved electrostatic force microscopy (trEFM) can be used to characterize local trap formation in conjugated polymer blends.[28] However, in that work, we did not study the spatial variations in photooxidation across a heterogeneous film. Likewise, Sengupta et al. have applied cAFM and SKPM to study photooxidation of polymer blends[31] but focused their studies only on differences between light and dark exposed regions of an OPV film and not on variations in photooxidation across the structurally heterogeneous domains of the bulk heterojunction film.

Here we bridge this critical gap to demonstrate that local composition affects the rate of photooxidation in nanostructured polymer solar cells. We do so by comparing

Special Issue: Paul F. Barbara Memorial Issue

Received: September 12, 2012
Revised: December 8, 2012
Published: December 20, 2012

dx.doi.org/10.1021/jp3090843 | *J. Phys. Chem. B* 2013, 117, 4654−4660

trEFM with conventional device measurements on blends of the model polymers poly(9,9′-dioctylfluorene-*co*-bis-*N*,*N*′-(4-butylphenyl)-bis-*N*,*N*′-phenyl-1,4-phenylene-diamine) (PFB) and poly(9,9′-dioctylfluorene-*co*-benzothiadiazole) (F8BT).

2. MATERIALS AND METHODS

2.1. Materials and Device Fabrication. PFB (MW = 80 000−120,000, PDI = 2.0) was purchased from American Dye Source (ADS232GE). F8BT (MW = 10 000−20 000, PDI < 3) was purchased from Sigma-Aldrich (product no. 698687). Structures for both materials are shown in Figure 1. Xylene

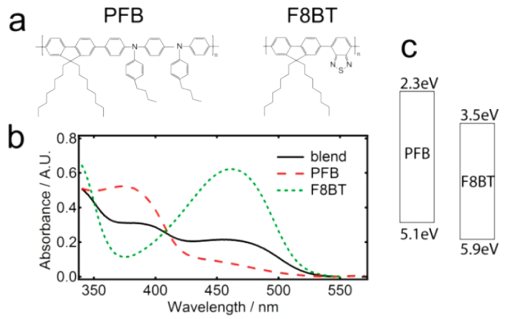

Figure 1. (a) Chemical structures of PFB and F8BT. (b) UV−vis absorbance spectra for our PFB, F8BT, and 1:1 blend films. (c) HOMO and LUMO levels of PFB and F8BT taken from literature.[39,40]

solvent was purchased from Sigma Aldrich (product no. 214736), degassed, and dried with 4 Å molecular sieves before use. 1:1 weight ratio PFB:F8BT solutions were made from mixing 20 mg/mL of PFB in xylenes solution and 20 mg/mL F8BT in xylenes solution. To form devices, 90 nm of PEDOT:PSS (HC Stark PEDOT 4083, lot no. LVW950) was spincoated onto an ITO substrate (Thin Film Devices, OLED/solar applications) and annealed at 120 °C under a N_2 atmosphere for 1 h. The PFB:F8BT solution was then spincoated onto the PEDOT:PSS-covered ITO in N_2 glovebox to form an 80 nm active layer. For trEFM, the film was then loaded into a flow cell with a 150 cc/min dry N_2 flow.

2.2. Photooxidation. After the PFB:F8BT blend films were made, a UV−vis spectrum was taken on one of the films to extract the absorption at each of the three degrading wavelengths of trEFM. Then, the films were exposed without top electrodes to different wavelengths, making the absorbed photon dose to be 6.0×10^{10} photons/μm^2, equal to that used in the trEFM measurements; for the in situ experiments, see below. The PFB:F8BT films were then loaded into an evaporator, and 60 nm thick Al top electrodes were deposited at 0.1 nm/s with a base pressure of 1.2×10^{-6} mbar in an Edwards 306 AUTO evaporator. EQE measurements were performed under vacuum with light from a halogen lamp dispersed by a Spectra Pro 2150i monochromator from Acton Research Corporation.

2.3. GATR-FTIR. The degradation procedures were the same as those for devices. Measurements were carried out on a Nicolet 8700 FT-IR spectrometer (Thermo Scientific) equipped with a HgCdTe detector, GATR grazing angle ATR accessory (Harrick Scientific) with a 65° fixed incident angle and a 56 in-oz slip clutch. The spectrometer and accessory were purged with dry N_2 gas. Each spectrum was taken with 256 averages. Each raw spectrum was corrected with atmospheric suppression and ATR correction; the baseline was then subtracted.

2.4. AFM. trEFM measurements were carried out on MFP-3D-BIO (Asylum Research)-based AFM with custom modifications using 300 kHz Pt-coated cantilevers (BudgetSensor ElectriTap300). trEFM was carried out in a flow cell at a lift height of 10 nm. For all trEFM data, the flow cell was connected to flowing nitrogen. The flow cell used here has a 1.50 to 2.55 mL fluid volume after engaging the tip. For photooxidation, the flow cell was connected to compressed air and exposed to light calibrated to yield an absorbed photon dose of $6.0 \times 10^{10}/\mu m^2$. The system was then purged again with nitrogen for another 20 min before taking the postoxidation trEFM images. The trEFM setup used is shown in Figure 2 and is described in detail elsewhere.[32,33] The 365,

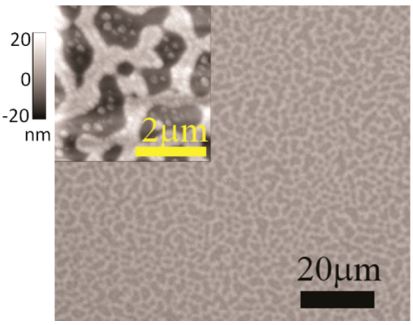

Figure 2. Photoluminescence image of a 1:1 PFB:F8BT blend. Excitation at 470 nm, emission filtered at 530 nm. Inset is the AFM topography of the same film. AFM *z*-scale bar is shown on the left.

405, and 455 nm LEDs were purchased from LED Engin (product numbers LZ1-00U600, LZ1-00UA00, LZ1-00DB00, respectively). Incident illumination power was calibrated using a Si diode and film absorbance spectra to ensure a constant absorbed photon dose at each wavelength.

3. RESULTS AND DISCUSSION

For these experiments, we chose the well-characterized model polyfluorene copolymer blend PFB:F8BT because this system provides a morphology that can be easily tailored by casting from different solvents[34,35] and because the composition of the resulting structures has been well-characterized by a range of experimental methods.[36−38]

Figure 1 shows the structures, absorption spectra, and energy levels[39,40] of PFB and F8BT as well as the optical properties of a 1:1 blend cast from xylenes. The absorbance spectra of both materials are consistent with those of classic PFB/F8BT studies,[34,35] with PFB absorbing most strongly at ∼380 nm and F8BT absorbing most strongly at ∼470 nm. To first order, the blend absorption appears primarily as a superposition of the two component peaks, with each material contributing roughly the same optical density at ∼405 nm. The different absorption peaks of the two materials prove to be useful later because they allows us to preferentially excite each material.

Figure 2 shows a photoluminescence image of a PFB:F8BT blend film excited at 470 nm, collected with an emission filter centered at 530 nm (inset is the topography of the PFB:F8BT blend from an AFM measurement). At 530 nm, the blend emission comes predominantly from the F8BT,[34,35] and we

dx.doi.org/10.1021/jp3090843 | J. Phys. Chem. B 2013, 117, 4654−4660

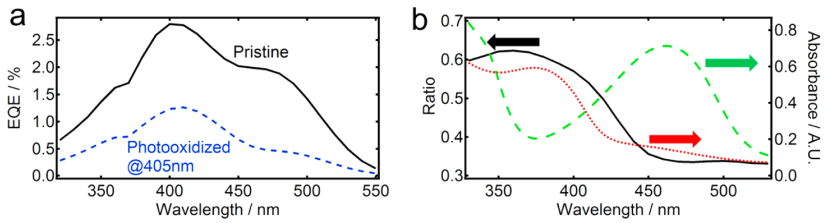

Figure 3. (a) EQE spectra of pristine and photooxidized samples. Black solid line is for pristine film. Blue dashed line is for 405 nm photooxidation. (b) The ratio of EQE versus wavelength post-/pre-photooxidation (black line), plotted on the left axis. Overlaid are the absorbance of PFB (red dotted line) and F8BT (green dashed line), respectively, plotted for reference on the right axis.

thus attribute the bright regions in the PL image (higher topography regions in the AFM image) to be F8BT-rich domains, in good agreement with previous reports of PFB/F8BT blends cast from xylenes.[34,35] The large phase separation is due to the low boiling point of the xylenes solvent being used. Such a coarse ~500 nm scale morphology is not optimal for photodiode performance but is very useful for unambiguous assignment of the domain composition and facilitates our studies of the differences in stability between different domains. Scanning-transmission X-ray microscopy (STXM) studies of similar compositions of this type of film have shown that the PFB-rich domains are ~70% PFB while F8BT-rich domains are ~90% F8BT.[38]

Figure 3a shows the external quantum efficiency (EQE) spectrum from a pristine device made from a 1:1 PFB:F8BT film of 80 nm thickness with 60 nm Al top contacts as a black trace. As expected, the PFB:F8BT combination is rather inefficient,[34,35] with a peak EQE between 2 and 3% when processed under these conditions. The pristine blend EQE trace shows features associated with the absorption spectra of both the PFB (shoulder at 405 nm) and F8BT (shoulder at 500 nm) components. Figure 3a also shows the EQE spectra from identical devices prepared on films that have been degraded in air under 405 nm illumination with absorbed photon dose of $6.0 \times 10^{10}/\mu m^2$. Importantly, the shoulder of the EQE curve beyond 450 nm (where F8BT dominates the blend absorption) degrades faster than the rest of the EQE curve, regardless of the illumination wavelength being used. Figure 3b shows this trend more clearly by plotting the ratio of device EQE before and after photooxidation. We note that after photoxidation the photocurrent response over the region from 450 to 550 nm has degraded more on a relative basis than the photocurrent response over the spectral range from 350 to 400 nm. Evidently the contribution of F8BT to the overall photocurrent decreases faster than the contribution from PFB for these samples.

We note that at these photon doses and exposure conditions the decrease in EQE cannot be from bleaching of the polymer absorption because there is no significant change in the UV−vis spectrum of the blend (see Supporting Information, Figure S1). Furthermore, there is little change even in the photoluminescence spectrum or intensity of the blend (see SI, Figure S2). Thus the loss in photocurrent is likely due to local trap formation, which changes the recombination/transport balance in the film so that even though absorption of photons is not significantly altered the successful extraction of photogenerated carriers is diminished. Because transport and recombination are highly morphology-dependent,[9] we hypothesize that any changes in transport/recombination due to photochemical degradation might also be morphology-dependent. Such a morphology dependence could arise due to many factors ranging from composition-dependent photochemistry to morphology-dependent filamentary transport of charge carriers in the context of energetic disorder.[41,42]

To examine local variations in photooxidation with structure, we employed trEFM. Figure 4 shows an abbreviated schematic

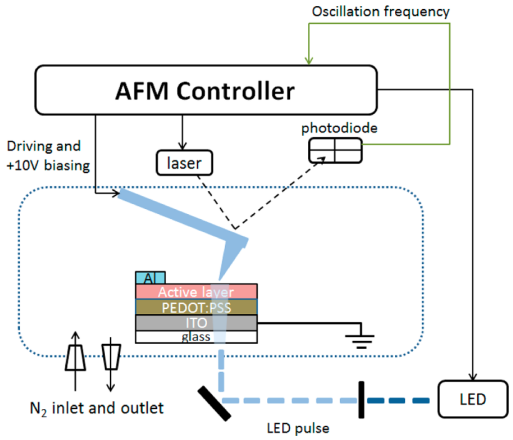

Figure 4. Schematic of trEFM setup. The sample was kept in a flow cell under a dynamic flow of dry N_2. The LED light was focused directly under the AFM tip to generate charges. The sample was grounded. +10 V was applied to the tip. The oscillation frequency shift of the cantilever is due to changes in the capacitance gradient that results from the changes in the distribution of charge carriers underneath the tip. The exponential decay of oscillation frequency is fitted to extract the charging rates at each point.

diagram of the trEFM apparatus that we use to measure the time rate of change of the capacitance and surface potential of a thin semiconductor film following illumination.[28,32,33] In this way, we can use trEFM as a noncontact method to measure spatial heterogeneity in local quantum efficiency due to both structural[32,33] and photochemical factors.[28] More efficient regions of the device deliver photogenerated charges to the top surface of the film at a faster rate, leading to faster charging of the tip−sample capacitor.

As depicted in Figure 4, we photodegraded films in situ using the same wavelengths (365 nm = preferential PFB excitation; 405 nm = equal PFB and F8BT excitation; and 455 nm = preferential F8BT excitation) that we used in the macroscopic photodiode experiments. In this way, we can directly image the relative changes in photocurrent arising from differences in photooxidation rates.

The top row of photooxidation in Figure 5 shows trEFM images of the same area of a pristine PFB/F8BT blend

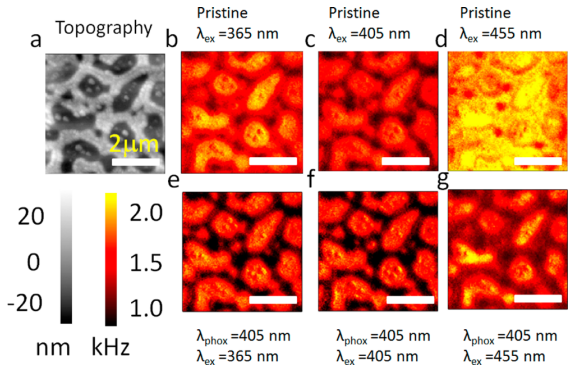

Figure 5. Charging rate maps of a given sample area. (a) Topography of the sample under investigation. (b–d) trEFM images scanned at 365, 405, and 455 nm illumination, respectively, when the sample was pristine. (e–g) trEFM images scanned at 365, 405, and 455 nm illumination, respectively, when the sample was photooxidized with 405 nm illumination.

collected with 365, 405, and 455 nm excitation sources. In each image, the bright-yellow regions correspond to faster photoinduced charging rates (more efficient local current generation and collection). The images show clear contrast, with the PFB-rich domains showing the fastest (most efficient) local rates when the film is excited at 365 or 405 nm. When the F8BT domains are preferentially excitedk, the film shows more uniform contrast but with distinct suppression of the photocurrent near the visible domain boundaries at 455 nm.

The spatial contrast in the pristine PFB:F8BT films shown in Figure 5b–d is a convolution of the compositionally induced variations in light absorption at each location and spatial variations in the quantum efficiency of the film. The local spatial variations in photocurrent collection in the PFB:F8BT system are known to be very sensitive to the exact film morphology, and undergo rapid changes in contrast near the 50:50 blend composition used in this study.[32] Here, we have used only one blend composition, and our focus is instead on exploring how image contrast evolves after photooxidation.

To photooxidize the film, we exposed it to an absorbed dose of 6.0×10^{10} photons per μm^2 from a 405 nm LED while the samples were in ambient air. We then purged the sample cell with dry nitrogen for 20 min and reimaged the samples with trEFM. Figure 5e–g shows the results, again probed with 365, 405, and 455 nm excitation. As expected, Figure 5e–g shows slower photoinduced charging rates after photooxidation, as would result from slower transport and increased recombination losses due to photochemically formed trap states.[28]

We note that Figure 5b–g also shows that the contrast between the different PFB-rich and F8BT-rich regions changes following photooxidation. Importantly, by comparing the charging rates before and after photooxidation in Figure 5, we observe faster degradation rates in the regions of higher topography (F8BT-rich domains). For instance, under 455 nm illumination, the charging rate goes from an overall almost homogeneous image (Figure 5d) to one with strong contrast (Figure 5g). Qualitatively similar results are obtained by photooxidizing at 365 or 455 nm (SI Figure S4, S5). Even when the film is degraded with 365 nm light (preferential excitation of PFB), the strongest contrast in charging rate is observed by probing with 455 nm light (preferential excitation of F8BT), with the largest loss of charging rate occurring in the F8BT-rich regions. In other words, the trEFM data show that the F8BT-rich domains lose their ability to generate/harvest photocurrent faster than the PFB-rich domains. To better visualize the changes in trEFM charging contrast due to photooxidation, we plot the trEFM data as retained charging rate ratio images. We define the retained charging rate at each pixel as:

$$R_{CR} = \frac{k_{phox}}{k_{pristine}} \quad (1)$$

where k_{phox} is the retained charging rate after photooxidation and $k_{pristine}$ is the charging rate on the fresh film without photooxidation. Each sample area was imaged before and after photooxidation at a single degrading wavelength, with the three probing wavelengths (365, 405, and 455 nm).

Figure 6 shows a 3 × 3 matrix of such retained charging rate (R_{CR}) images along with the associated film topography. The

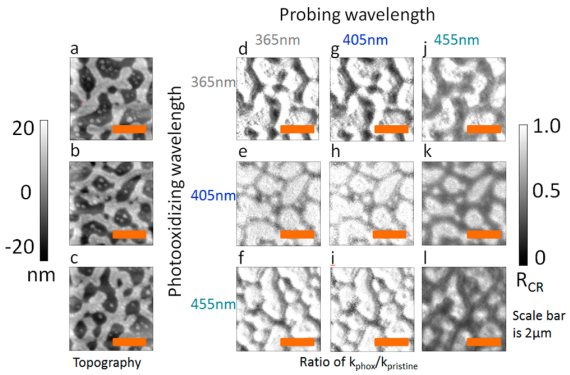

Figure 6. Charging ratio images of given areas. For each row, the image on the left-hand side is the topography of area under investigation. (a) for d, g, and j; (b) for e, h, and k; and (c) for f, i, and l. For the 3 × 3 block on the right, each one is the charging ratio image before and after photooxidation. For example, each pixel in panel e is the charging rate ratio probed with 365 nm illumination before and after photooxidation with 405 nm illumination. All of the charging rate ratio images share the same scale bar on the right. The average value of charging rate is lower when probing with 455 nm illumination.

data shown correspond to 21 total scans and 3 separate photooxidations. Bright areas are those that show little degradation after air/light exposure while dark areas are those that show significant degradation. These images provide dramatic visual evidence of our contention that the F8BT-rich regions of the film are losing their photocarrier generation/collection efficiency faster than the PFB-rich domains. Figure 6d–l shows that regardless of what wavelength is used to photooxidize the film and no matter what wavelength is used to photoexcite the film during for trEFM measurement the result is always the same: the F8BT-rich domains are darker in the ratio images, indicating they retained a smaller fraction of their initial efficiency after photooxidation. The images are all displayed with the same *z*-axis color scale. We do observe a greater extent of photooxidation in Figure 6j–l, all probed with 455 nm, perhaps because this wavelength is preferentially absorbed by F8BT.

Qualitatively, Figure 6 shows clearly that for all excitation wavelengths the F8BT-rich domains are losing their ability to generate photocurrent more rapidly than the PFB-rich

dx.doi.org/10.1021/jp3090843 | J. Phys. Chem. B 2013, 117, 4654–4660

domains. A quantitative analysis (SI Table S1) shows that the degradation of the F8BT-rich domains is anywhere from 1.1 to 2.5 times faster than the PFB-rich domains depending on the degradation and probing wavelengths used. On the upper end, these ratios (SI Table S1) are just outside the ratio of F8BT concentration present in these domains, and one might thus interpret our data as indicating that degradation is simply linearly proportional to local F8BT concentration within a domain. However, an examination of the wavelength-dependent data in Figure 6 (and the ratios at different wavelengths, SI Table S1) shows that at wavelengths where only F8BT absorbs the response of the F8BT within the F8BT-rich regions is falling off *faster* than the response of the F8BT within the PFB-rich regions.

The trEFM photooxidation data are not only consistent with the device data but thus add a suggestive level of missing detail. Indeed, the trEFM data suggest that the reason that the F8BT photoresponse shown in Figure 3 is falling off faster in the macroscopic photodiode measurements is because the regions where most of the F8BT absorption is taking place (the F8BT-rich domains) suffer from faster relative photooxidation overall.

These images provide important evidence in support of the hypothesis that local film structure will affect the local stability of the blend during photovoltaic operation. The origin of this local variation is a matter for speculation. It seems troubling that the F8BT-rich regions would lose performance fastest, as we would generally expect F8BT to be more oxidatively stable than PFB due to its greater ionization potential (Figure 1).[39,40] Indeed, when we subjected neat films of PFB and F8BT to photooxidation experiments characterized by grazing angle attenuated total reflection GATR-FTIR, we found that at the same dosage PFB degrades much faster than F8BT, evidenced by the dramatic difference in keto-defect peak ~1720 cm^{-1}, Figure 7. This is the carbonyl stretch of fluorenone.[28,43] Keto-

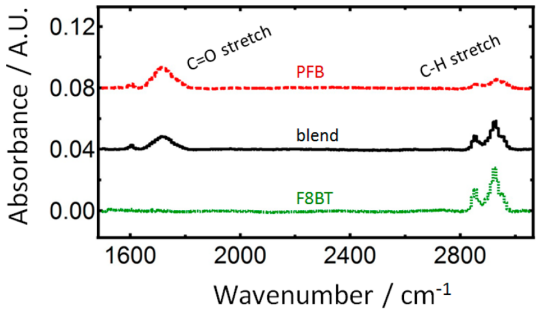

Figure 7. GATR-FTIR absorbance spectrum of PFB, blend, and F8BT after photooxidation with absorbed photon dose of 2.0 × $10^{12}/\mu m2$ with 405 nm LED. Ketone defect formation is indicated by C═O stretch ~1720 cm^{-1}.

defects have been found to be electron trapping.[44] However, we point out that the photochemical reaction is a complex process that yields a variety of products. Their respective charge-transport properties are not well-investigated, and blends undergoing photoinduced charge transfer may react differently than pristine materials.

In PFB/F8BT-based OLEDs it has been reported that dedoping of the PEDOT:PSS layers as a result of pinhole defects in the electrode could explain performance losses over time.[45] However, we do not believe that such a mechanism can explain our photodegradation data because the current density should be higher in the PFB-rich domains and lower in the F8BT-rich domains, thus, if the loss of device performance was from dedoping of the underlying PEDOT:PSS layer, then we should expect the PFB-rich domains to degrade faster, which is the opposite of what we observe.

Given these contradictions and the evidence for lower oxidative stability of our PFB relative to our F8BT samples, we speculate that the origin of the spatial variation in stability observed in Figures 5 and 6 could be due to the breakdown of nanoscopic PFB hole transport pathways in the blend. Ironically then, our working hypothesis would suggest that the F8BT-rich domains are degrading fastest because they have a lower fraction of less stable PFB (typically ~10%,[38] the exact composition may depend on the microscopic location, processing conditions such as spin-coating speed, and temperature, but there is no doubt of dominance of F8BT in the F8BT-rich domains,[36−38] making the few PFB-based hole-transport pathways that exist in those domains more susceptible to low levels of damage).

To test this hypothesis, we used conductive AFM (cAFM) to measure the hole current through the film injected by a gold tip. Because of the better alignment of the HOMO level of PFB with gold,[39,40] hole current is predominantly carried by the PFB component in both phases in the blend, which is confirmed by Figure 8b because there is a larger PFB composition in the

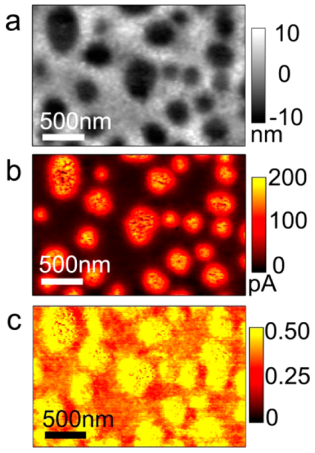

Figure 8. Current image of a PFB:F8BT blend after photooxidation. (a) Topography image of the sample area. (b) Current image of pristine sample under 5 V bias. (c) Retained current ratio image plotting the ratio of injected hold current before and after photooxidation, showing that whereas the PFB-rich domains have much higher hole injection current densities, in both cases, the F8BT-rich domains show the biggest proportional decrease in hole current following photooxidation.

lower topography, PFB-rich regions.[36−38] After photooxidation with 405 nm at the photon dose used in trEFM, we observe a larger loss of hole current in the F8BT-rich phases shown in Figure 8c. Figure 8c is a hole current ratio image, defined as hole current post-/pre-photooxidation. Each pixel in the image is of the value:

$$R_{current} = \frac{I_{phox}}{I_{pristine}} \quad (2)$$

where $I_{pristine}$ is the current before photooxidation and I_{phox} is the current of the same pixel after photooxidation. The current ratio image suggests that proportionally hole current loss is higher in the F8BT-rich domain than in the PFB-rich domain. If photooxidation was merely doping the polymer, then we would expect a rise in the hole current.[24,46] However, we see a drop of current over the entire image. This drop would be consistent with a breakdown of hole transport pathways due to photooxidation and we therefore conclude that our cAFM data are consistent with our hypothesis that the loss of photocurrent in the F8BT-rich domains could be from the degradation of hole transport pathways. However, we point out that this hypothesis will still need to be tested further and hope our findings will stimulate future experimentation.

4. CONCLUSIONS

We have used a combined study of trEFM and device EQE measurements to show that the rate of device aging in nanostructured polymer solar cells can depend on local composition in a model polyfluorene copolymer blend solar cell. After photooxidizing the films, we observed that the device EQE spectra show a reduced contribution from the spectral region attributable to F8BT absorption. Importantly, the in situ trEFM data show that this result can be explained by a relatively faster decay of the photocurrent contributions from the F8BT-rich domains to the net device photocurrent, even while the F8BT present in PFB-rich domains appears to continue to contribute to the device photocurrent. Consistent with our FTIR and cAFM data, we speculate that this differential degradation could be the result of broken percolation networks of the minority PFB chains within the F8BT-rich networks. Overall, these data show that local compositional heterogeneity can affect device aging and that an understanding of photochemical degradation and trap formation on the nanoscale could prove to be invaluable in understanding and improving the lifetime performance of organic solar cells.

■ ASSOCIATED CONTENT

Supporting Information

Additional notes on UV−vis absorbance and photoluminescence spectrum pre-/post-photooxidation, lack of degradation of the films during imaging, charging rates probed with different wavelengths after photooxidation with 365 and 455 nm illumination, degradation versus time data, and quantitative values for the ratio of the R_{CR} plots computed separately for PFB-rich and F8BT-rich domains. This material is available free of charge via the Internet at http://pubs.acs.org

■ AUTHOR INFORMATION

Corresponding Author

*E-mail: ginger@chem.washington.edu.

Notes

The authors declare no competing financial interest.

■ ACKNOWLEDGMENTS

We thank Dr. Rajiv Giridharagopal and Dr. Cody Schlenker for helpful discussions and Dr. David C. Coffey for initial work on this project. D.S.G acknowledges NSF DMR1005504 for supporting the research on which this manuscript is based, and AFOSR for shared equipment.

■ REFERENCES

(1) Halls, J. J. M.; Walsh, C. A.; Greenham, N. C.; Marseglia, E. A.; Friend, R. H.; Moratti, S. C.; Holmes, A. B. *Nature* **1995**, *376*, 498−500.
(2) Yu, G.; Gao, J.; Hummelen, J. C.; Wudl, F.; Heeger, A. J. *Science* **1995**, *270*, 1789−1791.
(3) http://www.polyera.com/newsflash/polyera-achieves-world-record-organic-solar-cell-performance (accessed Jan 13, 2013).
(4) http://www.heliatek.com/newscenter/latest_news/heliatek-erzielt-mit-107-effizienz-neuen-weltrekord-fur-seine-organische-tandemzelle/?lang=en (accessed Jan 13, 2013).
(5) http://newsroom.ucla.edu/portal/ucla/ucla-engineers-create-tandem-polymer-228468.aspx (accessed Jan 13, 2013).
(6) Coakley, K. M.; McGehee, M. D. *Chem. Mater.* **2004**, *16*, 4533−4542.
(7) Kippelen, B.; Bredas, J. L. *Energy Environ. Sci.* **2009**, *2*, 251−261.
(8) Krebs, F. C.; Gevorgyan, S. A.; Alstrup, J. *J. Mater. Chem.* **2009**, *19*, 5442−5451.
(9) Groves, C.; Reid, O. G.; Ginger, D. S. *Acc. Chem. Res.* **2010**, *43*, 612−620.
(10) Jorgensen, M.; Norrman, K.; Krebs, F. C. *Sol. Energy Mater. Sol. Cells* **2008**, *92*, 686−714.
(11) Reese, M. O.; Nardes, A. M.; Rupert, B. L.; Larsen, R. E.; Olson, D. C.; Lloyd, M. T.; Shaheen, S. E.; Ginley, D. S.; Rumbles, G.; Kopidakis, N. *Adv. Funct. Mater.* **2010**, *20*, 3476−3483.
(12) Reese, M. O.; Morfa, A. J.; White, M. S.; Kopidakis, N.; Shaheen, S. E.; Rumbles, G.; Ginley, D. S. *Sol. Energy Mater. Sol. Cells* **2008**, *92*, 746−752.
(13) Yang, X. N.; van Duren, J. K. J.; Janssen, R. A. J.; Michels, M. A. J.; Loos, J. *Macromolecules* **2004**, *37*, 2151−2158.
(14) Seemann, A.; Sauermann, T.; Lungenschmied, C.; Armbruster, O.; Bauer, S.; Egelhaaf, H. J.; Hauch. *J. Sol. Energy* **2011**, *85*, 1238−1249.
(15) Chen, L.-M.; Hong, Z.; Li, G.; Yang, Y. *Adv. Mater.* **2009**, *21*, 1434−1449.
(16) Hau, S. K.; Yip, H.-L.; Baek, N. S.; Zou, J.; O'Malley, K.; Jen, A. K. Y. *Appl. Phys. Lett.* **2008**, *92*, 2533011−2533013.
(17) Drees, M.; Hoppe, H.; Winder, C.; Neugebauer, H.; Sariciftci, N. S.; Schwinger, W.; Schaffler, F.; Topf, C.; Scharber, M. C.; Zhu, Z.; et al. *J. Mater. Chem.* **2005**, *15*, 5158−5163.
(18) Krebs, F. C.; Spanggaard, H. *Chem. Mater.* **2005**, *17*, 5235−5237.
(19) Kim, B. J.; Miyamoto, Y.; Ma, B.; Frechet, J. M. J. *Adv. Funct. Mater.* **2009**, *19*, 2273−2281.
(20) Krebs, F. C.; Norrman, K. *Prog. Photovoltaics* **2007**, *15*, 697−712.
(21) Bässler, H.; Schonherr, G.; Abkowitz, M.; Pai, D. M. *Phys. Rev. B* **1982**, *26*, 3105−3113.
(22) Pasveer, W. F.; Cottaar, J.; Tanase, C.; Coehoorn, R.; Bobbert, P. A.; Blom, P. W. M.; de Leeuw, D. M.; Michels, M. A. J. *Phys. Rev. Lett.* **2005**, *94*, 2066011−2066014.
(23) Zhuo, J.-M.; Zhao, L.-H.; Png, R.-Q.; Wong, L.-Y.; Chia, P.-J.; Tang, J.-C.; Sivaramakrishnan, S.; Zhou, M.; Ou, E. C. W.; Chua, S.-J.; et al. *Adv. Mater.* **2009**, *21*, 4747−4752.
(24) Abdou, M. S. A.; Orfino, F. P.; Son, Y.; Holdcroft, S. *J. Am. Chem. Soc.* **1997**, *119*, 4518−4524.
(25) Coffey, D. C.; Reid, O. G.; Rodovsky, D. B.; Bartholomew, G. P.; Ginger, D. S. *Nano Lett.* **2007**, *7*, 738−744.
(26) Pingree, L. S. C.; Reid, O. G.; Ginger, D. S. *Adv. Mater.* **2009**, *21*, 19−28.
(27) Giridharagopal, R.; Ginger, D. S. *J. Phys. Chem. Lett.* **2010**, *1*, 1160−1169.
(28) Reid, O. G.; Rayermann, G. E.; Coffey, D. C.; Ginger, D. S. *J. Phys. Chem. C* **2010**, *114*, 20672−20677.
(29) Balke, N.; Bonnell, D.; Ginger, D. S.; Kemerink, M. *MRS Bull.* **2012**, *37*, 633−637.
(30) O'Dea, J. R.; Brown, L. M.; Hoepker, N.; Marohn, J. A.; Sadewasser, S. *MRS Bull.* **2012**, *37*, 642−650.

(31) Sengupta, E.; Domanski, A. L.; Weber, S. A. L.; Untch, M. B.; Butt, H.-J. r.; Sauermann, T.; Egelhaaf, H. J.; Berger, R. D. *J. Phys. Chem. C* **2011**, *115*, 19994−20001.
(32) Coffey, D. C.; Ginger, D. S. *Nat. Mater.* **2006**, *5*, 735−740.
(33) Giridharagopal, R.; Rayermann, G. E.; Shao, G.; Moore, D. T.; Reid, O. G.; Tillack, A. F.; Masiello, D. J.; Ginger, D. S. *Nano Lett.* **2012**, *12*, 893−898.
(34) Arias, A. C.; MacKenzie, J. D.; Stevenson, R.; Halls, J. J. M.; Inbasekaran, M.; Woo, E. P.; Richards, D.; Friend, R. H. *Macromolecules* **2001**, *34*, 6005−6013.
(35) Snaith, H. J.; Arias, A. C.; Morteani, A. C.; Silva, C.; Friend, R. H. *Nano Lett.* **2002**, *2*, 1353−1357.
(36) Stevenson, R.; Arias, A. C.; Ramsdale, C.; MacKenzie, J. D.; Richards, D. *Appl. Phys. Lett.* **2001**, *79*, 2178−2180.
(37) Brenner, T. J. K.; McNeill, C. R. *J. Phys. Chem. C* **2011**, *115*, 19364−19370.
(38) McNeill, C. R.; Watts, B.; Thomsen, L.; Ade, H.; Greenham, N. C.; Dastoor, P. C. *Macromolecules* **2007**, *40*, 3263−3270.
(39) Moons, E. *J. Phys.: Condens. Matter* **2002**, *14*, 12235−12260.
(40) Morteani, A. C.; Dhoot, A. S.; Kim, J. S.; Silva, C.; Greenham, N. C.; Murphy, C.; Moons, E.; Cina, S.; Burroughes, J. H.; Friend, R. H. *Adv. Mater.* **2003**, *15*, 1708−1712.
(41) Tessler, N.; Preezant, Y.; Rappaport, N.; Roichman, Y. *Adv. Mater.* **2009**, *21*, 2741−2761.
(42) Coehoorn, R.; Pasveer, W. F.; Bobbert, P. A.; Michels, M. A. J. *Phys. Rev. B* **2005**, *72*, 1522061−15220620.
(43) Liu, L. L.; Tang, S.; Liu, M. R.; Xie, Z. Q.; Zhang, W.; Lu, P.; Hanif, M.; Ma, Y. G. *J. Phys. Chem. B* **2006**, *110*, 13734−13740.
(44) Yang, X. H.; Jaiser, F.; Neher, D.; Lawson, P. V.; Bredas, J. L.; Zojer, E.; Guntner, R.; de Freitas, P. S.; Forster, M.; Scherf, U. *Adv. Funct. Mater.* **2004**, *14*, 1097−1104.
(45) Kim, J. S.; Ho, P. K. H.; Murphy, C. E.; Baynes, N.; Friend, R. H. *Adv. Mater.* **2002**, *14*, 206−209.
(46) Meijer, E. J.; Detcheverry, C.; Baesjou, P. J.; van Veenendaal, E.; de Leeuw, D. M.; Klapwijk, T. M. *J. Appl. Phys.* **2003**, *93*, 4831−4835.

Supporting Information

Morphology Dependent Trap Formation in Bulk Heterojunction Photodiodes

Guozheng Shao, Glennis E. Rayermann, Eric Smith, and David S. Ginger*

Department of Chemistry, University of Washington, Seattle WA, 98195

*ginger@chem.washington.edu

We observe virtually no change in absorbance of the blend before and after photooxidation with 6.0×10^{10} photons/ μm^2 at 405 nm (or 2.9 J/cm^2), as shown in Fig. S1.

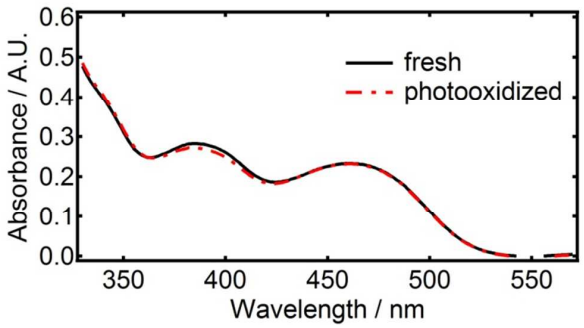

Figure S1. UV-vis spectrum of PFB:F8BT blend before (black solid line) and after (red dashed line) photooxidation with 6.0×10^{10} photons absorbed per μm^2.

We observe slight photoluminescence quenching following photooxidation as demonstrated by the the PL spectra for a 1:1 PFB:F8BT blend before and after photooxidation in Fig. S2. These measurements were carried out on a Nikon TE-2000 inverted microscope with output directed through a fiber optic cable (diameter = 100 μm, UV-VIS transmission, Ocean Optics, Dunedin, FL) to a portable CCD spectrometer (USB2000, Ocean Optics) and illumination from a metal halide lamp (Lumen Dynamics, X-cite 120). Measurements were conducted in a closed flow cell with dynamic N_2 flow. Excitation was filtered at 405nm with bandwidth of 20 nm, emission was filtered using a 425 nm longpass filter.

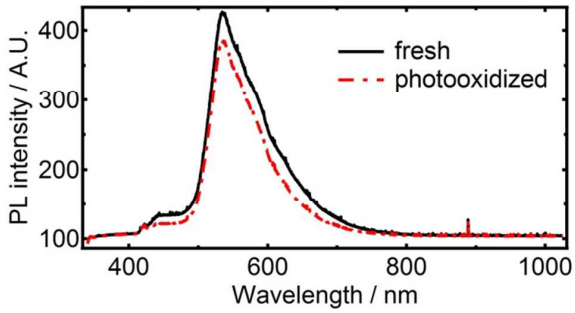

Figure S2. Photoluminescence spectrum of PFB:F8BT blend before (black solid line) and after (red dashed line) photooxidation with 6.0×10^{10} photons absorbed per μm^2.

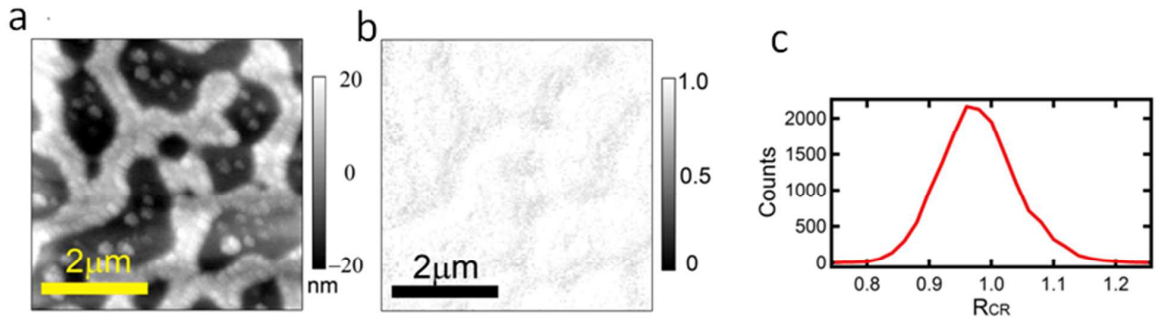

Figure S3. Control study of possible degradation in the flow cell with dynamic nitrogen flow, the same sample area was scanned under trEFM in a row to show the contrast. a) is the area being scanned, b) is the charging rate ratio image as described in the main text, c) is the histogram of b), the average value is 0.994, showing virtually no degradation.

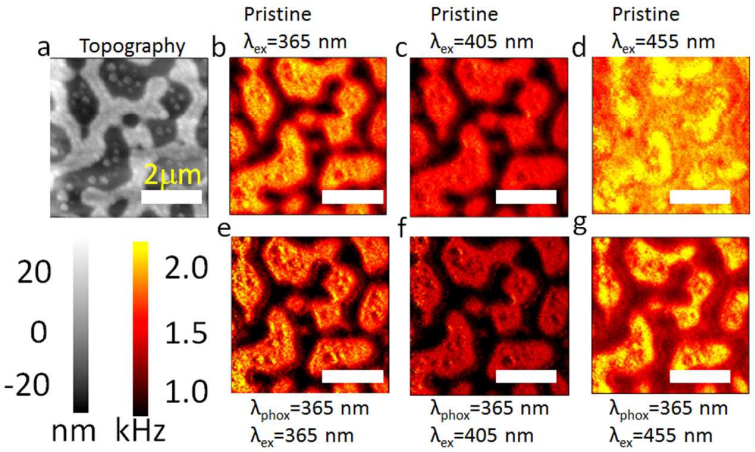

Figure S4. (a) The topography before photooxidation of a sample used in images b-g . (b-d) Charging rate maps with the same sample area as in (a), but generated by trEFM and scanned at 365 nm, 405 nm and 455 nm, respectively when the sample was fresh. (e-g) trEFM images scanned at 365nm, 405nm and 455nm, respectively after being photooxidized with 365 nm illumination.

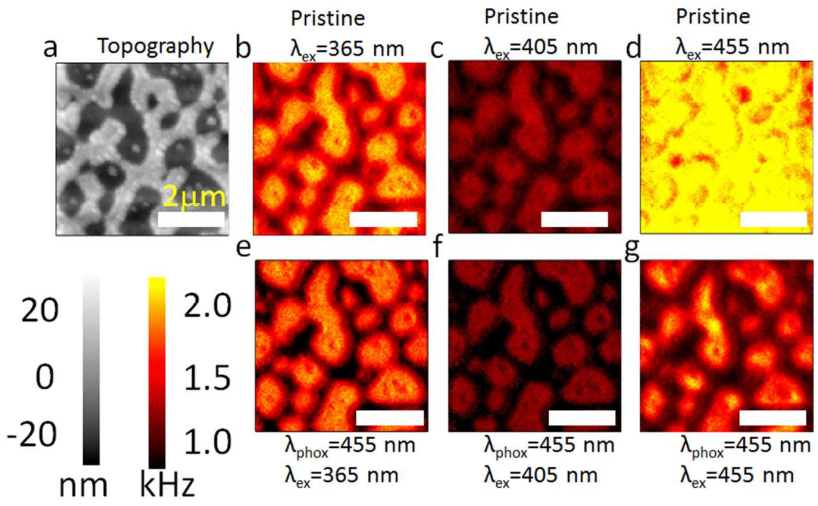

Figure S5. (a) The topography before photooxidation of a sample used in images b-g . (b-d) Charging rate maps with the same sample area as in (a), but generated by trEFM and scanned at 365 nm, 405 nm and 455 nm, respectively when the sample was fresh. (e-g) trEFM images scanned at 365nm, 405nm and 455nm, respectively after being photooxidized with 455 nm illumination.

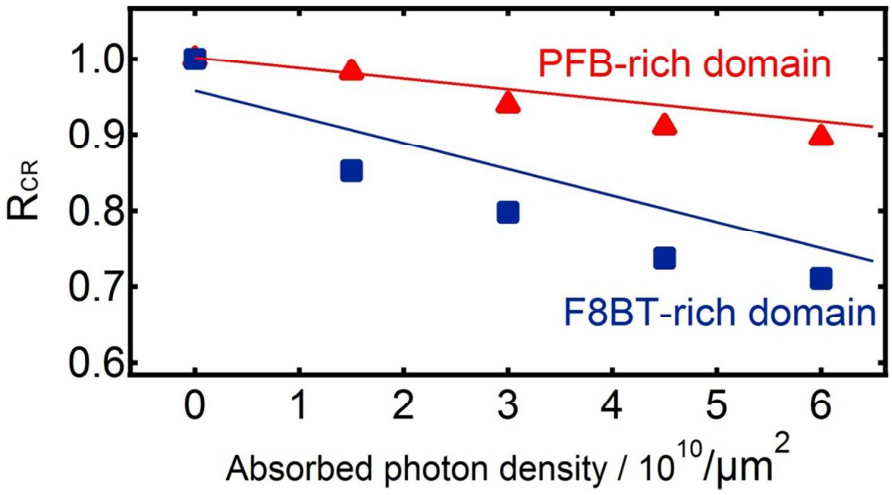

Figure S6. Degradation of the two domains under different absorbed photon dose, both photooxidizing and probing wavelengths are 365 nm. Red triangles and blue squares are for the PFB-rich and F8BT-rich domains, respectively. Red and blue lines are the respective linear fittings, $y = -0.014x + 1.00$ (red line) and $y = -0.035x + 0.96$ (blue line).

PFB-rich domains	Photooxodizing wavelength / nm		
Probing wavelength / nm	365	405	455
365	0.90	0.91	0.92
405	0.80	0.93	0.94
455	0.89	0.84	0.70

F8BT-rich domains	Photooxodizing wavelength / nm		
Probing wavelength / nm	365	405	455
365	0.71	0.77	0.52
405	0.66	0.87	0.54
455	0.52	0.53	0.30

Table S1. Quantitative analyses of the two domains under different photooxidizing and probing wavelengths.

Chapter 5. HALLMARKS OF REVERSIBLE SEPARATION OF LIVING, UNPERTURBED CELL MEMBRANES INTO TWO LIQUID PHASES

https://doi.org/10.1016/j.bpj.2017.09.029

My contributions to this work: In collaboration with SPR, I collected data for Figure S5(C); Figures 3, 4, S9, S10, and S11; and Figure S6(B). I performed all data processing for and created Figures 3, 4, S9, S10, and S11. I collaborated with SPR on yeast sample preparation as well as development of the temperature cycling protocol [Table S3] and the cell-free vacuole mounting method. I aided in the creation of Figure S5. I co-wrote and co-edited the manuscript and supporting material, contributed to peer-review responses, and was responsible for the final manuscript submission.

Biophysical *Journal*
Article

Biophysical Society

Hallmarks of Reversible Separation of Living, Unperturbed Cell Membranes into Two Liquid Phases

Scott P. Rayermann,[1] Glennis E. Rayermann,[1] Caitlin E. Cornell,[1] Alexey J. Merz,[2,*] and Sarah L. Keller[1,*]
[1]Department of Chemistry and [2]Department of Biochemistry, University of Washington, Seattle, Washington

ABSTRACT Controversy has long surrounded the question of whether spontaneous lateral demixing of membranes into coexisting liquid phases can organize proteins and lipids on micron scales within unperturbed, living cells. A clear answer hinges on observation of hallmarks of a reversible phase transition. Here, by directly imaging micron-scale membrane domains of yeast vacuoles both in vivo and cell free, we demonstrate that the domains arise through a phase separation mechanism. The domains are large, have smooth boundaries, and can merge quickly, consistent with fluid phases. Moreover, the domains disappear above a distinct miscibility transition temperature (T_{mix}) and reappear below T_{mix}, over multiple heating and cooling cycles. Hence, large-scale membrane organization in living cells under physiologically relevant conditions can be controlled by tuning a single thermodynamic parameter.

INTRODUCTION

Scientists have invested decades of effort into probing the lipid and protein composition of cell membranes for evidence of heterogeneity, which has the potential to control protein sorting, signal transduction, and other processes (1). Aside from several important exceptions, especially in yeast (e.g., (2–10)), that extensive body of work has implied that the length scale of compositional heterogeneity in the membranes of unstimulated cells is limited to nanoscales, especially in plasma membranes of mammalian cells (reviewed in (11–14)). Submicron domains in membranes gained notoriety as "rafts," and, more recently, as dynamic, short-lived "platforms" (12,15). These concepts are controversial because both terms are loosely or inconsistently defined, and because nanoscale domains are, at best, challenging to observe directly. In contrast to cell membranes, model lipid membranes spontaneously demix on large (μm) length scales into two well-defined liquid phases. This demixing follows thermodynamic principles (16,17). The concept of phase separation is subject to established, quantitative rules that enable rigorous verification of predictions. These rules apply equally well to simple bilayer membranes composed of only three types of lipids, the complex bilayer membranes of giant plasma membrane vesicles blebbed from cells, and phase-separated cytoplasmic droplets recently implicated across a variety of cell biological activities (18–20).

Tantalizing hints have been reported since the 1960s that living membranes are capable of separating into coexisting liquid phases, just as model membranes are. Pioneering experiments investigated the vacuole, the lysosomal organelle of budding yeast. Using freeze fracture electron microscopy (EM), Moor and Mühlethaler (2) found that vacuole membranes of unfixed yeast contained domains depleted of large proteins. Domains in vacuole membranes are physiologically regulated: large proteins are randomly distributed across vacuolar membranes in the logarithmic phase of yeast growth, whereas protein-depleted domains appear when yeast are in the stationary phase (as nutrients are exhausted and the rate of cell division slows) (3,4,6,7,9). In many cases, the domains in vacuole membranes are ~200 nm or larger, and are therefore resolvable using conventional optical microscopy (6).

The visual similarity of domains that form in both synthetic and cell-derived model membranes (Fig. 1, *a* and *b*, respectively) to domains that form in yeast vacuole membranes in vivo (Figs. 1 *c* and S2) is striking. In Fig. 1 *c*, contrast between the two domain types is provided by

Submitted July 18, 2017, and accepted for publication September 22, 2017.
*Correspondence: merza@uw.edu or slkeller@chem.washington.edu
Scott P. Rayermann and Glennis E. Rayermann contributed equally to this work.
Editor: David Cafiso.
https://doi.org/10.1016/j.bpj.2017.09.029

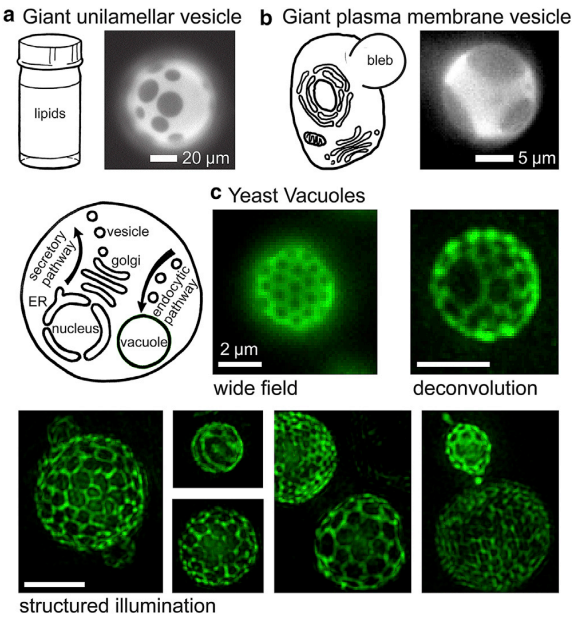

FIGURE 1 Micron-scale, coexisting liquid phases appear in membranes of synthetic and biologically derived model systems at equilibrium, and similar patterns appear on vacuole membranes of living yeast cells. (*a*) Giant unilamellar vesicles produced from ternary mixtures of synthetic lipids, imaged by wide-field epifluorescence microscopy. (*b*) Giant plasma membrane vesicles blebbed from adherent cells, imaged by standard epifluorescence. (*c*) Vacuoles within living yeast cells in the stationary phase of growth. Cells expressing a fluorescent vacuole membrane protein fusion (Vph1-GFP) were grown at 30°C and imaged at ambient temperature (~22°C) using either standard wide-field epifluorescence illumination, wide-field illumination with z-sectioning followed by iterative deconvolution, or structured illumination microscopy (3D-SIM) followed by iterative deconvolution. Information on the growth and imaging procedures is in the Materials and Methods. A version of this figure without green pseudocolor appears in Fig. S1. Scale bars in (*c*), 2 μm. ER, endoplasmic reticulum. To see this figure in color, go online.

green fluorescent protein (GFP)-tagged Vph1 (Vph1-GFP), an integral membrane subunit of the vacuolar proton ATPase. Elegant experiments revealed that Vph1 is one of many proteins and lipids that segregate to one of the two domain types in vacuole membranes of living cells (6). In recent work, the live cell results with Vph1 were unambiguously linked to the early freeze fracture EM observations by immunogold labeling of freeze fracture replicas (9). In other words, freeze fracture EM and optical microscopy of intact vacuoles in living cells observe exactly the same membrane structures.

Two hallmarks of a membrane separating into liquid phases are 1) coalescence of domains on short timescales and 2) reversible mixing and demixing as a single thermodynamic parameter is varied. Previous attempts to observe these hallmarks in vacuole membranes have been inconclusive. Although multiple domains have been observed to merge into one larger domain, they did so on long timescales (6). Similarly, although the fractions of mixed and demixed vacuole membranes have been observed to vary with temperature changes from 30 to 40°C (by Moeller et al. in 1981), subsequent research using live yeast reported that "vacuolar structures did not visibly change when samples were visualized at a range of temperatures from 20 to 55°C" (by Toulmay and Prinz in 2013) (4,6). Salient details of the early work are: the yeast were fixed before freeze fracture, the fraction of vacuoles exhibiting domains decreased from >75% to ~50% when the temperature of stationary phase yeast was increased from 30 to 40°C, and that fraction recovered when temperature was returned to 30°C (4). The authors concluded that a solid (gel) phase transition had occurred (4).

Additional observations are consistent with, but do not prove, vacuole domains being due to membrane demixing into two coexisting liquid phases. 1) A variety of domain morphologies are evident in vacuole membranes, including pseudohexagonal arrays, stripes, and "half-moons" with only one large domain of each type (6,7). 2) Under the studied growth conditions, ~25% of vacuole membranes resembled half-moons (6). 3) On cell-free vacuoles, domains persisted after proteolytic digestion of proteins on the cytoplasmic faces of isolated vacuoles (6). 4) All labels used, which included 14 different endogenous protein markers and three lipid-sensitive probes, partitioned into one or the other of only two types of domains (6,9). 5) Vacuoles typically contain 7–15 mol % sterol (21,22), and the vacuole sterol content appears to increase during stationary phase (9). When ergosterol (the major sterol of yeast membranes) is depleted with drugs or genetic manipulations, domain formation is impaired (6,7,9). Synthetic membranes exhibit coexisting liquid phases only when one of their lipid components is a sterol such as ergosterol or cholesterol (23). 6) More broadly, several mutations that affect the lipid composition of vacuolar membranes result in the absence of membrane domains (6,7,9). Domain formation is linked to the availability of lipids and sterols, which are delivered to the vacuole via lipid esters stored in cytoplasmic lipid droplets, through a process called microlipophagy (7,9,24). Although all six of these findings are consistent with the hypothesis that vacuole domains arise through phase separation, none of them presents a direct test.

We now test key predictions of the phase-separation hypothesis. If the phases are liquids, then domains are predicted to merge and rearrange on short timescales. If a miscibility transition occurs, the membranes are predicted to reversibly demix at a constant transition temperature. We conclude that vacuole domains exhibit hallmark behaviors of phase separation.

MATERIALS AND METHODS

Table S1 in the Supporting Material lists methods and conditions for each figure and movie.

Synthetic membranes

Giant unilamellar vesicles (GUVs) were electroformed (25) and imaged as previously described (18,26). In Figs. 1, S1, S3, and S4 and Movie S8, the GUVs are composed of 35 mol % diphytanoyl-phosphatidylcholine, 35 mol % dipalmitoyl-phosphatidylcholine (Avanti Polar Lipids, Alabaster, AL), and 30 mol % cholesterol (Sigma, St. Louis, MO). The GUV in Fig. S4 is composed of 40 mol % di(13:0)-phosphatidylcholine, 20 mol % diphytanoyl-phosphatidylcholine, and 40 mol % cholesterol. All GUVs are labeled with 0.8 mol % Texas Red dipalmitoyl-phosphatidylethanolamine (Invitrogen, Carlsbad, CA).

Giant plasma membrane vesicles

The vesicle in Fig. 1 *b* was imaged at 10°C under control conditions in (27). Briefly, vesicles were prepared by incubating adherent RBL-2H3 cells in a buffer containing dithiothreitol and formaldehyde, and imaged on an inverted epifluorescence microscope (Olympus, Center Valley, PA) (27).

Yeast cell culture

A BY4742 derivative, *MAT α his3Δ1 lys2Δ0 ura3Δ0 leu2Δ0 VPH1-GFP::HIS3MX6*, was used. In general, when yeast are placed in fresh growth media, their growth follows a characteristic sequence of events. A "log phase" of rapid growth is followed by a "stationary phase" in which yeast vacuoles fuse to become as large as 5 μm in diameter (28,29). Cultures (200 mL) were grown in synthetic complete media at 30°C in a shaking incubator for ~20 h until the optical density of the culture was ~1.7, using 600 nm wavelength light. The culture was then grown for an additional ~43 h to reach the stationary phase, where the optical density using 600 nm wavelength light falls in the range of 6.8–7.8. This procedure is depicted in Fig. S5, B and C.

Vph1-GFP fusion protein

Yeast vacuoles were labeled by fusing the Vph1 protein to GFP, using homologous recombination. The fusion protein was expressed from the chromosomal *VPH1* locus under the native promoter, at normal cellular copy number. The Vph1 fusions are known to retain physiological function and were previously shown to not spontaneously aggregate within the vacuole membrane, even during vacuole:vacuole docking (30). Vph1-GFP has been shown to colocalize in yeast vacuoles to the same membrane domains as the fluorescent tracer FM4-64, which partitions preferentially to the liquid-disordered phase in GUVs (6). Filipin, a dye that binds sterols, partitions preferentially to vacuole regions depleted in Vph1-GFP (6).

Yeast imaging

Yeast are typically 5–10 μm in diameter, vacuoles are 3–5 μm, and domains in vacuole membranes are often close in size to the Abbe diffraction limit (~200 nm). Yeast were imaged by the four imaging techniques described in detail below. Image sequences collected by these techniques were then processed using a Kalman filter algorithm implemented in Image J (public domain http://rsbweb.nih.gov/ij/) to reduce detector and shot noise. For some experiments, yeast cells were adsorbed to cover slips coated with concanavalin A lectin (Elastin Products Company, Inc., Owensville, MO).

Imaging: wide-field illumination

Yeast cells were imaged with an electron-multiplying charge-coupled device camera on an Olympus IX71 fluorescence microscope as previously described, using a 60 × 1.4 NA oil immersion objective (31). To reduce noise, multiple exposures were averaged. In the wide-field micrograph in Fig. 1 *c* and all images of Fig. S2, eight consecutive 400 ms exposures were averaged. The micrographs in Fig. S6*B* were obtained by averaging four consecutive 200 ms exposures. To preserve the fidelity of images, no adjustments other than averaging and brightness levels were made (e.g., contrast was not altered).

Imaging: HILO illumination

To increase the signal-to-background ratio, yeast were imaged using highly inclined laminated optical sheet (HILO) illumination (32,33) on a home-built Nikon Ti-U system with a 561-nm dipole-pumped solid-state laser (MPB Communications, Pointe-Claire, QC, Canada). A Nikon CFI Plan Apo Lambda 100 × 1.45 NA objective was used along with a dichroic quadband with 488/561/647/752 lines (Chroma) and an ET605/70m filter. Images were acquired on an electron-multiplying charge-coupled device (iXon Ultra 897, Andor) operating in frame transfer mode at 10 Hz, as described (34). To preserve the fidelity of images, no adjustments other than averaging and brightness levels were made (e.g., contrast was not altered).

Imaging: deconvolution microscopy

Iteratively deconvolved wide-field sequences of images were acquired on a DeltaVision system (GE Healthcare, Little Chalfont, UK) equipped with a CMOS camera and a 60 × 1.40 NA objective (Olympus). Cell suspensions were introduced to homemade flow chambers made from #1.5 cover slips passivated with concanavalin A. Unbound cells were washed out with depleted media taken from the supernatant of 1 mL of sample spun down at 1200 rpm for 2 min or (for hypoosmotic shock experiments) with water. Z-stacks were acquired at 200 nm spacing, usually at 0.15 s exposure per frame, and were deconvolved using SoftWorx software (GE Healthcare). From the deconvolved Z-stacks, brightest-point projections were computed. The projection time series datasets were then corrected for photobleaching using a histogram-matching algorithm implemented in ImageJ, and, finally, were Kalman filtered to reduce noise, also in ImageJ.

Imaging: structured illumination microscopy

Samples were mounted as for deconvolution and imaged using an OMX-SR instrument (GE Healthcare) equipped with a 63 × 1.42 NA objective (Olympus). The immersion oil refractive index was typically 1.516. Z-stacks were acquired at 120 nm spacing and images were deconvolved using the SoftWorx deconvolution package. Weiner spatial filter constants from 0.001 to 0.010 yielded similar reconstructions.

Imaging: standard epifluorescence

Both the synthetic GUV membranes and blebbed giant plasma membrane vesicle membrane imaged in Figs. 1, *a* and *b*, S3, and S4, and in Movie S8 were imaged as previously described (18,35). To preserve the fidelity of images, no adjustments other than averaging and brightness levels were made (e.g., contrast was not altered).

Thermal cycling

For both in vivo and cell-free yeast vacuole samples, temperature was controlled by air from a heat gun and monitored using a calibrated thermocouple. The thermocouple tip was inserted between the cover slip and slide to make direct contact with the sample. The edges of the cover slip and slide were sealed with vacuum grease to prevent water loss due to evaporation. In experiments in which temperature data was collected, a graph is provided

within the figures and, for the in vivo vacuoles, within the movies. The synthetic membrane GUV shown in Fig. S3 and Movie S8 was temperature controlled as previously described, and the temperature was cycled around its miscibility transition temperature of 46.1°C.

Cell lysis to create cell-free vacuoles

Cells were harvested in a swinging-bucket rotor (3200 × *g*) for 10 min at room temperature, resuspended in 0.1 M Tris (pH 9.4) and 10 mM dithiothreitol, and incubated for 10 min at 30°C. The cells were again sedimented in a swinging-bucket rotor (3200 × *g*) for 5 min at room temperature and then resuspended in spheroplast buffer (600 mM sorbitol, 50 mM potassium phosphate pH 7.5, and 8% v/v depleted media, saved from the first centrifugation step). Lytic enzyme (Zymolyase 20T, Seikigaku; further purified by ion exchange chromatography) was added to threefold higher concentration than in our standard vacuole prep (36) to adjust for cell wall composition in yeast grown into the stationary phase, and the cells were incubated for 1 h at 30°C. The spheroplasted cells were sedimented in a swinging-bucket rotor (3200 × *g*) for 5 min at 4°C. For hypoosmotic lysis, spheroplasts were resuspended in 15% ficoll buffer (10 mM Pipes-KOH pH 6.8, 200 mM sorbitol, and 15% w/v ficoll) and diethylaminoethyl-dextran was added to a final concentration of 0.005–0.01% w/v. Spheroplasts were incubated for 2 min on ice, then 3 min at 30°C. The resulting spheroplast lysates were stored on a wet ice bath for no more than 4 h before use.

Mounting cell-free vacuoles on slides

A thin agarose cushion was prepared by spin coating 55 μL of molten 0.8% (w/v) agarose in Pipes sorbitol buffer (10 mM Pipes-KOH pH 6.8 and 200 mM sorbitol) on plasma-cleaned glass cover slips. Vacuole lysates were diluted 1:10 with molten 0.8% w/v low-melt agarose in Pipes sorbitol buffer. The solution was mixed by gentle vortexing, deposited onto agarose-coated slides, and imaged by the same procedure as for living cells. Immobilization of vesicles within agarose gels does not affect the diffusion coefficient of individual lipids in vesicle membranes (37).

Osmotic gradient

A simple flow cell was constructed from two cover slips joined along their edges by spacers of double-sided tape. The bottom cover slip was coated in concanavalin A. Yeast cells in their depleted media were drawn into the flow cell by capillary action and absorbed to the concanavalin A-coated cover slip. To induce hypoosmotic swelling of the vacuole, a volume of deionized water, equal to the volume of sample loaded into the flow cell, was deposited at one end of the microfluidic chamber. Fluid was then wicked from the opposite end of the flow cell to introduce water into the flow cell.

RESULTS AND DISCUSSION

The first hallmark of liquid phases that we observe in vacuole membranes is that two domains can coalesce in timescales of seconds. In synthetic GUVs with taut membranes, liquid domains diffuse freely over the vesicle surface, collide with other domains, and coalesce as in Fig. S4 until eventually only one domain of each type remains (38). In synthetic GUVs with excess area (more area than necessary to enclose a spherical volume), domains in pseudohexagonal arrays are observed to bulge in to or out of the vesicles and are hindered from colliding (17,39–41). Similarly, the pseudohexagonal domains of yeast vacuoles bulge inward toward the vacuole lumen (6,9,24) and appear to be hindered from colliding. When bulging domains are not labeled, the labeled background membrane has a faceted appearance, as in Fig. 2.

We hypothesized that domain collision in vacuoles might be triggered by applying a hypoosmotic gradient to yeast cells, which causes the vacuoles inside to swell due to elevated internal turgor pressure. This was indeed the case: we capture events of domains colliding and quickly coalescing in Fig. 2 and Movie S1. We observe the reverse spontaneous process in Fig. S7 and Movie S3 (played at 30× speed) by applying a hyperosmotic gradient. During coalescence, the domain boundaries rearrange to minimize the total length of domain interfaces. This is consistent with minimization of energy arising from line tension between the two membrane phases.

Once the kinetic barrier for two domains to collide is overcome, the fastest coalescence of domains that we observe in yeast vacuoles occurs on the same timescale (seconds) as coalescence of domains that can be an order of magnitude larger in synthetic vesicles (38). These observations are consistent with the expectation that fluids in living yeast cells, namely the cytoplasm and the vacuole contents (including high concentrations of high molecular mass polyphosphate), have higher viscosities than the viscosities of fluids used in synthetic GUV preparations (42–44).

Domain coalescence is technically challenging to image, so is rarely observed. Coalescence can be identified only when domains are large enough to image without

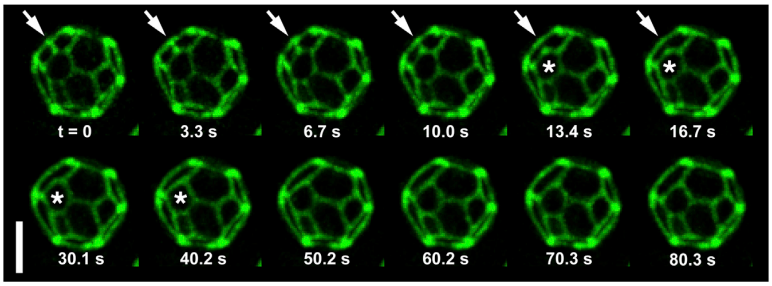

FIGURE 2 Rapid coalescence of in vivo micron-scale domains in a single yeast vacuole membrane over time. Yeast cells were grown as in Fig. 1, mounted in a flow chamber, subjected to a hypoosmotic gradient, and imaged by z-sectioning and iterative deconvolution at ambient temperature (~23°C). Maximum brightness projections of the vacuole hemisphere closest to the microscope objective are presented. Arrows denote a region where two dark domains coalesce. Stars (*) denote a domain that changes shape from a hexagon to a pentagon, minimizing the total length of the domain interface. The scale bar represents 2 μm. Movie S1 corresponds to the above sequence, played at 10× speed. The dynamic shift in the shape of the starred domain from a hexagon to a pentagon, from seconds 13.4–40.2 above, appears in seconds 1–4 of Movie S1. To see this figure in color, go online.

superresolution techniques, yet small enough to merge. Observation of domain coalescence in Fig. 2 required deconvolution of image stacks and reconstruction of only one hemisphere of the vacuole, the full three-dimensional image obscured the merging event. These technical challenges likely lead to overrepresentation of slow events within Fig. S6 and Movie S2 (played at 30× speed), and the previous literature (6). We speculate that slow coalescence events result because a subset of vacuole domains are associated with lipid droplets or with nuclear contact sites (7,9,24). Therefore, only the fastest coalescence events in vacuoles (as in Fig. 2 of the main text) are relevant for comparison with timescales in model systems.

The second hallmark of liquid phases is the existence of a miscibility transition with respect to an intrinsic thermodynamic variable such as temperature, pressure, or membrane composition, as in the schematic in Fig. S8. Cyclic changes in any one of these thermodynamic variables cause domains to reversibly appear and disappear in synthetic vesicles (16,45). To test whether the domains in yeast vacuole membranes arise from demixing of a single liquid phase into two coexisting liquid phases, we subjected yeast to rapid temperature cycles.

In Figs. 3 and S9 and Movies S4 and S5 (both played at 3× speed), we cycle the temperature of yeast cells in the stationary phase of cell growth. At the standard growth temperature of 30°C, yeast vacuoles exhibit dark domains on a bright background marked by GFP-Vph1 (Fig. 1 *c*). At temperatures above ~37°C, the domains disappear and the membrane is uniformly labeled.

EM results show that large proteins within a uniformly-labeled membrane are randomly distributed across the entire membrane (9). In our experiments, domains nucleate upon cooling and are large enough to image within seconds. By comparison, transcription and protein synthesis in yeast occur on timescales of at least minutes. The ability of the vacuole membrane to abruptly and reversibly switch between two states (namely, the presence and absence of domains), at a distinct temperature, and over multiple heating and cooling cycles, is a defining feature of a phase transition.

Cell viability is not affected by the temperature cycling regime used in our experiments (Fig. S5 A; Tables S2 and S3). Moreover, individual yeast cells that exhibit domains in their vacuole membranes successfully grow and undergo mitosis when supplied with fresh nutrients (6). Within a population of yeast cells, the T_{mix} of the vacuole membrane varies from cell-to-cell, just as it does in plasma membrane vesicles (46), as might be expected for any biological parameter regulated by an array of biochemical and physiological variables.

To verify that the cyclical disappearance and reappearance of vacuole domains is intrinsic to the membrane rather than originating from factors in the yeast cytoplasm, we extended the results of Fig. 3 to cell-free vacuoles. Figs. 4 and S10 and Movie S6 (played at 3× speed) show

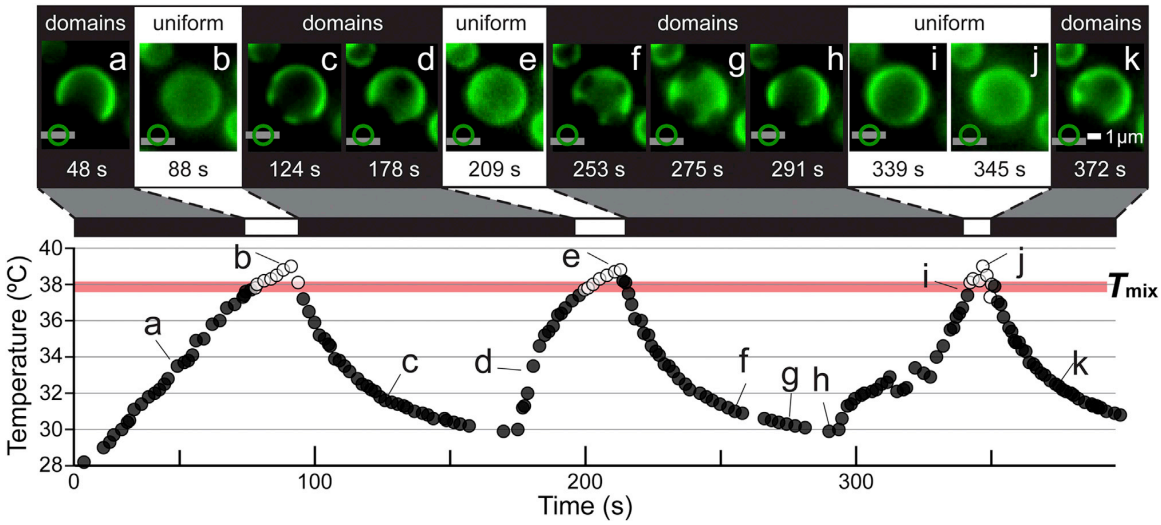

FIGURE 3 Micron-scale domains in an in vivo yeast vacuole reversibly vanish and reemerge through three temperature cycles. Micrographs (*a*)–(*k*), representing 48 and 372 s, respectively, correspond to the labeled locations in the plot of temperature versus time. In the lower left-hand corner of each micrograph, a symbol illustrating the focal plane (*horizontal line*) at either the top, equator, or bottom of the vacuole (*circle*) specifies the focal plane at which the vacuole was imaged in each micrograph. The temperature at which open symbols on the graph change to filled symbols (and vice versa) is T_{mix}. A thick, horizontal line, labeled T_{mix}, is drawn to highlight the transitions; the line is not a statistical fit. Vacuoles were imaged using HILO illumination. Movie S4 corresponding to this figure appears in the Supporting Material and plays at 3× speed such that micrograph (*a*) appears at 16 s in Movie S4 and micrograph (*k*) appears at 2 min and 4 s. To see this figure in color, go online.

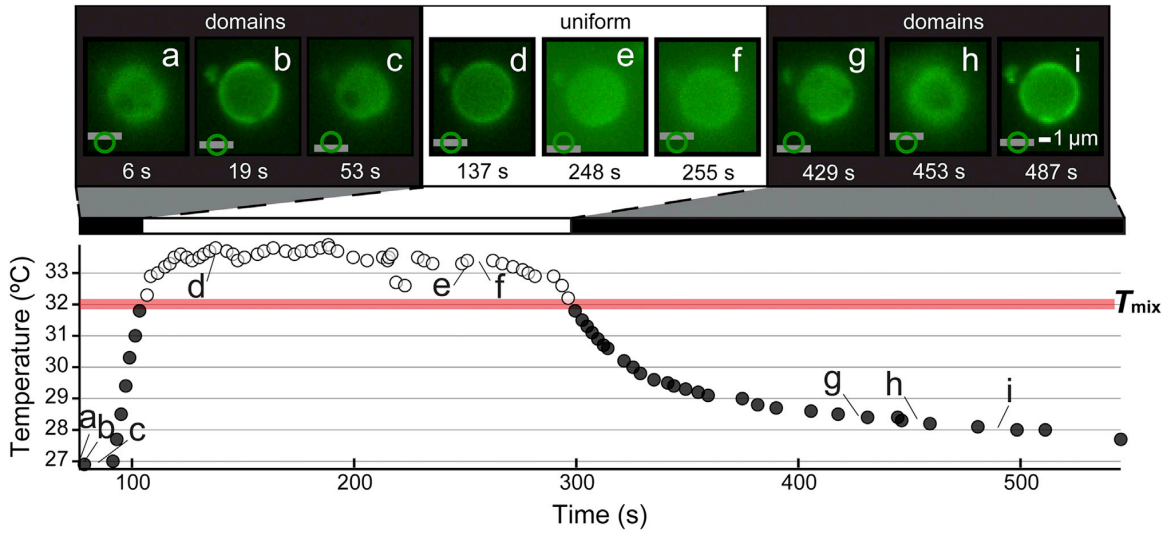

FIGURE 4 Micron-scale domains in a cell-free yeast vacuole reversibly vanish and reappear through temperature cycles. This figure is one of three cycles in Fig. S10. Micrographs (*a*)–(*i*) correspond to the labeled locations in the plot of temperature versus time. To counteract effects of photobleaching of Vph1-GFP through time, brightness levels were increased in micrographs (*e*) and (*f*), and excitation intensity was increased in micrographs (*g*), (*h*), and (*i*). Other details are as described for Fig. 3. Movie S6 corresponding to this figure appears in the Supporting Material and plays at 3× speed; such that micrograph (*a*) appears at 2.1 s in Movie S6 and micrograph (*i*) appears at 2 min and 42.5 s. Preparation of cell-free vacuoles is described in the Materials and Methods. To see this figure in color, go online.

that domains in cell-free vacuoles reversibly vanish and reappear as the temperature is cycled. The location at which domains reappear depends on the speed of cycling. When temperature is quickly cycled (as occurred in Figs. 3, S10, *top*, and S11, *rapid* and Movie S7, which plays at 3× speed), domains disappear and renucleate at approximately the same positions on the vacuole. The same effect occurs when synthetic GUVs undergo rapid temperature cycling (as in Fig. S3 and Movie S8, which plays at 10× speed). This is because as the temperature increases, domains disappear through a process in which the edge blurs, as in Movie S5 (played at 3× speed); domains do not disappear by becoming continually smaller. Edge blurring is expected when labeled molecules are suddenly free to diffuse over the entire surface of the membrane. When the temperature is held above T_{mix} for longer periods, such that lipids and proteins have ample time to diffuse across the membrane and mix uniformly, domains nucleate at new positions, both on vacuoles (Figs. 4, S10, *bottom*, and S11, *slow* and Movie S9, which plays at 3× speed) and on synthetic vesicles (Fig. S3 and Movie S8, which plays at 10× speed). In the language of condensed matter physics, this behavior is consistent with domains arising through a mechanism of nucleation and growth rather than with fluctuations arising through a mechanism of spinodal decomposition of a membrane poised near a miscibility critical point (18,35).

The location of domains in vacuole membranes does not appear to be governed by static protein scaffolds. By mass, about half of the vacuole membrane is protein, comparable to ~70% for a plasma membrane (21). Although vacuole membranes may be associated with protein scaffolds, we observe that domains have variable sizes, move across the surface of vacuoles, smoothly and quickly coalescence into larger domains, and renucleate in new locations. In addition, domains persist after digestion of proteins on the cytoplasmic face of isolated vacuoles (6). All of these properties are inconsistent with domain edges constrained by static scaffolds.

The coalescence of small domains into larger ones followed by reorganization of domain edges within yeast vacuole membranes (as in the starred domain in Fig. 2) implies that the domains result from a miscibility phase transition rather than from the extensive cross-linking used to induce micron-scale domains in stimulated cell membranes (12), from cell polarization (47–49), from vacuolar fragmentation or deep invaginations due to hyperosmotic stress (50), or from the regulated assembly of contacts between docked yeast vacuoles (30,51). Neither the presence nor the absence of domains is perturbed by ATP depletion (6). We can also rule out contact between lipid droplets and vacuoles as a direct driver of vacuole domain formation because only a subset of the domains in vacuole membranes correlates with the presence of docked lipid droplets (7,9,24). The presence of many more domains than droplets requires an additional mechanism, such as phase separation. The localized release of sterols into the vacuole membrane through microlipophagy

of docked lipid droplets, via the Npc1/2 system (7,9,24), appears to be an indirect driver of phase separation across the entire membrane. Finally, we note that the assembly of docking domains before bilayer-bilayer fusion is consistent with, and may be driven by, membrane phase behavior (30,51,52).

CONCLUSION

Here, we show that large-scale membrane organization in yeast vacuoles is the result of demixing of the membrane into coexisting liquid phases and that this demixing is fully reversible. This mechanism operates in live cells imaged using noninvasive methods. In model vesicle membranes, demixing occurs equally upon a change in temperature or membrane composition. At constant temperature, cells may regulate membrane phase separation in response to external or internal cues. For example, the NPC1/2 cholesterol transport system controls domain formation (9). Moreover, the Slt2/Mpk1 kinase is essential for the formation of phase-separated domains in the yeast vacuole (6). Previously, we demonstrated that Slt2/Mpk1, a key node in the protein kinase C-Rho1 signaling pathway, regulates both lipid acyl chain composition and bilayer fluidity (53). The knowledge that vacuole membranes reversibly demix into coexisting liquid phases enables direct application of physical rules of membrane phase behavior established in model systems to living biological membranes. The description of domains as arising from a mechanism of phase separation rather than as less well-defined "raft-like" (9) domains provides a tractable paradigm for future investigations of the regulation and mechanisms of in vivo membrane domain partitioning.

SUPPORTING MATERIAL

Eleven figures, three tables, and nine movies are available at http://www.biophysj.org/biophysj/supplemental/S0006-3495(17)31072-X.

AUTHOR CONTRIBUTIONS

S.L.K. and A.J.M. conceived the project and supervised the experiments. S.P.R., G.E.R., A.J.M., and C.E.C. performed experiments and collected data. S.L.K., A.J.M., S.P.R., and G.E.R. designed research, wrote the article, and designed figures.

ACKNOWLEDGMENTS

We thank Liz Manrao, Dan Nickerson, Rachael Plemel, Tyler Chozinski, Marco Howard, Lauren Gagnon, and Aaron Halpern for technical advice. Micrographs provided by Ellyn Gray and Sarah Veatch (Fig. 1 *B*), and Joan Bleecker (Fig. S4) are used with permission. We are grateful to Professors Linda Wordeman and Joshua Vaughan for providing microscope time.

This material is based upon work supported by the National Science Foundation (NSF) Graduate Research Fellowship Program under grant DGE-1256082 to G.E.R., by NSF grant MCB-1402059 to S.L.K., by the National Institute of General Medical Sciences of the National Institutes of Health (NIH) under award T32GM008268 to C.E.C., and by NIH grant GM077349 to A.J.M.

REFERENCES

1. Simons, K., and D. Toomre. 2000. Lipid rafts and signal transduction. *Nat. Rev. Mol. Cell Biol.* 1:31–39.
2. Moor, H., and K. Mühlethaler. 1963. Fine structure in frozen-etched yeast cells. *J. Cell Biol.* 17:609–628.
3. Moeller, C. H., and W. W. Thomson. 1979. An ultrastructural study of the yeast tomoplast during the shift from exponential to stationary phase. *J. Ultrastruct. Res.* 68:28–37.
4. Moeller, C. H., J. B. Mudd, and W. W. Thomson. 1981. Lipid phase separations and intramembranous particle movements in the yeast tonoplast. *Biochim. Biophys. Acta.* 643:376–386.
5. Spira, F., N. S. Mueller, …, R. Wedlich-Söldner. 2012. Patchwork organization of the yeast plasma membrane into numerous coexisting domains. *Nat. Cell Biol.* 14:640–648.
6. Toulmay, A., and W. A. Prinz. 2013. Direct imaging reveals stable, micrometer-scale lipid domains that segregate proteins in live cells. *J. Cell Biol.* 202:35–44.
7. Wang, C.-W., Y.-H. Miao, and Y.-S. Chang. 2014. A sterol-enriched vacuolar microdomain mediates stationary phase lipophagy in budding yeast. *J. Cell Biol.* 206:357–366.
8. Murley, A., R. D. Sarsam, …, J. Nunnari. 2015. Ltc1 is an ER-localized sterol transporter and a component of ER-mitochondria and ER-vacuole contacts. *J. Cell Biol.* 209:539–548.
9. Tsuji, T., M. Fujimoto, …, T. Fujimoto. 2017. Niemann-Pick type C proteins promote microautophagy by expanding raft-like membrane domains in the yeast vacuole. *Elife.* 6:e25960.
10. Murley, A., J. Yamada, …, J. Nunnari. 2017. Sterol transporters at membrane contact sites regulate TORC1 and TORC2 signaling. *J. Cell Biol.* 216:2679–2689.
11. Simons, K., and M. J. Gerl. 2010. Revitalizing membrane rafts: new tools and insights. *Nat. Rev. Mol. Cell Biol.* 11:688–699.
12. Lingwood, D., and K. Simons. 2010. Lipid rafts as a membrane-organizing principle. *Science.* 327:46–50.
13. Levental, I., and S. Veatch. 2016. The continuing mystery of lipid rafts. *J. Mol. Biol.* 428 (24 Pt A):4749–4764.
14. Kraft, M. L. 2017. Sphingolipid organization in the plasma membrane and the mechanisms that influence it. *Front. Cell Dev. Biol.* 4:154.
15. Munro, S. 2003. Lipid rafts: elusive or illusive? *Cell.* 115:377–388.
16. Veatch, S. L., and S. L. Keller. 2002. Organization in lipid membranes containing cholesterol. *Phys. Rev. Lett.* 89:268101.
17. Baumgart, T., S. T. Hess, and W. W. Webb. 2003. Imaging coexisting fluid domains in biomembrane models coupling curvature and line tension. *Nature.* 425:821–824.
18. Honerkamp-Smith, A. R., P. Cicuta, …, S. L. Keller. 2008. Line tensions, correlation lengths, and critical exponents in lipid membranes near critical points. *Biophys. J.* 95:236–246.
19. Brangwynne, C. P. 2013. Phase transitions and size scaling of membrane-less organelles. *J. Cell Biol.* 203:875–881.
20. Hyman, A. A., C. A. Weber, and F. Jülicher. 2014. Liquid-liquid phase separation in biology. *Annu. Rev. Cell Dev. Biol.* 30:39–58.
21. Schneiter, R., B. Brügger, …, S. D. Kohlwein. 1999. Electrospray ionization tandem mass spectrometry (ESI-MS/MS) analysis of the lipid molecular species composition of yeast subcellular membranes reveals acyl chain-based sorting/remodeling of distinct molecular species en route to the plasma membrane. *J. Cell Biol.* 146:741–754.
22. Zinser, E., C. D. Sperka-Gottlieb, …, G. Daum. 1991. Phospholipid synthesis and lipid composition of subcellular membranes in the unicellular eukaryote Saccharomyces cerevisiae. *J. Bacteriol.* 173:2026–2034.

23. Beattie, M. E., S. L. Veatch, …, S. L. Keller. 2005. Sterol structure determines miscibility versus melting transitions in lipid vesicles. *Biophys. J.* 89:1760–1768.

24. Moeller, C. H., and W. W. Thomson. 1979. Uptake of lipid bodies by the yeast vacuole involving areas of the tonoplast depleted of intramembranous particles. *J. Ultrastruct. Res.* 68:38–45.

25. Angelova, M. I., S. Soléau, …, P. Bothorel. 1992. Preparation of giant vesicles by external AC electric fields. *Prog. Colloid Polym. Sci.* 89:127–131.

26. Blosser, M. C., A. R. Honerkamp-Smith, …, S. L. Keller. 2015. Transbilayer colocalization of lipid domains explained via measurement of strong coupling parameters. *Biophys. J.* 109:2317–2327.

27. Gray, E., J. Karslake, …, S. L. Veatch. 2013. Liquid general anesthetics lower critical temperatures in plasma membrane vesicles. *Biophys. J.* 105:2751–2759.

28. Li, S. C., and P. M. Kane. 2009. The yeast lysosome-like vacuole: endpoint and crossroads. *Biochim. Biophys. Acta.* 1793:650–663.

29. Armstrong, J. 2010. Yeast vacuoles: more than a model lysosome. *Trends Cell Biol.* 20:580–585.

30. Wang, L., E. S. Seeley, …, A. J. Merz. 2002. Vacuole fusion at a ring of vertex docking sites leaves membrane fragments within the organelle. *Cell.* 108:357–369.

31. Angers, C. G., and A. J. Merz. 2009. HOPS interacts with Apl5 at the vacuole membrane and is required for consumption of AP-3 transport vesicles. *Mol. Biol. Cell.* 20:4563–4574.

32. Konopka, C. A., and S. Y. Bednarek. 2008. Variable-angle epifluorescence microscopy: a new way to look at protein dynamics in the plant cell cortex. *Plant J.* 53:186–196.

33. Tokunaga, M., N. Imamoto, and K. Sakata-Sogawa. 2008. Highly inclined thin illumination enables clear single-molecule imaging in cells. *Nat. Methods.* 5:159–161.

34. Chozinski, T. J., A. R. Halpern, …, J. C. Vaughan. 2016. Expansion microscopy with conventional antibodies and fluorescent proteins. *Nat. Methods.* 13:485–488.

35. Veatch, S. L., P. Cicuta, …, B. Baird. 2008. Critical fluctuations in plasma membrane vesicles. *ACS Chem. Biol.* 3:287–293.

36. Schwartz, M. L., and A. J. Merz. 2009. Capture and release of partially zipped trans-SNARE complexes on intact organelles. *J. Cell Biol.* 185:535–549.

37. Lira, R. B., J. Steinkühler, …, K. A. Riske. 2016. Posing for a picture: vesicle immobilization in agarose gel. *Sci. Rep.* 6:25254.

38. Stanich, C. A., A. R. Honerkamp-Smith, …, S. L. Keller. 2013. Coarsening dynamics of domains in lipid membranes. *Biophys. J.* 105:444–454.

39. Bacia, K., P. Schwille, and T. Kurzchalia. 2005. Sterol structure determines the separation of phases and the curvature of the liquid-ordered phase in model membranes. *Proc. Natl. Acad. Sci. USA.* 102:3272–3277.

40. Hamada, T., Y. Miura, …, M. Takagi. 2007. Dynamic processes in endocytic transformation of a raft-exhibiting giant liposome. *J. Phys. Chem. B.* 111:10853–10857.

41. Ursell, T. S., W. S. Klug, and R. Phillips. 2009. Morphology and interaction between lipid domains. *Proc. Natl. Acad. Sci. USA.* 106:13301–13306.

42. Wintersmith, J. R., L. Zou, …, E. K. Mann. 2007. Determination of interphase line tension in Langmuir films. *Phys. Rev. E Stat. Nonlin. Soft Matter Phys.* 75:061605.

43. Williams, S.-P., P. M. Haggie, and K. M. Brindle. 1997. 19F NMR measurements of the rotational mobility of proteins in vivo. *Biophys. J.* 72:490–498.

44. Fujino, T., K. Hirota, …, T. Tahara. 2008. In-cell viscosity measurement using a fluorescence up-conversion microscope. *Chem. Lett.* 37:1240–1241.

45. Nicolini, C., J. Kraineva, …, R. Winter. 2006. Temperature and pressure effects on structural and conformational properties of POPC/SM/cholesterol model raft mixtures–a FT-IR, SAXS, DSC, PPC and Laurdan fluorescence spectroscopy study. *Biochim. Biophys. Acta.* 1758:248–258.

46. Gray, E. M., G. Díaz-Vázquez, and S. L. Veatch. 2015. Growth conditions and cell cycle phase modulate phase transition temperatures in RBL-2H3 derived plasma membrane vesicles. *PLoS One.* 10:e0137741.

47. Bagnat, M., and K. Simons. 2002. Cell surface polarization during yeast mating. *Proc. Natl. Acad. Sci. USA.* 99:14183–14188.

48. Wedlich-Soldner, R., S. Altschuler, …, R. Li. 2003. Spontaneous cell polarization through actomyosin-based delivery of the Cdc42 GTPase. *Science.* 299:1231–1235.

49. Makushok, T., P. Alves, …, D. Brunner. 2016. Sterol-rich membrane domains define fission yeast cell polarity. *Cell.* 165:1182–1196.

50. Takatori, S., T. Tatematsu, …, T. Fujimoto. 2016. Phosphatidylinositol 3,5-bisphosphate-rich membrane domains in endosomes and lysosomes. *Traffic.* 17:154–167.

51. Fratti, R. A., Y. Jun, …, W. Wickner. 2004. Interdependent assembly of specific regulatory lipids and membrane fusion proteins into the vertex ring domain of docked vacuoles. *J. Cell Biol.* 167:1087–1098.

52. McNally, E. K., M. A. Karim, and C. L. Brett. 2017. Selective lysosomal transporter degradation by organelle membrane fusion. *Dev. Cell.* 40:151–167.

53. Lockshon, D., C. P. Olsen, …, B. K. Kennedy. 2012. Rho signaling participates in membrane fluidity homeostasis. *PLoS One.* 7:e45049.

Supporting Material for:

Hallmarks of reversible separation of living, unperturbed cell membranes into two liquid phases

Scott P. Rayermann, Glennis E. Rayermann, Caitlin E. Cornell,
Alexey J. Merz, and Sarah L. Keller

This PDF file includes:

Figs. S1 to S11
Tables S1 to S3
Captions for Movies S1 to S9

Other supporting information for this manuscript includes the following:

Movies S1 to S9

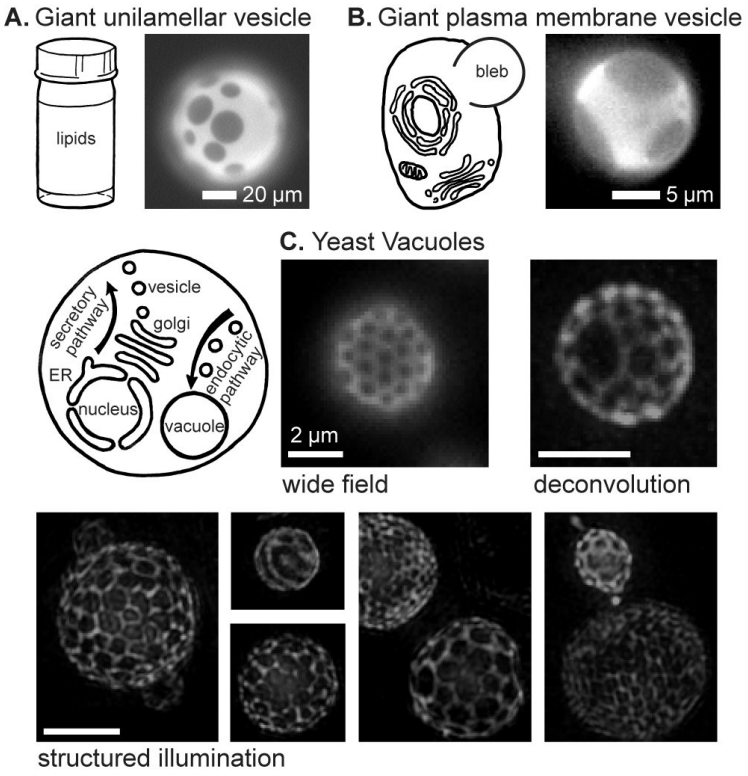

Fig. S1
A greyscale version of Fig. 1. Micron-scale, coexisting liquid phases appear in membranes of synthetic and biologically-derived model systems at equilibrium, and similar patterns appear on vacuole membranes of living yeast cells. (A) Giant unilamellar vesicles produced from ternary mixtures of synthetic lipids, imaged by wide-field epifluorescence microscopy. (B) Giant plasma membrane vesicles blebbed from adherent cells, imaged by standard epifluorescence. (C) Vacuoles within living yeast cells in the stationary phase of growth. Cells expressing a fluorescent vacuole membrane protein fusion (Vph1-GFP) were grown at 30 ˚C and imaged at ambient temperature (~22 ˚C) using either standard wide-field epifluorescence illumination, wide-field illumination with z sectioning followed by iterative deconvolution, or structured illumination microscopy (3D-SIM) followed by iterative deconvolution. Information on the growth and imaging procedures is in the Methods. A version of this figure with green pseudocolor appears in Fig. 1. Scale bars in (C) = 2 µm.

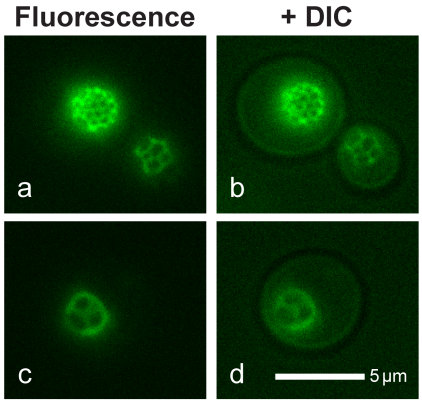

Fig. S2.

In the stationary phase of growth, yeast cells typically contain only one large vacuole. In panels **a** and **c**, yeast cells are imaged by wide-field illumination. In panels **b** and **d**, overlay composites show both wide-field illumination and differential interference contrast microscopy (DIC) to reveal the outline of the whole cell. All vacuoles in this figure exhibit membrane domains.

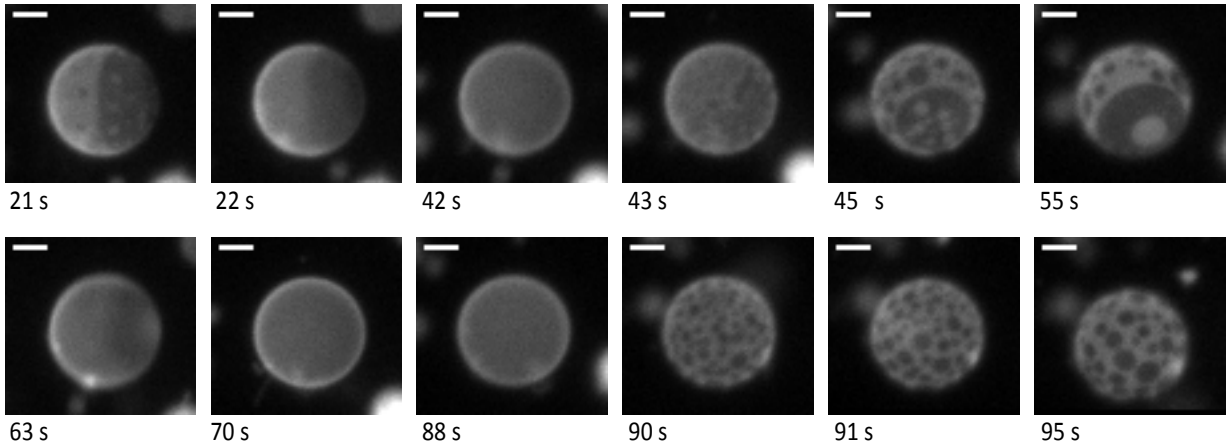

Fig. S3.
Fluorescence microscopy images showing reversible phase separation in a membrane of a single, synthetic, giant unilamellar vesicle (GUV) through time as temperature is cycled. Movie S8 corresponds to this figure and plays at 10x speed; time points in the movie are listed in square brackets []. In the top line, temperature is quickly cycled from below T_{mix} (at 21 s [2.1 s in Movie S8], when large domains are visible) to above T_{mix} (at 42 s [4.2 s], when sharp domain boundaries can no longer be distinguished), to below T_{mix} again (at 43 s [4.3 s]). This sequence of images demonstrates that after rapid cycling, domains re-nucleate (at 43 s [4.3 s]) primarily at the same locations on the surface of the GUV from which they disappeared, resulting in domain distributions (at 55 s [5.5 s]) similar to the original distributions (at 21 s [2.1 s]).

In contrast, in the bottom line, the same temperature cycle is repeated more slowly in the same GUV. At 55 s [5.5 s in Movie S8], the GUV membrane is below T_{mix} and has large domains. At 63 s [6.3 s], the GUV is above T_{mix} and sharp domain boundaries can no longer be distinguished. The GUV is held above T_{mix} for a time that is sufficiently long for all membrane components to mix uniformly (until 88 s [8.8 s]). As a result, when the temperature is lowered below T_{mix} again, small domains nucleate over the entire surface of the vesicle, as shown in the image at 90 s [9 s]. Those domains grow by collision and coalescence over time (as in Fig. S3), resulting in the image at 95 s [9.5 s]. The scale bar is 20 μm.

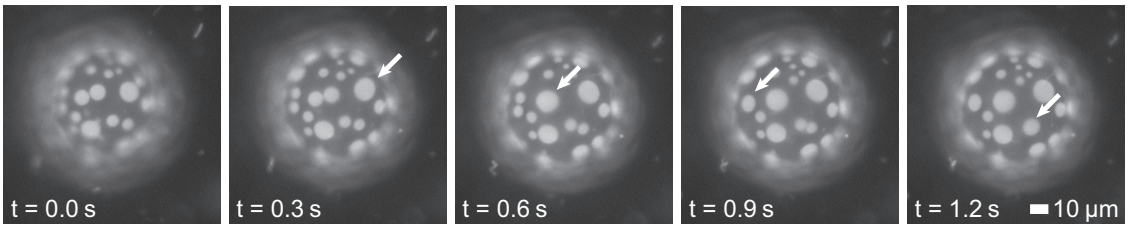

Fig. S4.

Micron-scale, liquid domains on the surface of a model giant unilamellar vesicle (GUV) collide and coalesce. Coalescence of liquid domains occurs when the membrane has no excess area (i.e. when it has no more area than is needed to cover the surface of a sphere with the interior volume). Arrows show single domains that had previously appeared as two separate domains in the preceding frame of the video. As time progresses, all domains eventually merge until the vesicle has only one domain of each type (not shown). As an analogy to explain why coalescence is characteristic of separation of two liquid phases, consider a bulk mixture of two immiscible liquids like oil and water. When the mixture is shaken, droplets of oil disperse within the water. With time, the droplets coalesce until all the oil lies in a separate layer on top of the water. Images provided by Joan Bleecker and used with permission.

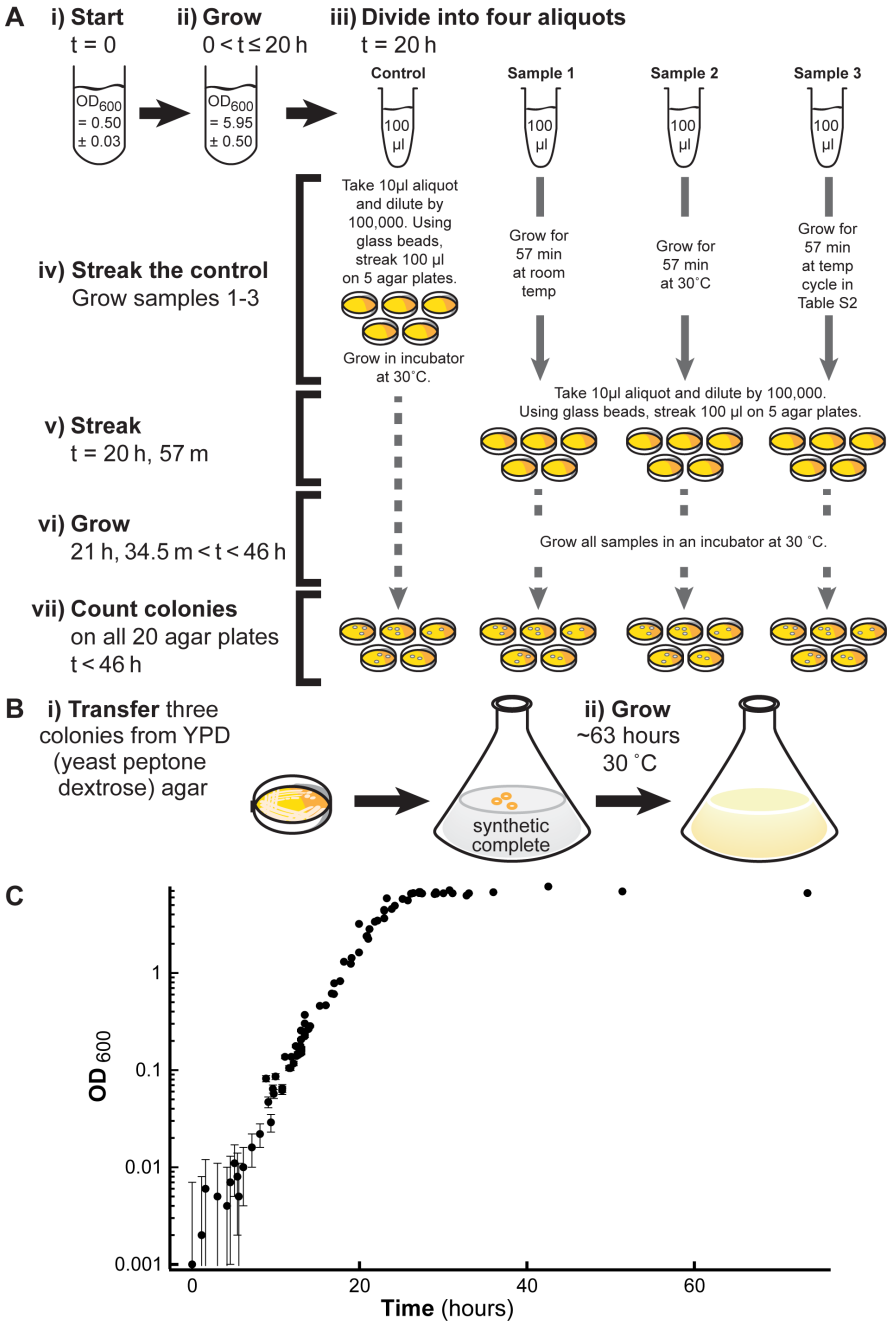

Fig. S5.

(A) Protocol for yeast viability experiment (results in Table S1). (B) Growth protocol to grow 3 colonies of yeast in 200 mL of media for ~63 hours. (C) Growth curve of the yeast in this study, where OD_{600} is the optical density at 600 nm as described in the methods of the main text. Error bars are based on the variation in OD_{600} readings for media blanks.

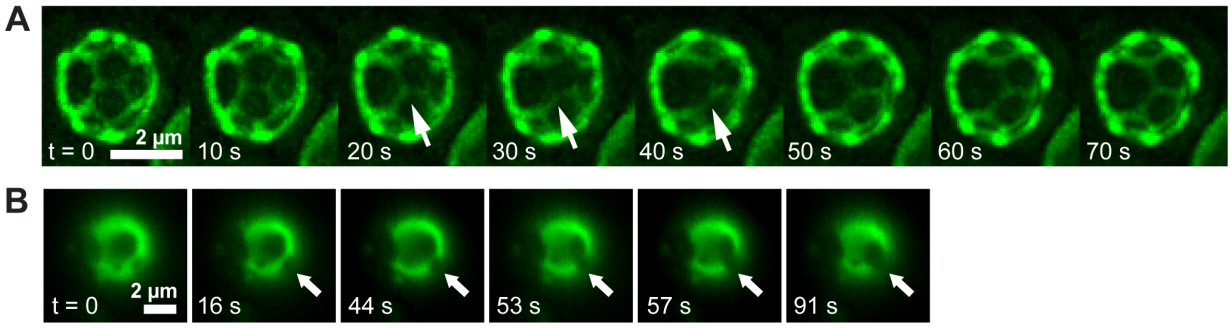

Fig. S6.
Coalescence of micron-scale domains in the membranes of two *in vivo* yeast vacuoles over time at a constant temperature. The vacuoles were inside yeast cells in the stationary phase of growth as in Fig. S2. The images in **A** result from deconvolution of twelve Z–sections of the top hemisphere of the vacuole. The arrows indicate a region in which two domains begin to coalesce. Movie S2 corresponds to this set of images and is played at 30x speed. The images in **B** were captured by wide-field illumination. The arrows point to a region where two domains diffuse into contact with each other, collide, and coalesce.

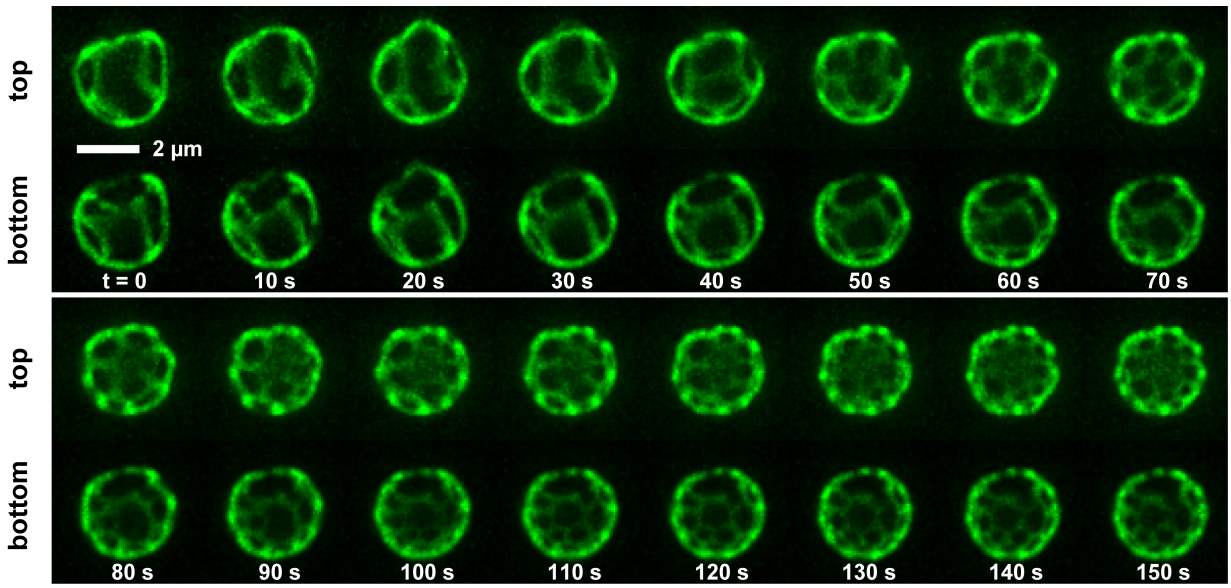

Fig. S7.
The *in vivo* liquid domains in a yeast vacuole sometimes become smaller after osmotic gradients are applied to yeast cells. At each time interval, z-sections were acquired and iteratively deconvolved. Renderings correspond to the two hemispheres of the vacuole, labeled as top and bottom. Movie S3 corresponds to this figure and is played at 30x speed.

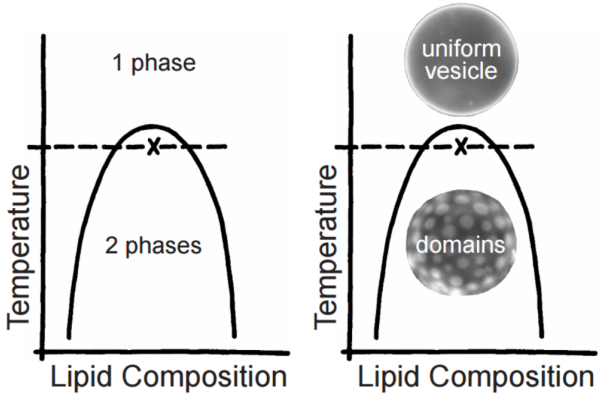

Fig. S8.

Schematic for coexistence behavior of two liquid phases in a synthetic membrane of a giant unilamellar vesicle. Vesicle images correspond to a membrane with lipid composition x shown on the figure. For all temperatures and compositions that fall within the curve, the membrane demixes into two liquid phases. Specifically, domains nucleate and grow through a process of collision and coalescence (as shown in Fig. S3). Outside the curve, the membrane is in one, fully mixed phase. Changes in thermodynamic variables, such as composition or temperature, result in a phase transition from one regime to another.

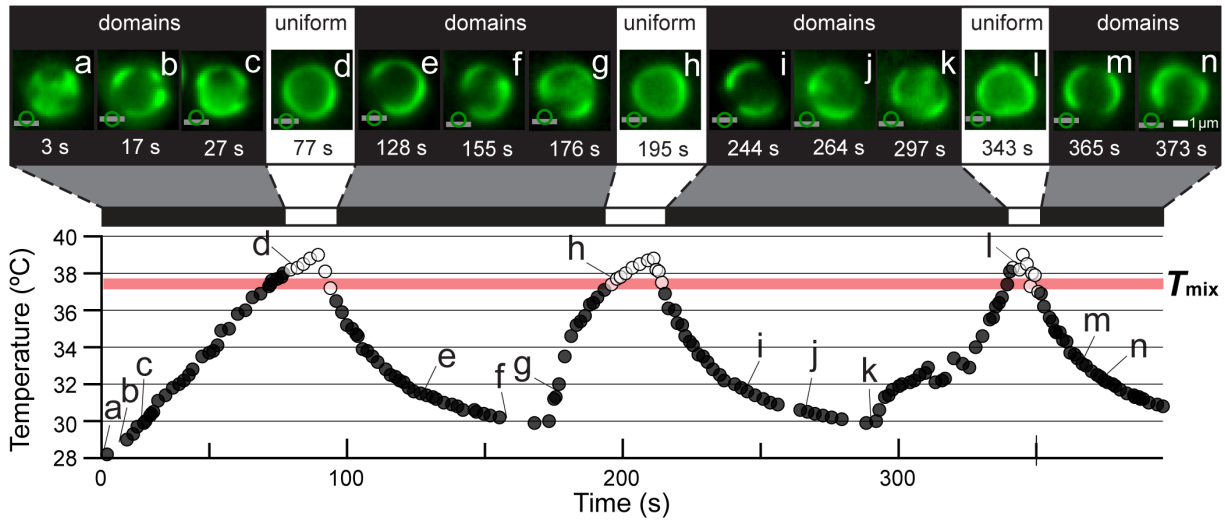

Fig. S9.
Micron-scale domains *in vivo* in a yeast vacuole reversibly appear and vanish through multiple temperature cycles. Micrographs *a* through *n* correspond to the labeled locations in the plot of temperature vs. time. A symbol illustrating the focal plane (grey line) at either the top, equator, or bottom of the vacuole (green circle) specifies the focal plane at which the vacuole was imaged in each micrograph. Several micrographs were recorded at times that fall between temperature points. Open symbols indicate that the vacuole was uniform; filled symbols indicate micron-scale domains. The temperature at which open symbols on the graph transition to filled (and *vice versa*) is T_{mix}. A thick, horizontal red line is drawn to highlight the transitions; the line is not a statistical fit. Imaged by HILO illumination. Movie S5 corresponds to this figure and plays at 3x speed such that micrograph *a* appears at 1 second in Movie S5 and micrograph *n* appears at 2 minutes and 4.3 seconds.

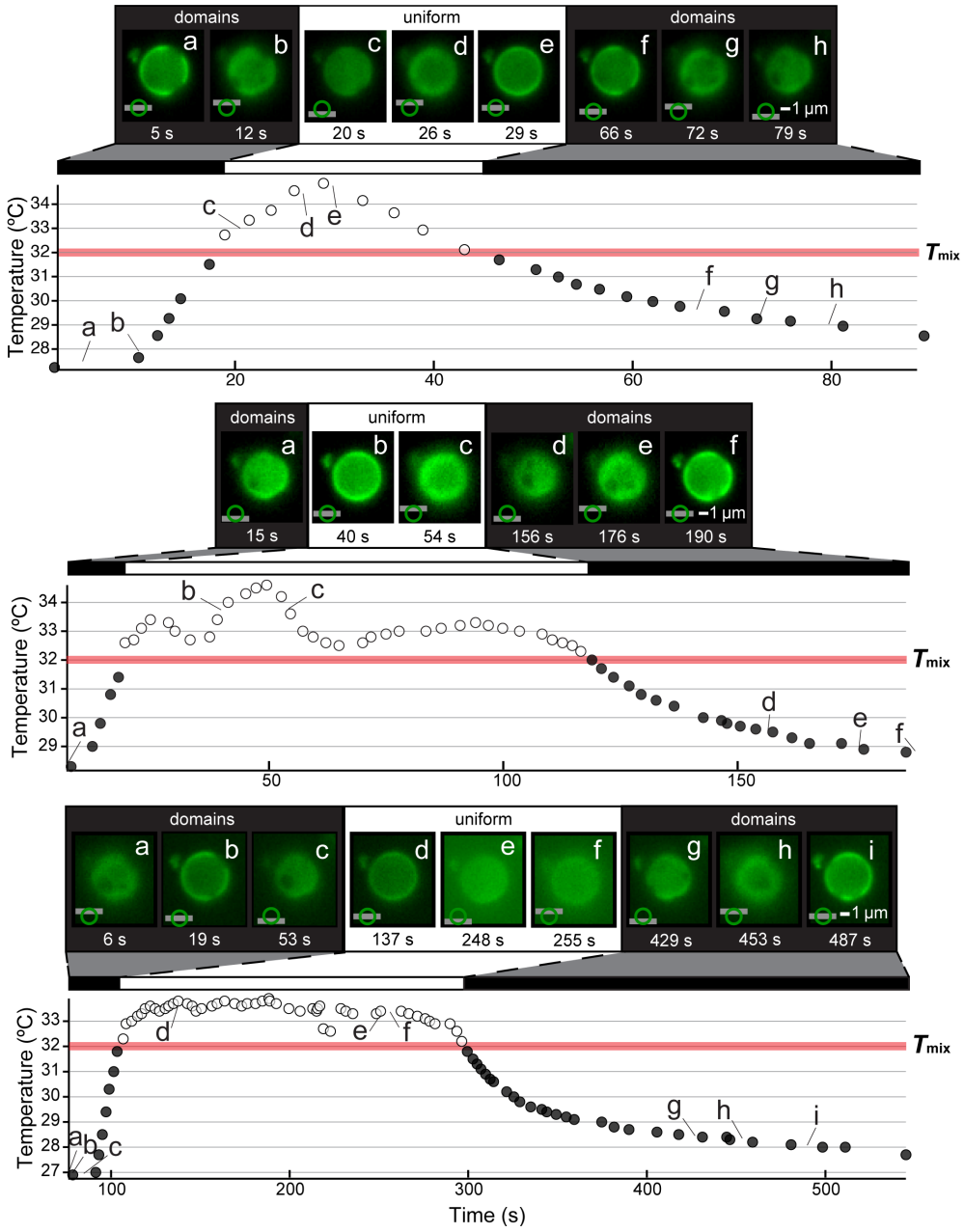

Fig. S10.
Micron-scale domains in a cell-free yeast vacuole reversibly vanish and reappear through multiple temperature cycles. Lowercase letters (e.g. *a* through *i*) correspond to labeled locations in the plots of temperature vs. time. A symbol illustrating the focal plane (grey line) at either the top, equator, or bottom of the vacuole (green circle) specifies the focal plane at which the vacuole was imaged in each micrograph. Open symbols indicate that the vacuole was uniform; filled symbols indicate micron-scale domains. The temperature at which open symbols on the graph transition to filled symbols (and *vice versa*) is T_{mix}. A thick, horizontal red line is drawn to highlight the transitions; the line is not a statistical fit. Imaged by HILO illumination. The bottom panel of this figure corresponds to Fig. 4 of the main text and to Movie S6, which is played at 3x speed.

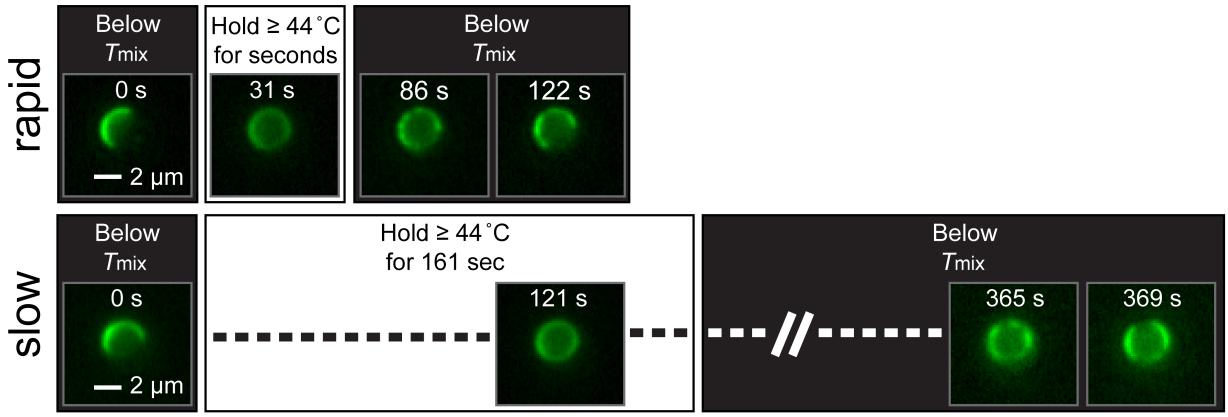

Fig. S11.
Examples of rapid and slow temperature cycling of a vacuole in a single yeast cell. The top line of images shows rapid cycling. Movie S7 corresponds to this top line and plays at 3x speed. The vacuole begins below T_{mix} and has a single large domain. The temperature increases monotonically for ~30 s [~10 s in Movie S7], when the vacuole reaches a temperature above T_{mix} and appears uniform. At 86 s [~28 s in Movie S7], temperature has returned below T_{mix} and domains are visible again. This sequence of images demonstrates that after rapid cycling, domains re-nucleate primarily at the same locations on the surface of the vacuole from which they disappeared, resulting in domain distributions at 122 s [~41 s in Movie S7] similar to the original distribution at 0 seconds.

In the bottom line of images, the same temperature cycle is executed more slowly. Movie S9 corresponds to this bottom line and plays at 3x speed. The vacuole is held above T_{mix} for a time that is sufficiently long (> 2 min) for membrane components to mix more uniformly. As a result, when the temperature is lowered below T_{mix} again, smaller domains nucleate at different locations on the surface of the membrane from which they previously disappeared, as shown in the image at 365 s [~122 s in Movie S9] and at 369 s [123 s in Movie S9]. HILO illumination was used to acquire the images.

These concepts are illustrated again in the GUV in Fig. S11 and Movie S8, which plays at 10x speed.

Figure/Movie	Microscopy Technique	Temperature Conditions	System	Osmotic Gradient
Fig. 1*A,* Fig. S1*A*	Standard epifluorescence	25°C	Synthetic GUV membrane	No
Fig. 1*B*, Fig. S1*B*	"Control" conditions in reference (29)	10°C	Giant plasma membrane vesicle	No
Fig. 1*C*, Fig. S1*C*	Wide-field illumination, iterative deconvolution, and structured illumination	Ambient (~22°C)	*In vivo* yeast vacuole	No
Fig. 2/Movie S1	Iterative deconvolution	Ambient (~22°C)	*In vivo* yeast vacuole	Yes
Fig. 3/Movie S4	HILO illumination	Thermal cycling	*In vivo* yeast vacuole	No
Fig. 4/Movie S6	HILO illumination	Thermal cycling	Cell-free yeast vacuole	No
Fig. S2	Wide-field illumination and differential interference contrast	Ambient (~22°C)	*In vivo* yeast vacuole	No
Fig. S3/Movie S8	Standard epifluorescence	Thermal cycling	Synthetic GUV membrane	No
Fig. S4	Standard epifluorescence (by Joan Bleecker)	Constant temperature	Synthetic GUV membrane	No
Fig. S5*A*, *B*	N/A – sketch of growth protocols			
Fig. S5*C*	N/A – growth curve for yeast strain *MAT α his3Δ1 lys2Δ0 ura3Δ0 leu2Δ0 VPH1-GFP::HIS3MX6*			
Fig. S6*A*/Movie S2	Iterative deconvolution	Ambient (~22°C)	*In vivo* yeast vacuole	Yes
Fig. S6*B*	Wide-field illumination	Ambient (~22°C)	*In vivo* yeast vacuole	Yes
Fig. S7/Movie S3	Iterative deconvolution	Ambient (~22°C)	*In vivo* yeast vacuole	Yes
Fig. S8	N/A – sketch of membrane coexisting phase behavior			
Fig. S9/Movie S5	HILO illumination	Thermal cycling	*In vivo* yeast vacuole	No
Fig. S10/Movie S6 (S10 bottom panel)	HILO illumination	Thermal cycling	Cell-free yeast vacuole	No
Fig. S11/Movies S7 and S9	HILO illumination	Thermal cycling	*In vivo* yeast vacuole	No

Table S1.
A summary of conditions and methods used with each experiment presented in the figures and movies of the main text and this *SI Appendix*.

	Control:	**Sample 1:** Grown at room temp (~22 ˚C)	**Sample 2:** Grown at 30 ˚C	**Sample 3:** Grown with temp. cycle
Trial 1, Plate 1	87	101	77	101
Trial 1, Plate 2	108	97	109	102
Trial 1, Plate 3	99	79	133	85
Trial 1, Plate 4	84	113	110	61
Trial 1, Plate 5	99	105	109	133
Trial 1 Average ± S.D.	**95 ± 10**	**99 ± 13**	**108 ± 20**	**96 ± 26**
Trial 2, Plate 1	110	110	99	122
Trial 2, Plate 2	68	101	85	119
Trial 2, Plate 3	111	99	106	116
Trial 2 Average ± S.D.	**96 ± 25**	**103 ± 6**	**97 ± 11**	**119 ± 3**

Table S2.

Cell viability is unaffected by temperature cycling. A single yeast preculture was grown, diluted to $OD_{600} = 0.50 \pm 0.03$, and then subjected to the protocol in Figure S8*A*. Within experimental uncertainty (which is calculated as standard deviation = S.D.) the average number of colonies in samples 1, 2, and 3 are indistinguishable from the control.

Step	Temp (˚C)	Duration (mm:ss)
1	25	15:00
2	45	0:01
3	35	0:01
4	32.6	0:01
5	31.1	0:01
6	30.4	0:01
7	29	0:01
8	28	2:00
9	27	2:00
10	26	2:00
11	25.4	0:01
12	Go to step 2, twice	

Step	Temp (˚C)	Duration (mm:ss)
13	42.5	0:01
14	41.6	0:19
15	44.1	0:01
16	35.1	0:01
17	34.1	0:01
18	33.1	0:01
19	32.1	0:01
20	31.1	0:01
21	29.6	2:00
22	28.7	2:00
23	28.2	1:42
24	30.4	0:10

Step	Temp (˚C)	Duration (mm:ss)
25	32.6	0:10
26	34.8	0:10
27	36.9	0:01
28	38	0:10
29	39	0:01
30	35	0:01
31	33.9	0:01
32	32.8	0:01
33	32.1	0:01
34	31	0:10
35	29.9	0:30
36	Go to step 24, twice	

Table S3.

Temperature cycling protocol. Within the cell viability assay illustrated in Fig. S8*A*, the temperature of sample 3 in Table S1 was varied in a MJ Mini Thermal Cycler (BIO-RAD, Hercules, CA) using the protocol in this table. Steps 24-36 mimic the conditions of Fig. 3 in the main text and in Fig. S7. The entire protocol elapses over 57 min, 35 seconds. “Duration” denotes the time for which the particular temperature was held once it was reached, before moving to the next programmed temperature.

Movie S1.
A video of *in vivo* vacuole domains merging and their subsequent rearrangement as shown in Fig. 2. This movie plays at ~10x speed.

Movie S2.
A video of *in vivo* vacuole domains merging and their subsequent rearrangement as shown in Fig. S6*A*. This movie plays at ~30x speed.

Movie S3.
A video of *in vivo* vacuole domains becoming smaller as shown in Fig. S7. The left half corresponds to the top hemisphere of the vacuole and the right half corresponds to the bottom hemisphere. This movie plays at ~30x speed.

Movie S4.
A video of *in vivo* vacuole domains vanishing and reappearing with the temperature cycle shown in Fig. 3 as an inset in a plot of temperature through time. The movie plays at ~3x speed.

Movie S5.
A video of *in vivo* vacuole domains vanishing and reappearing with the temperature cycle shown in Fig. S9 as an inset in a plot of temperature through time. The movie plays at ~3x speed.

Movie S6.
A video of cell-free vacuole domains vanishing and reappearing with the temperature cycle shown in Figs. 4 and S10-bottom. The movie plays at ~3x speed.

Movie S7.
A video of *in vivo* vacuole domains vanishing and reappearing with a rapid heat cycle as shown in Fig. S11-rapid. The movie plays at ~3x speed.

Movie S8.
A video of giant unilamellar vesicle (GUV) domains vanishing and reappearing with fast vs. slow temperature ramps as shown in Fig. S3. The movie plays at ~10x speed.

Movie S9.
A video of *in vivo* vacuole domains vanishing and reappearing with a slow temperature cycle as shown in Fig. S11-slow. The movie plays at ~3x speed.

Chapter 6. TRUE OR FALSE: THE TECHNICAL ANALSYIS OF *MADONNA AND CHILD*

My contributions to this work: I collected all data, some collaboratively while being trained by Dr. Gregory D. Smith and Fiona Beckett at the Indianapolis Museum of Art. I processed all data and I created all figures with contributions from Erica Schuler (who generated the FCIR image for Figure 6.10b) and Fiona Beckett (who color-corrected technical photographs (Figure 6.3a, Figure 6.6, and Figure 6.12a) and instructed me in stitching together X-radiographs (Figure 6.7a)). I wrote the main text as well as the figure captions and translated all relevant literature sources written in French. I collaborated with Anna Stein, who provided curatorial and provenance research as well as Italian translation. This project was conceived and supervised by Dr. Gregory D. Smith. Prof. Sarah L. Keller and Dr. Gregory D. Smith aided in editing figures and text.

6.1 ABSTRACT

The Indianapolis Museum of Art's (IMA) *Madonna and Child* (IMA#51.98) was acquired by its donors as a school of Duccio Trecento Italian panel painting. However, stylistic anomalies and potential red flags in the known provenance led to questions of its authenticity and subsequent reattribution to Icilio Federico Joni, an Italian artist, restorer, and forger active in the first half of the twentieth century. The IMA's *Madonna and Child* is a modern fake, created to convincingly imitate the tempera paintings of Italian masters.

In response to the vogue for medieval Italian paintings and the corresponding lack of interest in modern Italian works, Joni created new pieces made to look old, and delighted in fooling experts with his fraudulent panels. Joni taught other artists the techniques he used and detailed some of his counterfeiting methods in his memoir *Affairs of a Painter*.

As an artist, Joni presents an interesting example of the renewed interest in tempera painting in the 20th century. While many of his contemporaries looked to the past to aid the expression of their modern artistic vision, Joni looked to the present to help him best emulate the artistic vision of the past. When operating as a forger, he leveraged the knowledge of medieval-era techniques he gained while apprenticing in a gilding workshop, studying at the Academy of Fine Arts in Siena, and restoring medieval artworks. Utilizing this strong technical background, he constantly experimented with materials and techniques in service of making credible fakes. Joni had no qualms about dipping into the modern artist's toolbox in order to create works with the appearance of centuries old masterpieces.

The technical analysis of the IMA's *Madonna and Child* provides a case study to understand how a modern imitation of a medieval tempera painting was created. A variety of analytical tools were used, including imaging techniques, pyrolysis gas chromatography/mass

spectrometry (Py-GC-MS), Fourier transform infrared (FTIR) spectroscopy, Raman spectroscopy, X-ray fluorescence (XRF) spectrometry, scanning electron microscopy (SEM) coupled with energy-dispersive X-ray spectroscopy (EDS), chemical staining, and polarized light microscopy (PLM). The data gathered from the IMA's *Madonna and Child* using these methods informs a thorough discussion of the binding medium, the pigments used, and the methods for generating the expected aged appearance. These results are compared to those from technical studies of forgeries by Joni and his students as well as methods Joni documented himself.

6.2 INTRODUCTION

The Indianapolis Museum of Art's (IMA) *Madonna and Child* (IMA#51.98) (Figure 6.1) is a panel painting (Figure 6.2) in the style of the Trecento (14th century) school of Duccio, a Sienese artist, depicting the Virgin and Christ child. It has a thick (7 cm) wood panel support with an engaged frame, gilded background, and the brushwork has the hatching characteristic of egg tempera paintings. The sides and back of the panel are coated in a thick layer of opaque, waxy substance (Figure 6.3). There is a crack running from the top of the panel to the bottom with losses in the engaged frame on either side of this crack. In the damaged area of the frame, the underlying canvas is exposed, revealing a textile with plain weave. *Craquelure* is present across the painting's surface. The *Madonna and Child* was displayed at the IMA as the work of Duccio or one of his followers until its authenticity was questioned in 1992.

Figure 6.1. *Madonna and Child*, tempera and gold leaf on wood panel, 89.9 x 54.0 x 7.0 cm, Indianapolis Museum of Art (IMA) at Newfields, Indianapolis, Indiana, USA, IMA#51.98. Left: The panel alone. Right: The panel in its modern custom frame.

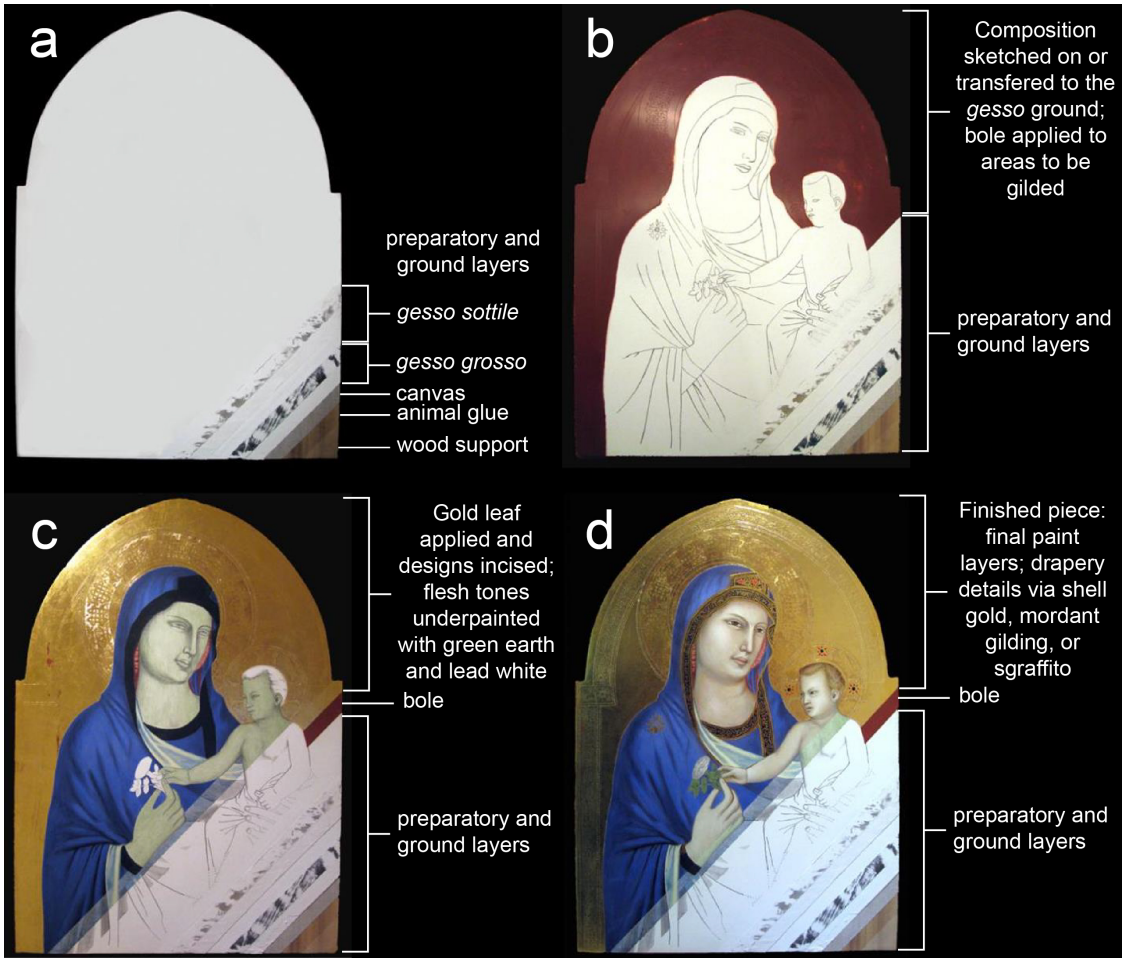

Figure 6.2. The creation process of a medieval Italian tempera panel painting as seen from a reconstruction, which duplicates the materials and methods of the original artist as much as possible, of Giotto di Bondone's c. 1320-1330 *Madonna and Child*. In the lower right-hand corner, the layered structure of the work remains visible in cross-sectional "cut-aways." a) The wood support, commonly poplar, is coated with animal glue and then covered with a canvas. The ground is comprised of gesso, particles of gypsum ($CaSO_4$) bound in animal glue. *Gesso grosso* has larger particles, while *gesso sottile* has smaller particles. After the *grosso* and *sottile* layers are each applied a fine dusting of charcoal is added, then scraped away to ensure a smooth surface. b) The composition is either directly sketched or transferred onto the ground, typically using a carbon-containing material (charcoal or ink). Bole prepares areas for gilding. c) Gold leaf is applied to the bole, and then designs (e.g. halos) are incised and/or punched into the leaf. Flesh tones are underpainted with a mixture of green earth and lead white, bound in egg yolk. This green-hued layer is a key step to building depth. d) The finished artwork. Final paint layers (pigment particles in egg yolk) are applied. Details on the drapery are added using shell gold, mordant gilding, or *sgraffito*. Figure adapted from https://www.artcons.udel.edu/outreach/kress/painting-reconstruction/giotto-di-bondone.

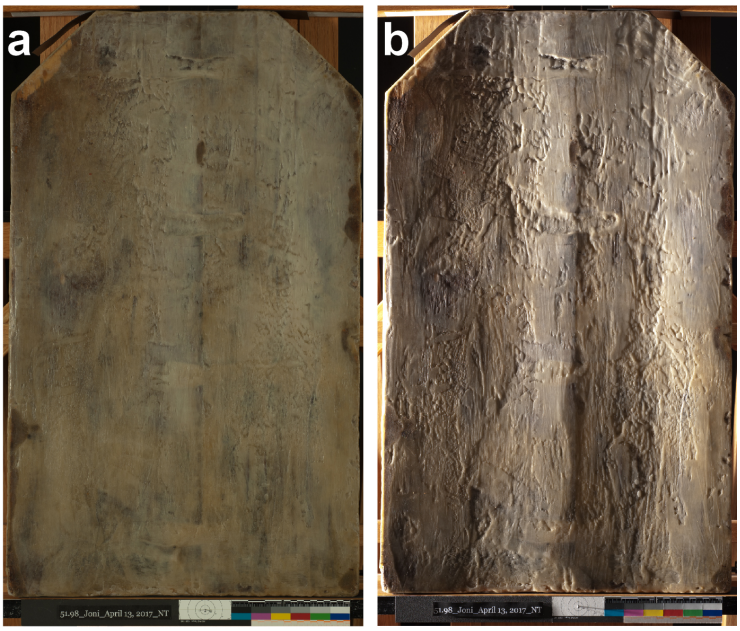

Figure 6.3. Images of the back of the *Madonna and Child* taken with a) diffuse and b) raking illumination.

6.2.1 *Provenance and history of the* Madonna and Child

Mr. and Mrs. Joseph E. Cain, the painting's donors, acquired the *Madonna and Child* on August 5, 1947 from an Italian art firm. The bill of sale describes the artwork as a "Sienese School of the early XIVth Century (from the collection of the Counts Orsini-Baroni, Florence, Italy)." Subsequent to its donation to the museum – at the time the John Herron Art Institute – the initial inspection report from May 16, 1951 indicates that the artwork arrived "well coated with wax," with a "disjoin" in the center as well as many areas of loss in the ground and paint layers including abrasions and "moderate scars." The conservator's report notes both the "prominent crackle" and "marked grime under [the] varnish." The varnish itself is described as "darkened" and "yellowed." The earliest dated visual documentation of the *Madonna and Child* is a black and white photograph reproduced on the cover of *The Bulletin of the Art Association of Indianapolis, Indiana* published in October 1952 (Figure 6.4).

Figure 6.4. Black and white photograph of the *Madonna and Child* reproduced on the cover of *The Bulletin of the Art Association of Indianapolis, Indiana* published in October 1952.[1]

In the same year, Robert O. Parks, curator at the John Herron Art Institute, consulted several art historians regarding the *Madonna and Child*. On May 15, 1952, Dr. Richard Offner wrote "I believe that the panel and some of the surface are original but virtually the whole of it in its present character are modern. I have not tried to remove the panel from the structure in which it was incased [see Figure 6.1, right] and have, therefore, not had the opportunity of examining the wood. I feel fairly sure of the above statement, nevertheless." A transcription from 1975 indicates that on July 26, 1952, Bernard Berenson told Parks: "You could safely catalogue it as Ugolino with a question mark." In a letter dated December 16, 1952, E.P. Richardson – then the director of the Detroit Institute of Arts – wrote that the *Madonna and Child* has a "closer resemblance to the Master of Badia a Isola (especially the gold "comb-like" decorations on the Virgin's robe) than to Meo da Siena or Ugolino di Nerio." It is important to note that of the three

experts, only Offner inspected the artwork in person – both Berenson and Richardson based their assessments on a photograph.

In May 1969, the *Madonna and Child* underwent a major conservation treatment: the varnish was removed, the painting was cleaned, the center vertical crack was repaired with wax, areas of loss were inpainted with plastic paint, and the surface was varnished with B-72. Comparison of Figure 6.1 and Figure 6.4 indicates that no major compositional changes occurred during the 1969 conservation treatment.

Offner's assessment seems to have led to a misapprehension that the *Madonna and Child*'s appearance in 1952 was the result of extensive modern overpaint (i.e. from restoration) that was removed in 1969 as part of a conservation campaign. This misapprehension persisted for decades: in *A Catalogue of European Paintings: Indianapolis Museum of Art* published in 1970, an editor's note about the *Madonna and Child* reads "Recent conservation reveals that the original paint surface, shown in the illustration, was preserved under the restorer's paint mentioned above" and written references to overpaint that had been removed in 1969 continued through the 1990s. However, corroborating the conclusion that no significant overpaint removal occurred in 1969 (as determined by comparing Figure 6.1 and Figure 6.4) is an April 1962 entry in the *Madonna and Child* conservation file, which states that "no major paint restoration [is] evident" based on examination with infrared.

The *Madonna and Child* remained catalogued as a Ducciesque Trecento painting until 1992, when Ronda Kasl joined the IMA and questioned the painting's authenticity. Kasl's consultation with scholars at the National Gallery of Art resulted in the reattribution of the *Madonna and Child* as either a restoration or fake by Icilio Federico Joni.

6.2.2 *Icilio Federico Joni*

Icilio Federico Joni (1866–1946) was an Italian artist, restorer, and forger (Figure 6.5). In his youth, he apprenticed in a gilding workshop before studying at the Fine Arts Academy in Siena.[2] Over the course of his lifetime, he utilized this technical training to create original works of art, restore medieval artworks, and create modern imitations complete with the aged appearance of medieval paintings. At the Fine Arts Academy (*Istituto di Belle Arti*), Joni and his contemporaries learned restoration techniques and "would not have felt any dismay filling the gaps and losses in an ancient painting 'with more or less ability and knowledge of the style of that time and the artist […] masterfully cheating [the artist's] work [so that the viewer] could not distinguish the new from the old.'"[3] Over the course of his technical training, Joni developed a love for the work of medieval Italian artists; the development of his personal artistic passion and talents coincided with a vogue for medieval Italian paintings in prestigious, private collections. Encouraged by local antiquities merchants to contribute an answering supply for the increasing demand for medieval artworks, he created *ex novo* "antique" paintings which began to appear in art markets around 1890.[2] Eventually, Joni essentially formed a workshop of his own by training other artists to employ his techniques for creating medieval-style paintings, including mimicking the expected aged appearance of centuries-old artworks.[4]

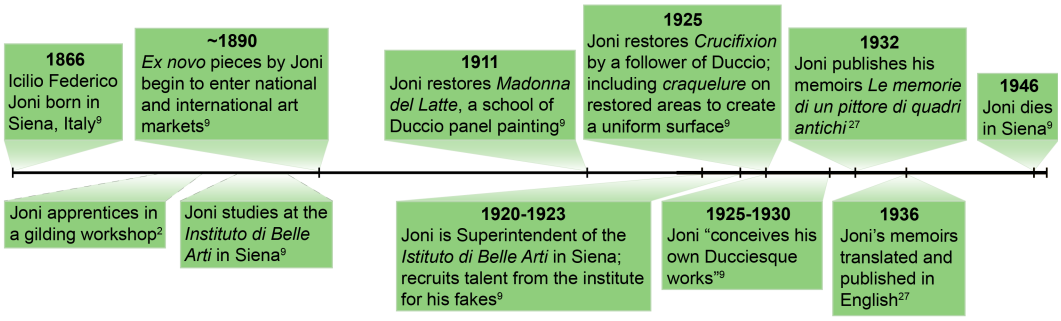

Figure 6.5. Timeline of selected events in Joni's life.

In *L'art d'imiter*, Mauro Natale's discussion of the historical context for Joni's fraudulent endeavors points out the particular cultural and social context in which the forgeries and imitations produced by Joni and his contemporaries were created. In response to the increasing demand from foreign art collectors for ancient paintings, driven in part by "the formation of grand private collections," there was a rapid growth in the production of fakes.[5] Mauro notes that "the fakes emerge as one manifestation of the reaction to the industrialization of the country" and that "it was in the shadow of the [art] academics in Siena and Florence, with their proximity to the antiquarian boutiques and restorers, that the most talented fakers and forgers were born."[5] As noted by Muir *et al.*, this phenomenon of creating new paintings following in ancient styles fits into the Arts and Crafts movement of the time, whose artists looked to the past to aid the expression of their modern artistic vision.[6] For Joni and his fellow Italian forgers, this "pride in local traditions resulted in the creation of a skilled and secret profession," which, combined with the economic demand for these types of paintings, typically from foreigners, resulted in "a punitive spirit directed towards their unwitting clients: the deceived collectors seemed rapacious and the counterfeiter could assume the role of someone righting social wrongs."[5]

6.3 METHODS

6.3.1 *Technical photography*

Visible and ultraviolet-induced visible fluorescence (UVF) images were captured using a Nikon D700 camera under diffuse irradiation conditions with either a daylight fluorescent lamp (4000K, OSRAM Dulux L 2G11) or long wavelength blacklight (NorelcoF40/BLB). UVF imaging used a Kodak Wratten 2E and Peca 918 filter set to limit the spectral sensitivity of the camera sensor. A visible light AIC Photodocumentation color target (Robin Myers Imaging) and a UV fluorescence color standard (UV Innovations) were used to adjust the images for color

accuracy. The X-radiograph of *Madonna and Child* was assembled in Adobe Photoshop from six overlapping plates collected at a distance of 36 inches (91.44 cm) from the X-ray tube, with three-minute exposures at a 28 keV voltage and 3 mA current. The infrared reflectogram was collected using an Opus Instruments Osiris A1 infrared camera with InGaAs array detector operating at a wavelength of 0.9-1.7 μm.

6.3.2 *Cross-section analysis*

Cross-sections of paint layers were prepared by mounting an excised sample in Liquid Bio-Plastic (Ward's Science) mounting medium. The samples were either pre-oriented in the mounts using a drop of fast drying Superglue or placed on a half-cast resin block in a silicon mold before being encased in mounting medium. Once the poured resin had cured fully, the section was polished on Micromesh cloth up to 12,000 grit fineness. Darkfield images of the sectioned samples were acquired on a Zeiss AxioImager M2m compound microscope with a 20X or 50X objective using an MRc5 digital photomicrography camera. The same area was then examined under UV irradiation from an X-cite 120Q mercury vapor lamp source for signs of visible luminescence. A DAPI filter cube set allowed narrowband excitation between 325 and 375 nm with observation throughout the visible spectrum ($\lambda_{em} > 412$ nm).

6.3.3 *Polarized light microscopy (PLM)*

Disperse samples were prepared by dissolving binding media with one drop of dimethylformamide on a glass microscope slide, then a clean coverslip was placed on top and the sample was gently mulled. Images were acquired with plane polarized or cross-polarized light on a Zeiss AxioImager M2m compound microscope with a 40X objective using an MRc5 digital photomicrography camera.

6.3.4 *Fourier transform infrared (FTIR)*

Fourier transform infrared (FTIR) microspectroscopy was performed on a Continuum microscope with an MCT A detector coupled to a Nicolet 6700 spectrometer purged with dry, CO_2-free air. The spectra are the sum of 32–128 coadditions at 4 cm^{-1} spectral resolution. Microsamples were crushed on a diamond compression cell and held on a single diamond window during the analysis. Sample identification was performed using the Infrared and Raman Users Group (IRUG) reference spectral library.

6.3.5 *Raman microspectroscopy*

Raman spectra were acquired using a Bruker Senterra microspectrometer on a Z-axis gantry with a 50X or 100X ultra-long working distance objective. The spectrometer utilizes 3 selectable excitation lasers (532, 633, and 785 nm), an Andor Peltier-cooled CCD detector, and a 50 μm confocal pinhole. Laser power at the sample was generally below 5mW. The spectra are the result of 5-40 sec integrations with 2-30 coadditions. The analysis spot size was on the order of 1 μm, and the spectral resolution was in the range of 9-18 cm^{-1}. OPUS software allowed for automated cosmic spike removal, peak shape correction, and spectral calibration.

6.3.6 *Pyrolysis - gas chromatography – mass spectrometry (PY-GC-MS)*

A small scraping of paint was analyzed by PY-GC-MS. Samples were derivatized on-line using 25 wt% tetramethylammonium hydroxide (TMAH) in methanol from Sigma-Aldrich. The sample was analyzed using a Frontier Lab Py-2020D double-shot pyrolyzer system with a 300 ºC interface to a Thermo Trace gas chromatograph and an ISQ single quadrupole mass spectrometer. A Thermo TG-5MS capillary column (30 m x 0.25 mm x 0.25 μm) was used for the separation with 1 mL/min of He as the carrier gas. The split injector was set to 300 ºC with a

split ratio of 20:1. The GC oven temperature program was 40 ºC for 2 min, ramped to 300 ºC at 20 ºC/min, followed by a 10 min isothermal period. The MS transfer line was at 300 ºC, the source at 230 ºC, and the MS quadrupole at 150 ºC. The mass spectrometer was scanned from 40-600 amu at a rate of 2.59 scans/sec with 3 min solvent delay. The electron multiplier was set to the auto-tune value. Samples were placed into a 50 µL stainless steel Eco-cup, and 3 µL of a 25% methanolic solution of TMAH were introduced for derivatization. After 3 min the cup was placed into the pyrolysis chamber where it was purged with He for 3 min. Samples were pyrolyzed using a single-shot method at 550 ºC for 0.2 min. Sample identification was aided by searching the NIST MS library and by comparison to pyrograms of authentic samples.

6.3.7 *Scanning electron microscopy with energy dispersive spectrometry (SEM-EDS)*

Electron micrographs of cross sections were created using a Zeiss EVO MA15 scanning electron microscope operated in variable pressure mode at 25 Pa of room air. A five segment backscattered electron detector (BSE), a variable pressure secondary electron detector (VPSE), and a Bruker Quantax 200 energy dispersive spectrometer (EDS) were used to acquire images. Electron accelerating voltage was set at 15 keV to ensure generation of X-rays for all heavy metals in the sample while a beam current of 1 nA yielded ~ 6 kcps detector signal with a few percent dead time. A sample working distance of 8.5 mm optimized EDS detection. The SEM was controlled using Zeiss SmartSEM software while the EDS spectra were collected and analyzed using Bruker Esprit 1.9.4 software.

6.3.8 *X-ray fluorescence (XRF) spectrometry*

A Bruker Artax microfocus XRF with rhodium tube, silicon-drift detector, and polycapillary focusing lens (~70 um spot) was used in the analysis. Experimental parameters

included 50 keV tube voltage, 600 μA current, and 60 sec live time acquisitions. A helium purge gas allowed for light element detection. Elemental survey spectra were collected in the region from 0 to 50 keV. Elemental maps was generated by collecting spectra with 40 sec live time acquisitions over a 0.22 mm^2 area using a step size of 0.03 mm and using the escape background correction and Bayes deconvolution available in Bruker's Spectra ARTAX 7.6.0.0 software.

6.3.9 *Microchemical Analysis*

Fluorescent stains were applied dropwise, and then the excess was wiped off. The fluorescein isothiocyanate (FITC) stain used is 0.1 g FITC in 15 mL of anhydrous acetone, imaged with λ_{ex} = 490 nm and λ_{em} = 525 nm. The Rhodamine B (RHOB) stain used is 3 mg in 5 mL of ethanol, imaged with λ_{ex} = 540 nm and λ_{em} = 625 nm.

6.4 Results and Discussion

6.4.1 *Technical Photography*

Raking light brings the large central crack, repaired during the 1969 conservation treatment, into sharp visual relief. The crack coincides with the location where the two planks of the panel meet (see Figure 6.7). The sides and back of the panel are coated in a thick, visually opaque, and highly textured layer of beeswax (Figure 6.3), identified via Fourier transform infrared (FTIR) spectroscopy. Medieval artists sometimes used surface coatings on the back of panel paintings for aesthetic and/or functional reasons (e.g. preventing absorption of moisture or protection against insects); wax is a common historical conservation treatment.[7] In the case of the *Madonna and Child*, it is unclear whether the wax coating, which predates the artwork's donation to the IMA, is purely protective or whether it is meant to obscure any telltale signs of fraudulence.

Figure 6.6. Raking light images: the illumination source is positioned at an acute angle to the painting's a) left and b) right, revealing a large central crack that runs along the length of the painting and four circular deformations protruding from the surface just above the Christ child's proper left foot.

X-radiography (Figure 6.7) reveals that the panel support is comprised of two parallel planks of wood, with the grain running lengthwise along the vertical axis of the painting, as expected for a wooden support prepared in the Middle Ages.[7] These two planks are joined by four butterfly cleats cut so that their grain is perpendicular to the grain of the panel planks (Figure 6.7c), consistent with medieval technique in which cleats were used to align the planks prior to gluing.[7] Two rectangular wooden plugs are held in place with wooden dowels, whose grain appears as bright white in the X-radiograph (Figure 6.7d). Medieval artisans used such plugs to correct defaults in the wood, such as knots or warped areas.[7] Modern hardware, such as metal nails and screws, (Figure 6.7e, f) is present: while the presence of the headless screw is puzzling, the modern nails are located only in damaged or stressed areas of the artwork along the central crack. The engaged frame is held in place by eight nails (Figure 6.7g), which do not appear machine-made due to lack of uniformity in their dimensions in a style (a rectangular

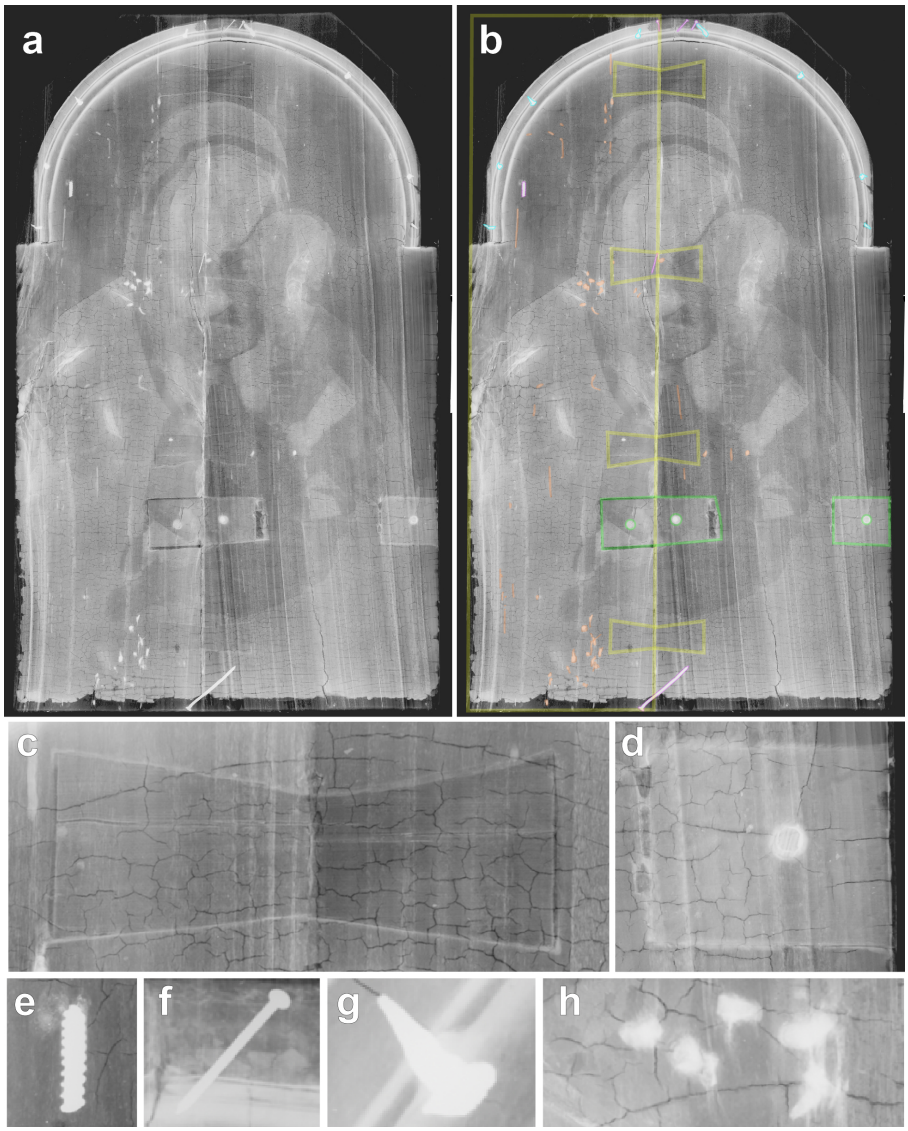

Figure 6.7. a) X-radiograph of IMA #51.98 Madonna and Child. b) X-radiograph with key features outlined. The outline of one of the two parallel planks of wood which comprise the panel as well as the four butterfly cleats which join them are shown in yellow (detail in (c)). Wooden plugs (rectangular) held in place with wooden dowels (circular) are shown outlined in green (detail in (d)). Cyan outlines highlight multiple square-headed nails along the curve of the engaged frame (detail in (g)). Modern nails (detail in (f)), as well as the threaded portion of a modern screw (detail in (e)), are outlined in magenta. Several of the filled woodworm channels are indicated by orange (detail in (h)). c) Detail of one of the butterfly cleats showing its horizontal grain. d) Detail of one of the plugs held in place with a dowel. e) Detail of the threaded portion of a modern screw. f) Detail of one of the modern nails. g) Detail of one of the square-headed nails. h) Detail of the filled-in woodworm channels.

shank narrowing to the tip) consistent with nails of medieval manufacture.[7] Multiple filled woodworm channels (Figure 6.7h) are present.

The construction of the *Madonna and Child*'s wooden support is consistent with medieval manufacture, as the placement of modern hardware indicates that the presence of machine-made nails is likely the result of conservation. In cases where it is clear that worm channels were filled prior to the application of the gesso ground layer, the presence of such channels is incriminating as "it is inconceivable that a medieval craftsman would have used wormy wood"[8] (Figure 6.8, left). This may also be the case with the IMA's *Madonna and Child*, but due to the thickness of the panel support, another scenario is that these worm channels were filled from the back of the panel as part of a conservation effort (Figure 6.8, right). It is not possible to determine which of these two scenarios is correct due to the opaque beeswax coating on the panel.

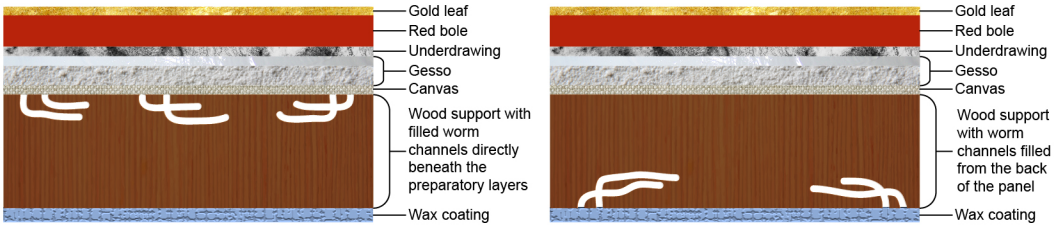

Figure 6.8. Diagrams of possible woodworm channel spatial arrangement within the *Madonna and Child*'s wood support. Left: the channels would have to have been filled prior to the application of the canvas and gesso (the preparatory layers), indicating the damage occurred before the painting's creation. Right: the larvae entered from the back of the panel, likely after the artwork's creation.

While the evident medieval construction of the *Madonna and Child*'s support stands in contrast to that of modern imitations – such as the panel support of the Joni workshop painting *Madonna and Child with Angels* (private collection) which is joined only by glue and lacks cleats or wooden joins of any kind[4] – the period-appropriate panel construction is not proof of the artwork's age. For example, scientific analysis of *Saint Catherine of Alexandria*, a Joni

workshop panel painting in the style of Andrea Vanni, indicates that it is "a Trecento product salvaged and largely altered by a not very scrupulous restorer."[5] In fact, Joni preferred using medieval panel supports for his *ex novo* artworks: a letter he wrote in 1945 describing methods for aging paintings begins with advice to obtain wood that is "very old and well seasoned, and that has an original patina on the back–better, if it's possible, the wood of an old panel."[9]

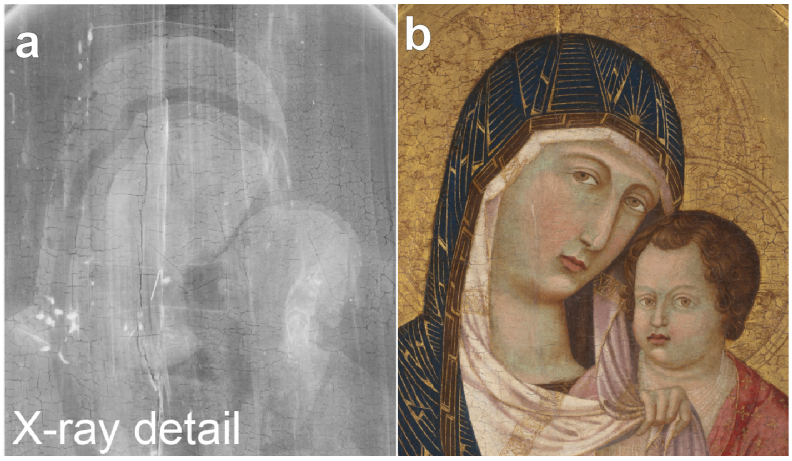

Figure 6.9 *Madonna and Child* a) X-ray detail showing the uniform underpainting of the Virgin and Christ child's faces side-by-side with b) a diffuse light image of the same area.

X-radiography reveals an unusual flesh underpainting technique (Figure 6.9), which is unexpected in a medieval painting but consistent with Joni's methods, as described by Gianni Mazzoni and Alberto Olivetti in "How to fake a Quattrocento painting—or detect the result:"

> X-ray analysis reveals the type of modeling used for flesh tones and highlights, an area in which Joni diverges from fifteenth-century practice. Genuine gold-ground paintings have a warm brown or terracotta green for the half tones, applied very thinly in the half shadows and shadows with pronounced lead white highlights on the cheeks, bridge of nose and upper lip. This creates a pronounced visual luminosity and shows up on the X-ray as strong white. Joni used much more solid underpainting on which the flesh tones would be laid—convincing proof of a recent attempt at fifteenth-century painting.[10]

Rather than white appearing only in select areas to define raised facial features – such as cheeks – as is typical in medieval Italian panel paintings (e.g. Duccio's *The Virgin and Child with Saint Dominic and Saint Aurea, and Patriarchs and Prophets*[11]), the X-radiograph of the IMA's *Madonna and Child* shows white covering the whole area of the subject's faces.

Figure 6.10. a) Infrared reflectogram. b) False-color infrared reflectogram (FCIR).

Infrared reflectography (IRR) imaging shows little to no underdrawing (Figure 6.10a), typically executed in an infrared-active carbon-containing pigment in medieval panel paintings (see Figure 6.11a). Pigment information can be gained by false-coloring the IRR image (FCIR) (Figure 6.10b), in which the IRR image is assigned to the FCIR red channel, the visible green channel is mapped to the FCIR blue channel, and the visible red channel is mapped to the FCIR green channel (Figure 6.11)[12]. The FCIR image indicates that only modern synthetic pigments are present in green-colored areas of flesh, as these areas appear pink/purple in the FCIR.[12]

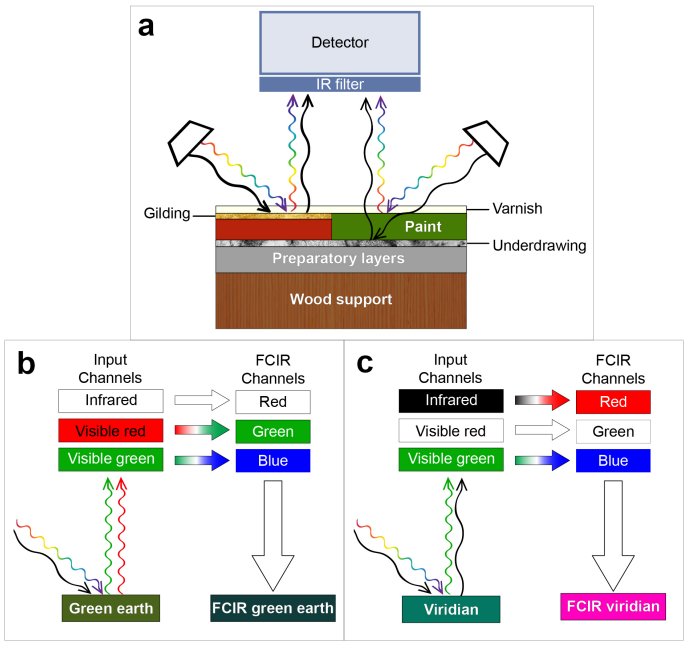

Figure 6.11. a) Diagram of how illumination interacts with the paint and underdrawing layers in IRR. Diagram of how FCIR can be used to distinguish between different pigments such as b) green earth and c) viridian. Figures adapted from reference 12.

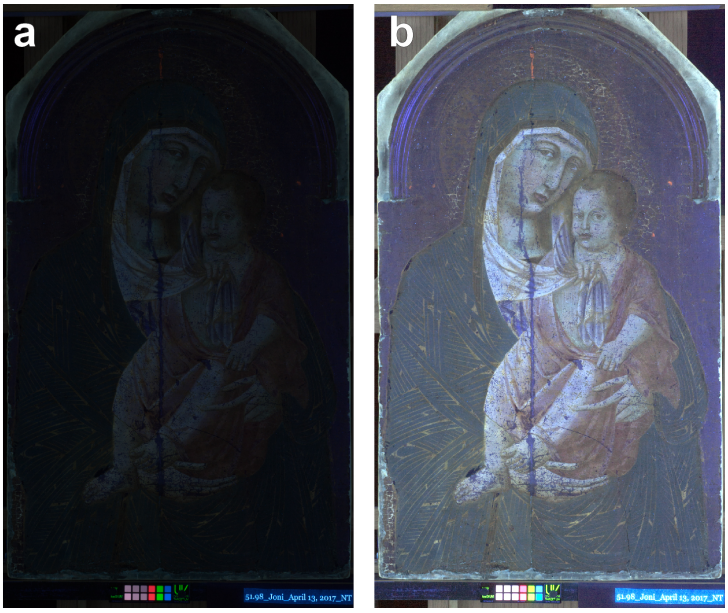

Figure 6.12. a) Ultraviolet fluorescence (UVF) image. b) UVF image in (a), lightened for easier visual readability.

Ultraviolet fluorescence (UVF) imaging (Figure 6.12a, b) clearly shows extensive modern inpainting visible in areas of damage and loss (which appear purple in the UVF images),

such as in the central crack and throughout areas of the Virgin's veil, most likely added during the conservation treatment in 1969. Areas of orange fluorescence in the gilding indicate modern inpainting. UVF indicates that there is no aged natural resin varnish on the painting, as its characteristic green fluorescence is not present, consistent with notes from the 1969 treatment in which the varnish was removed and replaced by B-72, a modern acrylic resin varnish.

6.4.2 *X-ray Fluorescence Spectroscopy (XRF)*

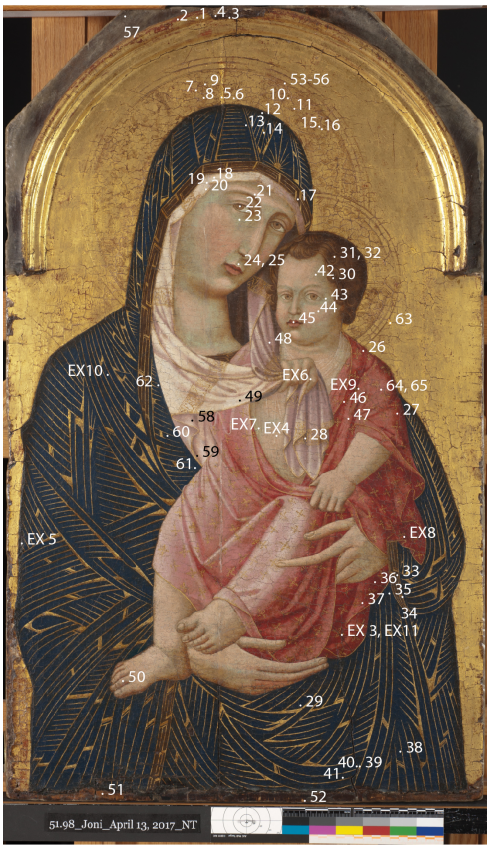

Figure 6.13. Numbered sampling locations are indicated by the dots. Locations with the number preceded by "EX" indicate excised samples. All other sampling locations indicate where X-ray fluorescence (XRF) spectra were collected.

XRF spectra were collected at multiple locations (Figure 6.13). Table 6.1 provides a brief overview of the XRF data, organized by color. There are variations in major, minor, and trace elements between sampling locations of the same color that are not reflected in the table (e.g.

barium is a minor or trace element in most red/pink sampling locations). The presence of titanium and zinc, indicators of modern synthetic pigments such as titanium white (TiO_2) and zinc white (ZnO), throughout the painting are red flags.

Table 6.1. Overview of elements detected by X-ray fluorescence spectrometry (XRF)

Color	Elements
Blue	Fe, Pb, Ti, Zn
Brown	Fe, Pb, Zn
Green	Cr, Fe, Pb, Ti, Zn
Red/Pink	As, Co, Fe, Pb, Ti, Zn
White	Ti, Pb, Zn

6.4.3 *Cross-section sampling*

Cross-section samples (Figure 6.14) were taken from the Christ child's red robe (EX3), the Virgin's blue mantle (EX5), and two areas of flesh (EX4 and EX7) (see Figure 6.13 for sampling locations). The red robe cross-section shows an upper red glaze layer (~15 μm thick) and a thick (~55 μm) pink paint layer on top of the ground, as well as part of an adjacent crack, which has an area in contact with the ground that is light brown color underneath an area which is darker brown. In the blue robe cross-section, gold detailing lies over a single layer of blue paint, which has pigment particles in a variety of colors (blue, brown, green, red, and white) and dimensions. There is little or no ground visible in this cross-section, which was unintentionally mounted slightly off-axis. Like the red robe cross-section, the flesh sample has a thick (~50 μm)

paint layer, directly on top of the ground. This paint layer is primarily white in color, aside from a few green pigment particles. The right side of the flesh cross-section has two thin (< 5 µm) beige paint layers, with a red pigment particle on top.

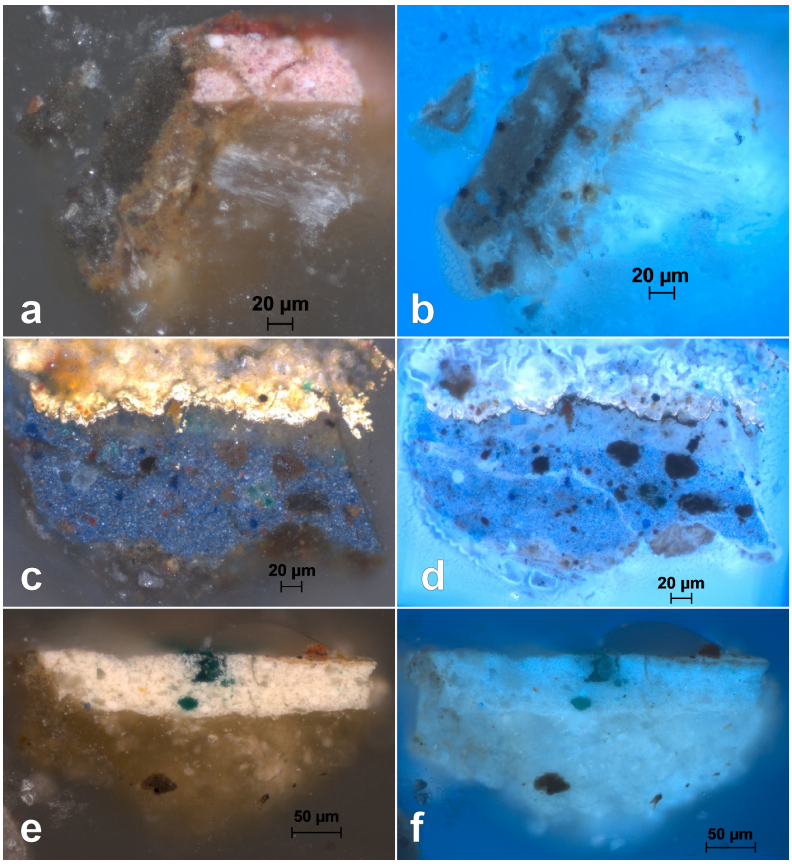

Figure 6.14. Cross-sections micrographs under visible (left column) and UV (right column) from the Christ child's red robe, EX3 (a, b); the Madonna's blue mantle, EX5 (c, d); and a flesh tone, EX7 (e, f). Note that for EX5 (c, d), the cross-section is at an angle.

6.4.4 *Pigment identification*

SEM-EDS on the blue robe cross-section suggests that the blue pigment in the *Madonna and Child* is ultramarine, $(Na,Ca)_8(AlSiO_4)_6(SO_4,S,Cl)_2$ (Figure 6.15a). Optical microscopy with plane polarized light shows small (~2-5 µm), homogenously-sized pigment particles with relatively even color distribution (Figure 6.15b), suggesting synthetic ultramarine.[13] Under cross-polarized illumination (Figure 6.15c), the same particles do not

exhibit the characteristic birefringence of minerals (e.g. diopside) present in lapis lazuli, the natural source of historic ultramarine.[13] Raman spectroscopy (Figure 6.16) confirmed that the blue pigment is synthetic ultramarine: it lacks a characteristic lapis lazuli peak at ~1326 cm^{-1} assigned to diopside and has a peak at ~377 cm^{-1}, which is present in synthetic but not naturally-derived ultramarine.[14] The method to produce artificial ultramarine was discovered in 1826, and the synthetic pigment became commercially available in 1828.[15]

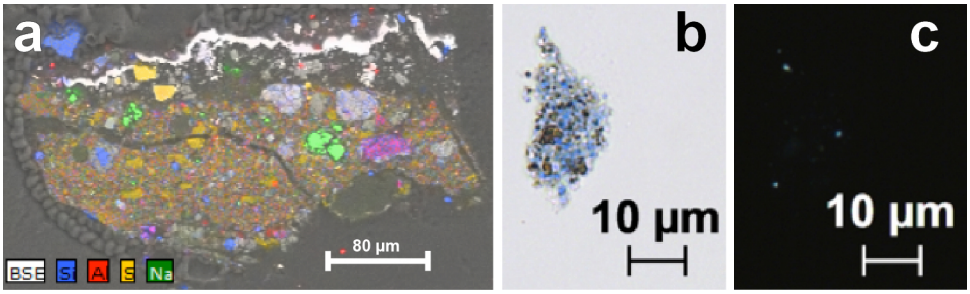

Figure 6.15. a) Elemental map showing Si, Al, S, and Na present throughout the blue layer consistent with ultramarine, a sulfur-containing sodium aluminum silicate. b) Micrograph of pigment particles from the Virgin's blue robe (EX0) under plane polarized light. c) Micrograph of the same pigment particles as (b) under cross-polarized illumination.

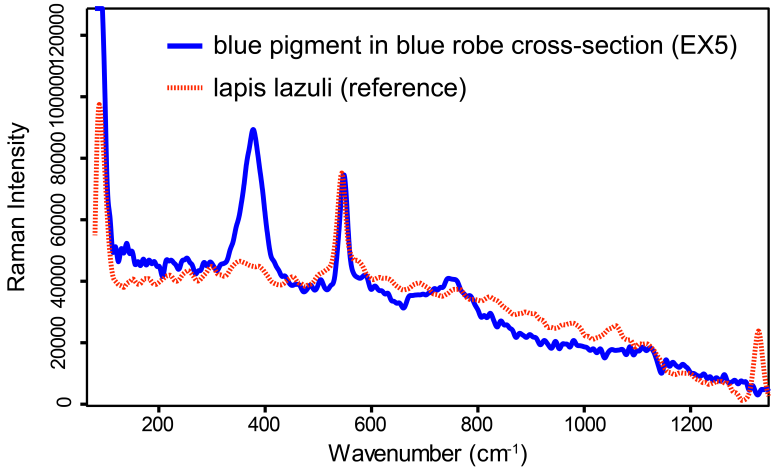

Figure 6.16. Raman spectra (λ_{ex} = 785 nm) showing that the blue pigment from a sample of the Virgin's robe (EX5) lacks the diopside peak of a lapis lazuli reference and has a peak at ~377 cm^{-1} observed in synthetic ultramarine.[14]

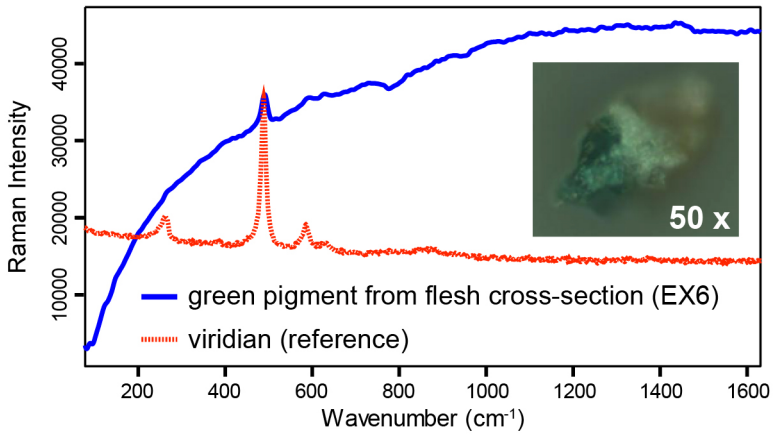

Figure 6.17. Raman spectra (λ_{ex} = 532 nm) showing that a green particle from a flesh sample (inset) has the sharp peak at 487 cm^{-1} characteristic of viridian, $Cr_2O_3 \cdot 2H_2O$.[16]

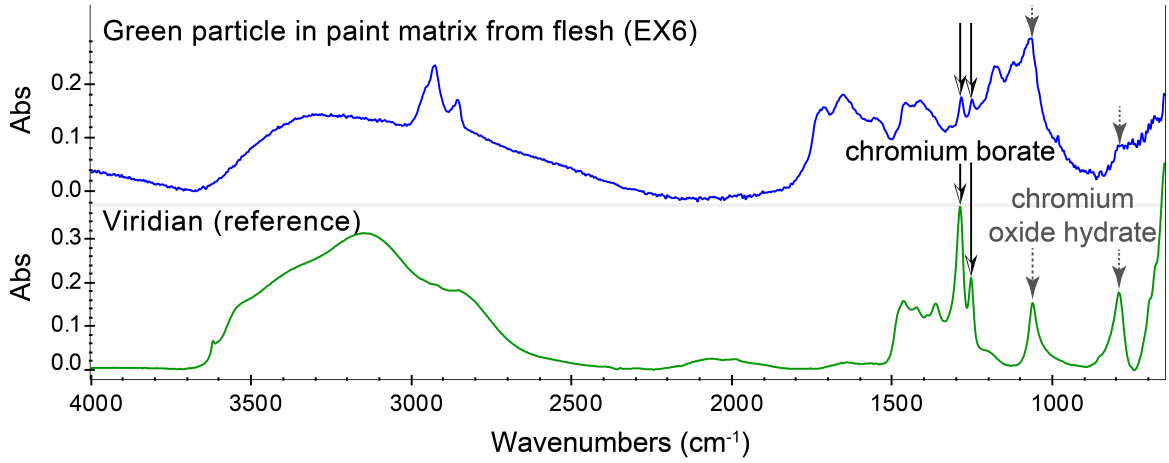

Figure 6.18. FTIR spectra of one of the green particles in the surrounding paint matrix from a flesh sample (EX6), shown in the inset of Figure 6.17 and a reference spectrum for viridian. Peaks attributed to chromium borate and chromium oxide hydrate[16] are marked on both spectra using different arrow styles.

As suggested by FCIR imaging (Figure 6.10) and detection of chromium via XRF (Table 6.1), the green pigment in the *Madonna and Child* contains chromium. Raman (Figure 6.17) and FTIR (Figure 6.18) spectroscopy determined that the chromium-based pigment is viridian, $Cr_2O_3 \cdot 2H_2O$, not chrome oxide green (Cr_2O_3). Per Zumbuehl *et al.*, FTIR peaks at 1288 and 1252 cm^{-1} indicate the presence of chromium borate, a chemical marker for Guignet green, a

type of viridian pigment manufactured using calcination. Zumbuehl *et al.* state that while high amounts of chromium borate are present in pre-World War II viridian, these boron-containing compound peaks are "rarely observed in pigment samples from paintings of the post-war period." The authors note that this shift in viridian composition coincides with the advent of alternative methods for making chromium oxide hydrate.[16]

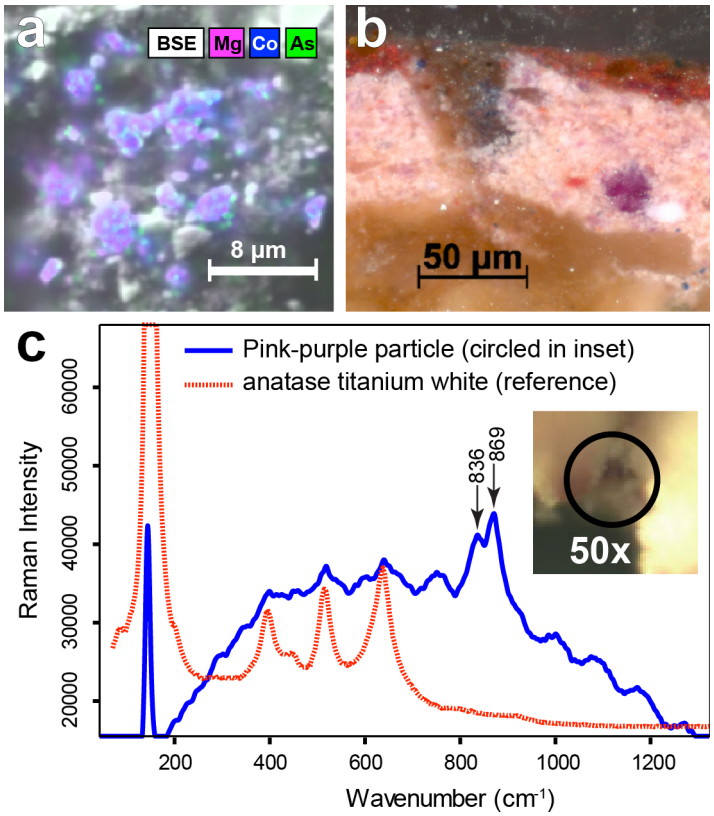

Figure 6.19. a) High magnification (7.08Kx) SEM-EDS of particles within the pink paint layer of EX3 (Figure 6.14a) that contain magnesium, cobalt, and arsenic. b) Visible light micrograph of a large example of one of the pink-purple pigment particles. c) Raman spectrum (λ_{ex} = 633 nm) of one of the pink-purple particles embedded in a paint matrix (inset) which includes titanium white.

XRF results also suggested that a cobalt- and arsenic-containing pigment is present in the red and pink areas of the *Madonna and Child* (Table 6.1). As seen with high-magnification SEM-EDS (Figure 6.19a) particles with a pink-purple appearance (Figure 6.19b) within the pink paint layer of the red robe cross-section (EX3) are comprised of cobalt and arsenic as well as

magnesium. Raman peaks at 836 and 869 cm^{-1} (Figure 6.19c) identify this pigment as a specific formulation of cobalt violet light made up of $Mg_{3-x}Co_x(AsO_4)_2$ and $Mg_3(AsO_4)_2$.[17] The earliest written record of cobalt violet light is from 1855.[18]

Titanium, a marker of modern synthetic pigments, was detected by XRF at every location on the painted surface (Table 6.1); SEM-EDS data from all cross-sections indicate that titanium is present throughout the thickness of the paint layer and not limited to upper layers added during a restoration or conservation campaign (Figure 6.20). Raman spectroscopy (Figure 6.21) identifies the titanium-containing pigment as the anatase form of titanium white (TiO_2). Furthermore, the lack of characteristic peaks for $BaSO_4$ at 987, 460, and 452 cm^{-1} suggests that the titanium white pigment is not one of the early formulations,[19,20] which were composites, the most common being titanium dioxide precipitated onto barium sulfate particles.[21] These composite titanium white pigments remained the only commercially available options until ~1922 at the earliest, following the discovery of an alternative synthetic route in 1920, which yielded pure (96-99%) anatase titanium dioxide pigments.[21]

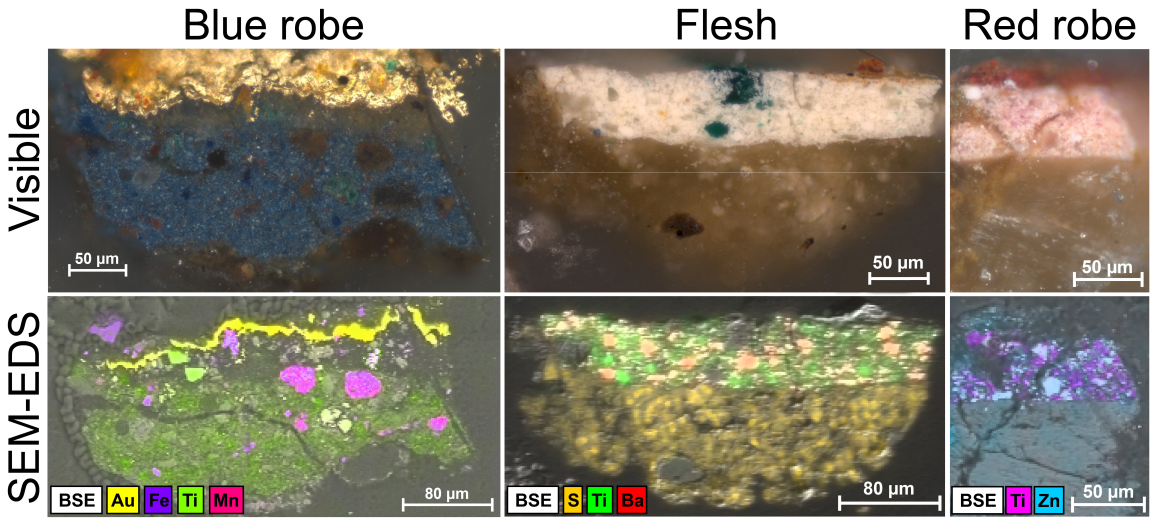

Figure 6.20 EDS data mapping the presence of titanium throughout the thickness of the paint layer in the blue robe, flesh, and red robe.

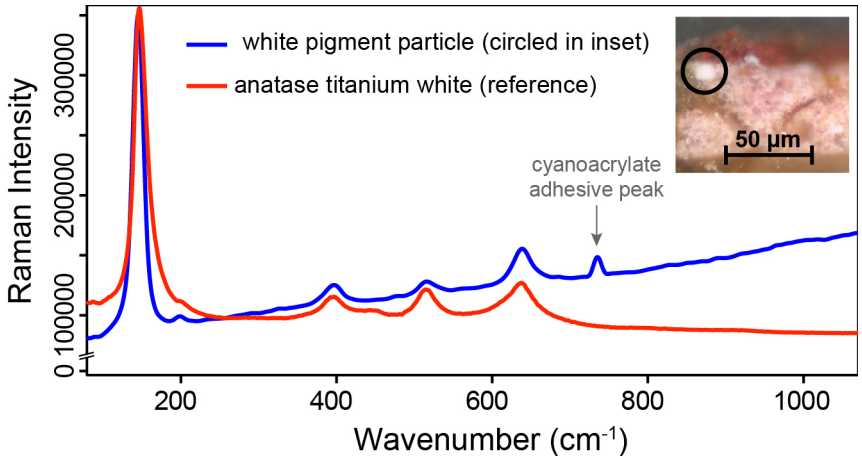

Figure 6.21. Raman spectra (λ_{ex} = 532 nm) of a white pigment particle in the pink paint layer of EX3 (circled in inset) and an anatase titanium white (TiO_2) reference. The peak at 735 cm^{-1} is due to a remnant of cyanoacrylate adhesive left from the cross-section mounting procedure.

None of the pigments discussed above existed prior to the 19th century (Figure 6.22); their presence throughout the entire thickness of the paint layers (rather than only the upper layer or in areas where losses have been filled through inpainting) negates the possibility that they are the result of modern restoration. The widespread use of anatase titanium white, a pigment that was not commercially available until 1918, provides a *terminus post quem* for the *Madonna and Child*. If the lack of barium sulfate peaks in the FTIR spectrum does indicate that the titanium white is not a composite pigment, then the *terminus post quem* may be as late as 1922.

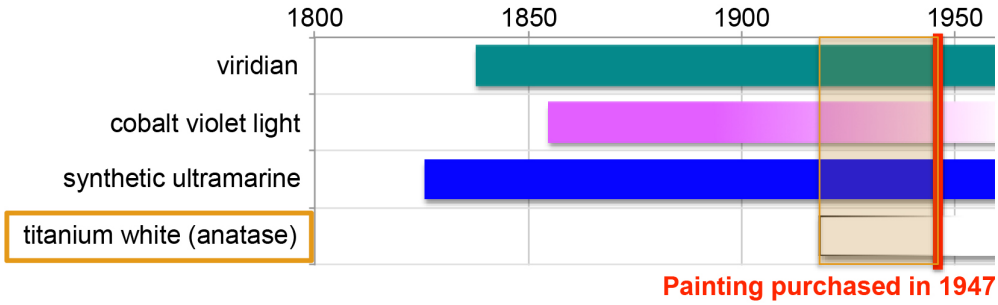

Figure 6.22. Timeline of modern pigments detected in the IMA's *Madonna and Child*, with dates of first use.

6.4.5 *Binding media analysis*

The FTIR spectrum of a disperse ground sample (EX11) extracted with first ethyl acetate and then boiling water, shows that the binding medium is hide glue. Hide glue was the traditional medium used to prepare gesso in 14th century Siena.[22]

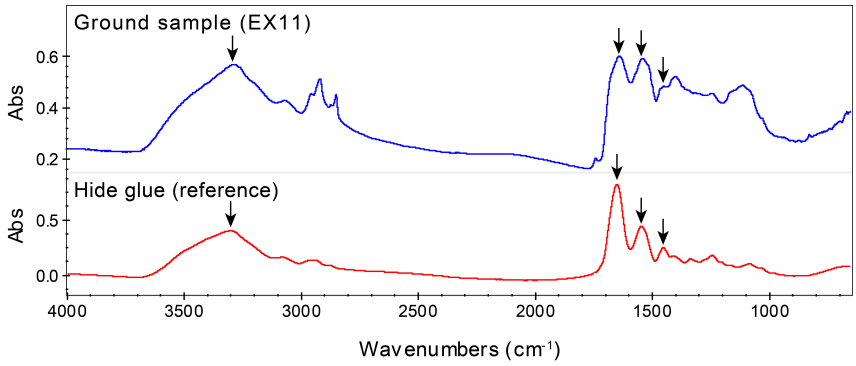

Figure 6.23. FTIR spectra of a disperse ground sample (EX11) binding media extracted with ethyl acetate followed by boiling water (top, blue trace) and a reference spectrum for hide glue (bottom, red trace). Characteristic peaks common to both spectra are marked with arrows.

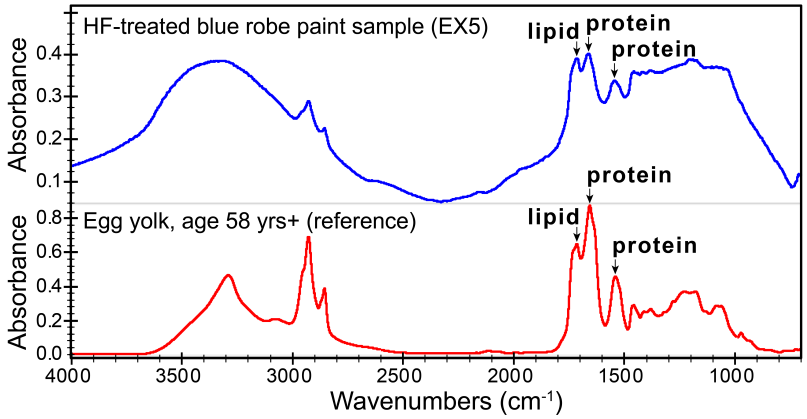

Figure 6.24. FTIR spectra of a sample of the blue paint from the Madonna's blue robe (EX5) treated with hydrofluoric acid (HF) (top trace, blue) and a reference spectrum of aged egg yolk.

The FTIR spectrum of a sample from the blue paint layer, collected from EX5, was treated with hydrofluoric acid to etch away the silicate structure of the ultramarine pigment.[23] Silicates have strong IR absorbance in the same region as the diagnostic lipid and protein peaks for binding media: the lipid ester absorption at 1740 cm^{-1}, indicative of an oil medium, as well as

the Amide I C=O stretch at 1654 cm^{-1} and the Amide II NH bend at 1542 cm^{-1}, which are markers for protein-containing binders, such as egg yolk.[24] While the FTIR spectrum matches a reference for egg yolk aged 58+ years, recent research has suggested that FTIR data is insufficient for identifying the constituents of complex organic binding media.[25]

Fatty acid methyl ester (FAME) ratios of samples from both the red and blue robes (EX9 and 10) were determined by pyrolysis-gas chromatography–mass spectrometry (PY-GC-MS). The ratio palmitic (P) to stearic (S) FAMEs for both samples from the *Madonna and Child* are below the lower bound expected for pure egg tempera, while the azelaic (A) to palmitic ratio exceeds maximum value for pure egg tempera. Typically, drying oils (e.g. linseed oil) have $A/P > 1$, while *tempera grassa* (a mixture of egg and drying oil) has $0.3 < A/P < 1$.[26] Thus, the FAMEs ratios suggest that the paint binder in the *Madonna and Child* is not pure egg yolk, but rather a mixture of containing oil. FAMEs analysis on the Fogg Art Museum's *Crucifixion* in the style of Altichiero (1965.85), a painting sold to the museum donors by Joni, resulted in similar P/S ratios, but much lower A/P values.

Table 6.2. Fatty acid methyl ester ratios determined by pyrolysis-gas chromatography–mass spectrometry (PY-GC-MS). P = palmitic, S = stearic, and A = azelaic.

Sample description	P/S	A/P
Blue paint layer (IMA#51.98)	2.34	0.40
Red paint layer (IMA#51.98)	2.29	0.36
Egg tempera literature values [26]	2.5 – 3.5	< 0.3
Fogg *Crucifixion*, blue paint sample [6]	2.26	0.13
Fogg *Crucifixion*, red paint sample [6]	2.32	0.06

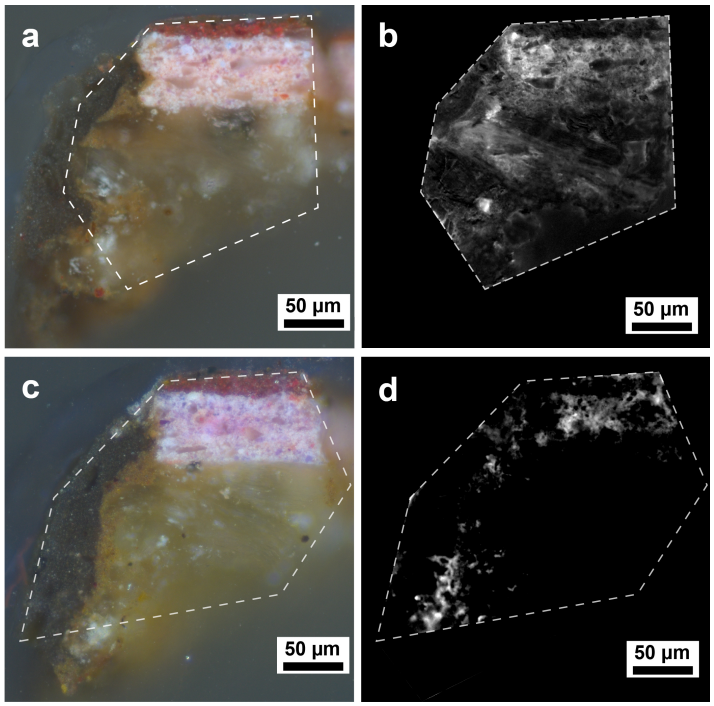

Figure 6.25. a) Micrograph of a cross section from the Christ child's red robe (EX3) under normal, visible illumination prior to fluorescein isothiocyanate (FITC) staining. The paint layer structure shows a thin red glaze top layer over a thick pink layer, which is directly in contact with the *gesso* ground. b) Brightness subtraction image of the cross-section before and after the FITC stain (within the outlined area of interest only). c) Micrograph of the cross section under normal, visible illumination prior to rhodamine B (RHOB) staining. d) Brightness subtraction image of the cross-section before and after the RHOB stain (within the outlined area of interest only).

In order to gain insight into the binding media present in different layers of the painting, the red robe cross-section (EX3) was stained for proteins with fluorescein isothiocyanate (FITC) and for lipids with rhodamine B (RHOB) (Figure 6.25). FITC staining indicates that protein is present in both the paint layers and the gesso, consistent with the expected egg yolk paint binder and a hide glue gesso binder. The protein signal is much stronger in the pink paint layer compared to the upper red glaze layer. RHOB staining suggests that some areas within the pink paint layer as well as the lighter brown (umber) portion of the crack are enriched in lipids. These results are consonant with Joni's *ex novo* painting techniques, including

stretching egg tempera with vinegar[9] and using linseed oil, copal resin and turpentine to fix the painting.[27]

6.4.6 *Evidence of artificial aging*

The *craquelure* has two size scales (Fig. 2a): a larger scale with deep cracks that penetrate into the gesso layer (Fig. 2b) and a smaller scale with shallow cracks limited to the paint layers (Fig. 2c). These two distinct networks are consistent with methods Joni used later in his career to generate *craquelure*: first inducing cracks in the gesso before creating *craquelure* on the painting's surface.[9] Some areas of the painting appear pockmarked due to the presence of dark-colored divots (Fig. 2a, c); similar surface features have been observed in known Joni fakes[8] – possibly air bubbles, generated during heat cycles of accelerated ageing, which burst at the painting's surface.[5] SEM-EDS on a cross-section of one of the deep cracks suggests umber (Fe_2O_3 + MnO_2) is in contact with the gesso layer within the crack (Fig. 2d, e). Joni advised using 'umber powder to remove the white [of the gesso] in case it appears in some small breakdown.'[9] Both SEM-EDS and Raman spectroscopy indicate the crack also contains an animal-derived (phosphorus-containing) black pigment[28] to visually enhance the *craquelure* (Fig. 2f); thus, the dark color of the cracks is not due to accumulated dust, dirt or fireplace soot as might be expected in a naturally aged painting.

XRF mapping (Figure 6.27) indicates that a layer of umber covers the dark-colored divots in the surface, like the deep cracks. Coincident with the location of the divot, titanium – present throughout the paint layers – has its lowest signal; calcium – a marker for the $CaSO_4$ gesso ground – has its highest signal; and iron and manganese – constituents of umber – have their highest signals. These results suggest that the divot contains umber and gesso.

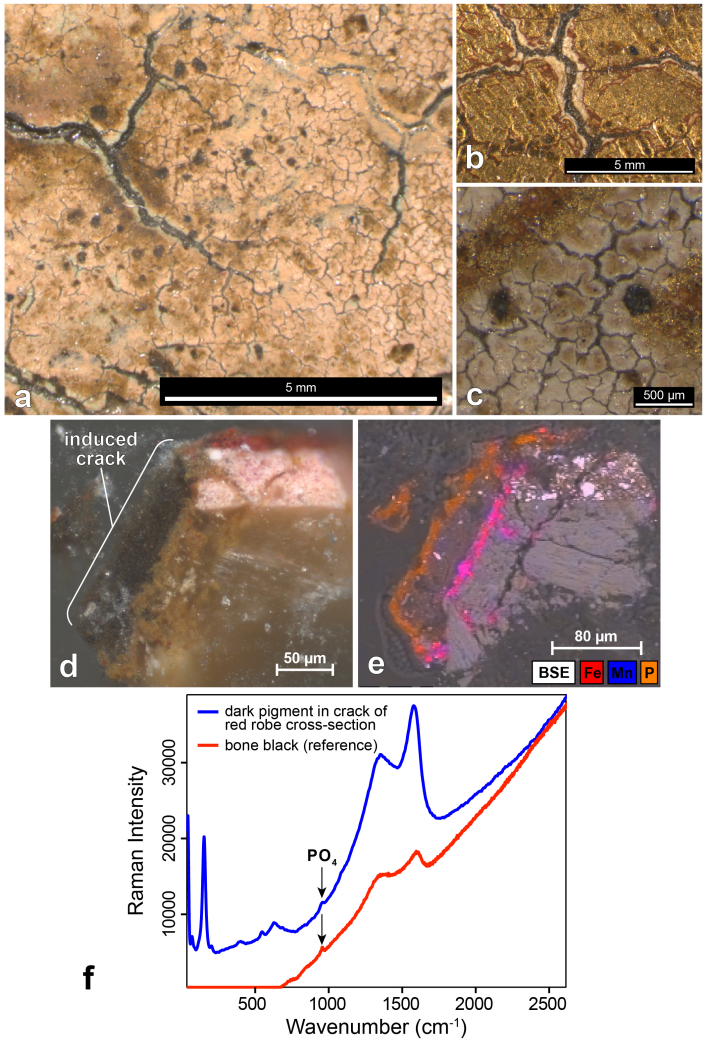

Figure 6.26. Evidence of artificial ageing. a) Detail of the Christ child's proper left toe showing *craquelure* composed of two size scales: a longer length scale that penetrates into the gesso and a shorter length scale limited in depth to the paint layers. Modern paint has been applied across some of the larger cracks, likely during the 1969 conservation treatment at the IMA. Some areas of the painting, particularly the flesh tones, exhibit a high concentration of divots that are dark in color, which give these areas a pockmarked appearance. b) Detail of the incised halo around the Virgin's head showing large scale, deep cracks which penetrate into the gesso. Around the edges of these larger cracks, the leaf and bole have worn away, leaving the ground visible. c) Detail of the Virgin's scarf showing small scale cracks within the paint layer, two examples of the dark-colored divots, and drapery details in gold. d) Micrograph of a cross-section from the Christ child's red robe that includes a large induced crack. e) SEM-EDS data mapping the locations where iron (Fe), manganese (Mn) and phosphorus (P) are detected in the cross-section shown in (d). f) Raman spectra (λ_{ex} = 532 nm) of the outer edge of the induced crack in the cross-section shown in (d) (blue line) and a bone black reference (red line). The arrows point to the phosphate (PO_4) peak.

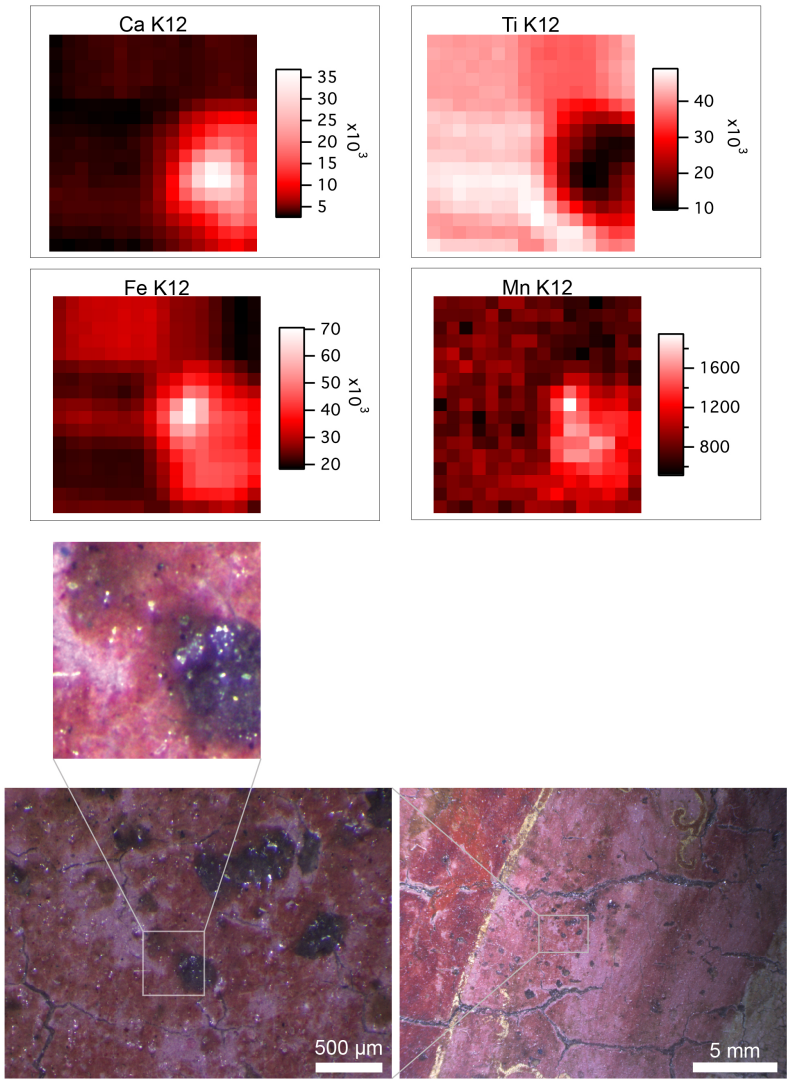

Figure 6.27. XRF maps of calcium (a marker for the gesso ground), titanium (a pigment which is present throughout the paint layer), and iron and manganese, the components of umber. These element maps correspond to the detail of the Christ child's red robe which has one of the dark-colored divots, as seen in the micrographs at bottom.

6.5 Conclusion

While the wood panel support may date to the medieval era, the IMA's *Madonna and Child* is a modern imitation of a Trecento-style painting. In both his memoir and letter from 1945, Joni talks about using pre-existing, medieval panels for his *ex novo* paintings. Widespread

presence of anatase titanium white throughout the paint layer provides 1918 as a *terminus post quem* for the *Madonna and Child*, while the 1947 purchase yields a *terminus ante quem*. This time period closely coincides with Joni's creation of paintings in the same style as the Madonna and Child, which may have begun in 1911 when he restored a painting by Duccio (Figure 6.4). Mazzoni states that Joni "conceived his own Ducciesque works" from 1925-1930. The artwork was purchased only a year after Joni's death. Although Italian artists of the 14th century may have used oils in glazes,[25] staining shows that an underlying paint layer is partially enriched in lipids, consistent with the FAMEs ratios, which indicate a medium other than the pure egg tempera expected of a Trecento panel painting. Due to the difficulty of painting with egg tempera paints, Joni as well as his contemporaries added various substances to improve its workability. Divots in the painting's surface may be an indicator of heat treatment used in accelerated aging. Identification of bone black as the pigment in the deeper network of cracks evinces an intentional visual enhancement. The two size scales of crack networks present in the *craquelure* as well as the umber directly on top of the gesso fit with specific recommendations Joni described in 1945 for simulating the expected appearance of ancient paintings. The idiosyncratic flesh underpainting further suggests the hand of either Joni or a member of his workshop. Although the *Madonna and Child* is a modern fake, it is a well-crafted one. The technical analysis supports the attribution of the artwork to either Joni or his workshop.

6.6 REFERENCES

1. Parks, R. O. Duccesque and Ghirlandaiesque Panel Paintings. *Bull. Art Assoc. Indianapolis, Indiana* **XXXIX,** 22–27 (1952).

2. Mazzoni, G. & Olivetti, A. Entre invention , restauration et vente : la peinture médiévale au début du XXe siècle. *Medievales* **7,** 73–90 (1988).

3. Angelelli, W. Brandi, il restauro antiquario e il falso. in *La teoria del restauro nel Novecento da Riegl a Brandi : atti del Convegno internazionale di Studi* (ed. Andaloro, M.) 239–255 (Nardini Editore, 2006).

4. Passafiume, J. Mystery of the Madonna and Child with Angels. in *AIC Paintings Specialty Group Postprints Volume 20* (ed. Parkin, H. M.) 38–45 (The American Institute for Conservation ofHistoric & Artistic Works, 2008).

5. Natale, M., Schweiz, R. & Schriftsteller, C. *L'Art d'imiter : images de la Renaissance italienne au Musée d'art et d'histoire : falsifications, manipulations, pastiches*. (Ville de Genève, 1997).

6. Muir, K., Khandekar, N., Icilio, F. & Joni, F. The Technical Examination of a Painting that Passed Through the Hands of Sienese Restorer and Forger Icilio Federico Joni. *J. Am. Inst. Conserv.* **45,** 31–49 (2006).

7. Uzielli, L. Historical Overview of Panel-Making Techniques in Central Italy. in *The structural conservation of panel paintings : proceedings of a symposium at the J. Paul Getty Museum, 24–28 April 1995* (eds. Dardes, K. & Rothe, A.) 110–136 (The Getty Conservation Institute, 1995).

8. Frinta, M. S. The Quest for a Restorer ' s Shop of Beguiling Invention : Restorations and Forgeries in Italian Panel Painting. *Art Bull.* **60,** 7–23 (1978).

9. Mazzoni, G. *Quadri antichi del Novecento*. *I colibrì / [Neri Pozza]; Colibrì / Neri Pozza. TA* - (Neri Pozza, 2011)

.

10. Mazzoni, G. & Olivetti, A. Joni, deliberate counterfeiter or creative artist? *The Art Newspaper* **25,** 16–17 (1993)

.

11. Gordon, D. *The Italian Paintings Before 1400*. *National Gallery Catalogues* (Yale University Press, 2011).

12. Cosentino, A. Infrared Technical Photography for Art. *e-Preservation Sci.* **13,** 1–6 (2016).

13. Eastaugh, N., Walsh, V., Chaplin, T. & Siddall, R. *Pigment Compendium: Optical Microscopy of Historical Pigments*. (Elsevier Butterworth-Heinemann, 2004).

14. Schmidt, C. M., Walton, M. S. & Trentelman, K. Characterization of Lapis Lazuli Pigments Using a Multitechnique Analytical Approach: Implications for Identification and Geological Provenancing. *Anal. Chem.* **81,** 8513–8518 (2009).

15. Eastaugh, N., Walsh, V., Chaplin, T. & Siddall, R. *The pigment compendium : a dictionary of historical pigments*. (Elsevier Butterworth-Heinemann, 2004).

16. Zumbuehl, S., Scherrer, N. C., Berger, A. & Eggenberger, U. Early Viridian Pigment Composition Characterization of a (Hydrated) Chromium Oxide Borate Pigment. *Stud. Conserv.* **54,** 149–159 (2009).

17. Casadio, F. *et al.* Pablo Picasso to Jasper Johns: a Raman study of cobalt-based synthetic inorganic pigments. *J. Raman Spectrosc.* **43,** 1761–1771 (2012).

18. Corbeil, M.-C., Charland, J.-P. & Moffatt, E. A. The Characterization of Cobalt Violet Pigments. *Stud. Conserv.* **47,** 237–249 (2002).

19. Brown, S. & Clark, R. J. H. Anatase: Important industrial white pigment and date-marker for artwork. *Spectrochim. Acta - Part A Mol. Biomol. Spectrosc.* **110,** 78–80 (2013).

20. Coupry, C. *et al.* Analyses de pigments blancs appliquées à l'étude chronologique des peintres de chevalet - blanc de titane. in *8th Triennial Meeting, Sydney, Australia, 6-11 September, 1987* 25–32 (1987).

21. Laver, M. Titanium Dioxide Whites. in *Artists' Pigments: A Handbook of Their History and Characteristics* (ed. FitzHugh, E. W.) 295–355 (Oxford University Press, 1997).

22. Duccio de Buoninsegna. in *Techniques of the World's Great Painters* (ed. Januszczak, W.) 14–17 (QED Publishing Limited, 1981).

23. Smith, G. D., Newton, K. E. & Altherr, L. Hydrofluoric acid pre-treatment of matte artists' paints for binding medium analysis by Fourier transform infrared microspectroscopy. *Vib. Spectrosc.* **81,** 46–52 (2015).

24. Meilunas, R. J., Bentsen, J. G. & Steinberg, A. Analysis of Aged Paint Binders by FTIR Spectroscopy. *Stud. Conserv.* **35,** 33 (1990).

25. DeGhetaldi, K. (University of D. From Egg To Oil: The Early Developlement of Oil Painting During the Quattrocento. (University of Delaware, 2016).

26. Colombini, M. P., Andreotti, A., Bonaduce, I., Modugno, F. & Ribechini, E. Analytical Strategies for Characterizing Organic Paint Media Using Gas Chromatography/Mass Spectrometry. *Acc. Chem. Res.* **43,** 715–727 (2010).

27. Joni, I. F. *Le Memoire Di Un Pittore Di Quadri Antichi: A fronte la versione in inglese*. (Protagon: Toscani, 2004).

28. Coccato, A., Jehlicka, J., Moens, L. & Vandenabeele, P. Raman spectroscopy for the investigation of carbon-based black pigments. *J. Raman Spectrosc.* **46,** 1003–1015 (2015).

APPENDIX: U.S. PATENT NO. US8686358 B2 (SUB-MICROSECOND-RESOLUTION PROBE MICROSCOPY)

(12) **United States Patent**
Ginger et al.

(10) **Patent No.: US 8,686,358 B2**
(45) **Date of Patent: Apr. 1, 2014**

(54) **SUB-MICROSECOND-RESOLUTION PROBE MICROSCOPY**

(75) Inventors: **David Ginger**, Seattle, WA (US); **Rajiv Giridharagopal**, Seattle, WA (US); **David Moore**, Seattle, WA (US); **Glennis Rayermann**, Seattle, WA (US); **Obadiah Reid**, Denver, CO (US)

(73) Assignee: **University of Washington through its Center for Commercialization**, Seattle, WA (US)

(*) Notice: Subject to any disclaimer, the term of this patent is extended or adjusted under 35 U.S.C. 154(b) by 254 days.

(21) Appl. No.: **13/232,859**

(22) Filed: **Sep. 14, 2011**

(65) **Prior Publication Data**

US 2012/0079630 A1 Mar. 29, 2012

Related U.S. Application Data

(60) Provisional application No. 61/382,804, filed on Sep. 14, 2010.

(51) **Int. Cl.**
G01Q 10/00 (2010.01)
G01Q 60/24 (2010.01)
G01B 5/28 (2006.01)

(52) **U.S. Cl.**
USPC **250/306**; 250/307; 73/104; 73/105; 850/1; 850/5; 850/8; 850/33; 324/456; 324/458; 324/754.01; 324/754.03

(58) **Field of Classification Search**
USPC 250/306, 307; 850/1, 5, 8, 10, 33, 40, 850/52, 63; 73/104, 105, 504.12, 504.15; 324/456, 458, 537, 676, 681, 683, 324/754.01, 754.03
See application file for complete search history.

(56) **References Cited**

U.S. PATENT DOCUMENTS

5,959,447	A *	9/1999	Bridges et al.	324/755.07
6,133,742	A *	10/2000	Bridges et al.	324/676
7,464,583	B1 *	12/2008	Kowalewski et al.	73/105
7,487,667	B2 *	2/2009	Matsumoto et al.	73/105
7,874,202	B2 *	1/2011	Matsumoto et al.	73/105
8,082,593	B2 *	12/2011	Sarioglu et al.	850/6
2006/0150719	A1 *	7/2006	Reinstadtler et al.	73/105
2007/0113630	A1 *	5/2007	Matsumoto et al.	73/105
2008/0041143	A1 *	2/2008	Sahin et al.	73/105
2009/0145209	A1 *	6/2009	Matsumoto et al.	73/105
2010/0175155	A1 *	7/2010	Sahin	850/6
2011/0041224	A1 *	2/2011	Raman et al.	850/40
2013/0143331	A1 *	6/2013	Ginger et al.	436/174

OTHER PUBLICATIONS

Schade, W., et al., "Spatially Resolved Femtosecond Time Correlation Measurements on a GaAsP Photodiode," Optics Communications 162(4):200-204, Apr. 1999.

Trautman, J.K., and J.J. Macklin, "Time-Resolved Spectroscopy of Single Molecules Using Near-Field and Far-Field Optics," Chemical Physics 205(1-5):221-229, Apr. 1996.

(Continued)

Primary Examiner — Bernard E Souw
(74) *Attorney, Agent, or Firm* — Christensen O'Connor Johnson Kindness PLLC

(57) **ABSTRACT**

Methods and apparatus are provided herein for time-resolved analysis of the effect of a perturbation (e.g., a light or voltage pulse) on a sample. By operating in the time domain, the provided method enables sub-microsecond time-resolved measurement of transient, or time-varying, forces acting on a cantilever.

18 Claims, 27 Drawing Sheets

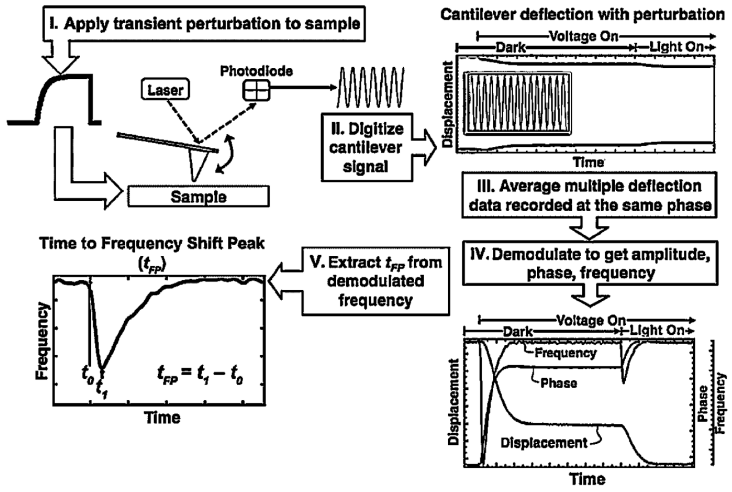

(56) **References Cited**

OTHER PUBLICATIONS

Albrecht, T.R., et al., "Frequency Modulation Detection Using HighQ Cantilevers for Enhanced Force Microscope Sensitivity," Journal of Applied Physics 69(2):668-673, Jan. 1991.

Ando, T., et al., "High-Speed Atomic Force Microscopy for Nano-Visualization of Dynamic Biomolecular Processes," Progress in Surface Science 83(7-9):337-437, Nov. 2008.

Balke, N., et al., "Real Space Mapping of Li-Ion Transport in Amorphous Si Anodes With Nanometer Resolution," Nano Letters 10(9):3420-3425, Sep. 2010.

Belaidi, S., et al., "Electrostatic Forces Acting on the Tip in Atomic Force Microscopy: Modelization and Comparison With Analytic Expressions," Journal of Applied Physics 81(3):1023-1030, Feb. 1997.

Boashash, B., "Estimating and Interpreting the Instantaneous Frequency of a Signal—Part 1: Fundamentals," Proceedings of the IEEE 80(4):520-538, Apr. 1992.

Clarke, T., and J.R. Durrant, "Charge Photogeneration in Organic Solar Cells," Chemical Reviews 110(11):6736-6767, Nov. 2010.

Coffey, D.C., and D.S. Ginger, "Time-Resolved Electrostatic Force Microscopy of Polymer Solar Cells," Nature Materials 5(9):735-740, Sep. 2006.

Coffey, D.C., et al., "Mapping Local Photocurrents in Polymer/Fullerene Solar Cells With Photoconductive Atomic Force Microscopy," Nano Letters 7(3):738-744, Mar. 2007.

Colchero, J., et al., "Resolution Enhancement and Improved Data Interpretation in Electrostatic Force Microscopy," Physical Review B 64(24):245403-1-245403-11, Dec. 2001.

Giridharagopal, R., and D.S. Ginger, "Characterizing Morphology in Bulk Heterojunction Organic Photovoltaic Systems," Journal of Physical Chemistry Letters 1(7):1160-1169, Apr. 2010.

Giridharagopal, R., et al., "New SPM Techniques for Analyzing OPV Materials," Materials Today 13(9):50-56, Sep. 2010.

Hamadani, B.H., et al., "Imaging of Nanoscale Charge Transport in Bulk Heterojunction Solar Cells," Journal of Applied Physics 109(12):124501-1-124501-7, Jun. 2011.

Ho, F., et al., "Ultrafast Voltage-Contrast Scanning Probe Microscopy," Nanotechnology 7(4):385-389, Dec. 1996.

Hosokawa, Y., et al., "Noncontact Estimation of Intercellular Breaking Force Using a Femtosecond Laser Impulse Quantified by Atomic Force Microscopy," Proceedings of the National Academy of Sciences USA (PNAS) 108(5):1777-1782, Feb. 2011.

Jaquith, M., et al., "Time-Resolved Electric Force Microscopy of Charge Trapping in Polycrystalline Pentacene," Journal of Physical Chemistry B Letters 111(27):7711-7714, Jul. 2007.

Jensen, S.E., et al., "Adaptive Control of Force Microscope Cantilever Dynamics," Journal of Applied Physics 102(5):054503-1-054503-7, Sep. 2007.

Kalinin, S.V., and D.A. Bonnell, "Imaging Mechanism of Piezoresponse Force Microscopy of Ferroelectric Surfaces," Physical Review B 65(12):125408-1-125408-11, Mar. 2002.

Kemiktarak, U., et al., "Radio-Frequency Scanning Tunnelling Microscopy," Nature Letters 450(7166):85-89, Nov. 2007.

Loth, S., et al., "Measurement of Fast Electron Spin Relaxation Times With Atomic Resolution," Science 329(5999):1628-1630, Sep. 2010.

Maturová, K., et al., "Scanning Kelvin Probe Microscopy on Bulk Heterojunction Polymer Blends," Advanced Functional Materials 19(9):1379-1386, May 2009.

Moore, A.M., et al., "Real-Time Measurements of Conductance Switching and Motion of Single Oligo(phenylene ethynylene) Molecules," Journal of the American Chemical Society 129(34):10352-10353, Aug. 2007.

Moore, E.W., et al., "Scanned-Probe Detection of Electron Spin Resonance From a Nitroxide Spin Probe," Proceedings of the National Academy of Sciences USA (PNAS) 106(52):22251-22256, Dec. 2009.

Nechay, B.A., et al., "Femtosecond Pump-Probe Near-Field Optical Microscopy," Review of Scientific Instruments 70(6):2758-2764, Jun. 1999.

Pingree, L.S.C., et al., "Imaging the Evolution of Nanoscale Photocurrent Collection and Transport Networks During Annealing of Polythiophene/Fullerene Solar Cells," Nano Letters 9(8):2946-2952, Aug. 2009.

Reid, O.G., et al., "Imaging Local Trap Formation in Conjugated Polymer Solar Cells: A Comparison of Time-Resolved Electrostatic Force Microscopy and Scanning Kelvin Probe Imaging," Journal of Physical Chemistry C 114(48):20672-20677, Dec. 2010.

Reid, O.G., et al., "Nanostructure Determines the Intensity-Dependence of Open-Circuit Voltage in Plastic Solar Cells," Journal of Applied Physics 108(8):084320-1-084320-8, Oct. 2010.

Rousso, I., et al., "Microsecond Atomic Force Sensing of Protein Conformational Dynamics: Implications for the Primary Light-Induced Events in Bacteriorhodopsin," Proceedings of the National Academy of Sciences USA (PNAS) 94(15):7937-7941, Jul. 1997.

Rugar, D., et al., "Single Spin Detection by Magnetic Resonance Force Microscopy," Nature 430(6994):329-332, Jul. 2004.

Sahin, O., et al., "An Atomic Force Microscope Tip Designed to Measure Time-Varying Nanomechanical Forces," Nature Nanotechnology 2(8):507-514, Aug. 2007.

Schade, W., et al., "Spatially Resolved Femtosecond Time Correlation Measurements on a GaAsP Photodiode," Optics Communications 162(4-6):200-204, Apr. 1999.

Shuttle, C.G., et al., "Experimental Determination of the Rate Law for Charge Carrier Decay in a Polythiophene: Fullerene Solar Cell," Applied Physics Letters 92(9):093311-1-093311-3, Mar. 2008.

Stark, M., et al., "Inverting Dynamic Force Microscopy: From Signals to Time-Resolved Interaction Forces," Proceedings of the National Academy of Sciences USA (PNAS) 99(13):8473-8478, Jun. 2002.

Terada, Y., et al., "Real-Space Imaging of Transient Carrier Dynamics by Nanoscale Pump—Probe Microscopy," Nature Photonics 4(12):869-874, Dec. 2010.

Weiss, S., et al., "Ultrafast Scanning Probe Microscopy," Applied Physics Letters 63(18):2567-2569, Nov. 1993.

Yang, X., et al., "Nanoscale Morphology of High-Performance Polymer Solar Cells," Nano Letters 5(4):579-583, Apr. 2005.

Yazdanian, S.M., et al., "Dielectric Fluctuations in Force Microscopy: Noncontact Friction and Frequency Jitter," Journal of Chemical Physics 128(22):224706-1-224706-13, Jun. 2008.

Yazdanian, S.M., et al., "Quantifying Electric Field Gradient Fluctuations Over Polymers Using Ultrasensitive Cantilevers," Nano Letters 9(6):2273-2279, Jun. 2009.

* cited by examiner

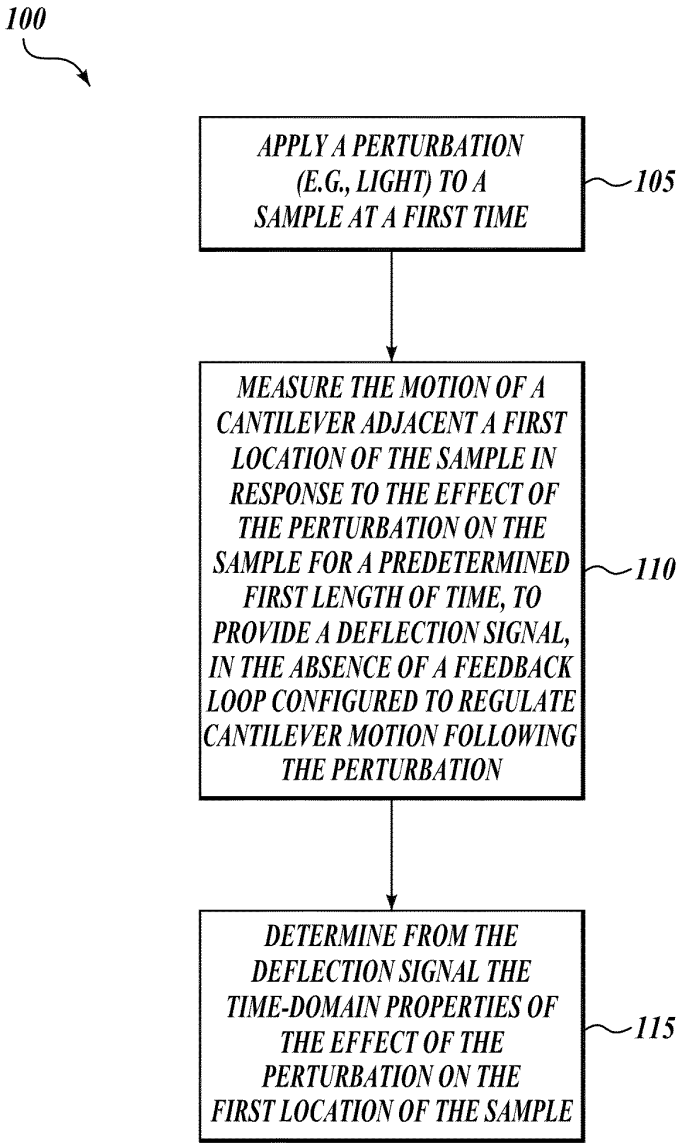
100
APPLY A PERTURBATION (E.G., LIGHT) TO A SAMPLE AT A FIRST TIME
105
MEASURE THE MOTION OF A CANTILEVER ADJACENT A FIRST LOCATION OF THE SAMPLE IN RESPONSE TO THE EFFECT OF THE PERTURBATION ON THE SAMPLE FOR A PREDETERMINED FIRST LENGTH OF TIME, TO PROVIDE A DEFLECTION SIGNAL, IN THE ABSENCE OF A FEEDBACK LOOP CONFIGURED TO REGULATE CANTILEVER MOTION FOLLOWING THE PERTURBATION
110
DETERMINE FROM THE DEFLECTION SIGNAL THE TIME-DOMAIN PROPERTIES OF THE EFFECT OF THE PERTURBATION ON THE FIRST LOCATION OF THE SAMPLE
115

Fig.1A.

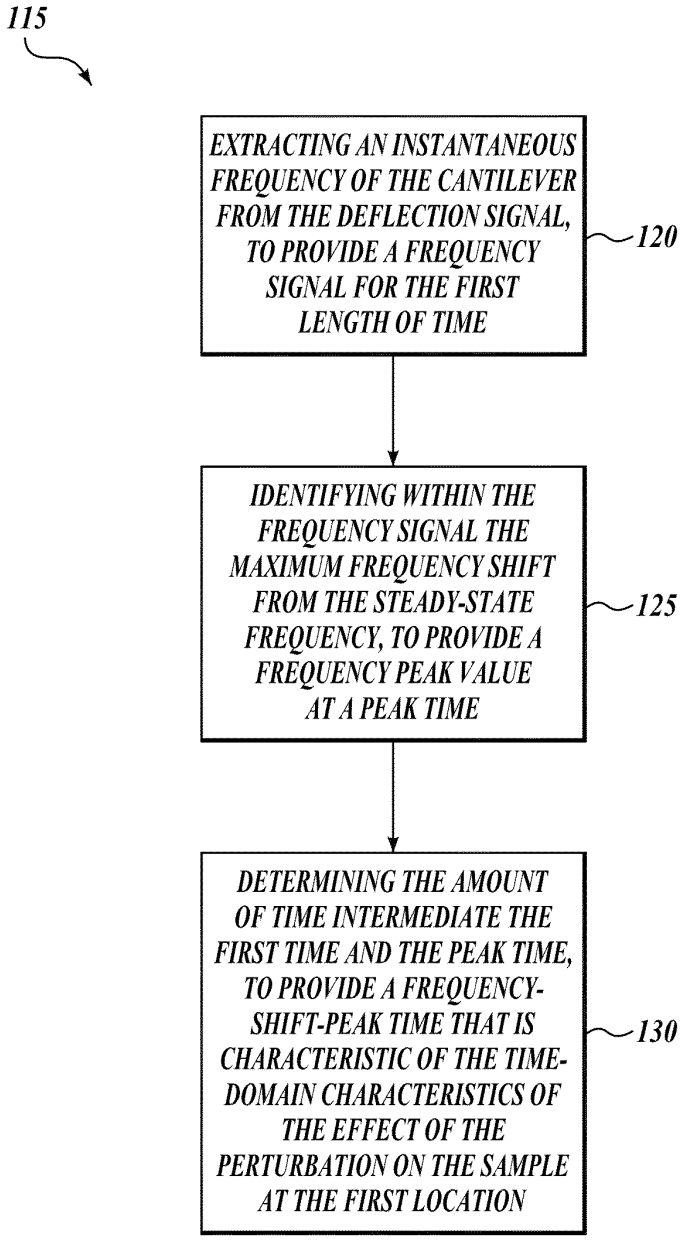
115
EXTRACTING AN INSTANTANEOUS FREQUENCY OF THE CANTILEVER FROM THE DEFLECTION SIGNAL, TO PROVIDE A FREQUENCY SIGNAL FOR THE FIRST LENGTH OF TIME
120
IDENTIFYING WITHIN THE FREQUENCY SIGNAL THE MAXIMUM FREQUENCY SHIFT FROM THE STEADY-STATE FREQUENCY, TO PROVIDE A FREQUENCY PEAK VALUE AT A PEAK TIME
125
DETERMINING THE AMOUNT OF TIME INTERMEDIATE THE FIRST TIME AND THE PEAK TIME, TO PROVIDE A FREQUENCY-SHIFT-PEAK TIME THAT IS CHARACTERISTIC OF THE TIME-DOMAIN CHARACTERISTICS OF THE EFFECT OF THE PERTURBATION ON THE SAMPLE AT THE FIRST LOCATION
130

Fig.1B.

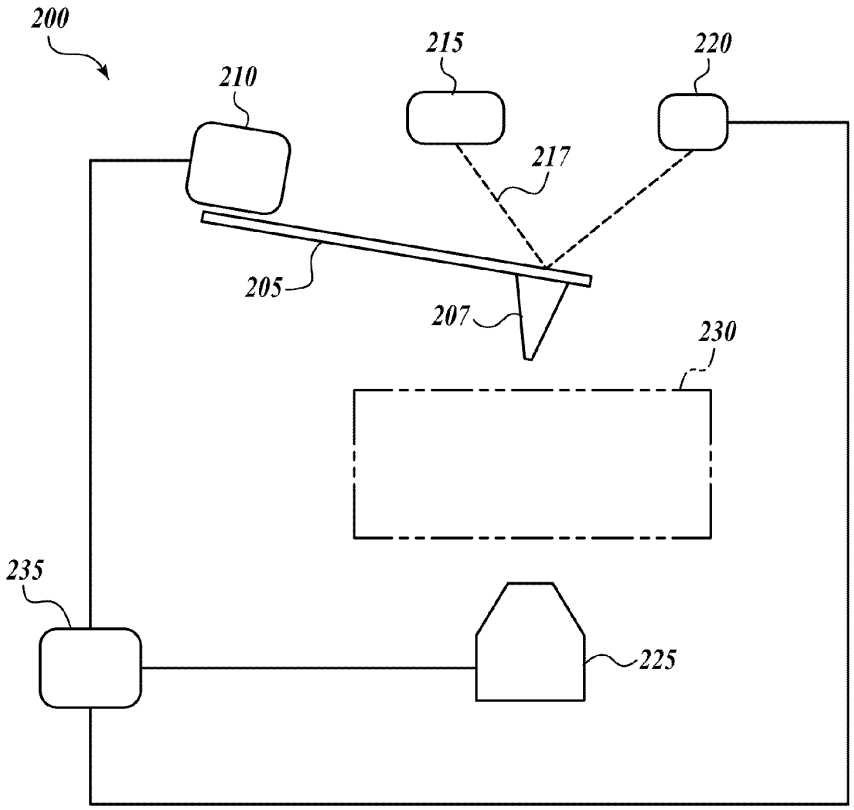

Fig.1C.

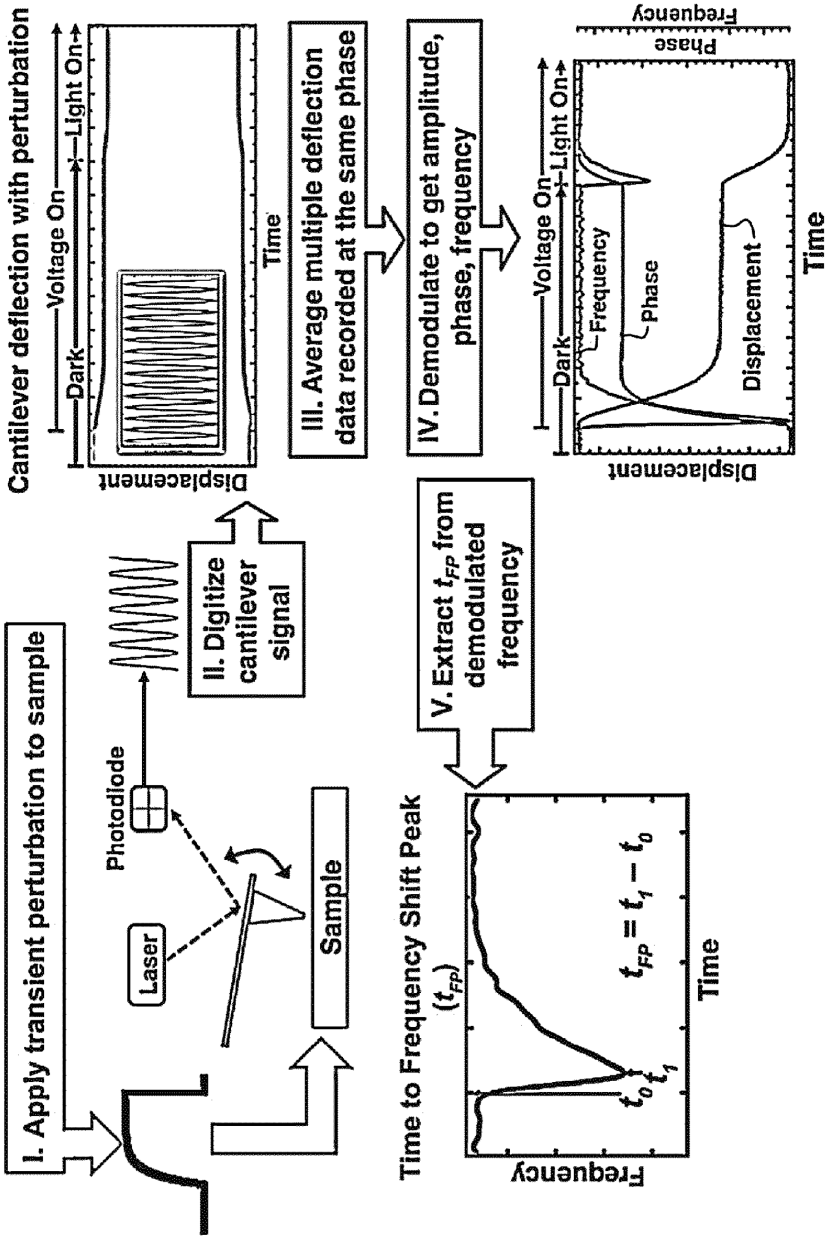
I. Apply transient perturbation to sample
Laser
Photodiode
Sample
II. Digitize cantilever signal
Cantilever deflection with perturbation
Voltage On
Light On
Dark
Displacement
Time
III. Average multiple deflection data recorded at the same phase
IV. Demodulate to get amplitude, phase, frequency
Frequency
Phase
Displacement
Time
V. Extract t_{FP} from demodulated frequency
Time to Frequency Shift Peak (t_{FP})
$t_{FP} = t_1 - t_0$
t_0 t_1
Frequency
Time

Fig. 1D.

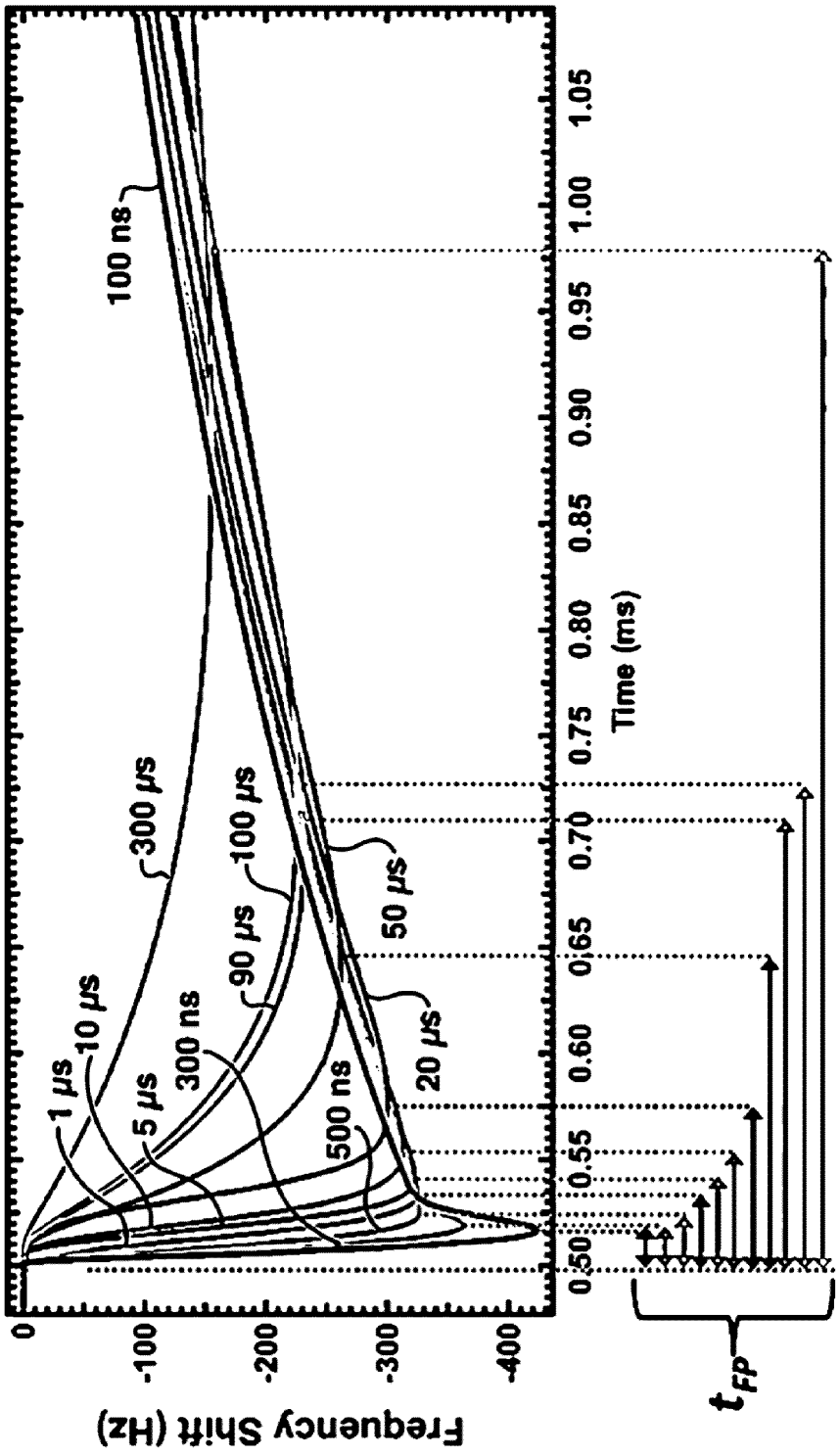
Frequency Shift (Hz)
0
-100
-200
-300
-400
Time (ms)
0.50
0.55
0.60
0.65
0.70
0.75
0.80
0.85
0.90
0.95
1.00
1.05
100 ns
300 µs
100 µs
90 µs
50 µs
20 µs
10 µs
1 µs
5 µs
300 ns
500 ns
t_{FP}

Fig. 1E.

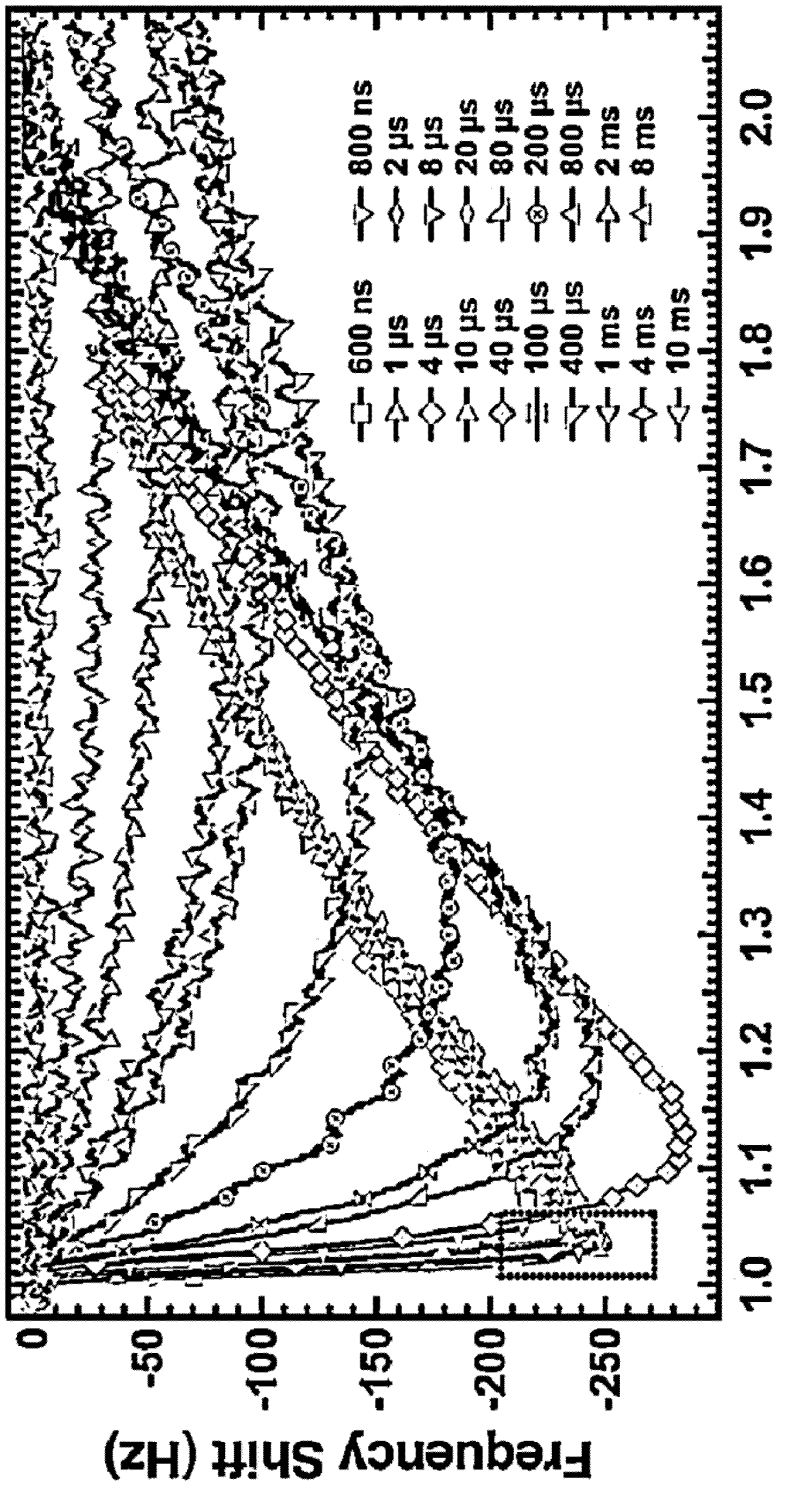
Frequency Shift (Hz)
0
-50
-100
-150
-200
-250
Time (ms)
1.0
1.1
1.2
1.3
1.4
1.5
1.6
1.7
1.8
1.9
2.0
600 ns
1 µs
4 µs
10 µs
40 µs
100 µs
400 µs
1 ms
4 ms
10 ms
800 ns
2 µs
8 µs
20 µs
80 µs
200 µs
800 µs
2 ms
8 ms

Fig. 2A.

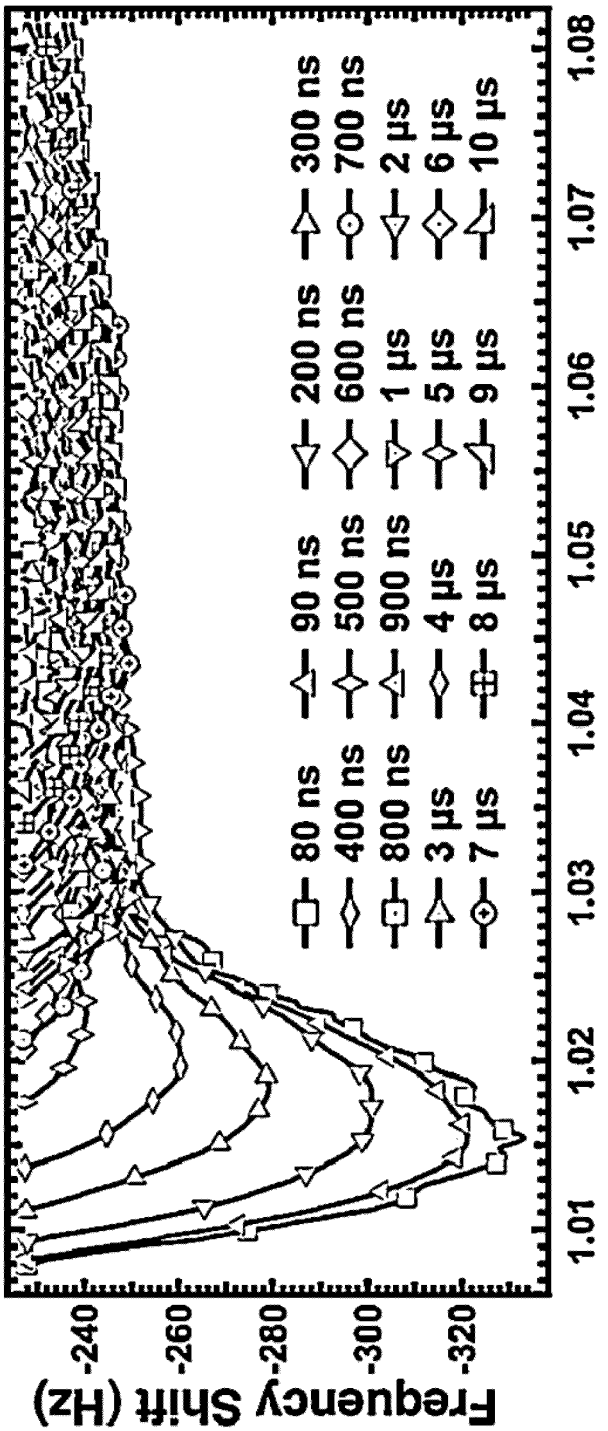
Frequency Shift (Hz)
-240
-260
-280
-300
-320
1.01
1.02
1.03
1.04
1.05
1.06
1.07
1.08
Time (ms)
80 ns
90 ns
200 ns
300 ns
400 ns
500 ns
600 ns
700 ns
800 ns
900 ns
1 µs
2 µs
3 µs
4 µs
5 µs
6 µs
7 µs
8 µs
9 µs
10 µs

Fig. 2B.

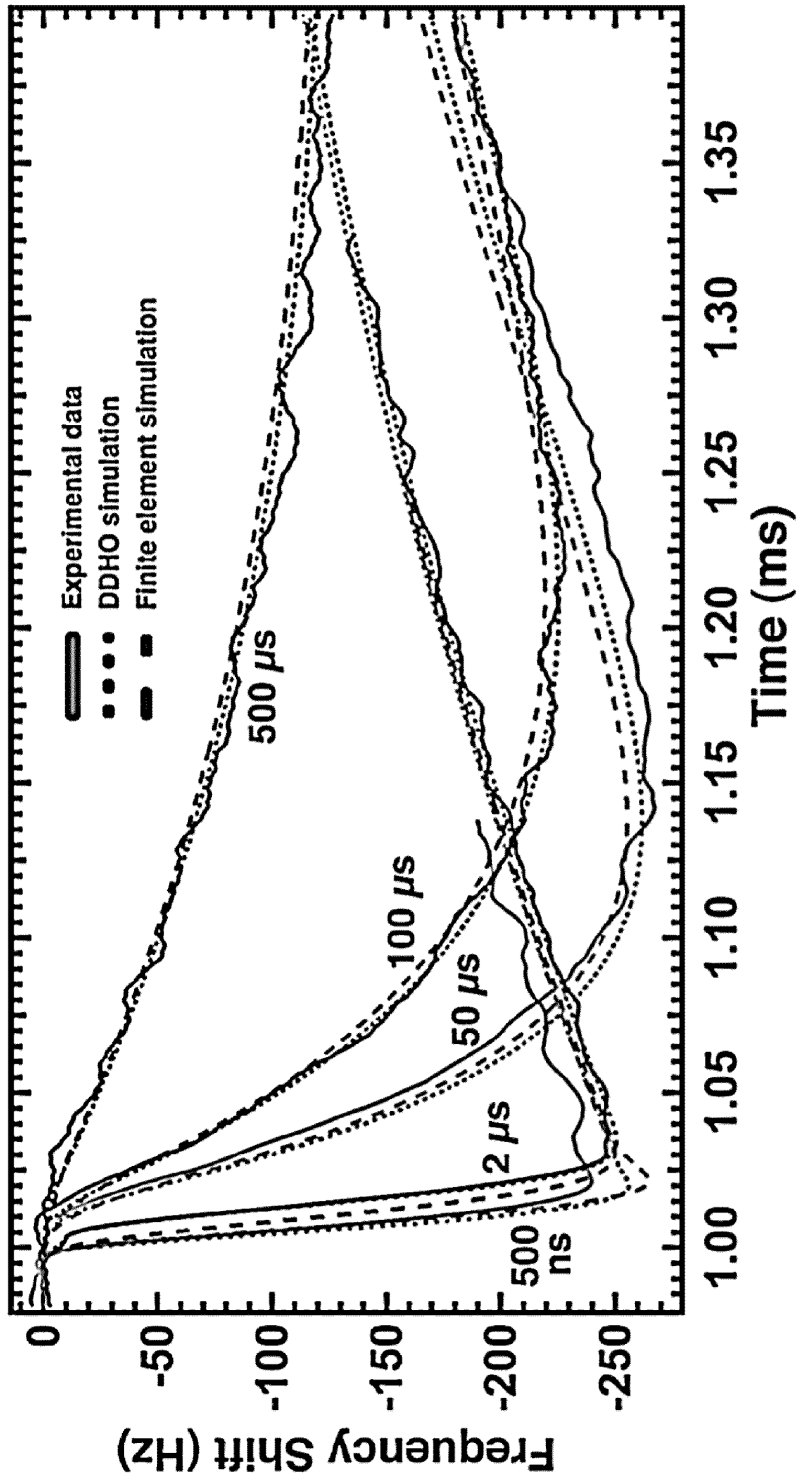
Experimental data
DDHO simulation
Finite element simulation
500 μs
100 μs
50 μs
2 μs
500 ns
Frequency Shift (Hz)
0
-50
-100
-150
-200
-250
1.00
1.05
1.10
1.15
1.20
1.25
1.30
1.35
Time (ms)

Fig.2C.

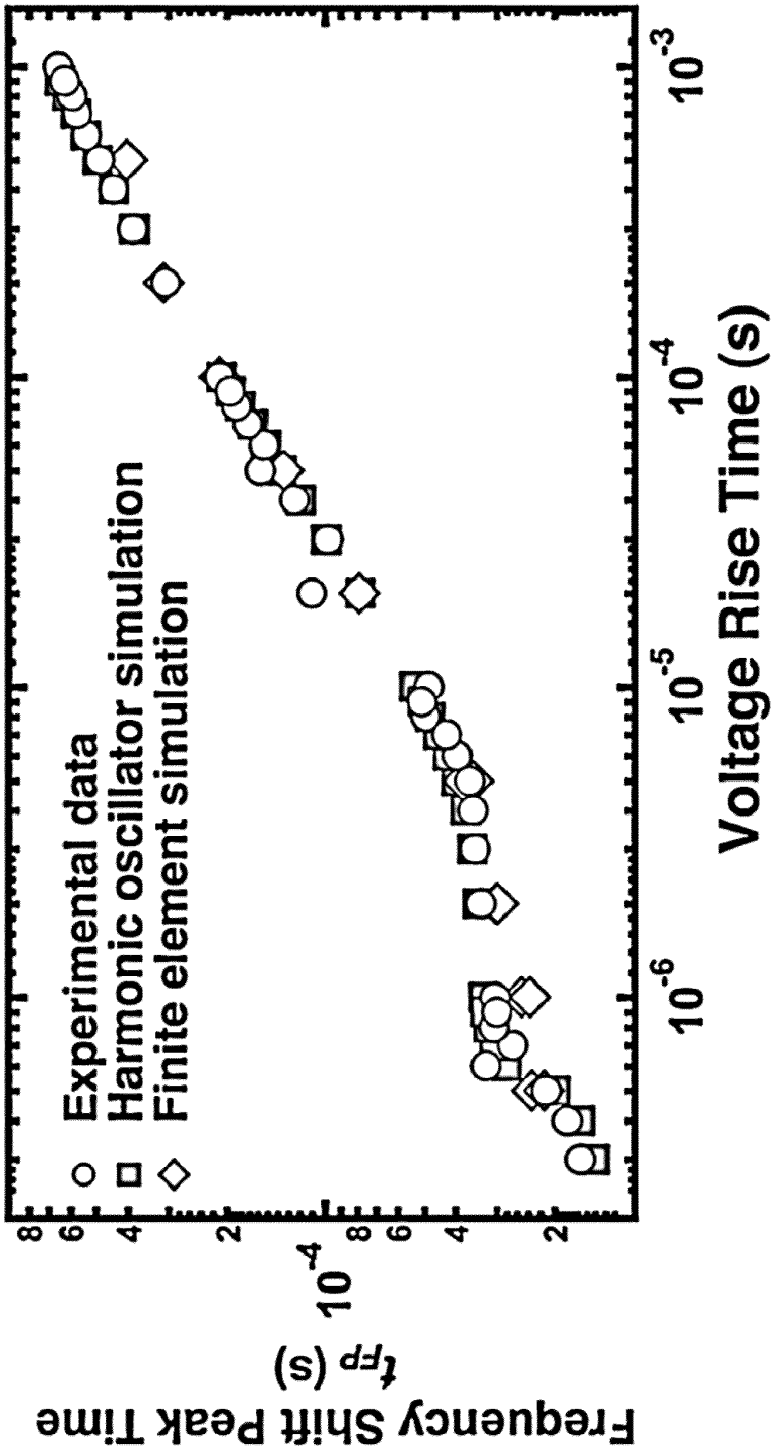
Frequency Shift Peak Time
t_{FP} (s)
10^{-4}
8
6
4
2
8
6
4
2
Experimental data
Harmonic oscillator simulation
Finite element simulation
10^{-6}
10^{-5}
10^{-4}
10^{-3}
Voltage Rise Time (s)

Fig.2D.

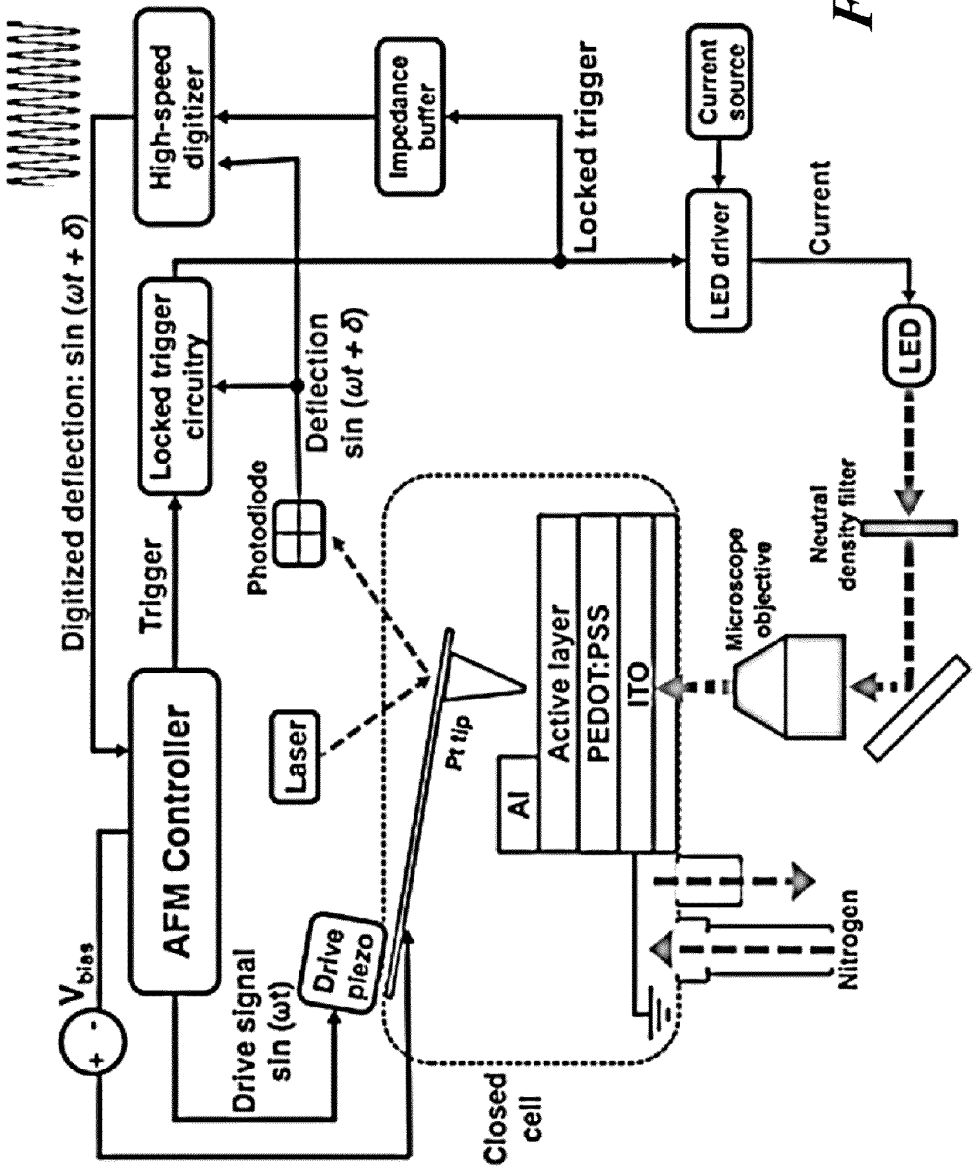
Digitized deflection: sin (ωt + δ)
High-speed digitizer
Impedance buffer
Locked trigger
Current source
LED driver
Current
LED
Trigger
Locked trigger circuitry
Deflection sin (ωt + δ)
Photodiode
Neutral density filter
Microscope objective
Laser
Pt tip
Al
Active layer
PEDOT:PSS
ITO
AFM Controller
Drive signal sin (ωt)
Drive piezo
Nitrogen
Closed cell
V bias

Fig. 3A.

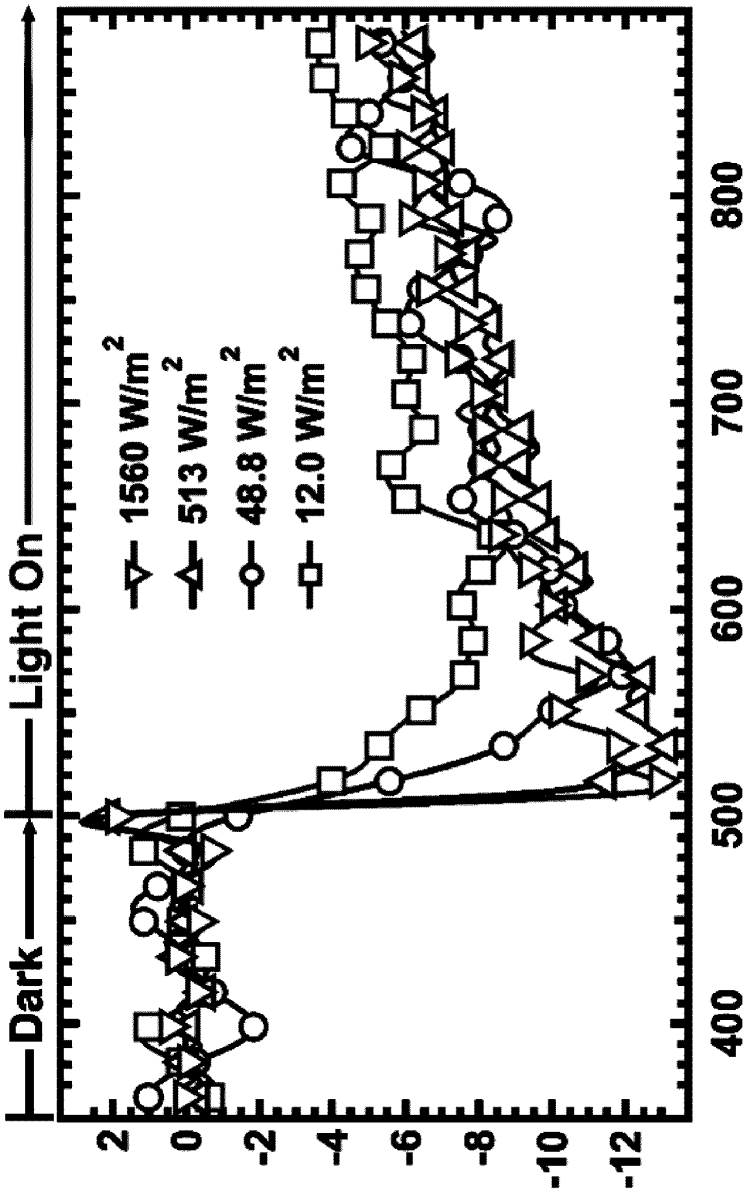
Dark
Light On
1560 W/m2
513 W/m2
48.8 W/m2
12.0 W/m2
2
0
-2
-4
-6
-8
-10
-12
400
500
600
700
800
Time (µs)

Fig.3B.

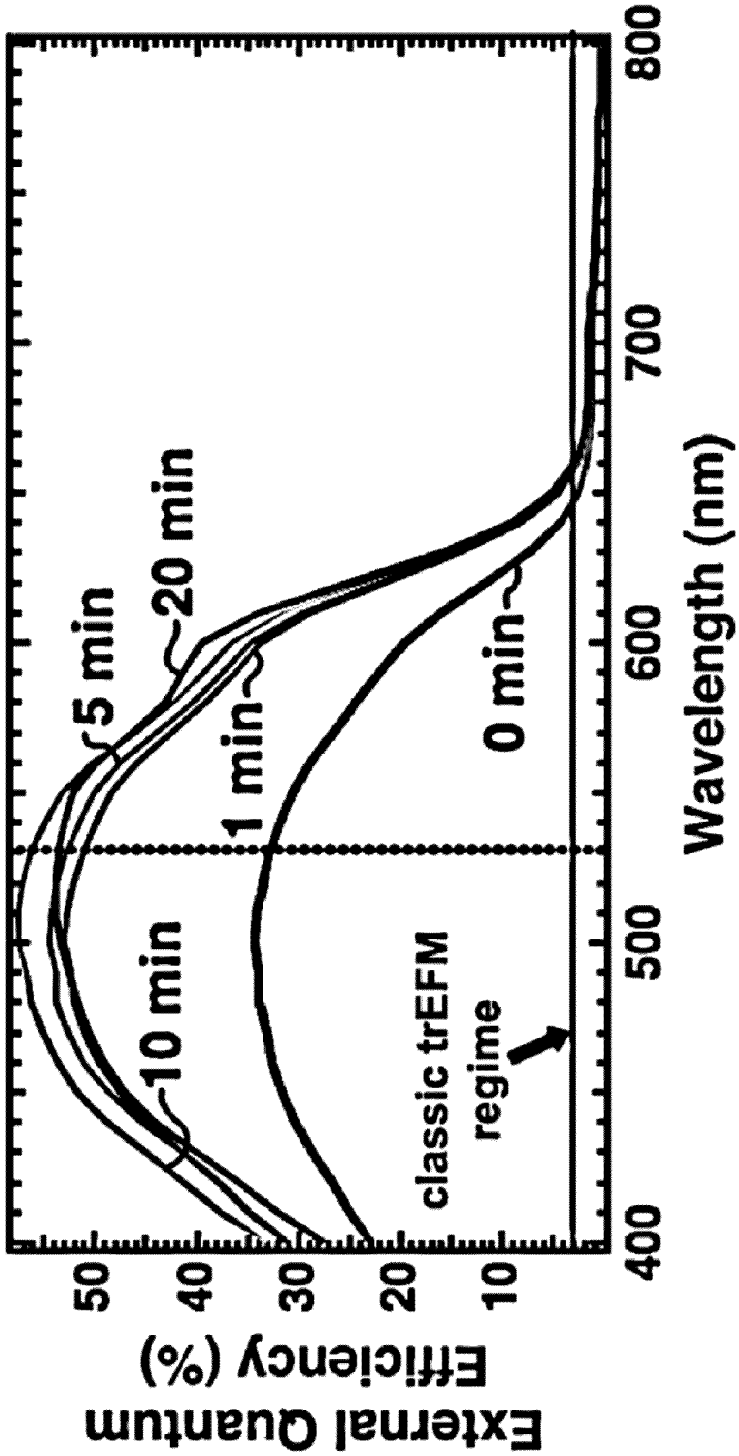
External Quantum Efficiency (%)
50
40
30
20
10
400
500
600
700
800
Wavelength (nm)
0 min
1 min
5 min
20 min
10 min
classic trEFM regime

Fig.3C.

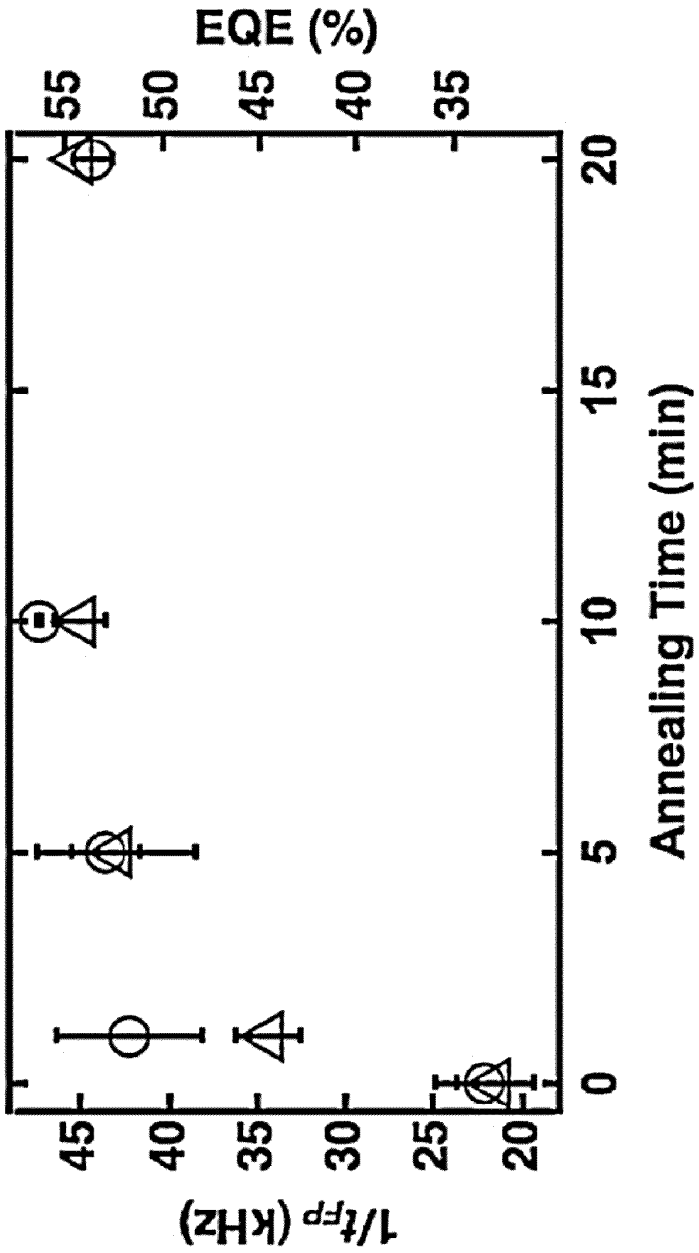
EQE (%)
55
50
45
40
35
20
15
10
5
0
Annealing Time (min)
45
40
35
30
25
20
1/t_FP (kHz)

Fig.3D.

Topography

Fig.3E.

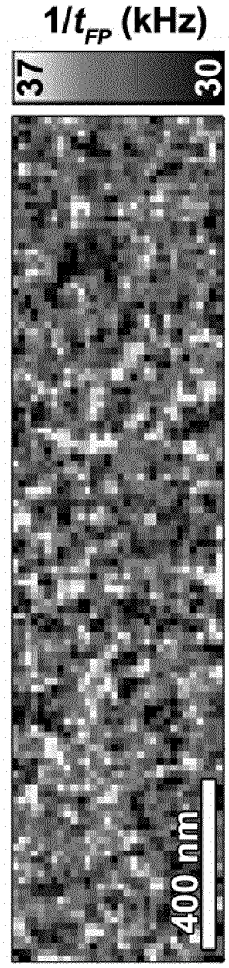

FF-trEFM

Fig.3F.

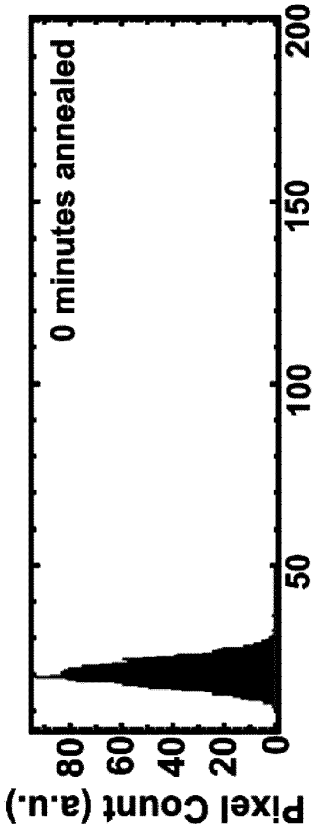
0 minutes annealed
Pixel Count (a.u.)
0
20
40
60
80
50
100
150
200
1/t_{FP} (kHz)

Fig.3G.

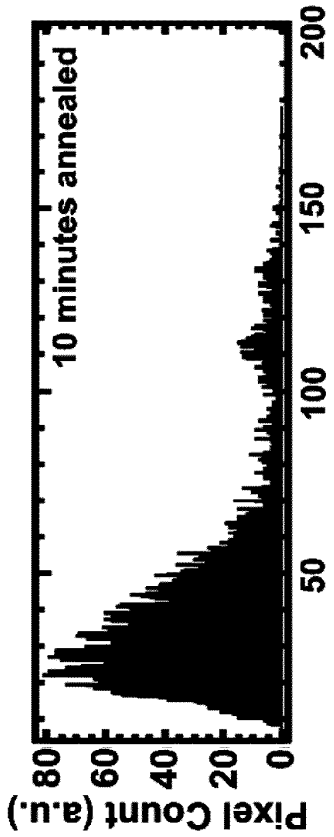
10 minutes annealed
Pixel Count (a.u.)
0
20
40
60
80
50
100
150
200
1/t_{FP} (kHz)

Fig.3H.

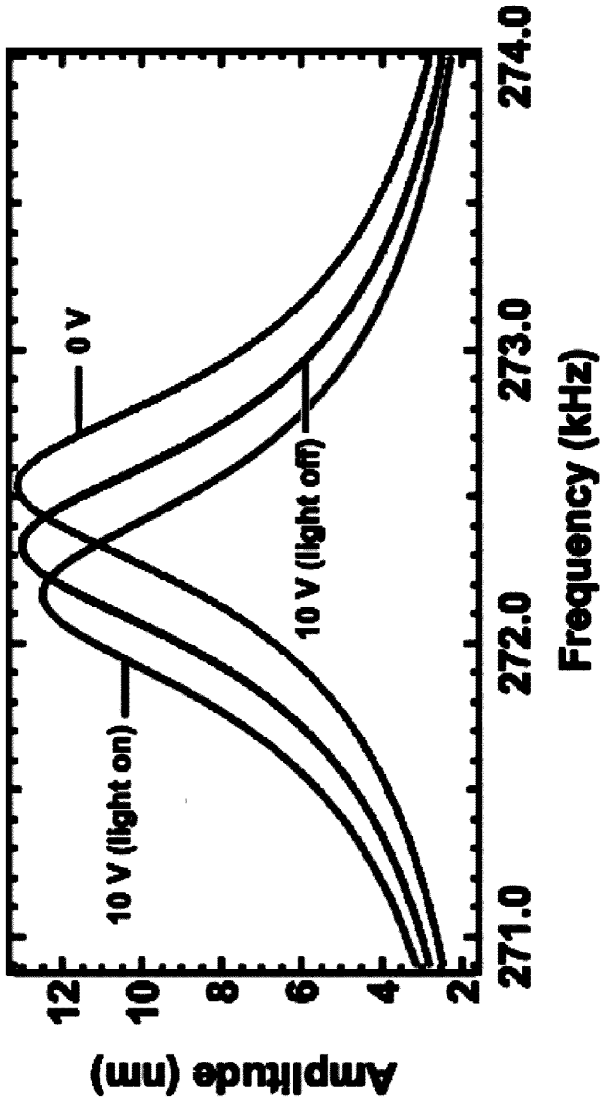
Amplitude (nm)
12
10
8
6
4
2
271.0
272.0
273.0
274.0
Frequency (kHz)
0 V
10 V (light off)
10 V (light on)

Fig. 4A.

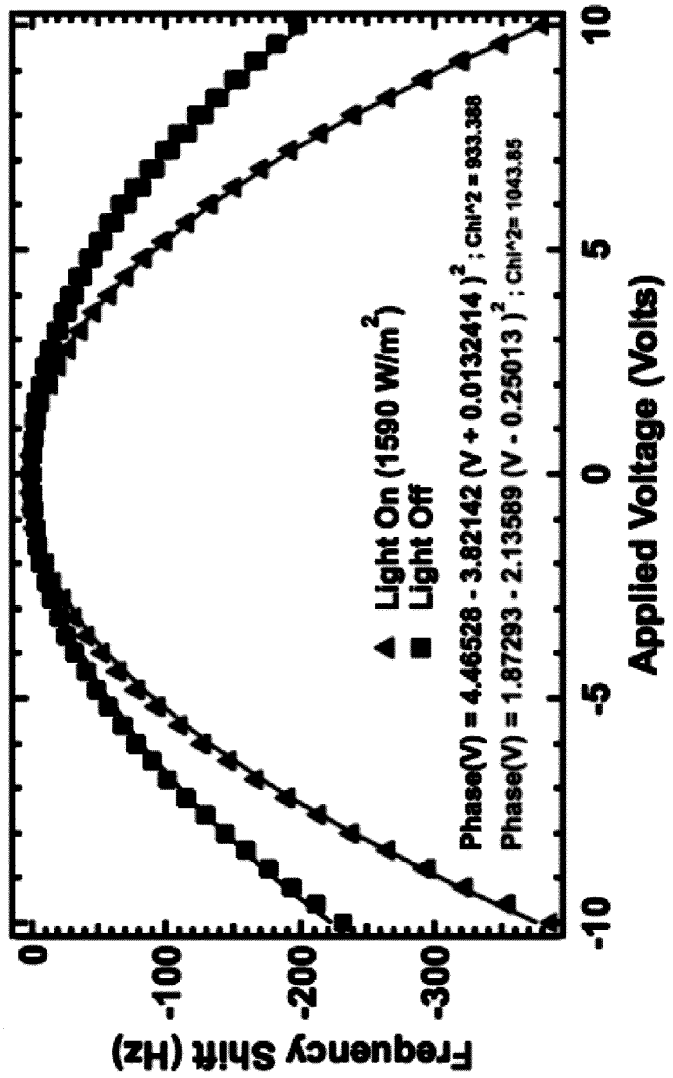
Frequency Shift (Hz)
0
-100
-200
-300
Applied Voltage (Volts)
-10
-5
0
5
10
Light On (1590 W/m2)
Light Off
Phase(V) = 4.46528 - 3.82142 (V + 0.0132414)2 ; Chi^2 = 933.388
Phase(V) = 1.87293 - 2.13589 (V - 0.25013)2 ; Chi^2= 1043.85

Fig.4B.

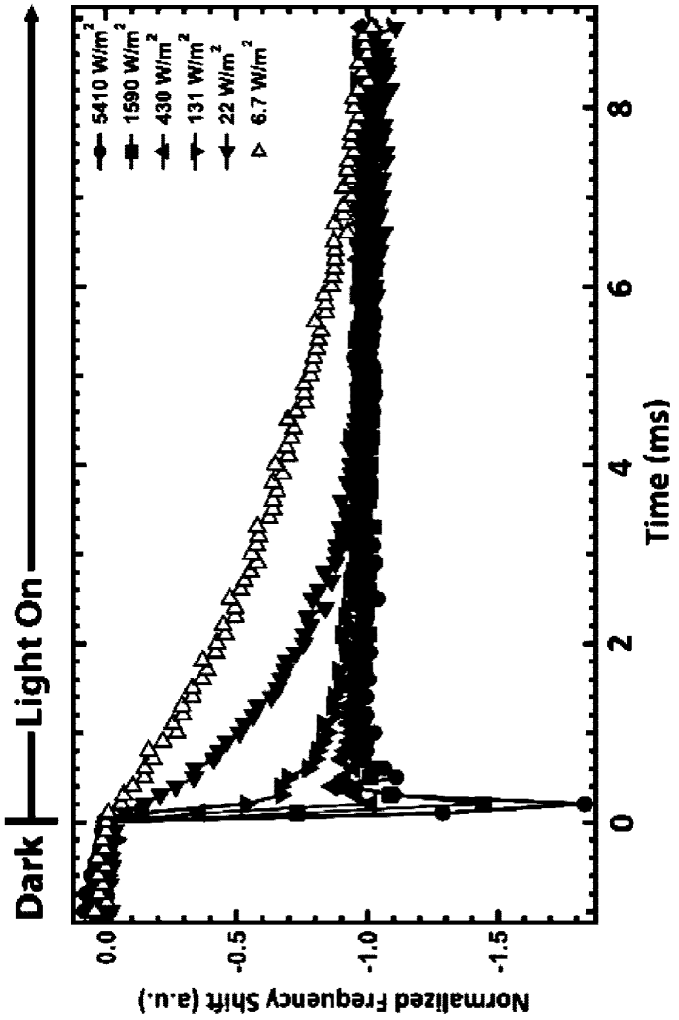
Dark
Light On
5410 W/m²
1590 W/m²
430 W/m²
131 W/m²
22 W/m²
6.7 W/m²
0.0
-0.5
-1.0
-1.5
Normalized Frequency Shift (a.u.)
0
2
4
6
8
Time (ms)

Fig. 5A.

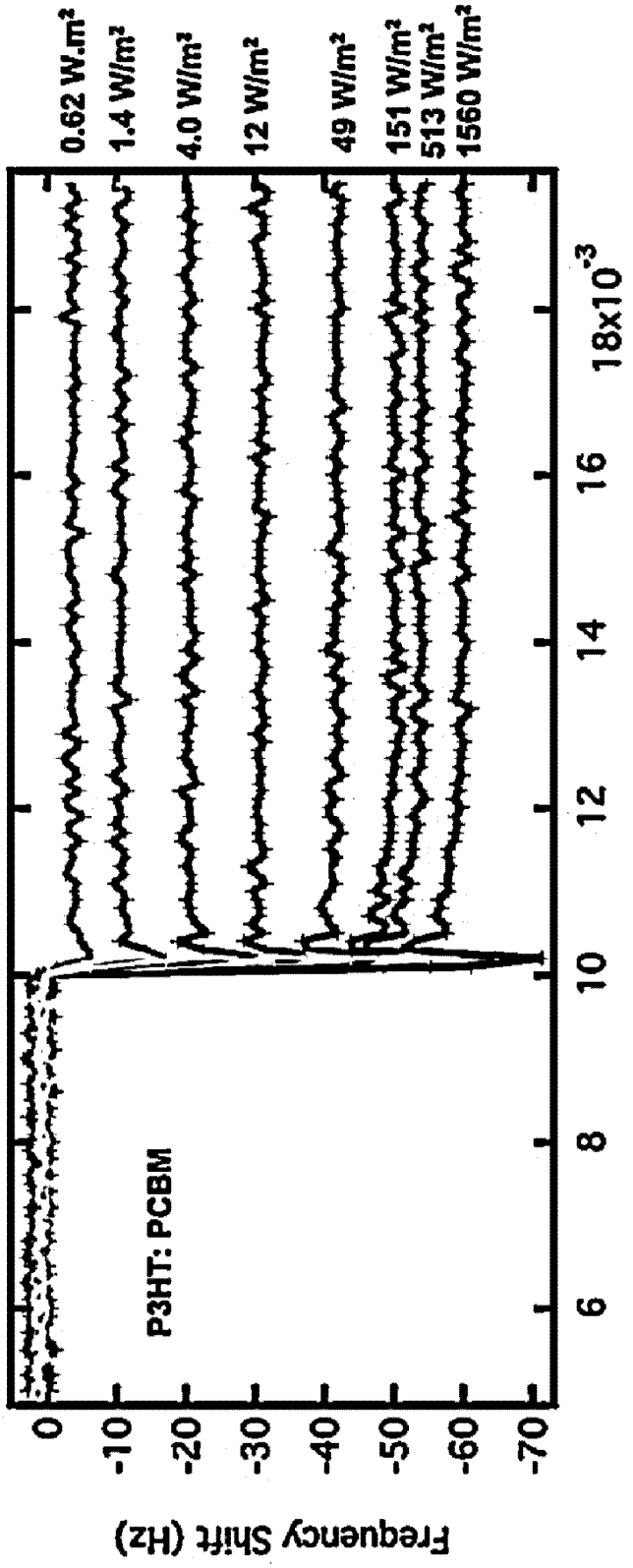
0.62 W.m²
1.4 W/m²
4.0 W/m²
12 W/m²
49 W/m²
151 W/m²
513 W/m²
1560 W/m²
P3HT: PCBM
Frequency Shift (Hz)
0
-10
-20
-30
-40
-50
-60
-70
6
8
10
12
14
16
18x10⁻³

Fig. 5B.

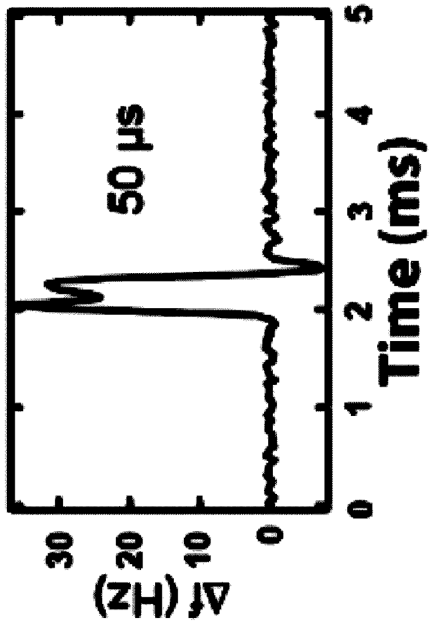
50 µs
Time (ms)
Δf (Hz)
0
1
2
3
4
5
0
10
20
30

Fig. 5D.

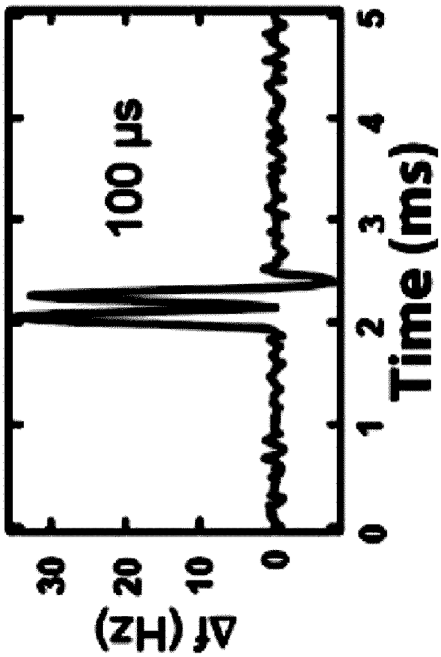
100 µs
Time (ms)
Δf (Hz)
0
1
2
3
4
5
0
10
20
30

Fig. 5C.

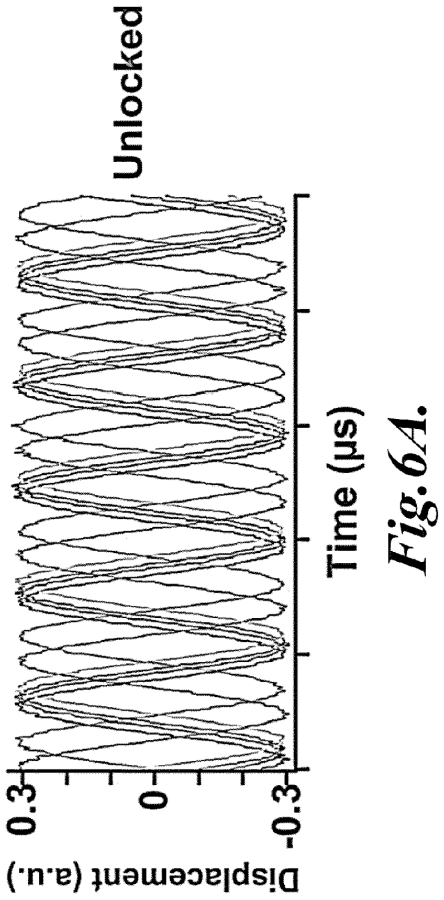
Unlocked
Displacement (a.u.)
0.3
0
-0.3
Time (µs)

Fig. 6A.

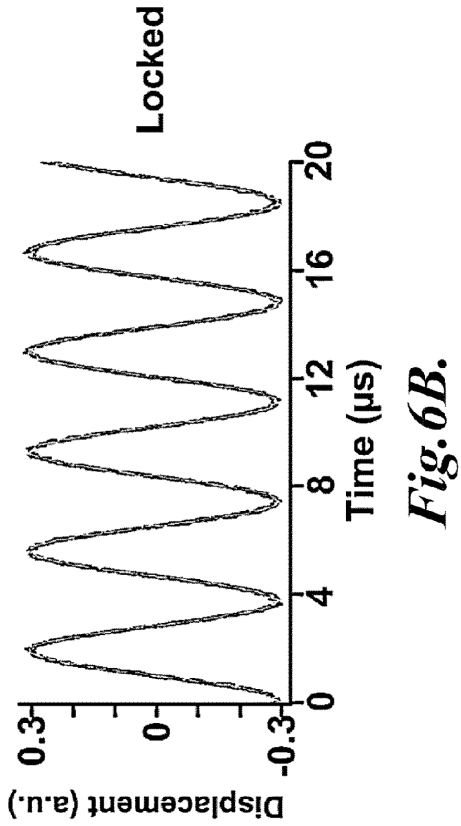
Locked
Displacement (a.u.)
0.3
0
-0.3
0
4
8
12
16
20
Time (µs)

Fig. 6B.

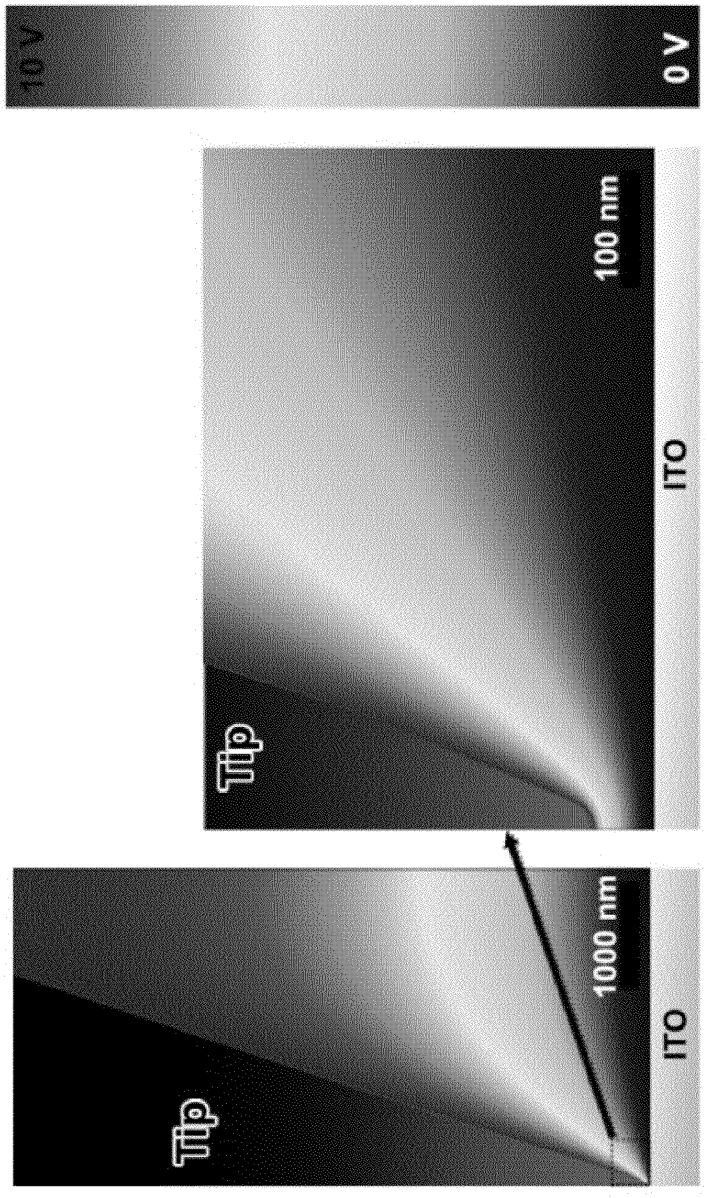

Fig. 7.

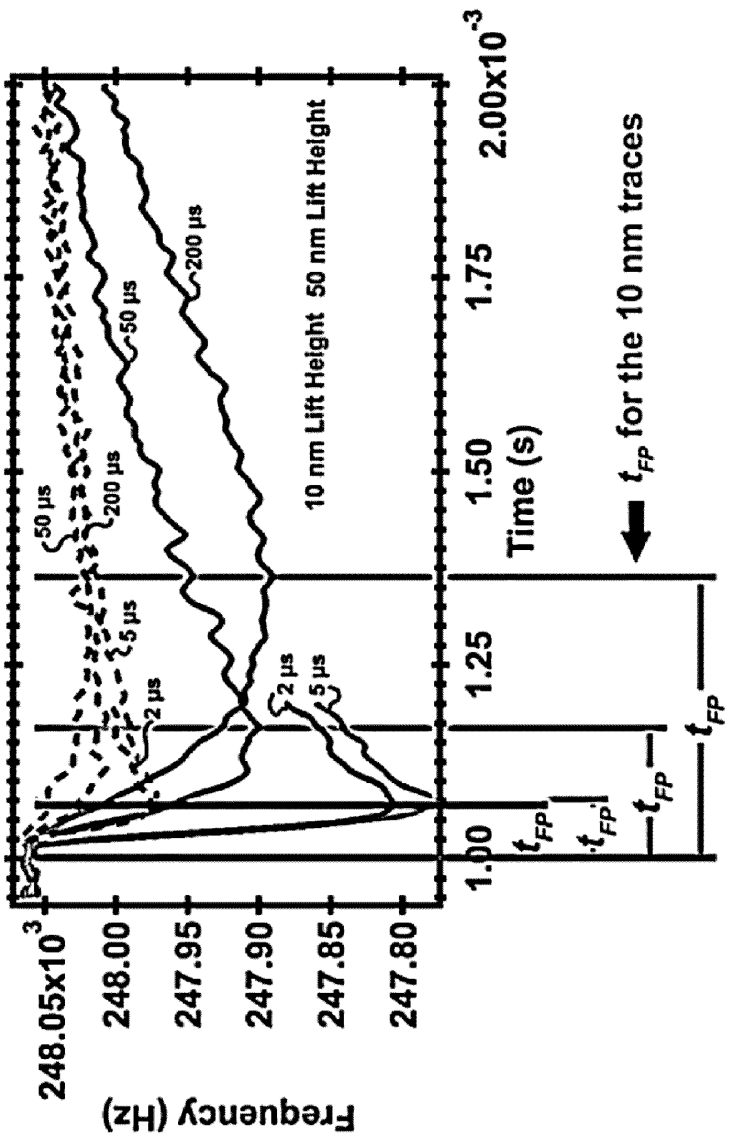
Frequency (Hz)
248.05x10^3
248.00
247.95
247.90
247.85
247.80
1.00
1.25
1.50
1.75
2.00x10^-3
Time (s)
50 µs
200 µs
5 µs
2 µs
10 nm Lift Height
50 nm Lift Height
t_{FP}
t_{FP}
t_{FP}
t_{FP} for the 10 nm traces

Fig. 8.

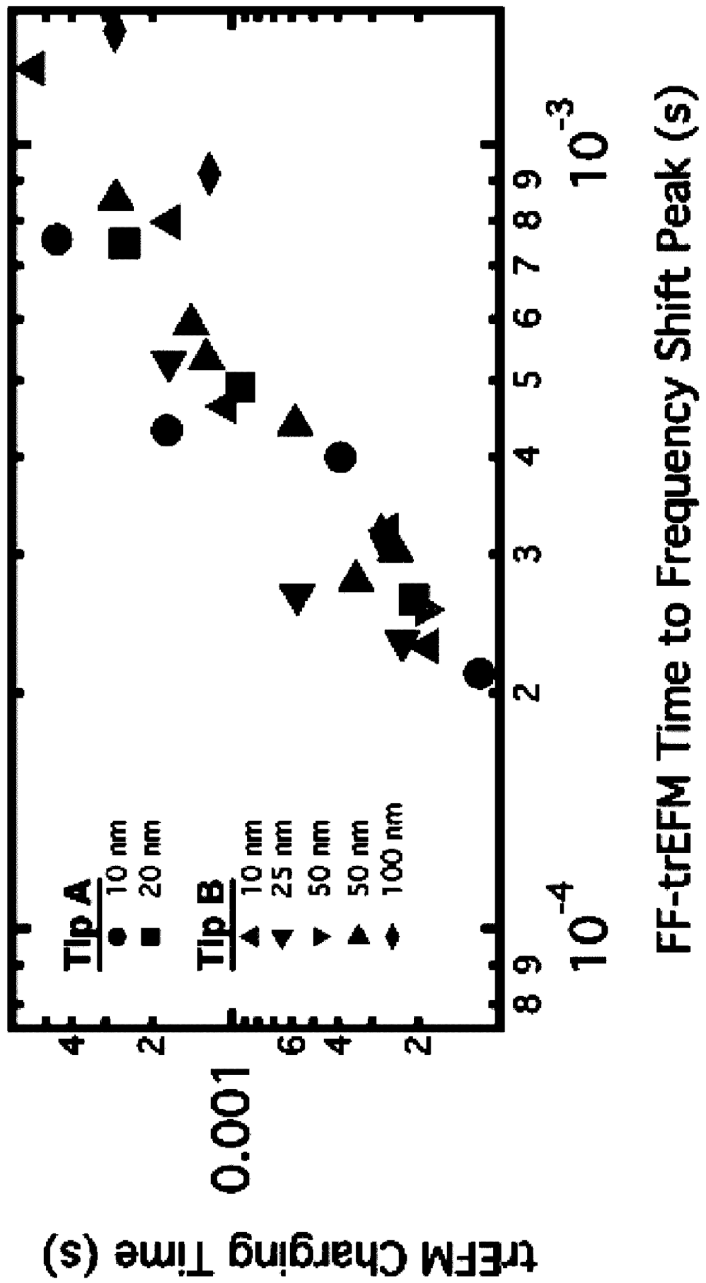
trEFM Charging Time (s)
0.001
Tip A
10 nm
20 nm
Tip B
10 nm
25 nm
50 nm
50 nm
100 nm
FF-trEFM Time to Frequency Shift Peak (s)

Fig. 9.

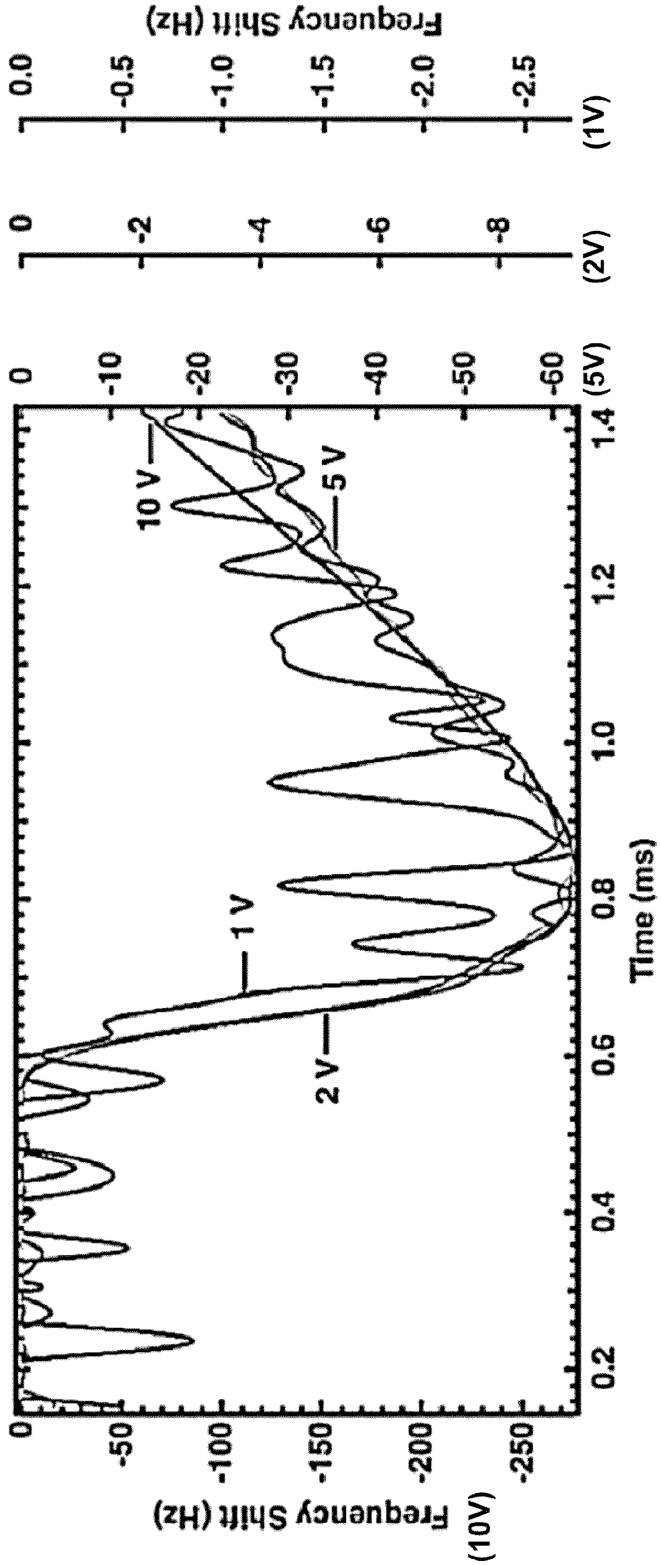
Frequency Shift (Hz)
0.0
-0.5
-1.0
-1.5
-2.0
-2.5
(1V)
0
-2
-4
-6
-8
(2V)
0
-10
-20
-30
-40
-50
-60
(5V)
10 V
5 V
1 V
2 V
0
-50
-100
-150
-200
-250
(10V)
Frequency Shift (Hz)
0.2
0.4
0.6
0.8
1.0
1.2
1.4
Time (ms)

Fig.10.

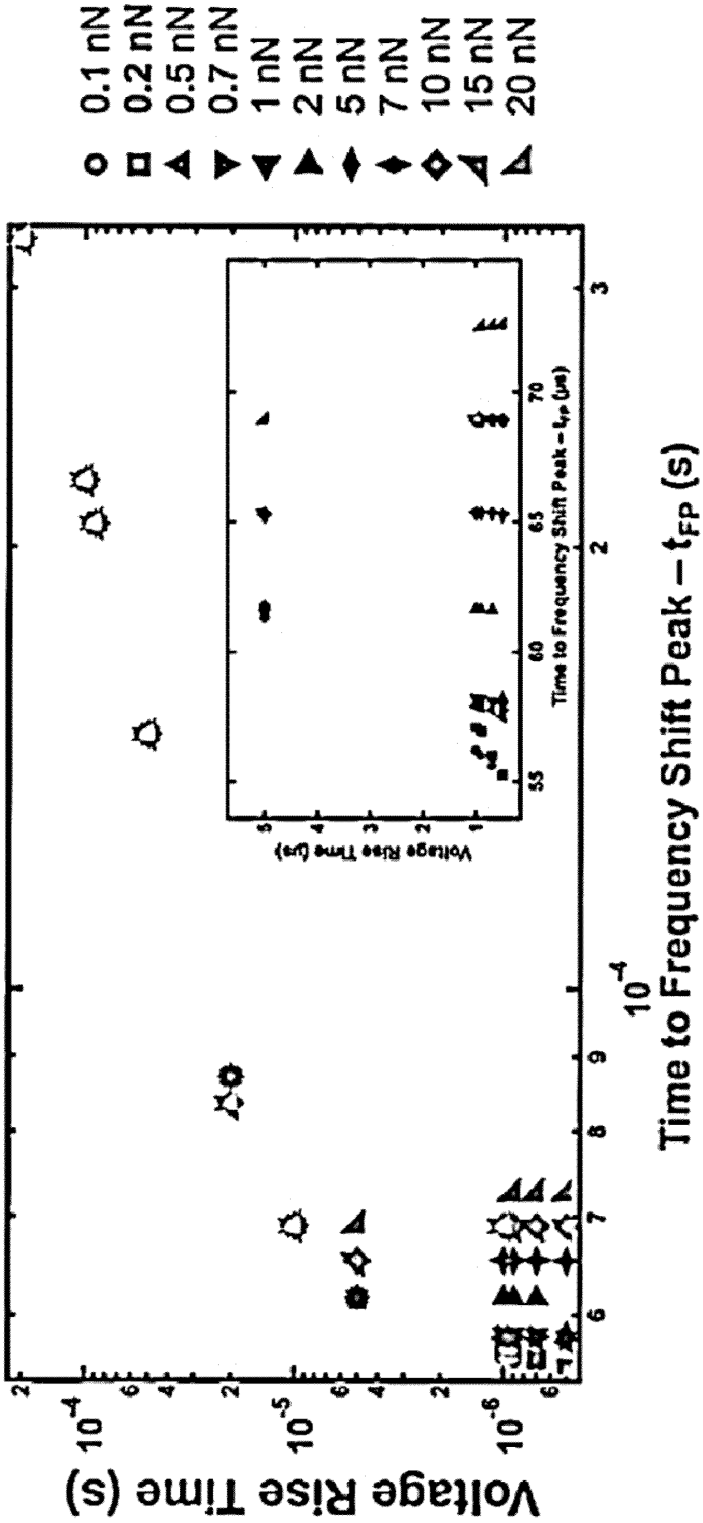
0.1 nN
0.2 nN
0.5 nN
0.7 nN
1 nN
2 nN
5 nN
7 nN
10 nN
15 nN
20 nN
Voltage Rise Time (s)
Time to Frequency Shift Peak – t_{FP} (s)
Voltage Rise Time (μs)
Time to Frequency Shift Peak – t_{FP} (μs)

Fig. 11A.

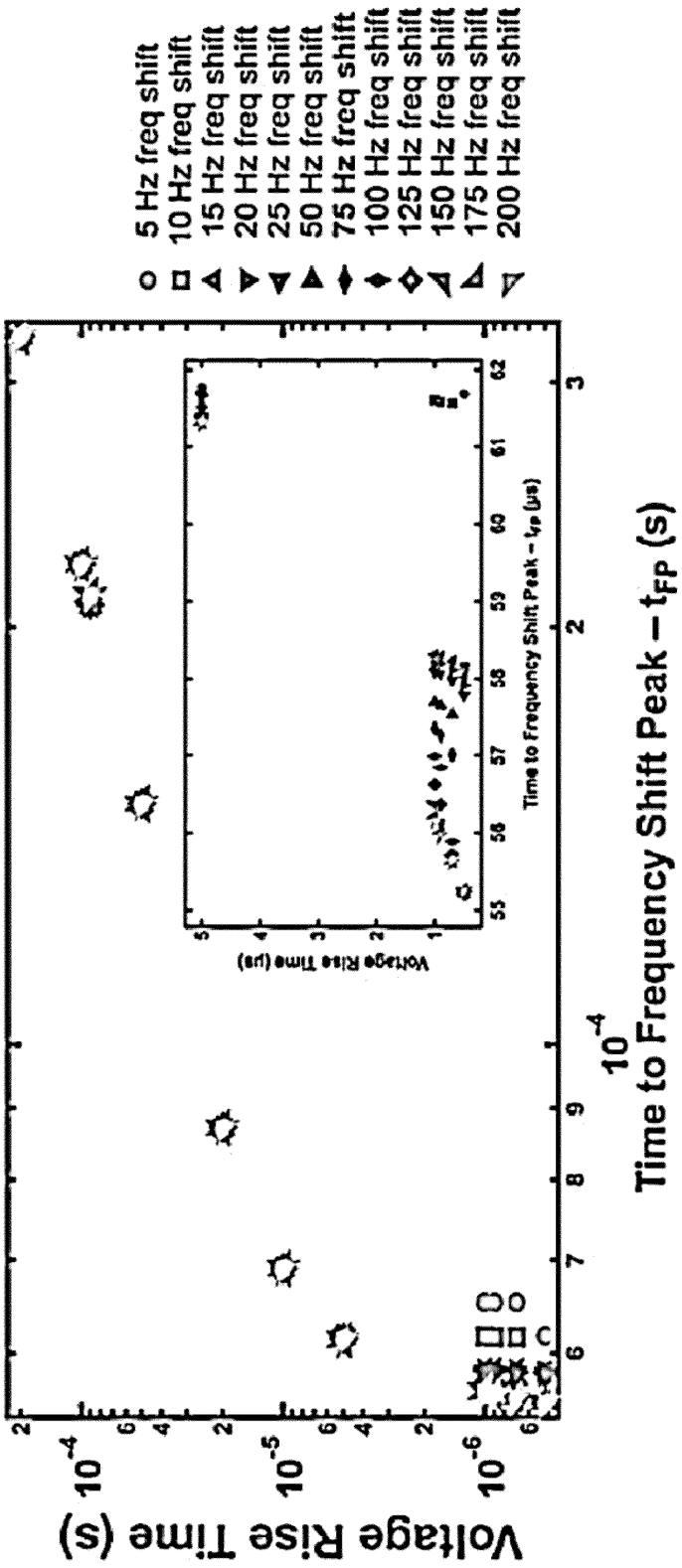
5 Hz freq shift
10 Hz freq shift
15 Hz freq shift
20 Hz freq shift
25 Hz freq shift
50 Hz freq shift
75 Hz freq shift
100 Hz freq shift
125 Hz freq shift
150 Hz freq shift
175 Hz freq shift
200 Hz freq shift
Voltage Rise Time (s)
Time to Frequency Shift Peak – t_{FP} (s)
Voltage Rise Time (μs)
Time to Frequency Shift Peak – t_{FP} (μs)

Fig. 11B.

SUB-MICROSECOND-RESOLUTION PROBE MICROSCOPY

CROSS-REFERENCE TO RELATED APPLICATION

This application claims the benefit of U.S. Provisional Application No. 61/382,804, filed Sep. 14, 2010, which is expressly incorporated herein by reference in its entirety.

STATEMENT OF GOVERNMENT LICENSE RIGHTS

This invention was made with Government support under contract DE-SC0001084 awarded by the Department of Energy and under contract DMR 0449422 awarded by the National Science Foundation. The Government has certain rights in the invention.

BACKGROUND

Atomic force microscopy (AFM) is widely used in fields ranging from biophysics to surface chemistry. Through the use of mechanical and electrical feedback modes, AFM methods are used to study diverse problems such as mechanical properties and glass transitions in polymer blends, surface polarization in ferroelectrics, photogeneration of charge in solar cells, and energy storage in batteries. However, one area where AFM methods have not generally found widespread success is in the study of fast local dynamics. The fastest AFM methods typically acquire image scan lines at rates of ~3 kHz, while studies reporting time-resolved AFM measurements with commercial instruments often measure local processes on time scales of milliseconds.

Attempts to achieve ultrafast temporal resolution with scanning probe instruments have largely employed sophisticated combinations of pulsed laser optics with either near-field scanning optical microscopy or scanning tunneling microscopy (STM). More recently, time-resolved STM methods limited to the current preamplifier bandwidth or using radio-frequency STM have been reported. These techniques can provide powerful probes in systems with suitable optical or electronic properties, but generally require complex, expensive specialty hardware and are restricted in their ability to study materials with low optical contrast or high conductivity. As a result, these probes have been limited primarily to niche applications.

What is desired, therefore, is an improved microscopy method capable of nanosecond-scale temporal resolution.

SUMMARY

This summary is provided to introduce a selection of concepts in a simplified form that are further described below in the Detailed Description. This summary is not intended to identify key features of the claimed subject matter, nor is it intended to be used as an aid in determining the scope of the claimed subject matter.

In one aspect, a time-resolved microscopy method is provided for measuring the response of a sample to a perturbation. The method uses a cantilever positioned adjacent a first location of the sample. In one embodiment, the method comprises the steps of:

(a) applying the perturbation to the sample at a first time;

(b) measuring the motion of the cantilever in response to the effect of the perturbation on the sample for a predetermined first length of time, to provide a deflection signal, in the absence of a feedback loop configured to regulate cantilever motion following the perturbation; and

(c) determining from the deflection signal the time-domain properties of the effect of the perturbation on the first location of the sample.

In another aspect, an apparatus is provided. In one embodiment, the apparatus includes:

a cantilever configured to measure the response of a sample adjacent the cantilever;

a drive controller configured to oscillate the cantilever at a drive frequency;

a detector in communication with the cantilever, which is configured to measure the response of the cantilever;

an excitation signal generator configured to apply a perturbation to the sample; and

a triggering circuit configured to coordinate the response of the cantilever and the perturbation such that the perturbation occurs at the about the same position in the cantilever oscillation cycle.

DESCRIPTION OF THE DRAWINGS

The foregoing aspects and many of the attendant advantages of this invention will become more readily appreciated as the same become better understood by reference to the following detailed description, when taken in conjunction with the accompanying drawings, wherein:

FIG. **1**A diagrammatically illustrates the steps of a representative method in accordance with the embodiments provided herein.

FIG. **1**B diagrammatically illustrates an embodiment of a variation of the method illustrated in FIG. **1**A, wherein frequency is used to determine the time-domain properties of the effect of a perturbation on a sample.

FIG. **1**C diagrammatically illustrates a representative apparatus for characterizing a sample in accordance with the embodiments provided herein.

FIG. **1**D is a block diagram illustrating feedback-free time-resolved electrostatic force microscopy (FF-trEFM) operation. After feedback is turned off, the cantilever signal is digitized and recorded with high sampling rate (typically 50 MHz). Multiple runs, with the excitation applied at the same phase, are averaged and demodulated to acquire the instantaneous frequency. The metric of interest is the time between excitation and maximum frequency shift from steady state (time to frequency shift peak, t_{FP}).

FIG. **1**E graphically illustrates instantaneous frequency of simulated cantilever behavior, using realistic cantilever parameters (ω_0=247.329 kHz, Q=363, k=27.7 N/m) with transient perturbations of root exponential form with characteristic time constants from 100 ns to 300 μs, showing the monotonic behavior of t_{FP} with perturbation rise time. Arrows at the bottom illustrate the t_{FP} time.

FIG. **2**A illustrates instantaneous frequency data following exponentially-shaped voltage pulses with rise times ranging from 600 ns to 10 ms. From 50 μs to 10 ms, as the rise time increases, the net frequency shift generally decreases due to an overlap between transient and steady-state harmonic oscillator behavior, while the t_{FP} consistently increases monotonically. Markers are spaced every 225 samples. Number of averaged pulses N=1250.

FIG. **2**B illustrates data from 80 ns to ~10 μs showing the t_{FP} values decrease monotonically even as the cantilever behavior becomes increasingly complicated at subcycle times. Markers are spaced every 40 samples. Number of averaged pulses N=1250.

FIG. **2**C illustrates comparing damped driven harmonic oscillator (DDHO) simulation (dotted), finite element simulation (dashed), and experimental (solid) instantaneous frequency at different rise times.

FIG. **2**D illustrates t_{FP} data for voltage pulses across four decades of rise times. Experimental data (circles) are compared with the data generated using the modified DDHO equations (squares) and data generated using a finite element model simulation (diamonds) from 500 ns to 800 μs.

FIG. **3**A is an instrumentation schematic for OPV characterization, showing the sample purged under constant nitrogen flow and transient perturbation caused by photoinduced charging via a pulsed LED (523 nm).

FIG. **3**B illustrates instantaneous frequency data for a range of light intensities on a ~51% EQE P3HT:PCBM film showing that photoinduced charging represents a transient force and force gradient effect similar to a root-exponential voltage of characteristic τ as in FIG. **2**.

FIG. **3**C illustrates external quantum efficiency (EQE) measurements on five P3HT:PCBM devices annealed at 110° C. for 0 (unannealed), 1, 5, 10 and 20 minutes. The green line is at the LED wavelength, ~523 nm. The shaded region indicates previously-accessible device efficiencies using traditional feedback-based methods.

FIG. **3**D illustrates spatially averaged $1/t_{FP}$ values (triangles) versus EQE (circles) for the four devices measured. The error bars represent standard deviation of the mean for several areas (t_{FP}) and several pixels (EQE).

FIGS. **3**E and **3**F illustrate topography (FIG. **3**E) and the FF-trEFM image (FIG. **3**F) of a ~51% EQE nanostructured organic photovoltaic device (P3HT:PCBM film) showing spatial variation in the $1/t_{FP}$ values with values as low as sub-30 μs when exposed to LED intensity of 513 W/m^2.

FIGS. **3**G and **3**H illustrate histograms of FF-trEFM $1/t_{FP}$ values for an unannealed (FIG. **3**G) and 1 minute annealed film (FIG. **3**H), showing that the average and standard deviation both increase with annealing time, consistent with reported short-circuit photocurrent image data.

FIG. **4**A graphically illustrates cantilever oscillation amplitude curves on an organic photodiode (PFB:F8BT) taken at 0 V, 10 V, and 10 V under 405 nm illumination, across a range of drive frequencies.

FIG. **4**B graphically illustrates frequency shift response showing the expected quadratic dependence on applied voltage as well as the change in differential capacitance gradient due to illumination. Data taken at 10 nm above the same sample with approximately 1590 W/m^2 intensity.

FIG. **5**A illustrates typical normalized classic trEFM data curves of the same PFB:F8BT organic photovoltaic sample, showing the time-resolved behavior in the frequency shift. As the intensity increases the frequency shift response resembles a step function due to the time resolution limit, with ringing due to the feedback circuit, in this case occurring at an incident 405 nm LED intensity of ~430 W/m^2.

FIG. **5**B: for an efficient organic photovoltaic (OPV) blend, P3HT:PCBM, saturation occurs even at intensities as low as <1 W/m^2 using a 532 nm LED in this case.

FIGS. **5**C and **5**D: through consecutive voltage pulses, it is possible to determine the lower limit of approximately 100 μs for the old trEFM method, wherein FIG. **5**C illustrates the distinction of consecutive voltage pulses using the embodiments provided herein and FIG. **5**D illustrates the same frequency of voltage pulse using a traditional time-resolved electrostatic force microscopy system, which cannot distinguish consecutive pulses as quickly as those of the embodiments provided herein (i.e., FIG. **5**C).

FIGS. **6**A and **6**B: Consecutive digitized deflection waves showing significant jitter without (FIG. **6**A) and with (FIG. **6**B) a triggering circuit. The circuit ensures that the voltage and light are applied at the same point in the cycle, thus improving averaging by eliminating the averaging errors that can occur in the unlocked trigger case.

FIG. **7**: Numerically calculated electrostatic potential maps (z-component) of the tip-sample junction, where the sample and tip are metals (such as Pt (left) and indium tin oxide (right), respectively).

FIG. **8**: At four different voltage pulse rise times taken at 10 nm (solid) and 50 nm (dashed) lift heights, the t_{FP} values are approximately the same. These data indicate that the t_{FP} metric is robust against vertical drift effects unlike metrics used in steady-state EFM such as frequency shift magnitude.

FIG. **9**: Data were acquired at several lift heights and light intensities (405 nm LED, intensities range from 1560 W/m^2 to 1.4 W/m^2) with two different tips. As expected, there is a correlation between the classic charging time (y-axis) and t_{FP} value (x-axis) and both techniques are fairly robust to lift height variations given that the data points fall on the same general trendline.

FIG. **10**: The instantaneous frequency is shown for a 150 μs rise time voltage pulse with four different voltages: 10 V, 5 V, 2 V, and 1 V. The t_{FP} value is approximately the same in that the instantaneous frequency trend is consistent the same across all voltages. The signal:noise varies with ΔV^2, therefore at 1 V the frequency data are significantly noisier, yet the trend is still observable for a frequency shift of only ~2.8 Hz versus a drive frequency of 248.603 kHz.

FIGS. **11**A and **11**B illustrate the effect of electrostatic force and force gradient on sub-cycle time resolution. Simulated data using root exponential voltage pulses by sweeping either (FIG. **11**A) the electrostatic force or (FIG. **11**B) the net frequency shift (effectively the change in electrostatic force gradient). (FIG. **11**A) Changing the force plays a significant role in the t_{FP} values in the sub-10 μs regime. (FIG. **11**B) Changing the frequency shift affects the proportionality between t_{FP} values at a given sub-10 μs level; as the frequency shift increases, the larger the difference in t_{FP} between two consecutive voltage rise times. Bolded values (0.2 nN in FIG. **11**A and 75 Hz in FIG. **11**B) indicate typical experimental conditions on a PFB:F8BT blend. Insets show the sub-5 μs data on a linear scale.

DETAILED DESCRIPTION

Methods and apparatus are provided herein for time-resolved analysis of the effect of a perturbation (e.g., a light pulse) on a sample. By reconstructing time domain information (in particular, the rise or decay time of a pulse, hereafter τ), the provided method enables sub-microsecond time-resolved measurement of transient, or time-varying, forces acting on a cantilever.

By extracting time-domain information, the embodiments described herein greatly exceed the resolution and experimental capabilities of current mechanical systems (such as atomic force microscope (AFM)-based systems). The transient, or time-varying, forces applied to the systems under study include forces such as light, magnetic fields, fast biological forces and motions, radio frequency (RF) pulses, and electrical forces. Accordingly, the systems and methods described herein provide a powerful new tool to observe the effects of various forces on a sample with a time resolution in the sub-microsecond scale, which enables the observation of the effects of the force as it impacts and dissipates in reaction to the sample. Such a tool is useful, for example, to study the

fundamental charge carrier transport and photo-generation phenomena in photovoltaic materials, as is described in more detail in the Example section below.

While the embodiments herein are primarily described with reference to AFM-related methods, it will be appreciated that any scanning probe microscopy (SPM) method compatible with the provided embodiments may be enhanced accordingly.

In one aspect, a time-resolved microscopy method is provided for measuring the response of a sample to a perturbation. The method uses a cantilever positioned adjacent a first location of the sample. In one embodiment, the method comprises the steps of:

(a) applying the perturbation to the sample at a first time;

(b) measuring the motion of the cantilever in response to the effect of the perturbation on the sample for a predetermined first length of time, to provide a deflection signal, in the absence of a feedback loop configured to regulate cantilever motion following the perturbation; and

(c) determining from the deflection signal the time-domain properties of the effect of the perturbation on the first location of the sample.

The method will be described further with reference to FIG. **1**, which is a flowchart illustrating the method **100** in three steps.

In the first step **105** of the method, a perturbation, such as light, a magnetic field, an RF pulse, etc., is applied to a sample at a first time. The sample can be any sample known to those of skill in the art, as described above. The first time is the time at which the perturbation affects the sample, and the first time is noted for later processing to determine the time-domain properties of the effect of the perturbation on the sample.

The sample studied can be any sample about which the transient, or time-varying, properties of the sample are to be characterized. Representative samples include materials that respond to light (e.g., photovoltaic materials), magnetism, electrical signals, and/or radio frequency (RF) pulses.

The method continues with a step **110** where the motion of a cantilever adjacent to a first location of the sample is measured. The first location can be any location on the sample and is a location of interest to a user performing the method. The effect of the perturbation on the sample at the first location is measured for a predetermined first length of time. The measured motion of the cantilever over the first length of time is a deflection signal that indicates the response of the cantilever to the perturbation. The combination of steps **105** and **110** are referred to herein as a "perturbation/measurement cycle".

The cantilever that is positioned adjacent the first location of the sample can be any cantilever known to those of skill in the art. Of particular use are cantilevers used with scanning probe microscopy (SPM) techniques, such as atomic force microscopy (AFM).

Notably, in step **110**, no feedback loop is used to regulate cantilever motion following the perturbation. In traditional SPM (e.g., AFM) methods, a feedback loop is used to maintain a characteristic of the cantilever motion during scanning. For example, if an oscillating cantilever is used in an AFM technique, the phase, amplitude, or frequency of the oscillation can be maintained at a fixed value and the positioning or the force applied to the cantilever is altered during scanning so as to maintain the constant characteristic. E.g., if a constant phase feedback loop is used, as an AFM cantilever is scanned across a sample surface, a change in phase detected by the cantilever is processed in a feedback loop and the positioning, or the oscillating force applied by the cantilever driver, is altered so as to maintain a constant phase.

In the present embodiments, the cantilever is positioned above a single location on a sample at a fixed height and the response of the cantilever to the sample at the first location after the perturbation is applied is determined without adjusting the characteristics of the cantilever using a feedback loop following the perturbation. That is, the cantilever is not adjusted in position, frequency of oscillation, etc. as an adjustment related to the response of the cantilever to the perturbation. This feedback-free regime allows the cantilever to oscillate freely, and those oscillations, in response to the response of the sample to the perturbation, yield the data required to extract time-domain properties from the deflection signal of the cantilever.

Accordingly, the method concludes with a step **115** of determining from the deflection signal of the cantilever the time-domain properties of the effect of the perturbation on the first location of the sample.

The techniques used to determine, from the deflection signal, the time-domain properties of the effect of the perturbation on the sample are generally known to those of skill in the art, although these techniques have not before been applied to applications such as those described in the embodiments described herein. Essentially, the goal of the method **100** is to quantitate the effect of the perturbation on the cantilever as the effect of the perturbation changes over time. In order to accomplish this, several different methods can be used to analyze the transient motion of the cantilever as a function of time, including a Hilbert Transform, as described in the Example below, a moving window fast Fourier transform, fitting of sine curves to portions of the signal, and other data analysis and signal processing methods known to those of skill in the art. These transformations all require certain input from the measurement system. The input required includes the conditions of the sample and the cantilever prior to the application of the perturbation and then the conditions of the cantilever as they change over time in response to the perturbation. The deflection signal of an AFM is an exemplary means for determining the effect of the perturbation on the sample over time, as the measurement of the deflection signal over time indicates the response of the cantilever to the sample, which is in turn responding to the perturbation. By collecting continuous or closely spaced data over a fixed time window, the response of the cantilever to the sample, which is in turn reacting to the perturbation, can be determined.

In certain embodiments, the cantilever is an oscillating cantilever. Oscillating cantilevers are known to those of skill in the art, and they are sometimes known, in the context of AFM, as tapping-mode cantilevers, AC cantilevers, intermittent contact-mode cantilevers, and the like. In one embodiment of the method, as illustrated in FIG. **1**B, an oscillating cantilever is used to determine the time-domain properties of the effect of the perturbation on the first location of the sample, as set forth in step **115** of the method **100** illustrated in FIG. **1**A. Referring to FIG. **1**B, the oscillating cantilever embodiment of step **115** is illustrated in FIG. **1**B and begins with a sub-step **120** of extracting an instantaneous frequency of the cantilever from the deflection signal to provide a frequency signal for the first length of time. This step requires, for example, determining an instantaneous phase of the cantilever from the deflection signal, and from the instantaneous phase, the frequency signal is determined. Such a transformation can be accomplished using the Hilbert Transform, moving window fast Fourier Transform, fitting of sine curves to portions of the signal, and other techniques known to those of skill in the art.

After the frequency signal for the first length of time is determined, the method **100** proceeds to a sub-step **125** of

identifying within the frequency signal the maximum frequency shift from the steady-state frequency (i.e., the frequency of the cantilever oscillation prior to the application of the perturbation), to provide a frequency peak value at a peak time.

Finally, the method **100** concludes with a sub-step **130** of determining the amount of time intermediate the first time and the peak time. This determination provides a frequency-shift-peak time (t_{FP}) that is characteristic of the time-domain characteristics of the effect of the perturbation on the sample at the first location. The t_{FP} is a figure of merit for the provided method that is used herein. However, it will be appreciated that other time-domain figures of merit may be used to characterize a sample. Therefore, the methods provided herein are not limited to methods for determining the t_{FP} of a sample location. Both sub-steps **120** and **125** are described in greater detail in the Example below. Specifically, the method steps illustrated in FIG. **1**B are set forth in greater detail, and in exemplary embodiments, with reference to FIG. **1**D (and subsequent figures) in the Example section below.

In certain embodiments, the methods described above (i.e., FIGS. **1**A and/or **1**B) further comprise a step of repeating the steps of applying the perturbation and measuring the motion of the cantilever in response to the effect of the perturbation multiple times at the first location using the same magnitude of perturbation. This embodiment includes averaging the multiple deflection signals to provide an averaged deflection signal. The averaged deflection signal is then used as the primary deflection signal when determining the time-domain properties of the effect of the perturbation on the first location of the sample. This embodiment may be better understood with reference to FIG. **1**A and the method **100** described therein. In the method **100**, the steps **105** and **110** relate to applying a perturbation to a sample and then measuring the motion of the cantilever adjacent the sample in response to the perturbation. In the presently described embodiments, the steps of applying a perturbation and then measuring the motion of the cantilever in response to the perturbation (steps **105** and **110**) are repeated two or more times and the results of those repetition cycles are then averaged to provide an averaged deflection signal for use in step **115**. By averaging the perturbation/measurement cycles at a given point, the signal-to-noise ratio is greatly improved, removing thermal, acoustic, and environmental noise that would ordinarily limit the accurate determination of the cantilever motion following a transient perturbation. Thus, while averaging increases the total measurement time, it does so while at the same time increasing the ability to characterize the time-domain properties of very fast behaviors in the sample. As set forth below in the examples, discrimination of differences of ~100 nanosecond between different transient perturbations can be achieved using the methods and apparatus disclosed herein.

In certain embodiments, when multiple perturbation/measurement cycles are performed, as set forth in certain embodiments above, the method further comprises the step of applying the perturbation and measuring the motion of the cantilever in response to the effect of the perturbation multiple times by synching (i.e., coordinating) the position of the cantilever and the perturbation, such that the perturbation occurs at about the same position in the cantilever oscillation cycle each time that the perturbation is applied. As used herein, when the perturbation is coordinated so as to occur at about the same position in the cantilever oscillation cycle, the term "about" means that the coordination results in the perturbation being applied with an accuracy that is better than the ultimately desired time resolution. In other words, to achieve sub-microsecond time resolution, two coordinated perturbation/measurement cycles must occur at the same point in subsequent oscillation cycles with an error less than a fraction of a microsecond.

In certain embodiments, the perturbation always occurs at the same position in the cantilever oscillation cycle.

Such coordination is typically accomplished using a triggering circuit, as set forth in the apparatus embodiments described below, although it will be appreciated that any apparatus or method for coordinating the position of the cantilever oscillation and the application of the perturbation is useful in the embodiments provided herein. The trigger circuit allows the data to be averaged to achieve sub-cycle time resolution. While an ideal trigger circuit would fire at the exact same position in the cantilever cycle, a practical trigger may have some phase jitter. However, increasing amounts of phase jitter from the trigger will necessarily reduce the achievable time resolution.

When a cantilever oscillates, the oscillation is essentially in the z direction, as defined as the direction extending perpendicularly from the sample surface probed by the cantilever. Essentially, the cantilever is vibrating up and down at a very fast rate (e.g., a 300 kilohertz rate). For consistency, when averaging similar perturbation/measurement cycles, the triggering circuit (or other coordination circuit) takes into account the vertical position above the sample at which the cantilever is positioned (e.g., is at an oscillation peak or trough) and the perturbation is applied at the same point in the oscillation cycle during each of the perturbation/measurement cycles used to average together a single deflection signal. For example, the triggering circuit may be configured to wait to deliver a perturbation (e.g., a light flash) until the cantilever is oscillating at a peak (as defined as the furthest in the z direction that the cantilever is above the sample). By only applying the perturbation when the cantilever is at a specific point in its oscillation cycle, the data can be averaged to obtain sub-cycle information about the effect of the perturbation on the sample. Furthermore, the position within the cantilever oscillation cycle at which the perturbation is applied can be chosen to minimize (or maximize) the relative contribution the sensitivity of the method to transient forces relative to transient force gradients.

In certain embodiments, the method further comprises rastering the cantilever across the sample to multiple locations while determining, from the deflection signal at each of the multiple locations, the time-domain properties of the effect of the perturbation on the multiple locations of the sample to provide an image of the sample. In this embodiment, the method is used in a similar fashion as is used in typical SPM methods where a cantilever is rastered across a surface, acquiring data at discrete points continuously across a surface so as to form a 2-(or 3-) dimensional image of the surface by combining each of the discrete points into a single data image (see, e.g., FIG. **3**F, and its description in the Example section, as an example of a rastered image obtained using the provided method and apparatus).

In the embodiments described herein, rastering can be performed by acquiring only a single perturbation/measurement cycle per location, or the cantilever can dwell at a single location for several perturbation/measurement cycles so as to acquire an average deflection signal (i.e., to improve signal quality). While dwelling to acquire an average signal provides an improved signal quality, such averaging can also be time-consuming while the perturbation/measurement cycle proceeds several times, compared to a single perturbation/measurement cycle per location on the sample. Accordingly, the number of perturbation/measurement cycles per location

on the sample can be varied according to the balancing of the time required to average a signal versus the quality of the signal desired by a user.

In FIG. **3**F, six averages were taken per point at a sampling rate of 5 MHz to achieve an optimal balance. Additionally, in the limit when lateral drift in the instrument is minimized, multiple data sets over the same region can be acquired and the signals can be further averaged together to improve signal: noise. To construct an image, a standard two-pass method is employed. In the first pass, the cantilever records a line using standard height-imaging. This height data is then used on a second pass, known to those who practice EFM, to control the height of the cantilever. Additionally, in the second pass, the cantilever is subject to the perturbation applied at each point and the deflection data digitized and recorded in the computer controlling the instrument. This process is repeated for each line in the image; in FIG. **3**F this is 64 lines with 128 data points per line. After data acquisition, the data for each line are processed point-by-point using the Hilbert transform method above to acquire the frequency shift peak time, thereby constructing an image.

The methods described above can be performed using any apparatus capable of performing each of the steps of the method as set out. In certain instances, these method steps may be performed on commercially available atomic force microscopes, with little or no modification. However, traditional AFMs do not include analysis software capable of the time-domain conversions required to perform the methods provided herein. Accordingly, the methods provided herein may be implemented in software stored on a computer-readable medium, as is known by those of skill in the art. The method may be performed on a computer attached to an atomic force microscope, such that the computer is configured to control the characteristics of the cantilever to coordinate the detection of the cantilever, to deliver the coordinated perturbation and to analyze the resulting deflection signal so as to transform the deflection data into time-domain data to determine the time-domain properties of the effect of the perturbation on the sample, in accordance with the embodiments provided herein.

In addition to the method embodiments set forth above, additional aspects provided herein include an apparatus configured to measure the time-domain properties of the effect of a perturbation on a sample. Such an apparatus is capable of, for example, performing the methods set forth above. However, it will be appreciated that the apparatus provided herein is not limited to an apparatus configured to perform the embodiments provided herein and may be used for additional uses.

In another aspect, an apparatus is provided. In one embodiment, the apparatus includes:

- a cantilever configured to measure the response of a sample adjacent the cantilever;
- a drive controller configured to oscillate the cantilever at a drive frequency;
- a detector in communication with the cantilever, which is configured to measure the response of the cantilever;
- an excitation signal generator configured to apply a perturbation to the sample; and
- a triggering circuit configured to coordinate the response of the cantilever and the perturbation such that the perturbation occurs at the about the same position in the cantilever oscillation cycle.

The apparatus may be better understood with reference to FIG. **1**C, which illustrates an apparatus **200**. The apparatus **200** includes a cantilever **205**. The cantilever can be any cantilever known to those of skill in the art, such as an atomic force microscope cantilever. The cantilever **205** may include a tip **207** that is made of the same, or different, material as the body of the cantilever **205**. Depending on the type of perturbation and the expected reaction of the sample **230** to the perturbation, the tip **207** or cantilever **205** material is selected. That is, if an electrical response from the sample **230** is expected, the cantilever **205** and tip **207** may be conductive and held at a potential in relation to the sample **230**, so as to register the electronic changes in the sample using electrostatic forces (e.g., electrostatic force microscopy (EFM)). Similarly, if a magnetic response is expected from a sample, the cantilever **205** is configured to register changes in the magnetic field of the sample.

The cantilever **205** is controlled by a drive controller **210**. When the cantilever **205** is oscillated, the drive controller **210** applies the oscillation drive signal at a particular frequency. The drive controller **210** may also control the positioning of the cantilever **205** in relation to the sample **230** (e.g., controls the height of the cantilever **205** above the sample).

The apparatus **200** also includes a detector **220** in communication with the cantilever **205** that is configured to measure the response of the cantilever **205** to the response of the sample in relation to the perturbation. In typical AFM systems, the detector **220** is an optical detector that detects an optical beam **217** (e.g., a laser) emitted from a light source **215** and reflected off the top of the cantilever **205** into the detector **220**. Small fluctuations in the oscillation/position of the cantilever **205** can be detected.

The apparatus **200** also includes an excitation signal generator **225** configured to apply a perturbation to the sample. The excitation signal generator **225** can apply a perturbation of any type known to those of skill in the art to the sample. Representative perturbation types have been discussed herein and include applying light, magnetic fields, electrical fields, RF pulses, or combinations thereof.

Finally, the apparatus **200** includes a triggering circuit **235** that is configured to coordinate the response of the cantilever **205** (i.e., via the detector **220**) and the perturbation (i.e., via the excitation signal generator **225**) such that the perturbation occurs at about the same position in the cantilever oscillation cycle. The triggering circuit **235** is configured to allow for averaging the deflection signal from multiple perturbation/measurement cycles, as set forth above with regard to the methods provided herein. Such averaging allows for improved signal quality.

In certain embodiments, the apparatus may also include a system controller that is in communication with the drive controller **210**. The system controller is configured to control the drive frequency applied by the drive controller. The system controller can also be in communication with the triggering circuit **235** and/or the detector **220**. It will be appreciated that the triggering circuit and system controller may all be integrally located in a single piece of equipment, or may be separate components of the larger apparatus.

In certain embodiments, the excitation signal generator **225** and the cantilever **205** are both configured to be in communication with a first location of a sample **230**. As illustrated in FIG. **1**C, when the cantilever **205** includes a tip **207**, the tip **207** and the excitation signal generator **225** are located on opposite sides of the first location of the sample **230**. It will be appreciated that this arrangement need not be specifically used, as long as the first location of the sample **230** is in contact (e.g., optical, electrical, magnetic, etc., contact) with the first location, and the cantilever **205** is adjacent to the first location **230** such that the response of the first location to the perturbation can be detected by the cantilever **205**.

In certain embodiments, the excitation signal generator **225** generates a perturbation that is transient or time-varying. As set forth above with regard to the methods provided herein, a transient or time-varying signal changes over time and therefore the time-domain properties of the effect of the perturbation on the sample can be used to characterize the material of the sample.

In certain embodiments, the apparatus **200** does not utilize a feedback loop to regulate the motion of the cantilever **205** following the perturbation. Particularly, as set forth above with regard to the method embodiments, the traditional use of a feedback loop to maintain constant phase frequency or amplitude of a cantilever oscillation is not employed in the presently described embodiments. By operating in a feedback-free regime, the present embodiments allow for the time-domain properties of the effect of the perturbation to be determined orders of magnitude more sensitively than those methods that utilize feedback loops to regulate cantilever motion.

In certain embodiments, the apparatus **200** also includes a positioning controller (not illustrated) that is configured to position the cantilever **205** in relation to the sample, for example, in the x, y, and z planes in relation to the sample surface. Such a positioning controller allows for the rastering of the cantilever **205** across the surface of the sample to multiple locations so as to form a two- or three-dimensional image of the sample surface.

The following example is intended to illustrate, and not limit, the embodiments disclosed herein.

Example

Feedback-Free Time-Resolved Electrostatic Force Microscopy (FF-trEFM)

To address the shortcomings of time-resolved microscopy methods fast frequency-shift feedback methods implemented in custom software on commercial AFM hardware were previously used to measure fast processes such as the accumulation of photogenerated charges in low-efficiency polymer solar cells on time scales approaching ~100 μs using time-resolved electrostatic force microscopy (trEFM). While fast compared to most atomic force microscopy (AFM) methods, even 100 μs is insufficient to study many processes of relevance in physical systems of interest (including more efficient organic and inorganic solar cells). In principle, one could achieve better time resolution by using more sophisticated feedback controls. However, any feedback system will ultimately face a signal/noise limit based on the slowest component in the loop. Here, we describe a feedback-free (FF-trEFM) approach to obtaining information about fast local force transients in an AFM and show that the method is capable of discerning useful information about fast local dynamics with transient rise times as short as ~200-300 ns.

The method, summarized in FIG. **1**D, relies upon analyzing the free oscillation dynamics of an atomic force microscope cantilever operating in conventional alternating current (AC)-mode on a commercial AFM with custom software and low-cost external hardware. The cantilever oscillation is digitized while a transient such as a voltage pulse or light pulse is triggered to initiate the local dynamics of interest. Importantly, a triggering circuit is employed to phase lock the trigger event to the cantilever motion (see also FIGS. **6**A and **6**B) so that the trigger always occurs at the same point in the cantilever oscillation, thereby improving the efficacy of signal averaging.

With the excellent signal/noise ratio achievable by averaging, the challenge becomes extracting the interesting dynamic behavior of the system from the cantilever motion. In AC-mode AFM, the cantilever motion can be described as a damped-driven harmonic oscillator. Following a transient perturbation, the force $F_z(t)$ and force gradient dF/dt experienced by the AFM tip may both change in time. These changes in turn alter the harmonic motion of the cantilever. The objective is thus to recover the time profiles of the $F_z(t)$ and/or dF/dt signals of interest from the resulting fast cantilever motion. In principle, with sufficient computational resources and some basic information about the system under investigation, one could attempt to reconstruct the temporal evolution of $F_z(t)$ and dF/dt by numerically integrating the equations of motion and fitting the resulting motion to the real tip data. Practically, we have found it faster and more convenient to employ a simplified data analysis procedure as described below.

As a proof of principle, we first consider detecting transients in a model damped driven harmonic oscillator governed by the classic equation of motion:

$$\frac{d^2z}{dt^2} + 2\beta\frac{dz}{dt} + \omega_0(t)^2 z = (F_0/m)\cos(\omega t) + F_e(t) \quad (1)$$

where z is the tip displacement, F_0 is the driving force applied to the cantilever, m is the cantilever mass, ω_0 is the resonance frequency of the cantilever that depends on factors such as the spring constant k and quality factor Q, and ω is the frequency of the driving force signal applied to the cantilever. F_e is an external force of interest acting on the cantilever that varies with time, and $\beta=\omega_0/2Q$ is the damping factor. Transient changes in the cantilever motion will arise from changes in the both force F_e, and its spatial derivative dF_e/dz; the latter effectively modifies the spring constant and thus shifts the instantaneous resonance frequency, with the shift $\Delta\omega_0$ being proportional to $(\partial F/\partial z)$.

As exponential decays are among the most ubiquitous signals resulting from small perturbations to a system, we consider a time dependent force F(t) and resonant frequency $\omega_0(t)$ of the form:

$$F_e(t\geq 0)=F_e(\infty)[1-\exp(-t/\tau)] \quad (2)$$

$$\omega_0(t\geq 0)=\omega_0(0)+\Delta\omega_0[1-\exp(-t/\tau)] \quad (3)$$

After a transient change in $F_e(t)$ and dF/dt (which effects a transient change in ω_0) the system will return to a steady state sinusoidal oscillation with a new equilibrium amplitude and phase on a characteristic timescale $2Q/\omega_0$, or ~3 ms for the cantilevers used here. While one might assume the $2Q/\omega_0$ time might limit the achievable time-resolution, the details of the fast transient motion prior to reaching the new steady state do encode information about τ on much shorter times and thus form the basis for subcycle time resolution. Extraction of this information is a matter of signal processing.

To demonstrate the feasibility of distinguishing different transient rise times or decays on fast timescales we first consider a theoretical damped driven harmonic oscillator governed by equation (1). This form represents the transient expected in many systems of interest, such as the charge accumulation and decay in nanostructured solar cells, and of systems exhibiting first order or pseudo-first order kinetics in general. To analyze the cantilever motion at early times we use numerical demodulation of the digitized cantilever signal and extract the envelope amplitude, instantaneous phase and

instantaneous frequency of the oscillating cantilever (details in supplementary information).

FIG. **1**E shows the instantaneous frequency recovered from a simulated cantilever following a transient change in F(z) and dF/dt according to equations (2)-(3) over 3 orders of magnitude, from 100 ns to 300 μs, while the cantilever parameters such as β, ω_0, F_e and k were chosen to agree with typical AFM experiments. Importantly, FIG. **1**E shows that the cantilever oscillation behavior is distinguishable for different $\tau<<2Q/\omega_0$ and even for $\tau<<1$ cantilever oscillation period. Furthermore, the data suggest a straightforward way to recover τ from an experimental data set. Notably, the time it takes for the instantaneous cantilever frequency to shift farthest from ω before relaxing, hereafter the time to first frequency shift peak (t_{FP}), is a monotonic function of τ. Thus, given adequate signal/noise one can in principle measure rise times or decays as short as 200 ns with widely available AFM cantilevers by generating a calibration curve of t_{FP} versus τ.

To demonstrate this method in practice, we use electrostatic force microscopy (EFM) as a test bed. In EFM, the tip and sample form a capacitor structure, and changes in the potential difference between the tip and sample change both the force and force gradient experienced by the oscillating cantilever. We can thus use programmed voltages applied to the tip by an arbitrary waveform generator to provide a model system with which to explore the performance of different data acquisition and analysis methods. Furthermore, since EFM can be used to detect photogenerated charge, time-resolved EFM has practical application in the local detection of charge carrier behavior below the diffraction limit in nanostructured semiconductors.

FIG. **2**A shows the instantaneous frequency obtained from the filtered, demodulated experimental data. A voltage with an exponential rise time was applied at t=1 ms to a Pt-coated cantilever oscillating 10 nm above a Au substrate. As with the simulated data, the cantilever returns to a new steady state oscillation with a new amplitude and phase on a timescale governed by $2Q/\omega_0$. FIG. **2**A further shows that, as for the simulated data, the t_{FP} is clearly different for each value of τ. We have further verified that the t_{FP} parameter is insensitive to cantilever lift height (see FIGS. **8** and **9**) and can be robustly extracted even at signal/noise levels well below those shown here (see FIG. **10**).

Along with the experimental data, FIG. **2**B plots instantaneous frequency vs. time for a full finite-element simulation of a conical-shaped tip with the tip-sample force calculated using the Maxwell stress tensor, $F_z=E_z^2\in_0\in_r$ where E_z is the electric field in the z direction and r is the radius of the tip at given height, integrated over the tip surface (see also FIG. **7**), as well as instantaneous frequency vs. time for a simple damped driven harmonic oscillator using experimentally-derived tip parameters. Notably, both the full finite-element method, and the simple harmonic oscillator model are able to reproduce the data across many orders of magnitude (FIG. **2**C). Indeed, there is near quantitative agreement between the simulations and the experimental behavior at rise times from sub-μs to 900 μs. At very short times (<1 μs) the simulations and experimental data show small quantitative deviations, which may be attributable in part to non-ideal tip shape, higher-order force corrections, and cantilever beam contributions. Though the quantitative frequency shift magnitude begins to differ, the t_{FP} value still scales with the rise time, with good agreement between the experiment and different simulation methods (FIG. **2**D).

The data in FIGS. **2**A-**2**D are striking. They demonstrate that experimentally, one can use the demodulated frequency to quantify rise or decay times for signals as fast as τ=200-300 ns—shorter than even a single cantilever oscillation period. To our knowledge, this is the fastest mechanically detected signal rise time that has been determined with AFM by orders of magnitude. We emphasize that, while performed with custom hardware and software, the method does not rely on expensive add-on instrumentation or rare custom probes and should therefore be readily accessible to a wide-range of AFM users. Indeed, we envision that with appropriate software modification, current-generation commercial AFMs have the hardware specifications necessary to implement time-resolved AFM with sub-microsecond accuracy.

There are many potential applications of faster time resolution scanning-probe analysis ranging from biophysics to solar energy. Here we demonstrate one example in the field of organic photovoltaics. Previously we have used a feedback-based time-resolved EFM (trEFM) method to study photoinduced charge generation in donor/acceptor polyfluorene copolymer blends used in organic photovoltaics. We have shown that charge accumulation following illumination is well approximated by single-exponential kinetics with the photo-charging rate being directly proportional to the local quantum efficiency and incident light intensity. However, operating under physically relevant (~1 sun) illumination conditions, characteristic charging times (determined by rate the photogenerated charges fill the tip-sample capacitor) are on the order of ~30-50 μs for blends with quantum efficiencies in the range of ~50-70%. In other words, the most interesting nanostructured organic systems such as poly(3-hexylthiophene):phenyl-C61-butyric acid methyl ester (P3HT:PCBM) remained inaccessible.

As a proof-of-concept, we applied FF-trEFM to the well-known polymer:fullerene OPV blend P3HT:PCBM by photoexciting the sample with a light step pulse and detecting the changes in resulting cantilever motion (FIG. **3**A). FIG. **3**B shows the light intensity-dependence of t_{FP}. At lower intensities, it takes longer for the film to become filled with enough photogenerated charge to screen the tip potential (i.e., τ increases), therefore t_{FP} shifts to longer times. The similar behavior from both photoinduced charging and exponential voltage signals lends confidence to our theoretical treatment of FF-trEFM in (1)-(3). Taken together, the two experiments imply that, at the same light intensity, the difference in t_{FP} reflects a difference in force gradient rise time τ, in this case the local charging efficiency.

P3HT:PCBM samples prepared with different thermal annealing times (FIG. **3**C), yield dramatically different external quantum efficiencies (EQE) as a function of wavelength, an effect attributed to changes in nanoscale film structure. However, even for the least efficient, unannealed blend classic feedback-based trEFM data are limited by instrument response (see FIG. **5**); the shaded region in FIG. **3**C shows the approximate EQE range accessible to classic feedback-based trEFM with our hardware.

FIG. **3**D shows a plot of $1/t_{FP}$, demonstrating that feedback-free trEFM can readily distinguish the differences between the samples with different EQEs as result from the different annealing times. For these experiments, we performed FF-trEFM and EQE measurements on the exact same organic semiconductor films, which were made into photovoltaic devices. The data in FIG. **3**D show that the measured $1/t_{FP}$ (triangles) value averaged over the image is directly proportional to EQE (circles). In fact, the data indicate that FF-trEFM can be used directly to predict the EQE that would be obtained from a photovoltaic device fabricated from a given P3HT/PCBM film morphology.

FIGS. **3**E and **3**F show a topography (FIG. **3**E) and $1/t_{FP}$ image (FIG. **3**F) for a film with an average EQE of 54%.

When comparing the distribution of $1/t_{FP}$ times across images of different films, the average and standard deviation of $1/t_{FP}$ both increase with device efficiency as shown in FIG. **3**D. This result is consistent with observations of nanoscale short-circuit photocurrent distributions on P3HT:PCBM devices, yet without the complications from tip work function and sample damage that can arise from such measurements, further confirming the utility of the FF-trEFM method.

We predict that FF-trEFM will not only enable studies of charge accumulation in more efficient nanostructured solar cells but will also enable the study of local recombination rates, which often have time constants in the range of 1-100 μs in OPV blends. Since any experiment with a time-dependent force gradient can use FF-trEFM, it should also be possible to utilize these methods in a host of new applications ranging from time-dependent magnetic force experiments to study fast local structural changes in biological samples. Because the method can in principle be implemented on much current generation AFM hardware, we hope it will ultimately become widely accessible.

Sample Preparation.

Au samples were prepared on degenerately-doped n-type Si(100) substrates (Silicon Quest International) with a 1 μm SiO_2 layer. The Si substrates were cleaved and sonicated in acetone and isopropyl alcohol prior to evaporation. Au films were formed by evaporating a 2.5 nm Cr adhesion layer followed by 55 nm Au. Au samples were sonicated in acetone and plasma cleaned prior to imaging.

Substrates for the OPV films were 1.5×1.5 cm^2 indium tin oxide (ITO)-coated glass substrates (TFD Inc.). Poly(ethylene dioxythiophene):poly(styrene-sulfonate) (PEDOT:PSS, Baytron P) was filtered and heated to 50° C. and deposited on the ITO and annealed at 100° C. for ~1 hour. Poly(3-hexylthiophene):phenyl-C_{61}-butyric acid methyl ester (P3HT:PCBM) films were formed from a 1:1 blend of P3HT (Rieke Metals, 90-93% RR) and PCBM (Nano-C, 99.5% pure) in chlorobenzene at ~42 mg/mL. The solution was stirred at 500 RPM at 55° C. overnight and was spin-coated warm onto the substrates at approximately 1500 RPM for 2 min. Aluminum top electrodes (85 nm) were then evaporated, creating devices of approximately 1.8 mm^2 based on overlap of ITO and Al electrodes. Films were annealed for various times at 110° C. on a preheated aluminum block mounted on a hot plate. All active layer preparation was in an inert environment, and all films were stored covered in aluminum foil in the glove box until imaged.

Instrumentation.

All FF-trEFM data were acquired using an MFP3D-BIO AFM (Asylum Research). Experiments on Au films were performed in ambient conditions, whereas those on P3HT:PCBM were performed under nitrogen using a closed fluid cell. For the Au data, we applied root exponential voltage pulses using an arbitrary waveform generator programmed via GPIB. For the P3HT:PCBM blends, we illuminated the samples using a 5 W, 523 nm LED (LedEngin LZ1-10G105) focused on the top surface of the film and co-aligned with the tip. Feedback-based trEFM data were acquired similar to that reported in previous work and described above. In each case, the cantilever deflection signal was routed into a triggering box to ensure that each light pulse was applied at the same phase. For voltage pulse tests on Au the same circuit was used as well. The sample was grounded relative to the tip in each case. Device measurements (external quantum efficiency) were performed under vacuum using a monochromated, 75 W Xenon lamp, with eight device pixels per film. External quantum efficiency measurements are from at least 3 batches of devices.

FF-trEFM Measurement.

FF-trEFM experiments were performed using in-house Igor Pro code and C-language XOP code to operate an external digitizer (Gage Compuscope USB 14400) for recording the cantilever motion at typical sample rates of 50 MHz. Prior to signal acquisition, the system was calibrated to ensure a correct translation factor between voltage and cantilever motion. The cantilever signal was averaged over numerous runs, typically 200, to improve the signal quality. Prior to each experimental run we measured the cantilever parameters such as the spring constant, Q, resonance frequency shift both with voltage and with applied light, and electrostatic force in order to properly model the motion (see Table 1). We changed the drive frequency applied to the cantilever and monitored the amplitude both before and after applying a voltage to the tip (to acquire the approximate electrostatic force) and before and, on P3HT:PCBM films, after applying light with the tip at a fixed voltage to acquire the approximate frequency shift and force due to photoinduced charging. DDHO simulations were performed using Igor Pro. Finite element method simulations were performed using COMSOL.

Cantilever Behavior in Response to Force Gradient Changes.

The cantilever in AFM behaves as a typical damped driven harmonic oscillator (DDHO), whose behavior is described by the well-known equations:

$$z(t<0) = A\cos(\omega t - \delta) \tag{4}$$

$$A = \frac{(F_0/m)}{\sqrt{(\omega_0^2-\omega^2)^2 + 4\omega^2\beta^2}} \tag{5}$$

$$\delta = \tan^{-1}[2\omega\beta/(\omega_0^2-\omega^2)] \tag{6}$$

where A is the amplitude, δ is the phase of the cantilever relative to the driving signal, F_0 is the driving force applied to the cantilever, m is the cantilever mass, ω_0 is the resonance frequency, ω is the frequency of the driving force signal applied to the cantilever, F_e is the electrostatic force due to the charging of the surface, and $\beta=\omega_0/2Q$ is the damping factor. When the drive frequency $\omega=\omega_0$, the amplitude and phase are at a peak and at π/2 respectively. As the resonance frequency

We measure the electrostatic force and cantilever properties by measuring the free cantilever parameters far from the surface (10 μm) and at a given lift height close to the surface (10 to 100 nm). The tip is then moved to the specified lift height, and the cantilever amplitude, phase, and deflection are recorded. This procedure is repeated several times and the curves are averaged together. For the OPV films, the voltage is held constant and the light is turned on to effect a change in the electrostatic force/force gradient.

FIG. **4** relates to resonance frequency response to changes in the electrostatic force gradient. (A) Cantilever oscillation amplitude curves on an organic photodiode (PFB:F8BT) taken at 0 V (black), 10 V (blue), and 10 V under 405 nm illumination (pink), across a range of drive frequencies. (B) Example frequency shift response showing the expected quadratic dependence on applied voltage as well as the change in differential capacitance gradient due to illumination. Data taken at 10 nm above the same sample with approximately 1590 W/m^2 intensity.

FIG. **4**A shows how the amplitude of the AFM cantilever behaves with no voltage, an applied voltage, and an applied voltage and constant illumination on a poly(9,9'-dioctylfluo-

rene-co-bis-N,N'-(4-butylphenyl)-bis-N,N'-phenyl-1,4-phenylenediamine:poly-(9,9'-dioctylfluorene-co-benzothiadiazole) (PFB:F8BT) film at a height of 20 nm above the sample. The amplitude decreases and the resonance frequency peak shifts to a lower frequency as $\partial^2C/\partial z^2$ changes increasingly by first applying a voltage and then by adding the photogenerated charges. Under illumination, $\partial^2C/\partial z^2$ increases and therefore the curvature in the parabola increases as shown in FIG. **4**B.

From the cantilever amplitude, phase, and deflection signals recorded across a range of drive frequencies before and after excitation, we can extract the relevant system parameters such as Q, β, k, amplitude, force, and resonance frequency. An example is shown in Table 1 below. Table 1 relates to cantilever parameters for the system in FIG. **4**. The data taken at 10 nm in FIG. **4** show how the Q, resonance frequency, and spring constant all decrease. The net electrostatic force is much larger from turning on the voltage than from turning on the light. LED power is ~1590 W/m^2. AMPINVOLS and DEFINVOLS are the inverted optical lever sensitivity settings for converting an amplitude and deflection signal from V to nm.

TABLE 1

Cantilever parameters for the system in FIG. 4A.

Calibration Parameters	10 μm, 0 V
Thermal Resonance Frequency (Hz)	272614
Thermal Spring Constant (N/m)	22.807
DEFINVOLS (m/V)	4.5273E−08
AMPINVOLS (m/V)	4.9348E−08
Mass (kg)	7.7758E−12
Q Factor	475.107
Beta (/s)	1802.35
Electrostatic force gradient dF/dZ (N/m)	−3.38189

	10 nm, 0 V (Dark)	10 nm, 10 V (Dark)	10 nm, 10 V (LED on)
Resonance Frequency (Hz)	272544	272325	272164
Amplitude (m)	1.3143E−08	1.3022E−08	1.2508E−08
Q Factor	427.578	421.701	406.168
Beta/Damping (/s)	2002.49	2028.77	2105.11
Driving Force (N)	7.0103E−10	7.0314E−10	7.0152E−10
Spring Constant (N/m)	22.807	22.7704	22.7804

	10 V versus 0 V	10 V, LED Off versus On
Net Electrostatic Force (N)	9.8038E−09	2.1314E−09
Net Frequency Shift (Hz)	−219	−159
Change in Spring Constant (N/m)	−0.0366372	−0.0266255
Change in Peak Amplitude (nm)	−1.2077E−10	−5.0787E−10

The net electrostatic force F_e is significantly higher for just applying the voltage versus no voltage (~9.8 nN) than for having the light on versus off (~2.1 nN). This is consistent with the observation in FIG. **3**B where the net frequency shift is smaller for the light than just turning on the voltage. The other factors scale as expected: Q decreases with voltage and again with light as the increase in F_e induces a stronger electrostatic attraction and thus more damping, and the spring constant decreases due to the change in electrostatic force gradient.

Limitation of Feedback-Based Methods.

Classic time-resolved electrostatic force microscopy (trEFM) uses a feedback-based method to track the change in resonance frequency. We discuss above how this is limited to a time-resolution of ~100 μs. In a typical organic photovoltaic film such as PFB:F8BT, prepared using a method similar to that reported previously by our group, the charging rate of the film scales with the light intensity. This effect is shown in FIG. **5**A, as the incident light intensity increases the change in $\partial F/\partial z$, the change in Δω increases until becoming a step function when the limit of the feedback electronics is reached, as evidenced by the trEFM data taken at light intensities beyond ~430 W/m^2. For an efficient blend like P3HT:PCBM, the behavior is different (possibly due to higher charge carrier mobility than in PFB:F8BT) but Δω changes as a step function even at low light intensities of <1 W/m^2 (FIG. **5**B). The time resolution limit can be determined by using consecutive voltage pulses and observing the point at which they can be distinguished, as in FIGS. **5**C and **5**D. Through consecutive voltage pulses, it is possible to determine the lower limit of approximately 100 μs for the old trEFM method, wherein FIG. **5**C illustrates the distinction of consecutive voltage pulses using the embodiments provided herein and FIG. **5**D illustrates the same frequency of voltage pulse using a traditional time-resolved electrostatic force microscopy system, which cannot distinguish consecutive pulses as quickly as those of the embodiments provided herein (i.e., FIG. **5**C).

FIG. **5** relates to limits of time-resolution by feedback-based trEFM. (A) Typical normalized classic trEFM data curves of the same PFB:F8BT organic photovoltaic sample, showing the time-resolved behavior in the frequency shift. As the intensity increases the frequency shift response resembles a step function due to the time resolution limit, with ringing due to the feedback circuit, in this case occurring at an incident 405 nm LED intensity of ~430 W/m^2. (B) For an efficient OPV blend, P3HT:PCBM, saturation occurs even at intensities as low as <1 W/m^2 using a 532 nm LED in this case. (C and D) Through consecutive voltage pulses, it is possible to determine the lower limit of approximately 100 μs for the old trEFM method.

Additional Instrumentation/Data Acquisition.

The data were acquired using the schematic shown in FIGS. **1**C and **3**A. The tip is actuated using the drive signal with frequency ω to shake the tip. At the same time, the MFP3D hardware is used to bias the tip (usually at 10 V). The deflection signal is fed into a trigger circuit. The circuit consists of a comparator and a D-flip flop, wherein the input deflection signal (after DC filtering) becomes a clock signal for the D-flip flop. The trigger signal is only passed at, approximately, the positive zero-crossing of the deflection signal; the phase can conceivably be changed depending on the reference signal sent to the comparator. The subsequent locked trigger is then used to simultaneously power the LED and to trigger the digitizer. The LED, with a peak wavelength at 405 nm or 523 nm, is optionally attenuated via neutral density filters and focused through an objective onto the top surface of the sample.

The deflection signal is averaged by taking numerous runs, typically 1000 to 1250 for point scans and 6 per pixel for imaging, typically at sample rates of 50 MHz and 5 MHz, respectively. Without the circuitry, there is significant noise in the resulting averaged wave of +/−a cycle, as in FIGS. **6**A (unlocked) and **6**B (locked). The triggering circuit ensures that each wave is acquired at the same point and eliminates this time-resolution bottleneck.

FIGS. **6**A and **6**B relate to using a phase-detecting circuit improves time resolution. Consecutive digitized deflection waves showing significant jitter without (FIG. **6**A) and with (FIG. **6**B) a triggering circuit. The circuit ensures that the voltage and light are applied at the same point in the cycle, thus improving averaging by eliminating the averaging errors that can occur in the unlocked trigger case.

Data Processing.

The averaged deflection signal z(t) is filtered using a software finite impulse response bandpass filter and a standard Blackman windowing function. The filtering does not adversely affect the t_{FP} as long as the bandpass window contains a sufficient number of coefficients. Furthermore, to preserve the integrity of the step response, particularly for fast perturbations, we use a causal form of the filter with limited time shift. For the frequency curves plotted in, for example, FIG. **1**E in the main text, the data are only shifted in time by ~10 μs. Using a standard noncausal filter results in no such shift at the expense of blurring the start time of the resulting pulse.

The envelope amplitude A(t) and the instantaneous phase θ(t) are digitally extracted through a standard software Hilbert Transform demodulation. Functionally, the Hilbert Transform phase shifts a signal by π/2; by combining the original signal u(t) with the phase-shifted signal û(t) it is possible to acquire A(t) and θ(t), and subsequently the instantaneous frequency f(t) through these equations

$$A(t) = \sqrt{u(t)^2 + \hat{u}(t)^2} \tag{7}$$

$$\theta(t) = \tan^{-1}[-\hat{u}(t)/u(t)] \tag{8}$$

$$f(t) = \frac{1}{2\pi}\frac{d}{dt}\theta(t) = \frac{1}{2\pi}\frac{d}{dt}[\tan^{-1}[-\hat{u}(t)/u(t)]] \tag{9}$$

For an arbitrary sinusoidal signal of the form A(t)exp [j(ωt+δ)], θ(t)=ωt+δ.

However, in our case the signal δ is really δ(t), and it is the signal of interest as it is the phase offset from the drive signal. The behavior of δ(t) reflects how the resonance frequency $\omega_0(t)$ changes, so to isolate this we simply subtract ωt from the θ(t) signal. The resulting instantaneous frequency shift is therefore dθ(t)/dt=dδ(t)/dt.

The value of t_{FP} involves finding the lowest value of the f(t) wave. We fit a polynomial curve the lowest frequency peak in the demodulated f(t) to find this value; the purpose of the curve is not physical in origin, it is to extract a value from the f(t). For the imaging data we take multiple images over the same location and average the waves at each location to reduce signal:noise. The resulting image is median-filtered to reduce the noise effects; this does not change the average value reported in FIG. **3**D and primarily eliminates erroneous low-t_{FP} values that can be detected.

While there are certainly other ways to probe the system (the time it takes for the phase of the signal to initially change, for example, or the time for the system to shift some set frequency from the drive), the choice of using t_{FP} is deliberate after numerous tests found this metric to be the most robust to sample drift, tip condition, and lift height.

Finite Element Simulations.

The tip response is also numerically simulated with COMSOL. Tip geometry is modeled with 2D axis geometry, as shown in FIG. **7**. The left side is the symmetry axis, upper boundary is the bottom of the cantilever and tip, the lower boundary is top of sample surface, area in between represents air. The tilted line revolves around the axis to form tip geometry, radius of the tip is 25 nm. The tip length and width are set to 6 μm and 1 μm, respectively. These are smaller than actual values (cantilevers used are typically 15 μm tall) and we do not include the full beam. The rationale behind this is that a predominately large portion of electric force is from the tip while the bulk of the tip and we therefore balance computation time with simulation accuracy.

FIG. **7** relates to numerical simulations of the tip-sample system. Electrostatic potential maps (z-component) of the tip-sample junction, where the sample and tip are metals (such as Pt and indium tin oxide, respectively).

Movement of tip is governed by the DDHO equations, and the time-dependent electric force between the tip and sample is calculated with the Maxwell stress tensor as discussed in the main text. In each time step of the simulation, the tip position is recalculated using the harmonic oscillation as well as the effect of force via the Maxwell stress tensor.

FF-trEFM Data with Variations in Lift Height.

The frequency shift is proportional to the force gradient and therefore decreases with as the tip moves farther from the surface. However, FIG. **8** indicates that the t_{FP} does not vary considerably when the lift height is changed. The dashed lines (50 nm) show approximately the same t_{FP} value as the solid lines (10 nm) when looking at the intersection of the t_{FP} lines with the respective curves.

FIG. **8** relates to lift height dependence of t_{FP} values. At four different voltage pulse rise times taken at 10 nm (solid) and 50 nm (dashed) lift heights, the t_{FP} values are approximately the same. These data indicate that the t_{FP} metric is robust against vertical drift effects unlike metrics used in steady-state EFM such as frequency shift magnitude.

FIG. **9** shows the monotonic link between t_{FP} and charging rate time for a PFB:F8BT film with two different tips. Below 100 nm lift heights, most of the data fall along the same trend line. At 100 nm, it is possible that as the distance increases the electrostatic force is no longer dominated by the intense field at the apex but rather is a sum of the tip apex, the conical tip structure, and the cantilever beam. Additionally, the signal-to-noise is much lower as the lift height increases due to the smaller net frequency shift. We find that using 10 to 50 nm for the lift height is optimal.

FIG. **9** relates to lift height data comparing FF-trEFM and feedback-based trEFM on a PFB:F8BT film. Data were acquired at several lift heights and light intensities (405 nm LED, intensities range from 1560 W/m^2 to 1.4 W/m^2) with two different tips. As expected, there is a correlation between the classic charging time (y-axis) and t_{FP} value (x-axis) and both techniques are fairly robust to lift height variations given that the data points fall on the same general trendline.

Voltage Dependence of t_{FP}.

We can use averaging to measure signals at low signal:noise. In FIG. **10**, we change the voltage while keeping other parameters the same and monitor the instantaneous frequency. Because frequency shift scales V^2, decreasing the applied voltage from 10 V to 1 V causes the net frequency shift to go from ~280 Hz (black) to ~2.8 Hz (blue) with a signal:noise level reduced by ~99%. However, the t_{FP} values are approximately constant as can be observed by the overlapping behavior of the frequency curves at various voltage levels, meaning that we can use FF-trEFM processing for signals operating near, for example, the typical V_{OC} level in a photovoltaic cell.

FIG. **10** relates to instantaneous frequency with changes in applied voltage. The instantaneous frequency is shown for a 150 μs rise time voltage pulse with four different voltages: 10 V, 5 V, 2 V, and 1 V. The t_{FP} value is approximately the same in that the instantaneous frequency trend is consistent the same across all voltages. The signal:noise varies with ΔV^2, therefore at 1 V the frequency data are significantly noisier yet the trend is still observable for a frequency shift of only ~2.8 Hz versus a drive frequency of 248.603 kHz.

Force and Force-Gradient Dependence in FF-trEFM.

In FIG. **2**D, the t_{FP} vs. voltage rise time behavior seems to exhibit a change in behavior right around the single cycle time (~4 μs for a 250 kHz cantilever) and below. However, we hypothesize that this effect is due to a combination of at least three interrelated factors: (1) the magnitude of the electrostatic force F_e, (2) the magnitude of the frequency shift and therefore the magnitude of the change in force gradient, $\Delta\partial F/\partial z$, (3) well-known Gibbs ringing phenomenon that is a side effect of using the Hilbert transform to extract information from a step function. We minimize (3) by oversampling at significantly beyond the Nyquist level and through, if necessary, upsampling the data in postprocessing. However, it is unavoidable particularly as filtering out high-frequency noise inevitably removes harmonics needed to recreate a step function.

Factors (1) and (2) cannot be controlled as they vary with the experiment, but we can use our simulations to determine how dependent FF-trEFM is on these effects. In FIGS. **11**A and **11**B we explore how the t_{FP} varies with rise time either by changing the electrostatic force F_e values (top) or force gradient dF_e/dz values (bottom) using our modified-DDHO simulation. Note that here we are displaying the data with voltage rise time on the y-axis. When we vary the electrostatic force, we see that the t_{FP} values only vary below a certain voltage rise time, at ~10 μs. For large force values (20 nN), the resolution cuts off at ~10 μs, and below this point the t_{FP} values do not follow an expected monotonic trend. At lower force values (<1 nN), the monotonicity is preserved even in the sub-1 μs regime, as is more clearly observed in the linear-scale inset.

FIGS. **11**A and **11**B illustrate the effect of electrostatic force and force gradient on sub-cycle time resolution. Simulated data using root exponential voltage pulses by sweeping either (A) the electrostatic force or (B) the net frequency shift (effectively the change in electrostatic force gradient). (A) Changing the force plays a significant role in the t_{FP} values in the sub-10 μs regime. (B) Changing the frequency shift affects the proportionality between t_{FP} values at a given sub-10 μs level; as the frequency shift increases, the larger the difference in t_{FP} between two consecutive voltage rise times. Bolded values indicate typical experimental conditions on a PFB:F8BT blend. Insets show the sub-5 μs data on a linear scale.

In FIG. **11**B, we vary the change in electrostatic force gradient $\Delta\partial F/\partial z$ by changing the net frequency shift, with the total shift being proportional to how much the electrostatic force gradient affects the spring constant. Below ~5 μs, the extent of the frequency shift determines the behavior in t_{FP}. The larger the change in resonance frequency (the larger $\Delta\partial F/\partial z$), the greater the change in t_{FP} with respect to changes in the voltage signal rise time and the more monotonic its behavior.

The force and force gradient counter each other. Raising the lift height or using very sharp tips would reduce F_e but would also reduce $\Delta\partial F/\partial z$. The simulations may explain the roll-off in the voltage pulse data on Au because on metals, F_e is upwards of 10 nN and therefore more of an issue. For dielectric samples like the OPV samples, these values are often sub-nN (see Table 1) and therefore may exhibit even better time-resolution than reported here.

While illustrative embodiments have been illustrated and described, it will be appreciated that various changes can be made therein without departing from the spirit and scope of the invention.

The invention claimed is:

1. An apparatus, comprising:

a cantilever configured to measure the response of a sample adjacent the cantilever;

a drive controller configured to oscillate the cantilever at a drive frequency;

a detector in communication with the cantilever, which is configured to measure the response of the cantilever;

an excitation signal generator configured to apply a perturbation to the sample; and

a triggering circuit configured to coordinate the response of the cantilever and the perturbation such that the perturbation occurs at the about the same position in the cantilever oscillation cycle.

2. The apparatus of claim **1**, further comprising a system controller in communication with the drive controller, said system controller being configured to control the drive frequency applied by the drive controller.

3. The apparatus of claim **2**, wherein the system controller is in communication with the triggering circuit.

4. The apparatus of claim **2**, wherein the system controller is in communication with the detector.

5. The apparatus of claim **1**, wherein the cantilever is an atomic force microscopy (AFM) cantilever, and wherein the detector is in optical communication with the cantilever through an optical beam reflected off the cantilever and into the detector, wherein said detector is an optical detector.

6. The apparatus of claim **1**, wherein the excitation signal generator is selected from the group consisting of a light source, a magnetic source, an electrical source, a radio frequency source, and combinations thereof.

7. The apparatus of claim **1**, wherein the excitation signal generator and the cantilever are both configured to be in communication with a first location on the sample.

8. The apparatus of claim **1**, wherein the excitation signal generator generates a perturbation that is transient or time-varying.

9. The apparatus of claim **1**, wherein the apparatus does not utilize a feedback loop to regulate cantilever motion following the perturbation.

10. The apparatus of claim **1**, further comprising a positioning controller configured to position the cantilever in relation to the sample.

11. A time-resolved microscopy method for measuring the response of a sample to a perturbation, using a cantilever positioned adjacent a first location of the sample, the method comprising the steps of:

(a) applying the perturbation to the sample at a first time;

(b) measuring the motion of the cantilever in response to the effect of the perturbation on the sample for a predetermined first length of time, to provide a deflection signal, without imposing feedback to regulate cantilever motion following the perturbation; and

(c) determining from the deflection signal the time-domain properties of the effect of the perturbation on the first location of the sample.

12. The method of claim **11**, wherein the cantilever is an oscillating cantilever vibrated at a steady-state frequency prior to the perturbation, and wherein determining the time-domain properties comprises the steps of:

(i) extracting an instantaneous frequency of the cantilever from the deflection signal, to provide a frequency signal for the first length of time;

(ii) identifying within the frequency signal the maximum frequency shift from the steady-state frequency, to provide a frequency peak value at a peak time; and

(iii) determining the amount of time intermediate the first time and the peak time, to provide a frequency-shift-peak time that is characteristic of the time-domain characteristics of the effect of the perturbation on the sample at the first location.

13. The method of claim **12**, wherein extracting an instantaneous frequency of the cantilever from the deflection signal comprises determining an instantaneous phase of the cantilever from the deflection signal.

14. The method of claim **11**, further comprising a step of repeating the steps of applying the perturbation and measuring the motion of the cantilever in response to the effect of the perturbation multiple times at the first location using the same magnitude of perturbation and averaging the multiple deflection signals to provide an averaged deflection signal, wherein the averaged deflection signal is used as the deflection signal when determining the time-domain properties of the effect of the perturbation on the first location of the sample.

15. The method of claim **14**, wherein the cantilever is an oscillating cantilever and wherein repeating the steps of applying the perturbation and measuring the motion of the cantilever in response to the effect of the perturbation multiple times comprises coordinating the position of the cantilever and the perturbation such that the perturbation occurs at about the same position in the cantilever oscillation cycle.

16. The method of claim **11**, further comprising rastering the cantilever across the sample to multiple locations while determining, from the deflection signal at each of the multiple locations, the time-domain properties of the effect of the perturbation on the multiple locations of the sample, to provide an image of the sample.

17. The method of claim **11**, wherein the perturbation is selected from the group consisting of a light signal, a magnetic signal, an electrical signal, a radio frequency pulse signal, and combinations thereof.

18. The method of claim **1**, wherein the perturbation is transient or time-varying.

* * * * *